The Hong Kong Polytechnic University
Department of Computing

Nonlocal Self-Similarity Based Prior Modeling for Image Denoising

Jun Xu

A thesis submitted in partial fulfillment

of the requirements for the degree of

Doctor of Philosophy

Dec. 2017

CERTIFICATE OF ORIGINALITY

We hereby declare that this thesis is my own work and that, to the best of my knowledge and belief, it reproduces no material previously published or written, nor material that has been accepted for the award of any other degree or diploma, except where due acknowledgement has been made in the text.

_____(Signed)

_____(Name of student)

Abstract

The nonlocal self-similarity (NSS) prior of natural images has been successfully used in many image restoration methods. In this thesis, we investigate the design of new and more effective NSS models for image denoising, especially real-world image denoising. A new dataset to benchmark the study of real-world image denoising method is also established.

To exploit the NSS prior from the external clean natural images, we propose a patch group (PG) based NSS prior learning scheme to learn explicit NSS models from natural images for high performance denoising. PGs are extracted from training images by putting nonlocal similar patches into groups, and a PG based Gaussian Mixture Model (PG-GMM) learning algorithm is developed to learn the NSS prior. We demonstrate that, owe to the learned PG-GMM, a simple weighted sparse coding model, which has a closed-form solution, can be used to perform image denoising effectively, resulting in high PSNR measure, fast speed, and particularly visually pleasing denoising outputs.

The noise in real-world images captured by digital cameras is hard to be characterized by the additive white Gaussian noise (AWGN) model. Therefore, many denoising methods developed under the AWGN assumption may not work well on real-world noisy images. To exploit the information in both external data and the given noisy image, we develop an external prior guided internal prior learning method for real-world noisy image denoising. We first learn external priors from an independent set of clean natural images. With the aid of learned external priors, we then learn internal priors from the given noisy image to refine the prior model. The external and internal priors are formulated as a set of orthogonal dictionaries to efficiently reconstruct the desired image. Extensive experiments are performed on several real-world noisy image datasets. The proposed method demonstrates highly competitive denoising performance, outperforming state-of-the-art denoising methods including those designed for real-world noisy images.

We then investigate how to utilize solely the internal NSS redundancy of noisy images for

real-world image denoising task. To this end, we propose a multi-channel (MC) optimization model for real-world color image denoising under the weighted nuclear norm minimization (WNNM) framework. We concatenate the RGB patches to make use of the channel redundancy, and introduce a weight matrix to balance the data fidelity of the three channels in consideration of their different noise statistics. The proposed MC-WNNM model has no analytical solution. We reformulate it into a linear equality-constrained problem and solve it via alternating direction method of multipliers. Each alternative updating step has a closed-form solution and the convergence can be guaranteed. Experiments on both synthetic and real-world noisy image datasets demonstrate the superiority of the proposed MC-WNNM model over state-of-the-art image denoising methods.

We also develop a trilateral weighted sparse coding (TWSC) scheme for robust real-world image denoising. Specifically, we introduce three weight matrices into the data and regularization terms of the sparse coding framework to characterize the statistics of real-world noise and image priors. TWSC can be reformulated as a linear equality-constrained problem and can be solved by the alternating direction method of multipliers. The existence and uniqueness of the solution and convergence of the proposed algorithm are analyzed. Extensive experiments demonstrate that the proposed TWSC scheme outperforms state-of-the-art denoising methods on removing real-world noise.

Finally, to benchmark the real-world image denoising problem, and to complement the previous datasets, we construct a new dataset which contains more comprehensive scene contents with more camera brands and camera settings. Extensive comparison experiments are performed on existing and our new benchmark datasets. The results show that our new dataset is more challenging than previous ones, and real-world image denoising is still a challenging task which needs broader and deeper study.

In summary, in this thesis we investigate in-depth the learning of NSS priors for image denoising, develop several new and effective denoising models, and present a new dataset of

real-world noisy images. The research outputs of this thesis not only enrich the understanding of NSS based statistical image modeling, but also demonstrate state-of-the-art performance in image denoising, especially real-world image denoising.

Keywords: Real-world image denoising, Nonlocal self-similarity, Sparse models, Low-rank models.

List of Publications

Conference Papers

1. **Jun Xu**, Lei Zhang, David Zhang, Xiangchu Feng, "Multi-channel Weighted Nuclear Norm Minimization for Real Color Image Denoising". International Conference on Computer Vision (ICCV), 1096–1104, Venice, Italy, 2017.

2. **Jun Xu**, Lei Zhang, Wangmeng Zuo, David Zhang and Xiangchu Feng, "Patch Group Based Nonlocal Self-Similarity Prior Learning for Image Denoising". International Conference on Computer Vision (ICCV), 244–252, Santiago, Chile, 2015.

Journal Papers (Published and under revision)

1. **Jun Xu**, Lei Zhang, David Zhang, "External Prior Guided Internal Prior Learning for Real Noisy Image Denoising". Major Revision in IEEE Transactions on Image Processing.

2. Dongwei Ren, Wangmeng Zuo, David Zhang, **Jun Xu**, Lei Zhang, "Partial Deconvolution with Inaccurate Blur Kernel". IEEE Transactions on Image Processing, 27(1), 511–524, 2018.

Papers Submitted

1. **Jun Xu**, Lei Zhang, David Zhang, "A Trilateral Weighted Sparse Coding Scheme for Realistic Image Denoising". Submitted to CVPR 2018.

2. **Jun Xu**, Deyu Meng, Lei Zhang, David Zhang, "Scaled Simplex Representation for Efficient Subspace Clustering". Submitted to CVPR 2018.

3. Zhetong Liang, **Jun Xu**, David Zhang, Zisheng Cao, Lei Zhang, "A Hybrid L1-L0 Layer Decomposition Model for Tone Mapping". Submitted to CVPR 2018.

Acknowledgement

First and foremost, I want to express my gratitude to my chief-supervisor, Prof. David Zhang, for his support and my co-supervisor, Prof. Lei Zhang, for his wonderful guidance, support and generosity. It is my great pleasure to be a student of them, who are always showing me the right direction, but allowing me to walk the path myself.

I would like to express my gratitude to Prof. Wangmeng Zuo, Prof. Xiangchu Feng and Prof. Deyu Meng in my Ph.D. study. Their valuable suggestions have greatly help me to do good research, and I am very thankful for their very constructive suggestions on my articles.

I want to express my gratitude to my lab and office mates, for their assistance, for their encouragement and for the wonderful time in The Hong Kong Polytechnic University I have shared with them.

Finally, I want to thank my family for inspiring me to pursue this route. I want to thank them for their endless love, support, and encouragement.

Contents

List of Figures

List of Tables

Chapter 1

Introduction

Nowadays, CCD or CMOS cameras are becoming more and more important in our daily life for their appplications in photography, security system, and robots, etc. The camera imaging pipeline is the key to transform the photons reflected by the real scene into the pixel values of an image, which can be displayed on a screen. During the camera imaging process, the noise is unavoidably generated due to many reasons. Two major reasons of noise generation are the discrete nature of light and the thermal agitation, which result in the photon shot noise and the dark-current noise, respectively. Image denoising aims to study how to recover the latent clean image from the captured noisy observation.

This chapter will introduce how the noise is modeled in the imaging process, how the image denoising problem is formulated, how to evaluate the image denoising performance, and the major denoising methods. Finally, we will summarize the contributions and the structure of this thesis.

1.1 The Formulation of Image Denoising

Due to the discrete nature of light and the thermal agitation, the camera sensors will have inaccurate measurements of image pixels. The measurement error is also called image noise.

The noise generated during the imaging pipeline can be categorized into random noise, spatial non-uniformity noise, and quantization noise [32, 38]. The random noise includes photon shot noise, dark current, and readout noise. The spatial non-uniformity noise includes fixed pattern noise (PRNU, DCNU) and CCD/CMOS specific noise. The quantization noise is the error generated in the final conversion from pixel measurements to pixel integers.

To better analyze the property of noise quantitatively, a simplified signal acquisition model [32] (for each pixel) can be described as follows:

$$\boldsymbol{P} = f((g_{cv}(\boldsymbol{C} + \boldsymbol{D}) + \boldsymbol{N}_{reset})g_{out} + \boldsymbol{N}_{out}) + \boldsymbol{Q}, \tag{1.1}$$

where $\boldsymbol{P}$ is the raw pixel value, and f is the camera response function (usually f is a linear function before attaining a saturation threshold). $\boldsymbol{C}$ is the number of absorbed electrons (charges) transformed from the photons via the photon-diodes in the camera sensor, which can be modeled by a Poisson distribution. $\boldsymbol{D}$ is the number of absorbed electrons generated in dark current by thermal generation, which is also often modeled by a Poisson distribution. $\boldsymbol{N}_{reset}$ is the thermal noise generated by the readout circuitry (or reset noise related to reset voltage), which can be well modeled by a Gaussian disribution. $\boldsymbol{N}_{out}$ is the readout noise, which is also modeled by a Gaussian distribution. g_{cv} is the equivalent capacitance (EC) of the photo-diode and the gain factor during charge to voltage conversion. g_{out} is the gain factor during voltage to pixel value conversion (readout). $\boldsymbol{Q}$ is the quantization error introduced during rounding to interger values, which is usually uniformly distributed and normally negligible compared to the readout noise

After some merging and simplifying, the signal acquisition model (1.1) can be formulated as follows:

$$\begin{aligned} \mathbf{P} &= f((g_{cv}(\mathbf{C} + \mathbf{D}) + \mathbf{N}_{reset})g_{out} + \mathbf{N}_{out}) + \mathbf{Q}, \\ &= f(g_{cv}g_{out}(\mathbf{C} + \mathbf{D}) + g_{out}\mathbf{N}_{reset} + \mathbf{N}_{out}) + \mathbf{Q}, \\ &= f(g\lambda + N_R) + \mathbf{Q}, \end{aligned} \tag{1.2}$$

where $g = g_{cv}g_{out}$ is the overall camera gain factor, $\lambda = \mathbf{C}+\mathbf{D}$ is the number of electrons in pixel capacitor, and $N_R = g_{out}\mathbf{N}_{reset} + \mathbf{N}_{out}$ is the overall readout noise. In summary, the overall noise generated in the camera imaging pipeline can be modeled by a mixed Poisson and Gaussian distribution [32], which can also be approximated by a single Gaussian distribution according to the Central Limit Theorem.

To evaluate the performance of existing image denoising methods, the most common type of tested noise is the additive white Gaussian noise (AWGN) [22, 30]. The images with AWGN noise are corrupted by random values following Gaussian distribution with zero mean and a certain standard deviation (std). However, the real-world noise in the photographs captured by CCD or CMOS cameras is very complex and can hardly be modeled by a simple Gaussian distribution. The mixed Poisson and Gaussian distribution [32] is also an ideal model for noise in the raw images captured by digital cameras. However, due the complex in-camera imaging pipeline, the noise in the output image will become much more complex than those in the raw image [45, 68]. This makes image denoising, especially real-world image denoising, a vary challenging task. The image denoising methods designed for the synthetic AWGN noise may fail when dealing with the real-world images captured by CCD or CMOS cameras.

As a classical yet fundamental problem for image quality enhancement in computer vision and photography, image denoising is generally modeled to recover the latent clean image $\boldsymbol{x}$ from the observed noisy image $\boldsymbol{y} = \boldsymbol{x} + \boldsymbol{n}$, where $\boldsymbol{n}$ is assumed to be the additive noise. In literature, most of the existing methods are designed for dealing with AWGN, where $\boldsymbol{n}$ follows Gaussian distribution $\mathcal{N}(0, \sigma^2)$. The AWGN noise is a neat testing bed for evaluating the image denoising methods. However, for real-world noisy images, the image noise $\boldsymbol{n}$ is no longer Gaussian and signal independent, which makes the real-world image denoising problem much more difficult.

From the perspective of machine learning, image denoising can be viewed as a regression problem, in which a *plausible* clean image can be obtained from the infinite number of possi-

ble candidates. The word *plausible* means that the denoised image should look like the noisy image but without the noise corruption. As indicated in [10], regression models, such as the famous least squares regression and LASSO [88], can be very inaccurate if we do not add proper prior to them. Similarly, image denoising problem would be very difficult if we do not employ suitable prior information of images. It is meaningful to exploit the prior information of the most *plausible* image given the input noisy image. The most commonly used framework in image denoising community is the Bayesian framework, which is also known as the maximum a-posterior (MAP) scheme. Under the MAP framework, the most *plausible* latent clean image is the one with maximum Bayesian probability for its noisy counterpart. The posterior probability can be computed with some explicit form which we will introduce in the following sections. In fact, the posterior probability can measure the distance of the latent clean image to the given noisy image. The closeness is usually measured by an ℓ_2 norm of the difference between the two images. There are many candidate images which have the same ℓ_2 norm distance to the given noisy image. But some images in the same distance are more *plausible* than the others due to the aspects of less artifacts, better structural preservation, and less remaining noise, etc. In general, more prior information of natural images can lead to better image denoising performance.

In order to evaluate the quality of denoised images, as well as compare the denoising performance of different methods, we need metrics of goodness for the denoised images. A natural problem is, how to measure the quality of the denoised image? To answer this question, we resort to the image quality assessment (IQA) metrics, which aim to provide solutions to measure the image quality for different applications such as image denoising, deblurring, super-resolution, etc.

According to whether the reference clean image is available or not, existing IQA metrics can be roughly divided into two categories: 1) full reference IQA; and 2) no reference IQA. Full reference IQA metrics are based on the assumption that the clean image is available in

order to compute a measure, while no reference IQA metrics can perform quality assessments without the reference image. The full reference IQA metrics include root-mean-square error (RMSE), peak signal-to-noise ratio (PSNR), and the structural similarity index (SSIM) [92], etc. Other IQA metrics include the multi-scale SSIM (MS-SSIM) [93], BLIINDS [81], and BIQI [66], etc. A detailed survey of existing IQA algorithms is out of the scope of this thesis. Please refer to [92] for more references.

RMSE: The root mean square error (RMSE) of the denoised image $\boldsymbol{y} \in \mathcal{R}^{M\times N}$ w.r.t. the original clean image $\boldsymbol{x} \in \mathcal{R}^{M\times N}$ is defined as the square root of the mean square error (MSE). The RMSE is usually employed to measure the ℓ_2-norm distance between the denoised image and the original clean image. It is a full reference IQA metric which is closely related to the PSNR metric. Usually, smaller RSME value indicates better image quality. The definition of RMSE is:

$$\text{RMSE}(\boldsymbol{x}, \boldsymbol{y}) = \sqrt{\frac{1}{MN}\sum_{i=1}^{M}\sum_{j=1}^{N}(\boldsymbol{x}_{ij} - \boldsymbol{y}_{ij})^2}. \tag{1.3}$$

PSNR: peak signal-to-noise ratio (PSNR) is the most commonly used full reference IQA metric for many image restoration tasks including denoising. The definition of PSNR can be formulated as follows (for 8-bit image):

$$\text{PSNR} = 20\log_{10}(\frac{2^8}{\text{RMSE}(\boldsymbol{x}, \boldsymbol{y})}). \tag{1.4}$$

As we can see, PSNR is closely related to the ℓ_2 norm distance between two images. The unit of PSNR is decibel (dB) and higher dB value indicates better image quality and lower RMSE. Though PSNR is very simple and intuitive, higher PSNR does not mean higher visual structural similarity. Hence, researchers resort to find alternative and better IQA metrics.

SSIM [92]: One seminal work in IQA is the structural similarity (SSIM) index metric, which is also a full reference IQA metric. In SSIM, each image patch is decomposed into three different components indicating three core informative parts of the original patch. The three components are luminance (mean value of the pixels in the patch), contrast (the standard

deviation of the patch), and structure (the mean subtracted patch). SSIM takes into account the fact that the human visual system is very sensitive to the relative changes in luminance, rather than the absolute changes in luminance. The value range of SSIM is between 0 and 1, where higher value indicate higher similarity (SSIM=1 indicates that the two images are exactly the same), as well as better image quality.

Other IQA Metrics: Besides the frequently used RMSE, PSNR and SSIM, there are many other IQA metrics for full reference and no reference IQA. For example, the MS-SSIM [93] is a multi-scale extension of the original SSIM. Some examples in no reference IQA include BLIINDS [81] and BIQI [66]. These IQA metrics capture the deviations from the expected statistics of the natural images. Specifically, BLIINDS measures the deviations from the expected histogram of certain features in DCT domain, while BIQI measures deviations from the expected distribution of wavelet coefficients in a multi-scale decomposition.

For different denoising tasks, we need different IQA metrics. For the synthetic noisy images corrupted by AWGN, we have the original clean images for the corresponding denoised images. Then we can directly measure the quality of the denoised image by some existing full reference IQA metrics. However, the original clean image does not always exists. For the real-world image denoising task, the corresponding clean image is hard to generate. A possible solution is to evaluate the image quality by human subjective or no reference IQA metrics. It should be noted that no IQA metric is perfect for the image denoising task, both in full reference and no reference cases. PSNR and SSIM are the de facto standard metrics in image restoration community. In addtion to the use of IQA metrics, it is essential to present the denoised images for human subjective evaluation.

1.2 Existing Denoising Methods

In this section, we will firstly review some well-known image denoising methods designed for AWGN, which is the most widely studied area in the literature. Though these methods

are mainly proposed for the AWGN noise, the idea can be transfered into other image denoising tasks such as real-world image denoising. Then we will review some existing methods proposed for real-world noisy images.

1.2.1 Synthetic Image Denoising

Image denoising is a classical problem in low level vision. It has been extensively studied in the past decades, and is still an active research topic for that it provides an ideal test bed for image modeling techniques. In synthetic image denoising, the synthetic image noise is often assumed to be AWGN. Other types of synthetic image noise, e.g., Poisson noise and salt-and-pepper noise, are also widely studied in literature. The Poisson noise can be transformed into the additive noise after the generalized Anscombe transformation [62].

A number of image denoising methods for AWGN have been developed in past decades. Existing denoising methods can be roughly categorized into three major categories: non-learning based methods, prior learning based methods, and discriminative learning based methods.

Non-learning based methods: This category of methods include wavelet/curvelet transformation based methods [16, 25, 86], filtering based methods [12, 77, 89, 105], generative methods [79, 111, 112], dictionary learning based methods [3, 30, 59, 61], sparse and low-rank representation based methods [22, 24, 36, 42, 58], discriminative learning based methods [13, 19, 83, 107], and the other methods [71, 72, 80].

The wavelet/curvelet transformation based methods perform image denoising in the transformed domain instead of the original image domain. By modeling the wavelet transform coefficients as Laplacian distributions, many wavelet shrinkage based denoising methods such as the classical soft-thresholding method [25] have been proposed. Chang et al. modeled the wavelet transform coefficients as generalized Gaussian distribution, and proposed the BayesShrink [16] algorithm. Besides, curvelet based methods are also proposed for image

denoising [86].

The filtering based methods design denoising filters to remove noise while preserving the details. The seminal work of bilateral filter [89] is a non-linear, edge preserving, and smoothing filter for image denoising. It replaces the intensity of each pixel by a weighted average of intensity values from nearby pixels. By considering the correlation of wavelet coefficients across scales, Portilla et al. [77] proposed to use Gaussian Scale Mixtures for image modeling and achieved promising denoising performance. Yu et al. [105] used Gaussian Mixture Model (GMM) to model image patches and perform denoising accordingly. The nonlocal means (NLM) filter [12] has a basic idea that to build a pointwise estimate of the image where each pixel is a weighted average of pixels centered at regions that are similar to the region centered at the estimated pixel.

The generative methods learn the priors of natural images for image denoising. The Fields of Experts (FoE) [79] proposed by Roth and Black models the filtering responses with Student's t-distribution to learn filters through Markov Random Field (MRF) [10]. By viewing image patches as samples of a multivariate variable vector and considering that natural images are non-Gaussian, Zoran and Weiss [111, 112] used GMM to learn the distribution of natural image patches, and achieved state-of-the-art denoising perfromance.

The dictionary learning based methods remove the noise by thresholding the coefficients over the selected dictionary atoms. The seminal work of K-SVD [30] learns an overcomplete dictionary for the extracted image patches under the sparse representation framwork [69, 70]. The dictionary can be chosen from the off-the-shelf dictionaries (e.g., wavelets and curvelets), or it can be learned from natural image patches.

The BM3D [22] method groups similar image patches into 3D data arrays, transform the image patches into the wavalet domain, then collaboratively filters the coefficients via shrinkage operations, and finally performs inverse transformation to recover the image. The BM3D algorithm has become a benchmark in image denoising. Mairal et al. [58] proposed the LSSC

algorithm to exploit NSS via group sparse coding. Dong et al. [24] unified NSS and local sparse coding into the so-called NCSR framework, which shows powerful image restoration capability. Since the NSS property has been demonstrated its effectiveness on image denoising task, low rank based methods [36, 42] have also been proposed to exploit the intrinsic NSS property of nonlocal similar patches. For example, the work of WNNM [36] method achieves state-of-the-art performance for AWGN denoising.

The discriminative learning based denoising methods learn discriminative priors from pairs of clean and noisy images [13, 19, 83, 107]. The multiple layer perception (MLP) [13] has been introduced in the image denoising community and achieves good performance. Later, Schmidt and Roth proposed the cascade of shrinkage fields (CSF) to perform denoising efficiently [83]. Chen et al. proposed the trainable nonlinear reaction diffusion (TNRD) [19], which achieves even better performance than CSF on image denoising as well as much faster speed. Recently, the residual network [37] has been applied into the image denoising task, and the developed DnCNN method [107] achieves state-of-the-art performance on image denoising.

The other methods include the partial differential equation (PDE) based methods [72] and total variation (TV) based methods [71, 80]. The PDE based nonlinear anisotropic diffusion [72] defines a class of efficient approaches, in which each diffusion step includes only the convolution operation with a few linear filters. The TV based methods [71, 80] have a principle that signals with excessive and possibly spurious detail have high TV, and hence reducing the TV of the signal tends to produce a close match to the original signal. It is widely accepted that natural image gradients exhibit heavy-tailed distributions [94], and the TV based methods [71, 80] actually assume Laplacian distributions of image gradients for denoising.

1.2.2 Real-world Image Denoising

Most of the above mentioned methods focus on AWGN removal, however, the assumption of AWGN is too ideal to be true for real-world noisy images captured by CCD or CMOS cameras, where the noise is much more complex and varies with different scenes, cameras and camera settings (ISO, shutter speed, and aperture, etc.) [45, 68, 74]. As a result, many denoising methods in literature, including those learning based methods, become less effective when applied to real-world noisy images.

During the last decade, several methods [2, 21, 41, 51, 53, 68, 76–78, 110] have been proposed for real-world image denoising problem. Almost all of these methods follow a two-stage framework: first estimate the parameters of the noise model (usually assumed to be Gaussian or mixture of Gaussians (MoG)), and then perform denoising with the estimated noise model. To the best of our knowledge, the study of real-world image denoising can be traced back to the BLS-GSM method [77], where Portilla et al. proposed to use Gaussian scale mixture model in over-complete oriented pyramids to estimate the latent clean images. In [76], Portilla proposed to use a correlated Gaussian model for noise estimation of each wavelet subband. Based on the robust statistics theory [41], Rabie modeled the noisy pixels as outliers, which could be removed via Lorentzian robust estimator [78]. The CBM3D method [21] is a representative color image denoising method and can be used in the real-world image denoising problem naturally. This method first transforms the RGB image into a luminance-chrominance space (e.g., YCbCr) and then applies the famous BM3D method [22] to each channel separately.

In [53], Liu et al. proposed the "Noise Level Function" to estimate the noise for each channel in natural images, and then use Gaussian conditional random field to obtain the latent clean image. Later, Lebrun el al. proposed a multiscale denoising algorithm called "Noise Clinic" [51] for blind image denoising task. This method generalizes the NL-Bayes [49] to deal with signal and frequency dependent noise. Therefore, the methods [50, 51, 110] perform

real-world color image denoising by concatenating the patches of RGB channels into a long vector. Zhu et al. [110] proposed a Bayesian method to approximate and remove the noise via a low-rank MoG model. The method in [68] models the cross-channel noise in real-world noisy images as multivariate Gaussian and the noise is removed by the Bayesian non-local means filter [46]. The commercial software Neat Image [2] estimates the noise parameters from a flat region of the given noisy image and filters the noise accordingly.

Despite the success of these methods, they also have clear limitations for the real-world image denoising task. On one hand, as suggested in [51, 53], Gaussian noise is assumed by [53, 76, 78] and may be inflexible for the noise in real-world noisy images. Hence, better approximation to the real-world noise would bring better image denoising performance [51, 53]. On the other hand, the real-world noise is signal dependent and have different statistics in different channels. It is hard to be modeled by explicit distributions such as Gaussian and MoG [45, 52, 53, 68, 74], and needs more complex modeling. Based on these observations, it is still needed to design robust and effective models for real-world image denoising.

1.3 Contribution and Thesis Organization

This thesis is mainly consisted of five works we have done during the PhD study, which focuses on designing new and better image denoising algorithms by proposing cutting-edge techniques for image modeling. The organization of the thesis is illustrated in Fig. 1.1.

In the first work, we propose to learn external nonlocal self-similarity (NSS) based priors and apply the learned model on removing AWGN noise. This is very different from the previous methods, which can be divided into three types: internal patch prior based methods [30, 105], internal NSS prior based methods [22, 24, 36, 58], and external patch prior based methods [111]. As far as we know, this work is the first to learn the NSS priors of natural clean images, while previous works only utilize the NSS priors of input noisy image for online denoising. The advantages of this offline learning lie in that it can preserve the details of

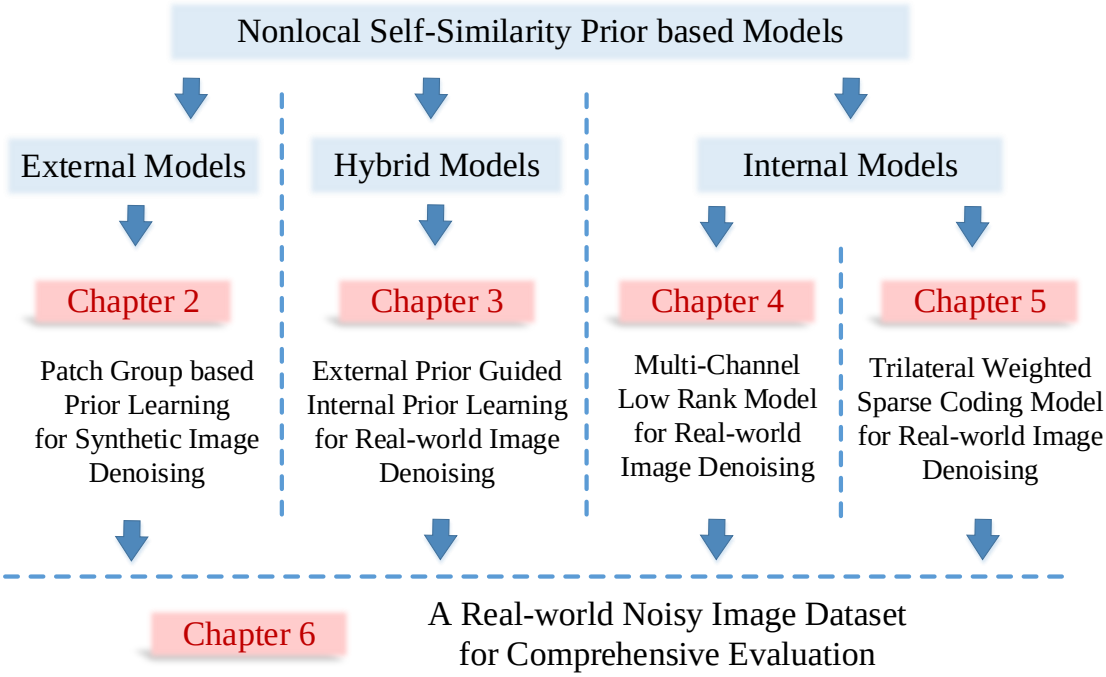

Figure 1.1 The organization of this thesis.

natural images while being much faster than most online denoising methods. The proposed method achieves state-of-the-art performance on AWGN removal effectively and efficiently. This work will be introduced in Chapter 2.

We then propose to exploit the NSS priors of natural images to deal with the complex noise in real-world noisy images. Specifically, we propose three methods for real-world image denoising, which are introduced as follows.

In the second work, we propose to learn the NSS prior from the external natural images, and then apply the learned external prior to guide the learning of the internal NSS prior of the input real-world noisy image. From the external perspective, the method can preserve the structures of natural images better than the internal methods, while from the internal perspective, the proposed method can recover the details of the input noisy image better than the external methods. The experiments on commonly used datasets demonstrate that the proposed

method can achieve better performance than state-of-the-art real-world image denoising methods as well as a commercial software Neat Image [2], which is embeded into the PhotoShop CS for image processing tasks. This work will be introduced in Chapter 3.

In the third work, we propose to employ the low rank model to describe the the internal NSS prior, basing on the fact that the similar image patches can be contanated as a matrix of low rank. We extend the WNNM model [36] to a multi-channel version to make it feasible for color image denoising. This method regards different channels in RGB images differently to adaptively process the real-world color noisy images. Experiments demonstrate that the proposed method can achieve better performance on real-world color image denoising than existing state-of-the-art methods, including some commercial software. This work will be introduced in Chapter 4.

In the fourth work, we propose to use the sparse coding based method with additional weighting scheme to deal with the real-world noisy images. We regard the noise in each local region as a Gaussian, and propose a triplely weighted scheme to deal with the complex real-world noise. Experiments show that the proposed method performs better and faster than the nuclear norm based method developed in Chapter 4. This work will be introduced in Chapter 5.

In the final work, to boost the research of real-world color image denoising, we construct a large benchmark dataset of real-world color noisy images. This dataset is collected by several representative cameras with comprehensive settings on contents, lighting, ISO, shutter, and aperture, etc. Based on this newly established dataset, we comprehensively evaluated existing denoising methods, including the methods designed for synthetic Gaussian noise and the methods designed especially for real-world noise. We believe that this new dataset will largely boost the research of the real-world image denoising. This work will be introduced in Chapter 6.

The structure of this thesis is organized as follows: in Chapter 2, we introduce the patch

group based prior learning method for synthetic image denoising; in Chapter 3, we introduce the external prior guided internal prior learning method for real-world image denoising; in Chapter 4, we introduce the multi-channel weighted nuclear norm minimization based method for real-world image denoising; in Chapter 5, we introduce the trilateral weighted sparse coding based method for real-world image denoising; in Chapter 6, we introduce the real-world noisy image datasets, and comprehensively evaluate the proposed methods with the state-of-the-art denoising methods designed for synthetic AWGN noise and real-world noise, including a commercial software developed especially for real-world noise; in Chapter 7, we conclude this thesis and provide some future work directions.

Chapter 2

Patch Group based Prior Learning for Image Denoising

2.1 Introduction

Image denoising is a classical problem in low level vision and has been extensively studied for several decades. Image denoising is still an active topic for that it not only serves as a baseline problem for other image resotration problems, but also provides an ideal test bed for image modeling techniques. In general, image denoising aims to recover the clean image $\boldsymbol{x}$ from its noisy observation $\boldsymbol{y} = \boldsymbol{x} + \boldsymbol{n}$, where $\boldsymbol{n}$ is assumed to be additive white Gaussian noise. A variety of image denoising methods have been developed in past decades, including filtering based methods [89], diffusion based methods [72], total variation based methods [71, 80], wavelet/curvelet based methods [16, 25, 86], sparse representation based methods [24, 30, 58], nonlocal self-similarity based methods [12, 22, 36, 42], etc.

Image modeling plays a central role in image denoising. By modeling the wavelet transform coefficients as Laplacian distributions, many wavelet shrinkage based denoising methods such as the classical soft-thresholding [25] have been proposed. Chang et al. modeled

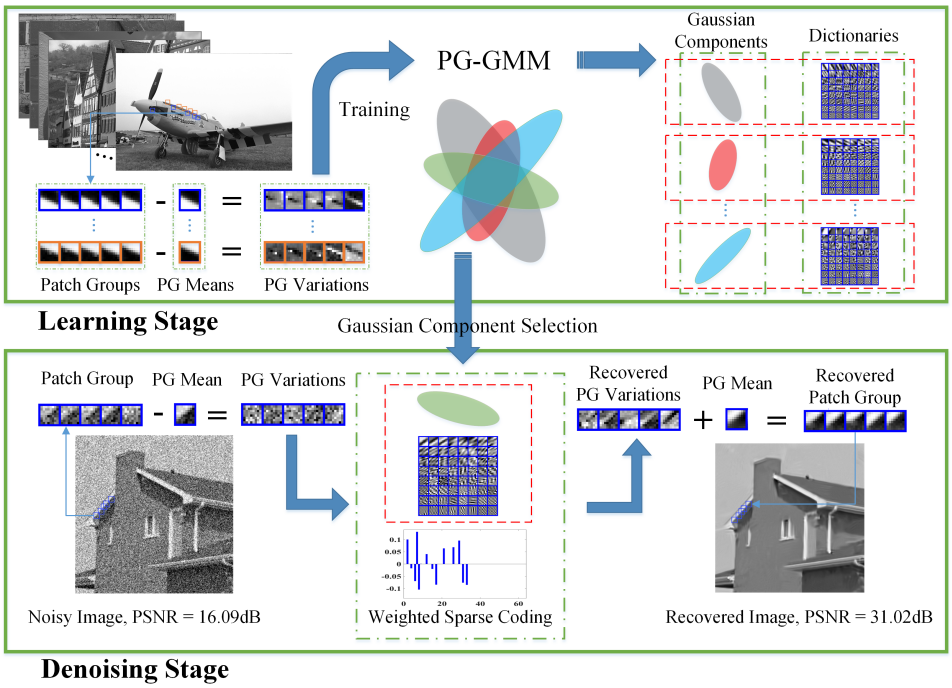

Figure 2.1 Flowchart of the proposed patch group based prior learning and image denoising framework.

the wavelet transform coefficients as generalized Gaussian distribution, and proposed the BayesShrink [16] algorithm. By considering the correlation of wavelet coefficients across scales, Portilla et al. [77] proposed to use Gaussian Scale Mixtures for image modeling and achieved promising denoising performance. It is widely accepted that natural image gradients exhibit heavy-tailed distributions [94], and the total variation (TV) based methods [71, 80] actually assume Laplacian distributions of image gradients for denoising. The Fields of Experts (FoE) [79] proposed by Roth and Black models the filtering responses with Student's t-distribution to learn filters through Markov Random Field (MRF) [10]. Recently, Schmidt and Roth proposed the cascade of shrinkage fields (CSF) to perform denoising efficiently [83].

Instead of modeling the image statistics in some transformed domain (e.g., gradient domain, wavelet domain or filtering response domain), another popular approach is to model the image priors on patches. One representative is the sparse representation based scheme which

encodes an image patch as a linear combination of a few atoms selected from a dictionary [30, 69, 70]. The dictionary can be chosen from the off-the-shelf dictionaries (e.g., wavelets and curvelets), or it can be learned from natural image patches. The seminal work of K-SVD [3, 30] has demonstrated promising denoising performance by dictionary learning, which has yet been extended and successfully used in various image processing and computer vision applications [44, 59, 95]. By viewing image patches as samples of a multivariate variable vector and considering that natural images are non-Gaussian, Zoran and Weiss [111, 112] and Yu et al. [105] used Gaussian Mixture Model (GMM) to model image patches, and achieved state-of-the-art denoising and image restoration results, respectively.

Natural images often have many repetitive local patterns, and a local patch can have many similar patches to it across the whole image. The so-called nonlocal self-similarity (NSS) prior is among the most successful priors for image restoration. The nonlocal means [12] and nonlocal regularization [73] methods improve much the image denoising performance over the conventional local self-similarity based methods. Dabov et al. [22] constructed 3D cubes of nonlocal similar patches and conducted collaborative filtering in the sparse 3D transform domain. The so-called BM3D algorithm has become a benchmark in image denoising. Mairal et al. [58] proposed the LSSC algorithm to exploit NSS via group sparse coding. The NSP [91] method fits the singular values of NSS patch matrix by Laplacian distribution. Dong et al. [24] unified NSS and local sparse coding into the so-called NCSR framework, which shows powerful image restoration capability. By assuming that the matrix of nonlocal similar patches has a low rank structure, the low-rank minimization based methods [36, 42] have also achieved very competitive denoising results.

Though NSS has demonstrated its great success in image denoising, in most existing methods only the NSS of noisy input image is used for denoising. For example, in BM3D [22] the nonlocal similar patches of a noisy image are collected as a cube for collaborative filtering. In NCSR [24], the nonlocal means are subtracted in the sparse domain to regularize the sparse

coding of noisy patches. In WNNM [36], the low-rank regularization is enforced to recover the latent structure of the matrix of noisy patches. We argue that, however, such utilizations of NSS are not effective enough because they neglect the NSS of clean natural images, which can be pre-learned for use in the denoising stage. To the best of our knowledge, unfortunately, so far there is not an explicit NSS prior model learned from natural images for image restoration.

With the above considerations, in this work we propose to learn explicit NSS models from natural images, and apply the learned prior models to noisy images for high performance denoising. The flowchart of the proposed method is illustrated in Fig. 2.1. In the learning stage, we extract millions of patch groups (PG) from a set of clean natural images. A PG is formed by grouping the similar patches to a local patch in a large enough neighborhood. A PG based GMM (PG-GMM) learning algorithm is developed to learn the NSS prior for the PGs. In the denoising stage, the learned PG-GMM will provide dictionaries as well as regularization parameters, and a simple weighted sparse coding model is developed for image denoising. Our extensive experiments validated that the proposed PG prior based denoising method outperforms many state-of-the-art algorithms quantitatively (in PSNR) while being much more efficient. More importantly, it delivers the best qualitative denoising results with finer details and less artifacts, owe to the NSS prior learned from clean natural images.

2.2 Patch Group Based Prior Modeling of Nonlocal Self-Similarity

Image nonlocal self-similarity (NSS) has been widely adopted in patch based image denoising and other image restoration tasks [12, 22, 24, 36, 58]. Despite the great success of NSS in image restoration, most of the existing works exploit the NSS only from the degraded image. Usually, for a given patch in the degraded image, its nonlocal similar patches are collected, and then the nonlocal means [12], or 3D transforms [22], or some regularization terms [24, 36,

58, 59] can be introduced for image restoration. However, how to learn the NSS prior from clean natural images and apply it to image restoration is still an open problem. In this work, we make the first attempt on this problem, and develop a patch group (PG) based NSS prior learning scheme.

2.2.1 Patch Group and Group Mean Subtraction

For each local patch (size: $p \times p$) of a given clean image, we can find the first M most similar nonlocal patches to it across the whole image. In practice, this can be done by Euclidean distance based block matching in a large enough local window of size $W \times W$. A PG is formed by grouping the M similar patches, denoted by $\{\boldsymbol{x}_m\}_{m=1}^M$, where $\boldsymbol{x}_m \in \mathbb{R}^{p^2 \times 1}$ is a patch vector. The mean vector of this PG is $\boldsymbol{\mu} = \frac{1}{M}\sum_{m=1}^M \boldsymbol{x}_m$, and $\overline{\boldsymbol{x}}_m = \boldsymbol{x}_m - \boldsymbol{\mu}$ is the group mean subtracted patch vector. We call

$$\overline{\boldsymbol{X}} \triangleq \{\overline{\boldsymbol{x}}_m\}, m = 1, ..., M \tag{2.1}$$

the group mean subtracted PG, and it will be used to learn the NSS prior in our work.

In Fig. 2.2, we show two different PGs, their group means, and the PGs after mean subtraction. One can see that before mean subtraction, the two PGs have very different local structures. After mean subtraction, the two PGs will have very similar variations. This greatly facilitates the prior learning because the possible number of patterns is reduced, while the training samples of each pattern are increased. We will discuss further the benefits of mean subtraction and the associated prior model learning in Section 2.4.

2.2.2 PG-GMM Learning

From a given set of natural images, we can extract N PGs, and we denote one PG as

$$\overline{\boldsymbol{X}}_n \triangleq \{\overline{\boldsymbol{x}}_{n,m}\}_{m=1}^M, n = 1, ..., N. \tag{2.2}$$

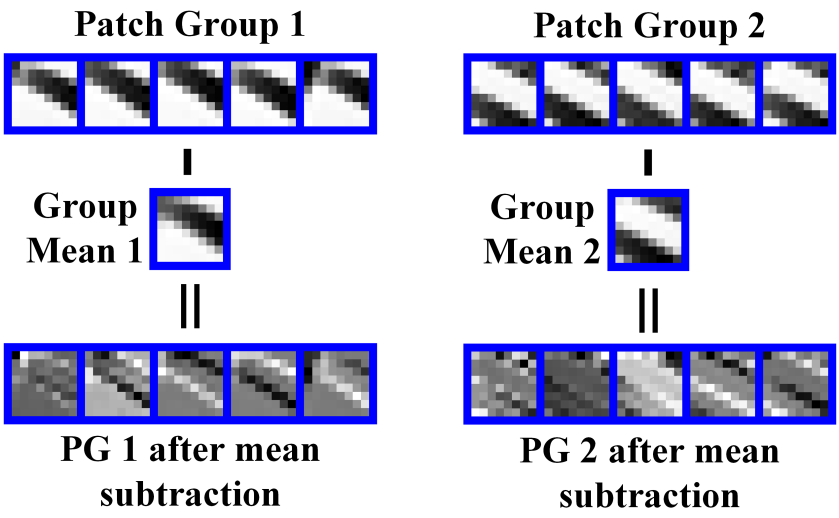

Figure 2.2 Different patch groups (PG) share similar PG variations.

The PGs $\{\overline{\boldsymbol{X}}_n\}$ contain a rich amount of NSS information of natural images, and the problem turns to how to learn explicit prior models from $\{\overline{\boldsymbol{X}}_n\}$. Considering that Gaussian Mixture Model (GMM) has been successfully used to model the image patch priors in EPLL [111] and PLE [105], we propose to extend patch based GMM to patch group based GMM (PG-GMM) for NSS prior learning.

With PG-GMM, we aim to learn a set of K Gaussians $\{\mathcal{N}(\boldsymbol{\mu}_k, \boldsymbol{\Sigma}_k)\}$ from N training PGs $\{\overline{\boldsymbol{X}}_n\}$, while requiring that all the M patches $\{\overline{\boldsymbol{x}}_{n,m}\}$ in PG $\overline{\boldsymbol{X}}_n$ belong to the same Gaussian component and assume that the patches in the PG are independently sampled. Note that such an assumption is commonly used in patch based image modeling [30, 58]. Then, the likelihood of $\{\overline{\boldsymbol{X}}_n\}$ can be calculated as

$$P(\overline{\boldsymbol{X}}_n) = \sum\nolimits_{k=1}^{K} \pi_k \prod\nolimits_{m=1}^{M} \mathcal{N}(\overline{\boldsymbol{x}}_{n,m} | \boldsymbol{\mu}_k, \boldsymbol{\Sigma}_k). \tag{2.3}$$

By assuming that all the PGs are independently sampled, the overall objective likelihood function is $\mathcal{L} = \prod_{n=1}^{N} P(\overline{\boldsymbol{X}}_n)$. Taking the log of it, we maximize the following objective function for PG-GMM learning

$$\ln \mathcal{L} = \sum_{n=1}^{N} \ln\Big(\sum_{k=1}^{K} \pi_k \prod_{m=1}^{M} \mathcal{N}(\overline{\boldsymbol{x}}_{n,m} | \boldsymbol{\mu}_k, \boldsymbol{\Sigma}_k)\Big). \tag{2.4}$$

As in GMM learning [10], we introduce hidden variables $\{\Delta_{nk}|n = 1, ..., N; k = 1, ..., K\}$ to optimize (2.4). If PG $\overline{\boldsymbol{X}}_n$ belongs to the kth component, $\Delta_{nk} = 1$; and $\Delta_{nk} = 0$ otherwise. Then the EM algorithm [23] can be used to optimize (2.4) via two alternative steps. In the E-Step, by the Bayes' formula, the expected value of Δ_{nk} is

$$\gamma_{nk} = \frac{\pi_k \prod_{m=1}^{M} \mathcal{N}(\overline{\boldsymbol{x}}_{n,m}|\boldsymbol{\mu}_k, \boldsymbol{\Sigma}_k)}{\sum_{l=1}^{K} \pi_l \prod_{m=1}^{M} \mathcal{N}(\overline{\boldsymbol{x}}_{n,m}|\boldsymbol{\mu}_l, \boldsymbol{\Sigma}_l)}. \tag{2.5}$$

In the M-step, since for each PG $\overline{\boldsymbol{X}}_n$, $\sum_{m=1}^{M} \overline{\boldsymbol{x}}_{n,m} = \mathbf{0}$, we have

$$\boldsymbol{\mu}_k = \frac{\sum_{n=1}^{N} \gamma_{nk} \sum_{m=1}^{M} \overline{\boldsymbol{x}}_{n,m}}{\sum_{n=1}^{N} \gamma_{nk}} = \mathbf{0}, \tag{2.6}$$

$$\boldsymbol{\Sigma}_k = \frac{\sum_{n=1}^{N} \gamma_{nk} \sum_{m=1}^{M} \overline{\boldsymbol{x}}_{n,m} \overline{\boldsymbol{x}}_{n,m}^T}{\sum_{n=1}^{N} \gamma_{nk}}. \tag{2.7}$$

The calculations of $\pi_k = \frac{1}{N} \sum_{n=1}^{N} \gamma_{nk}$ are similar to [10].

By alternating between the E-step and the M-step, the model parameters will be updated iteratively, and the update in each iteration can guarantee to increase the value of the log-likelihood function (2.5), and the EM algorithm will converge [10, 97]. Fig. 2.3 shows the convergence curve of the proposed PG-GMM algorithm by using the Kodak PhotoCD Dataset (http://r0k.us/graphics/kodak/) for training.

2.2.3 Complexity Analysis

In the training stage, there are N PGs, each of which has M patches, and hence we have $N \times M$ patches. In the M-step, we only need to calculate the covariance matrices since the mean of each Gaussian component is zero. The cost of this step is $O(p^4MN)$. In the E-step, the cost is $O(p^6MN)$. Suppose that the number of iterations is T, the overall complexity of PG-GMM training is $O(p^6MNT)$.

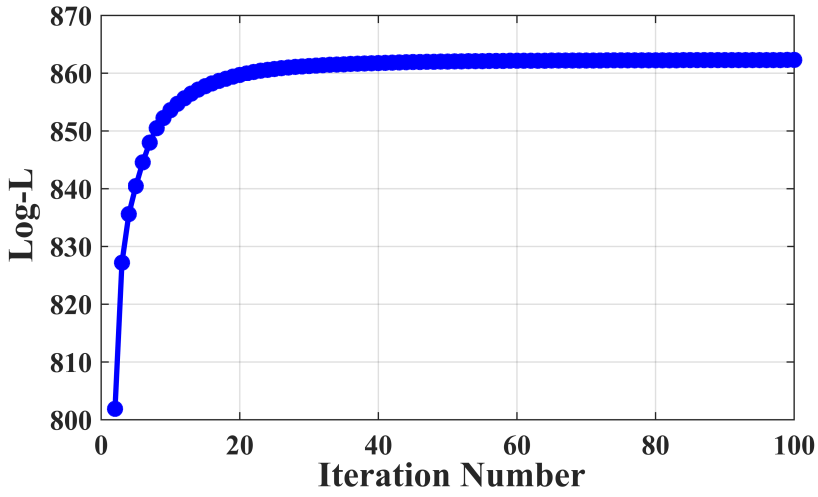

Figure 2.3 The convergence curve of log-likelihood in PG-GMM training on the Kodak PhotoCD Dataset.

2.2.4 Discussions

GMM has been used for patch based image prior learning and achieved promising results, e.g., EPLL [111] and PLE [105]. In this work, we extend the patch based image prior learning to PG based prior learning to model the NSS information. The developed PG-GMM method has some important advantages over the patch based GMM method.

First, in patch based GMM, the mean value of each patch is subtracted before learning the Gaussian components. This is to remove the DC (direct current) of each patch but will not change the essential structure of a patch. However, in PG-GMM the mean vector of all patches in a group is calculated and subtracted from each patch, and hence the structure of each patch is changed. As a result, many patches which originally have different local patterns may become similar after group mean subtraction (please refer to Fig. 2.2 for an example). This makes the PG-GMM learning process easier and more stable.

Second, as can be seen in Eq. (2.9), the mean vector of each Gaussian component in PG-GMM is naturally a zero vector. This implies that we only need to learn the covariance matrix

of each component without considering its mean. However, in patch based GMM [111], the mean vectors of Gaussians can only be forced to zero and there is no theoretical guarantee.

Third, due to reduction of possible patterns in PG-GMM and reduced number of variables to learn, we do not need to set a large number of Gaussian components in PG-GMM learning. For example, in EPLL [111], 200 Gaussian components are learned to achieve competing denoising performance with BM3D [22], while in PG-GMM learning only 32 Gaussian components are enough to outperform BM3D (please refer to the experimental section for details).

2.3 Image Denoising by Patch Group Priors

2.3.1 Denoising Model

Given a noisy image $\boldsymbol{y}$, like in the PG-GMM learning stage, for each local patch we search for its similar patches in a window centered on it to form a PG, denoted by $\boldsymbol{Y} = \{\boldsymbol{y}_1, ..., \boldsymbol{y}_M\}$. Then the group mean of $\boldsymbol{Y}$, denoted by $\boldsymbol{\mu}_y$, is calculated and subtracted from each patch, leading to the mean subtracted PG $\overline{\boldsymbol{Y}}$. We can write $\overline{\boldsymbol{Y}}$ as $\overline{\boldsymbol{Y}} = \overline{\boldsymbol{X}} + \boldsymbol{V}$, where $\overline{\boldsymbol{X}}$ is the corresponding clean PG and $\boldsymbol{V}$ contains the corrupted noise. The problem then turns to how to recover $\overline{\boldsymbol{X}}$ from $\overline{\boldsymbol{Y}}$ by using the learned PG-GMM priors. Note that the mean $\boldsymbol{\mu}_y$ of $\overline{\boldsymbol{Y}}$ is very close to the mean of $\overline{\boldsymbol{X}}$ since the mean vector of noise $\boldsymbol{V}$ is nearly zero. $\boldsymbol{\mu}_y$ will be added back to the denoised PG to obtain the denoised image.

Gaussian Component Selection

For each $\overline{\boldsymbol{Y}}$, we select the most suitable Gaussian component to it from the trained PG-GMM. As in [111], suppose that the variance of Gaussian white noise corrupted in the image is σ^2, the covariance matrix of the kth component will become $\boldsymbol{\Sigma}_k + \sigma^2\boldsymbol{I}$, where $\boldsymbol{I}$ is the identity matrix. The selection can be done by checking the posterior probability that $\overline{\boldsymbol{Y}}$ belongs to the

kth Gaussian component:

$$P(k|\overline{\boldsymbol{Y}}) = \frac{\prod_{m=1}^{M} \mathcal{N}(\overline{\boldsymbol{y}}_m|\boldsymbol{0}, \boldsymbol{\Sigma}_k + \sigma^2 \boldsymbol{I})}{\sum_{l=1}^{K} \prod_{m=1}^{M} \mathcal{N}(\overline{\boldsymbol{y}}_m|\boldsymbol{0}, \boldsymbol{\Sigma}_l + \sigma^2 \boldsymbol{I})}. \tag{2.8}$$

Taking log-likelihood of (2.8), we have

$$\ln P(k|\overline{\boldsymbol{Y}}) = \sum_{m=1}^{M} \ln \mathcal{N}(\overline{\boldsymbol{y}}_m|\boldsymbol{0}, \boldsymbol{\Sigma}_k + \sigma^2) - \ln C \tag{2.9}$$

where C is the denominator in Eq. (2.9) and it is the same for all components. Finally, the component with the highest probability $\ln P(k|\overline{\boldsymbol{Y}})$ is selected to process $\overline{\boldsymbol{Y}}$.

Weighted Sparse Coding with Closed-Form Solution

Suppose that the kth Gaussian component is selected for PG $\overline{\boldsymbol{Y}}$. For notation simplicity, we remove the subscript k and denote by $\boldsymbol{\Sigma}$ the covariance matrix of this component. In PG-GMM, the PGs actually represent the variations of the similar patches in a group, and these variations are assigned to the same Gaussian distribution. By singular value decomposition (SVD), $\boldsymbol{\Sigma}$ can be factorized as

$$\boldsymbol{\Sigma} = \boldsymbol{D}\boldsymbol{\Lambda}\boldsymbol{D}^T, \tag{2.10}$$

where $\boldsymbol{D}$ is an orthonormal matrix composed by the eigenvectors of $\boldsymbol{\Sigma}$ and $\boldsymbol{\Lambda}$ is the diagonal matrix of eigenvalues. With PG-GMM, the eigenvectors in $\boldsymbol{D}$ capture the statistical structures of NSS variations in natural images, while the eigenvalues in $\boldsymbol{\Lambda}$ represent the significance of these eigenvectors. Fig. 2.4 shows the eigenvectors for 3 Gaussian components. It can be seen that these eigenvectors encode the possible variations of the PGs. For one Gaussian component, the first eigenvector represents its largest variation, while the last eigenvector represents its smallest variation. For different Gaussian components, we can see that their eigenvectors (with the same index) are very different. Hence, $\boldsymbol{D}$ can be used to represent the structural variations of the PGs in that component.

For each patch $\overline{\boldsymbol{y}}_m$ in the PG $\overline{\boldsymbol{Y}}$, we propose to use $\boldsymbol{D}$ as the dictionary to sparsely encode $\overline{\boldsymbol{y}}_m$ as $\overline{\boldsymbol{y}}_m = \boldsymbol{D}\boldsymbol{\alpha} + \boldsymbol{v}$, where $\boldsymbol{\alpha}$ is the vector of sparse coding coefficients and $\boldsymbol{v}$ is the corrupted

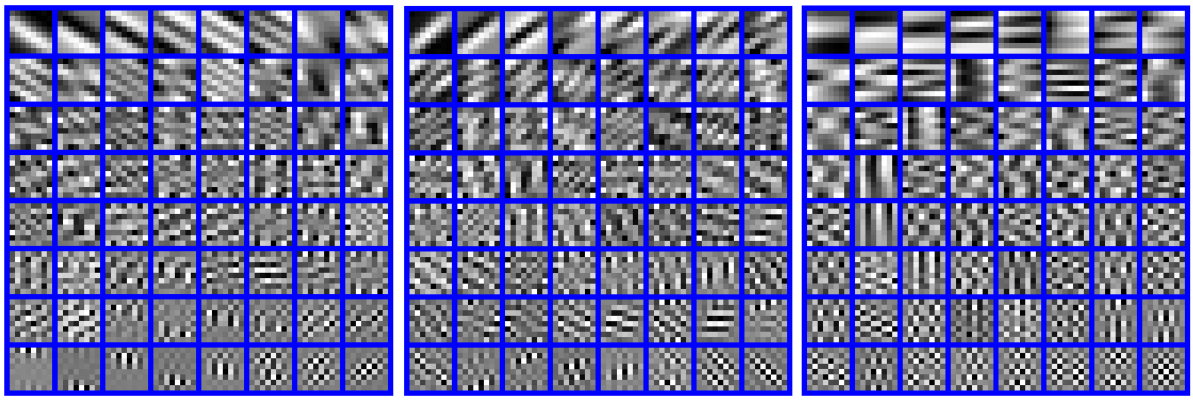

Figure 2.4 Eigenvectors of 3 Gaussian components from the learned PG-GMM, sorted by the values of corresponding eigenvalues.

noise. Meanwhile, we propose to introduce a weighting vector $\boldsymbol{w}$ to weight the coding vector $\boldsymbol{\alpha}$ (we will see in (2.16) that $\boldsymbol{w}$ is related to the eigenvalues in $\boldsymbol{\Lambda}$), resulting in the following simple but highly effective weighted sparse coding model:

$$\min_{\boldsymbol{\alpha}} \|\overline{\boldsymbol{y}}_m - \boldsymbol{D}\boldsymbol{\alpha}\|_2^2 + \|\boldsymbol{w}^T\boldsymbol{\alpha}\|_1. \tag{2.11}$$

From the viewpoint of Maximum A-Posterior (MAP) estimation, the optimal solution of (2.11) is $\hat{\boldsymbol{\alpha}} = \arg\max_{\alpha} \ln P(\boldsymbol{\alpha}|\overline{\boldsymbol{y}}_m)$. By Bayes' formula, it is equivalent to

$$\hat{\boldsymbol{\alpha}} = \arg\max_{\alpha}\{\ln P(\overline{\boldsymbol{y}}_m|\boldsymbol{\alpha}) + \ln P(\boldsymbol{\alpha})\}. \tag{2.12}$$

The log-likelihood term $\ln P(\overline{\boldsymbol{y}}_m|\boldsymbol{\alpha})$ is characterized by the statistics of noise $\boldsymbol{v}$, which is assumed to be white Gaussian with standard deviation σ. Hence, we have

$$P(\overline{\boldsymbol{y}}_m|\boldsymbol{\alpha}) = \frac{1}{\sqrt{2\pi}\sigma}\exp(-\frac{1}{2\sigma^2}\|\overline{\boldsymbol{y}}_m - \boldsymbol{D}\boldsymbol{\alpha}\|_2^2). \tag{2.13}$$

We assume that the sparse coding coefficients in $\boldsymbol{\alpha}$ follow i.i.d. Laplacian distribution. More specifically, for entry $\boldsymbol{\alpha}_i$, which is the coding coefficient of patch $\overline{\boldsymbol{y}}_m$ over the ith eigenvector in $\boldsymbol{D}$, we assume that it follows distribution $\frac{c}{\sqrt{2}\lambda_i}\exp(-c\sqrt{2}|\boldsymbol{\alpha}_i|/\boldsymbol{\lambda}_i)$, where $\boldsymbol{\lambda}_i = \boldsymbol{\Lambda}_i^{1/2}$ and c is a constant. Note that we adjust the scale factor of the distribution by (square root of) the

ith eigenvalue $\boldsymbol{\Lambda}_i$. This is because the larger the eigenvalue $\boldsymbol{\Lambda}_i$ is, the more important the ith eigenvector in $\boldsymbol{D}$ is, and hence the distribution of the coding coefficients over this eigenvector should have a longer tail (i.e., less sparse). Finally, we have

$$P(\boldsymbol{\alpha}) = \prod_{i=1}^{p^2} \frac{c}{\sqrt{2}\boldsymbol{\lambda}_i} \exp(-\frac{c\sqrt{2}|\boldsymbol{\alpha}_i|}{\boldsymbol{\lambda}_i}). \tag{2.14}$$

Putting (2.13) and (2.14) into (2.12), we have

$$\hat{\boldsymbol{\alpha}} = \arg\min_{\alpha} \|\overline{\boldsymbol{y}}_m - \boldsymbol{D}\boldsymbol{\alpha}\|_2^2 + \sum_{i=1}^{p^2} \frac{c * 2\sqrt{2}\sigma^2}{\boldsymbol{\lambda}_i}|\boldsymbol{\alpha}_i|. \tag{2.15}$$

By comparing (2.15) with (2.11), we can see that the ith entry of the weighting vector $\boldsymbol{w}$ should be

$$\boldsymbol{w}_i = c * 2\sqrt{2}\sigma^2/(\boldsymbol{\lambda}_i + \varepsilon), \tag{2.16}$$

where ε is a small positive number to avoid dividing by zero.

With $\boldsymbol{w}$ determined by (2.16), let us see what the solution of (2.11) should be. Since the dictionary $\boldsymbol{D}$ is orthonormal, it is not difficult to find out that (2.11) has a closed-form solution (detailed derivation can be found in the Appendix 8):

$$\hat{\boldsymbol{\alpha}} = \text{sgn}(\boldsymbol{D}^T\overline{\boldsymbol{y}}_m) \odot \max(|\boldsymbol{D}^T\overline{\boldsymbol{y}}_m| - \boldsymbol{w}/2, 0), \tag{2.17}$$

where sgn(•) is the sign function, $\odot$ means element-wise multiplication, and $|\boldsymbol{D}^T\overline{\boldsymbol{y}}_m|$ is the absolute value of each entry of vector $|\boldsymbol{D}^T\overline{\boldsymbol{y}}_m|$. The closed-form solution makes our weighted sparse coding process very efficient.

2.3.2 Denoising Algorithm

With the solution $\hat{\boldsymbol{\alpha}}$ in (2.17), the clean patch in a PG can be estimated as $\hat{\boldsymbol{x}}_m = \boldsymbol{D}\hat{\boldsymbol{\alpha}} + \boldsymbol{\mu}_y$. Then the clean image $\hat{\boldsymbol{x}}$ can be reconstructed by aggregating all the estimated PGs. In practice, we could perform the above denoising procedures for several iterations for better denoising outputs. In iteration t, we use the iterative regularization strategy [71] to add back to the

Alg. 1: Patch Group Prior based Denoising (PGPD)

Input: Noisy image $\boldsymbol{y}$, PG-GMM model

1. Initialization: $\hat{\boldsymbol{x}}^{(0)} = \boldsymbol{y}, \boldsymbol{y}^{(0)} = \boldsymbol{y}$;

for $t = 1 : IteNum$ **do**

2. Iterative Regularization: $\boldsymbol{y}^{(t)} = \hat{\boldsymbol{x}}^{(t-1)} + \delta(\boldsymbol{y} - \boldsymbol{y}^{(t-1)})$;

3. Estimate the standard deviation of noise;

   for each PG $\boldsymbol{Y}$ **do**

4. Calculate group mean $\boldsymbol{\mu}_y$ and form PG $\overline{\boldsymbol{Y}}$;

5. Gaussian component selection via (2.9);

6. Denoising by Weighted Sparse Coding (2.11);

7. Recover each patch in this PG via $\hat{\boldsymbol{x}}_m = \boldsymbol{D}\hat{\boldsymbol{\alpha}} + \boldsymbol{\mu}_y$;

   end for

8. Aggregate the recovered PGs to form the recovered image $\hat{\boldsymbol{x}}^{(t)}$;

end for

Output: The recovered image $\hat{\boldsymbol{x}}^{(IteNum)}$.

recovered image $\hat{\boldsymbol{x}}^{(t-1)}$ some estimation residual in iteration $t-1$. The standard deviation of noise in iteration t is adjusted as $\sigma^{(t)} = \eta * \sqrt{\sigma^2 - \|\boldsymbol{y} - \boldsymbol{y}^{(t-1)}\|_2^2}$, where η is a constant. The proposed denoising algorithm is summarized in Algorithm 1 (Alg. 1).

In the proposed algorithm, there are N PGs in an image and M patches in each PG. Then the computational cost for Gaussian component selection is $O(p^6NMK)$. The cost for iterative regularization and noise estimation is negligible. The cost for closed-form weighted sparse coding is $O(p^4NM)$. Suppose that there are T iterations, the overall complexity of our denoising algorithm is $O(p^6NMKT)$.

Figure 2.5 The 20 widely used test images.

2.4 Experiments

In this section, we perform image denoising experiments on 20 widely used natural images (shown in Fig. 2.5). More experiments on the Berkeley Segmentation Data Set [5] can be found in the supplementary file. As a common experimental setting in literature, additive white Gaussian noise with zero mean and standard deviation σ is added to the image to test the performance of competing denoising methods. We call our method *PG Prior based Denoising* (PGPD) in the following experiments. The Matlab source code of our PGPD algorithm can be downloaded at http://www4.comp.polyu.edu.hk/~cslzhang/code/PGPD.zip.

2.4.1 Implementation Details

Our proposed PGPD method contains two stages, the prior learning stage and the denoising stage. In the PG-GMM learning stage, there are 4 parameters: p, M, W and K. The patch size ($p \times p$) is set as $p = 6$ for $0 < \sigma \leq 20$, $p = 7$ for $20 < \sigma \leq 30$, $p = 8$ for $30 < \sigma \leq 50$, and $p = 9$ for $50 < \sigma \leq 100$. The window size (W) for PG searching is set to $W = 31$. The number (M) of patches in a PG is set to $M = 10$. The number (K) of Gaussian components is set to $K = 64$ for $p = 6$ and $K = 32$ otherwise. We extracted about one million PGs from the Kodak PhotoCD Dataset to train the PG-GMM.

In the denoising stage, there are 3 parameters: c, δ, and η. In our implementation, (c, δ, η) are set to (0.33, 0.10, 0.79), (0.29, 0.09, 0.73), (0.19, 0.08, 0.89), (0.15, 0.07, 0.98), (0.12, 0.06, 1.05),

Clean Noisy: 18.59 PPD: 28.85 PGPD: 29.09

Figure 2.6 Denoised images and PSNR (dB) results of *Hill* by the PPD method and PGPD method (the standard deviation of noise is $\sigma = 30$).

$(0.09, 0.05, 1.15)$, $(0.06, 0.05, 1.30)$ when $\sigma = 10, 20, 30, 40, 50, 75, 100$, respectively. In addition, on all noise levels we stop Algorithm 1 in 4 iterations.

2.4.2 Comparison with Patch Prior based Denoising

In this section, we compare the PSNR and visual quality of denoised images by the *Patch Prior based Denoising* (PPD) method and the *Patch Group Prior based Denoising* (PGPD) method. As can be seen from Table 2.1 and Figures 2.6-2.9, PGPD is much better than PPD both quantitatively and qualitatively. This validates the effectiveness of our learned PG based NSS prior. In the following sections, we will omit the results of the PPD method.

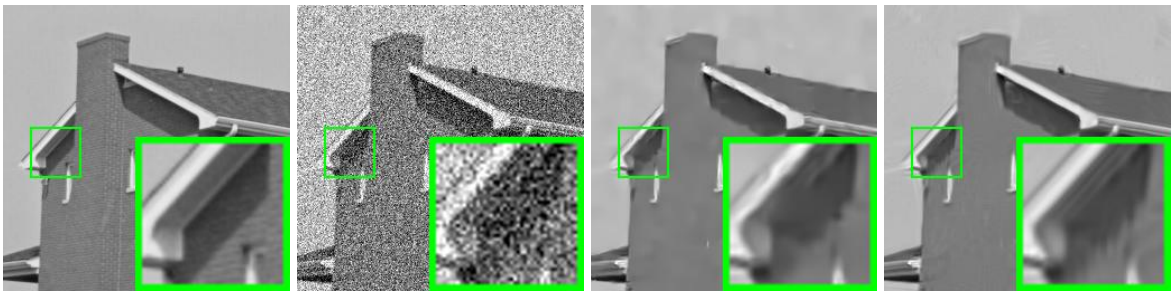

Clean Noisy: 16.06 PPD: 30.32 PGPD: 31.02

Figure 2.7 Denoised images and PSNR (dB) results of *House* by the PPD method and PGPD method (the standard deviation of noise is $\sigma = 40$).

Table 2.1 PSNR(dB) results of PPD and PGPD on the 20 natural images.

	$\sigma = 10$		$\sigma = 20$		$\sigma = 30$		$\sigma = 40$		$\sigma = 50$		$\sigma = 75$		$\sigma = 100$	
Images	**PPD**	**PGPD**	**PPD**	**PGPD**	**PPD**	**PGPD**	**PPD**	**PGPD**	**PPD**	**PGPD**	**PPD**	**PGPD**	**PPD**	**PGPD**
Airfield	31.02	31.18	27.97	28.19	26.33	26.46	25.20	25.30	24.33	24.44	22.69	22.90	21.54	21.82
Airplane	35.87	36.00	32.59	32.69	30.62	30.80	29.21	29.44	28.10	28.38	25.90	26.39	24.35	25.01
Baboon	30.46	30.55	26.54	26.67	24.54	24.63	23.23	23.39	22.30	22.47	20.71	21.09	19.99	20.38
Barbara	33.96	34.74	30.24	31.40	27.97	29.38	26.29	27.97	24.94	26.81	22.84	24.84	22.04	23.48
Boat	33.58	33.77	30.58	30.82	28.80	29.05	27.51	27.82	26.52	26.85	24.72	25.19	23.56	24.06
C. Man	33.91	34.14	30.12	30.35	28.25	28.53	27.05	27.33	26.13	26.46	24.36	24.64	22.80	23.23
Carhouse	34.35	34.47	30.61	30.73	28.62	28.80	27.29	27.51	26.27	26.53	24.44	24.85	23.21	23.67
Couple	33.78	34.03	30.47	30.71	28.54	28.84	27.16	27.53	26.07	26.50	24.22	24.70	23.12	23.55
Elaine	32.73	32.98	31.21	31.32	30.24	30.37	29.42	29.62	28.69	28.90	27.26	27.47	26.17	26.27
Hat	35.44	35.44	31.42	31.44	29.05	29.31	27.43	27.90	26.28	26.76	24.19	24.79	22.86	23.45
Hill	33.38	33.58	30.41	30.66	28.85	29.09	27.76	28.06	26.91	27.22	25.34	25.73	24.36	24.66
House	35.61	36.56	33.18	33.85	31.62	32.24	30.32	31.02	29.17	29.93	26.81	27.81	25.13	26.17
Lake	32.86	32.98	30.00	30.09	28.30	28.38	27.03	27.15	26.05	26.20	24.19	24.49	22.94	23.36
Leaves	33.87	34.45	29.84	30.46	27.51	27.99	25.88	26.29	24.56	25.03	21.94	22.61	19.77	20.95
Lena	35.59	35.81	32.75	32.94	30.98	31.27	29.67	30.10	28.61	29.11	26.68	27.40	25.41	26.09
Man	33.91	33.98	30.52	30.60	28.72	28.86	27.53	27.73	26.63	26.86	25.01	25.36	24.00	24.33
Monarch	34.27	34.53	30.40	30.68	28.27	28.49	26.81	27.02	25.66	26.00	23.51	24.00	21.89	22.56
Paint	34.16	34.31	30.52	30.62	28.39	28.42	26.88	26.94	25.70	25.82	23.50	23.89	22.05	22.65
Peppers	34.71	34.82	32.61	32.66	31.13	31.25	29.95	30.18	28.99	29.22	27.04	27.42	25.45	25.94
Zelda	35.50	35.51	32.21	32.21	30.35	30.43	29.07	29.23	28.06	28.24	26.37	26.56	25.28	25.41
Average	33.95	34.19	30.71	30.95	28.85	29.13	27.53	27.88	26.50	26.89	24.59	25.11	23.30	23.85

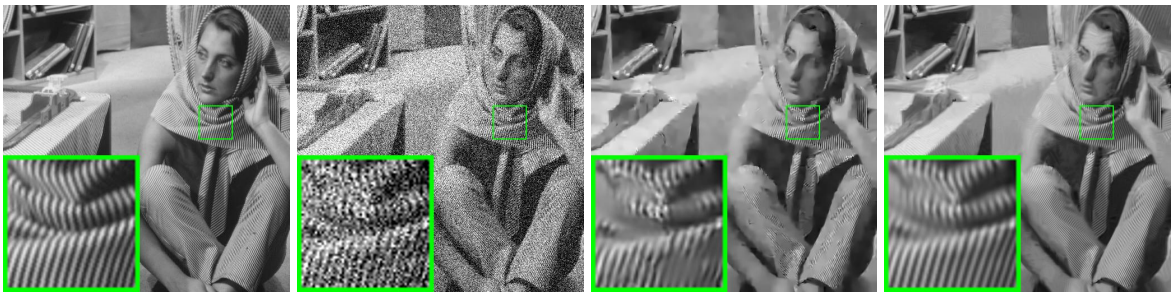

Clean Noisy: 14.16 PPD: 24.94 PGPD: 26.81

Figure 2.8 Denoised images and PSNR (dB) results of *Barbara* by the PPD method and PGPD method (the standard deviation of noise is $\sigma = 50$).

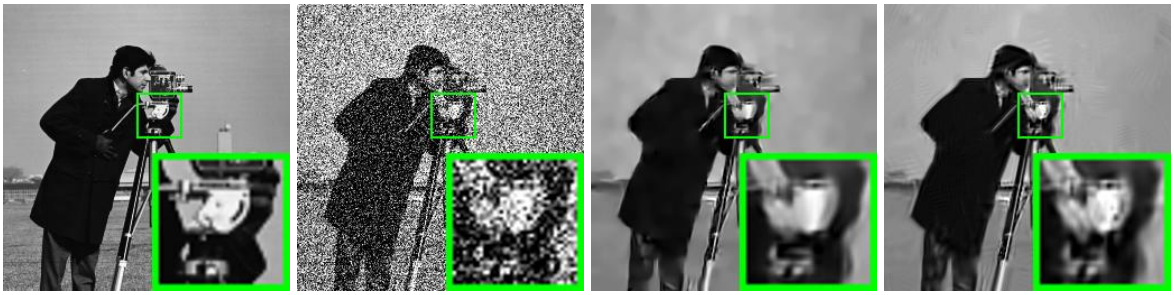

Clean | Noisy: 10.60 | PPD: 24.36 | PGPD: 24.64

Figure 2.9 Denoised images and PSNR (dB) results of *Cameraman* by the PPD method and PGPD method (the standard deviation of noise is $\sigma = 75$).

2.4.3 Comparison With the State-of-the-art Methods

We compare the proposed PGPD algorithm with BM3D [22], EPLL [111], LSSC [58], NCSR [24], and WNNM [36], which represent the state-of-the-arts of modern image denoising techniques and all of them exploit image NSS. The source codes of all competing algorithms are downloaded from the authors' websites and we use the default parameter settings.

To more clearly demonstrate the effectiveness of PG based NSS prior learning, we also compare with an extreme case of PGPD, i.e., letting $M = 1$ in the PG-GMM learning stage[1]. Clearly, this reduces to a patch based prior learning scheme and no NSS prior will be learned. We call this extreme case as *Patch Prior based Denoising* (PPD). The number of Gaussian components in PPD is set to 64, and the weighted sparse coding framework in it is the same as that in PGPD. All the other parameters in PPD are tuned to achieve its best performance.

2.4.4 Results and Discussions

We evaluate the competing methods from three aspects: PSNR, Speed, and Visual Quality.

PSNR. In Tables 2.2-2.4, we present the PSNR results on four noise levels $\sigma = 30, 40, 50, 75$. The results on noise levels $\sigma = 10, 20, 100$ can be found in the supplementary material. From

[1]Since there is only 1 patch in the PG, the group mean vector cannot be subtracted and we subtract the mean value of the patch from it.

Tables 2.2-2.4, we have several observations. Firstly, PGPD achieves much better PSNR results than PPD. The improvements are 0.24~0.52dB on average. This clearly demonstrates the effectiveness of PG-GMM in NSS prior learning. Secondly, PGPD has higher PSNR values than BM3D, LSSC, EPLL and NCSR, and is only slightly inferior to WNNM. However, PGPD is much more efficient than WNNM (see next paragraph). This validates the strong ability of PG based NSS prior in image denoising.

Speed. Efficiency is another important factor to evaluate an algorithm. We then compare the speed of all competing methods. All experiments are run under the Matlab2014b environment on a machine with Intel(R) Core(TM) i7-4770K CPU of 3.50GHz and 12.0 GB RAM. The run time (s) of competing methods on the test images is shown in Table 2.5. One can easily see that BM3D is the fastest method. The proposed PGPD is the second fastest, and it is much faster than the other methods. For a 256×256 image, BM3D costs about 0.8s while PGPD costs about 10s. However, please note that BM3D is implemented with compiled C++ mex-function and with parallelization, while PGPD is implemented purely in Matlab. EPLL is about 4 times slower than PGPD. Both LSSC and NCSR are very slow since they need to train online dictionary. Though WNNM has the highest PSNR, it suffers from huge computational cost due to the many online SVD operations. It is 10~16 times slower than PGPD.

Visual Quality. Considering that human subjects are the ultimate judge of the image quality, the visual quality of denoised images is also critical to evaluate a denoising algorithm. In Figures 2.10 to 2.13, we show some visual quality comparisons on different testing images. For example, Fig. 2.12 and Fig. 2.13 show the denoised images of *Airplane* and *Cameraman* by the competing methods, respectively. Due to the page limit, the results of PPD are not shown here, and more visual comparisons can be found in the supplementary file. We can see that BM3D tends to over-smooth the image, while EPLL, LSSC, NCSR and WNNM are likely to generate artifacts when noise is high. Owe to the learned NSS prior, the proposed PGPD method is more robust against artifacts, and it preserves edge and texture areas much better

Table 2.2 PSNR(dB) results of different denoising algorithms on 20 natural images.

	σ = 10						σ = 20					
Images	**BM3D**	**LSSC**	**EPLL**	**NCSR**	**WNNM**	**PGPD**	**BM3D**	**LSSC**	**EPLL**	**NCSR**	**WNNM**	**PGPD**
Airfield	31.32	31.51	31.37	31.40	31.47	31.18	28.13	28.48	28.18	28.07	28.40	28.19
Airplane	35.97	36.05	35.92	36.04	36.26	36.00	32.63	32.57	32.64	32.69	32.91	32.69
Baboon	30.58	30.67	30.62	30.61	30.79	30.55	26.61	26.75	26.71	26.64	26.84	26.67
Barbara	34.98	34.99	33.65	35.01	35.51	34.74	31.78	31.60	29.85	31.78	32.19	31.40
Boat	33.92	34.03	33.67	33.92	34.09	33.77	30.88	30.92	30.71	30.79	31.01	30.82
C. Man	34.18	34.24	34.05	34.18	34.44	34.14	30.48	30.59	30.38	30.47	30.75	30.35
Carhouse	34.45	34.52	34.32	34.51	34.70	34.47	30.74	30.77	30.66	30.79	30.90	30.73
Couple	34.04	34.01	33.88	34.00	34.14	34.03	30.76	30.74	30.60	30.60	30.82	30.71
Elaine	33.36	34.36	32.90	33.83	33.76	32.98	31.48	31.74	31.25	31.47	31.44	31.32
Hat	35.40	35.56	35.23	35.45	35.75	35.44	31.55	31.48	31.41	31.48	31.66	31.44
Hill	33.62	33.68	33.49	33.69	33.79	33.58	30.72	30.73	30.50	30.65	30.81	30.66
House	36.71	36.95	35.75	36.79	36.95	36.56	33.77	34.11	33.12	33.87	34.01	33.85
Lake	33.03	33.23	33.00	33.10	33.21	32.98	30.05	30.15	30.09	30.05	30.29	30.09
Leaves	34.04	34.52	33.39	34.52	35.20	34.45	30.09	30.46	29.55	30.45	31.10	30.46
Lena	35.93	35.85	35.62	35.85	36.06	35.81	33.05	32.89	32.74	32.95	33.12	32.94
Man	33.98	34.10	34.01	34.05	34.23	33.98	30.59	30.72	30.68	30.59	30.77	30.60
Monarch	34.12	34.44	34.36	34.51	35.03	34.53	30.35	30.59	30.60	30.62	31.11	30.68
Paint	34.00	34.35	34.09	34.15	34.50	34.31	30.36	30.59	30.50	30.33	30.77	30.62
Peppers	35.01	35.13	34.83	35.03	35.06	34.82	32.76	32.61	32.61	32.66	32.81	32.66
Zelda	35.62	35.54	35.57	35.49	35.69	35.51	32.29	32.06	32.29	32.10	32.30	32.21
Average	34.21	34.39	33.99	34.31	34.53	34.19	30.95	31.03	34.75	30.95	31.20	30.95

than the other methods. For example, in image *Airplane*, PGPD reconstructs the numbers "01568" more clearly than all the other methods including WNNM. In image *Cameraman*, PGPD recoveries more faithfully the fine structures of the camera area.

In summary, the proposed PGPD method demonstrates powerful denoising ability quantitatively and qualitatively, and it is highly efficient.

Table 2.3 PSNR(dB) results of different denoising algorithms on 20 natural images.

	$\sigma = 30$						$\sigma = 40$					
Images	**BM3D**	**LSSC**	**EPLL**	**NCSR**	**WNNM**	**PGPD**	**BM3D**	**LSSC**	**EPLL**	**NCSR**	**WNNM**	**PGPD**
Airfield	26.41	26.68	26.52	26.36	26.67	26.46	25.10	25.51	25.36	25.07	25.48	25.30
Airplane	30.71	30.62	30.68	30.70	30.97	30.80	29.20	29.21	29.28	29.28	29.58	29.44
Baboon	24.57	24.78	24.70	24.63	24.85	24.63	23.11	23.51	23.35	23.28	23.58	23.39
Barbara	29.81	29.60	27.64	29.62	30.31	29.38	27.99	28.17	26.06	28.20	28.76	27.97
Boat	29.12	29.06	28.97	28.94	29.24	29.05	27.74	27.77	27.72	27.65	27.96	27.82
C. Man	28.64	28.63	28.40	28.58	28.80	28.53	27.18	27.34	27.10	27.12	27.47	27.33
Carhouse	28.78	28.79	28.70	28.72	28.94	28.80	27.38	27.49	27.38	27.40	27.58	27.51
Couple	28.87	28.76	28.69	28.57	28.98	28.84	27.48	27.41	27.34	27.24	27.62	27.53
Elaine	30.45	30.54	30.26	30.26	30.46	30.37	29.52	29.55	29.46	29.59	29.60	29.62
Hat	29.37	29.22	29.22	29.16	29.44	29.31	27.74	27.60	27.73	27.66	27.85	27.90
Hill	29.16	29.09	28.94	28.97	29.25	29.09	27.99	28.00	27.86	27.83	28.12	28.06
House	32.09	32.40	31.48	32.07	32.52	32.24	30.65	31.10	30.20	30.80	31.31	31.02
Lake	28.34	28.36	28.41	28.31	28.59	28.38	26.98	27.13	27.19	26.99	27.34	27.15
Leaves	27.81	27.65	27.36	28.14	28.60	27.99	25.69	26.04	25.80	26.24	26.95	26.29
Lena	31.26	31.18	30.98	31.06	31.43	31.27	29.86	29.91	29.69	29.92	30.11	30.10
Man	28.86	28.87	28.87	28.78	29.00	28.86	27.65	27.64	27.68	27.54	27.80	27.73
Monarch	28.36	28.20	28.50	28.46	28.91	28.49	26.72	26.87	27.05	26.85	27.47	27.02
Paint	28.29	28.29	28.45	28.10	28.58	28.42	26.69	26.77	27.00	26.50	27.10	26.94
Peppers	31.26	31.17	31.10	31.11	31.38	31.25	29.97	30.00	29.93	30.07	30.18	30.18
Zelda	30.45	30.27	30.44	30.16	30.48	30.43	29.10	28.91	29.18	28.94	29.12	29.23
Average	29.13	29.11	28.92	29.03	29.37	29.13	27.69	27.80	27.62	27.71	28.05	27.88

2.4.5 Additional Results on the Berkeley Segmentation Data Set

In this section, we give the denoising results (PSNR and visual quality) on the Berkeley Segmentation Data Set [5]. This dataset contains 500 images of size 321×481. Since EPLL is trained on the 300 images in the training set and validation set, we use the 200 images in the testing set for comparison.

From Table 2.6, we can see that EPLL is comparable to BM3D and LSSC on the 200 test images. Though the proposed PGPD is trained on the Kodak PhotoCD dataset, in which the images have different resolution and statistics from the images in the Berkeley Segmentation

Table 2.4 PSNR(dB) results of different denoising algorithms on 20 natural images.

	σ = 50						σ = 75					
Images	**BM3D**	**LSSC**	**EPLL**	**NCSR**	**WNNM**	**PGPD**	**BM3D**	**LSSC**	**EPLL**	**NCSR**	**WNNM**	**PGPD**
Airfield	24.20	24.58	24.46	24.18	24.51	24.44	22.71	22.85	22.85	22.57	22.94	22.90
Airplane	28.24	28.15	28.19	28.18	28.55	28.38	26.40	26.16	26.14	26.10	26.68	26.39
Baboon	22.35	22.60	22.35	22.43	22.73	22.47	21.11	21.18	20.85	21.03	21.36	21.09
Barbara	27.23	27.03	24.83	26.99	27.79	26.81	25.12	25.01	22.94	24.72	25.81	24.84
Boat	26.78	26.77	26.74	26.67	26.97	26.85	25.12	25.03	25.01	24.87	25.29	25.19
C. Man	26.12	26.35	26.10	26.15	26.42	26.46	24.33	24.41	24.29	24.22	24.55	24.64
Carhouse	26.53	26.48	26.39	26.41	26.67	26.53	24.89	24.85	24.65	24.53	25.04	24.85
Couple	26.46	26.35	26.30	26.19	26.65	26.50	24.70	24.51	24.51	24.33	24.85	24.70
Elaine	28.94	28.75	28.77	28.85	28.97	28.90	27.41	27.27	27.38	27.16	27.53	27.47
Hat	26.77	26.41	26.62	26.51	26.78	26.76	24.77	24.31	24.65	24.48	24.77	24.79
Hill	27.19	27.14	27.04	26.99	27.34	27.22	25.68	25.57	25.60	25.40	25.88	25.73
House	29.69	29.99	29.12	29.62	30.32	29.93	27.51	27.75	27.09	27.22	28.25	27.81
Lake	26.13	26.15	26.24	26.02	26.41	26.20	24.49	24.25	24.50	24.26	24.66	24.49
Leaves	24.68	24.78	24.55	24.96	25.47	25.03	22.49	22.17	22.12	22.60	23.06	22.61
Lena	29.05	28.95	28.68	28.90	29.25	29.11	27.26	27.22	26.88	27.00	27.54	27.40
Man	26.81	26.72	26.79	26.67	26.94	26.86	25.32	25.10	25.26	25.10	25.42	25.36
Monarch	25.82	25.88	25.94	25.76	26.31	26.00	23.91	23.66	23.88	23.67	24.31	24.00
Paint	25.67	25.59	25.87	25.36	25.98	25.82	23.80	23.52	23.88	23.44	24.07	23.89
Peppers	29.12	29.06	28.98	29.07	29.34	29.22	27.28	27.14	27.15	26.96	27.55	27.42
Zelda	28.25	27.90	28.22	27.97	28.21	28.24	26.60	26.09	26.55	26.21	26.44	26.56
Average	26.80	26.78	26.61	26.69	27.08	26.89	25.04	24.90	24.81	24.79	25.30	25.11

Data Set, it still shows superiority over EPLL and other methods. In Figures 2.14-2.17, we compare the visual quality of the denoised images by the competing methods. For better visualization, the presented images are cropped to size of 321×321.

2.5 Conclusion

How to learn explicit models of nonlocal self-similarity (NSS) prior for image restoration is an open problem, and we made a good attempt on this by lifting the patch based image modeling to patch group (PG) based image modeling. A PG is a group of similar patches in an image

Table 2.5 Average run time (seconds) with standard deviation of different methods on images of size 256×256 and 512×512. BM3D uses parallelization and is implemented with compiled C++ mex-function while the other methods are implemented in Matlab.

	256×256						
σ	**BM3D**	**LSSC**	**EPLL**	**NCSR**	**WNNM**	**PPD**	**PGPD**
10	0.67 ± 0.09	186.90 ± 4.02	38.47 ± 0.10	126.43 ± 3.84	84.34 ± 1.42	10.15 ± 0.07	8.00 ± 0.05
20	0.70 ± 0.09	184.21 ± 5.82	38.47 ± 0.13	156.14 ± 5.26	84.70 ± 1.71	10.18 ± 0.15	8.09 ± 0.09
30	0.70 ± 0.09	212.07 ± 8.72	38.55 ± 0.09	149.31 ± 4.19	155.75 ± 0.94	10.34 ± 0.25	8.47 ± 0.07
40	0.67 ± 0.11	209.13 ± 6.99	38.51 ± 0.08	346.91 ± 18.65	157.35 ± 1.48	10.47 ± 0.21	9.80 ± 0.08
50	0.87 ± 0.04	221.36 ± 6.27	40.21 ± 1.82	326.93 ± 9.64	119.47 ± 4.65	10.88 ± 0.05	9.91 ± 0.13
75	0.89 ± 0.03	240.75 ± 6.08	40.91 ± 1.33	258.04 ± 11.80	179.30 ± 5.08	10.87 ± 0.27	11.73 ± 0.08
100	0.90 ± 0.03	257.25 ± 6.01	42.80 ± 1.93	252.74 ± 8.50	191.32 ± 1.47	10.90 ± 0.19	11.78 ± 0.08
	512×512						
σ	**BM3D**	**LSSC**	**EPLL**	**NCSR**	**WNNM**	**PPD**	**PGPD**
10	3.16 ± 0.12	746.53 ± 24.96	160.93 ± 2.81	624.83 ± 40.24	352.34 ± 3.87	41.79 ± 0.32	33.03 ± 0.25
20	3.32 ± 0.11	762.62 ± 31.25	159.80 ± 0.37	751.09 ± 42.89	351.09 ± 3.14	42.09 ± 0.41	33.26 ± 0.29
30	3.32 ± 0.09	856.82 ± 40.32	160.21 ± 0.18	709.90 ± 31.62	650.54 ± 7.23	42.36 ± 0.99	35.45 ± 0.24
40	3.18 ± 0.18	865.83 ± 40.96	160.23 ± 0.17	1620.74 ± 104.59	652.49 ± 10.49	41.70 ± 0.47	40.13 ± 0.23
50	3.85 ± 0.09	891.53 ± 48.60	161.36 ± 3.08	1492.78 ± 65.87	476.50 ± 12.34	41.75 ± 0.64	40.40 ± 0.28
75	3.91 ± 0.05	983.05 ± 69.96	165.66 ± 2.62	1156.82 ± 66.37	784.92 ± 18.32	41.88 ± 0.78	50.00 ± 0.25
100	3.94 ± 0.04	1087.57 ± 68.76	177.51 ± 7.16	1100.00 ± 26.64	824.56 ± 34.41	42.80 ± 1.09	50.32 ± 0.31

region. After group mean subtraction, a PG can naturally represent the NSS variations of natural images. A PG based Gaussian Mixture Model (PG-GMM) learning algorithm was developed to learned the NSS prior from natural images, and an associated weighted sparse coding algorithm was developed for high performance image denoising. The so-called *PG Prior based Denoising* (PGPD) algorithm not only achieves highly competitive PSNR results with state-of-the-art denoising methods, but also is highly efficient and preserves better the image edges and textures. The proposed method can be extended to other image processing tasks such as deblurring and super-resolution.

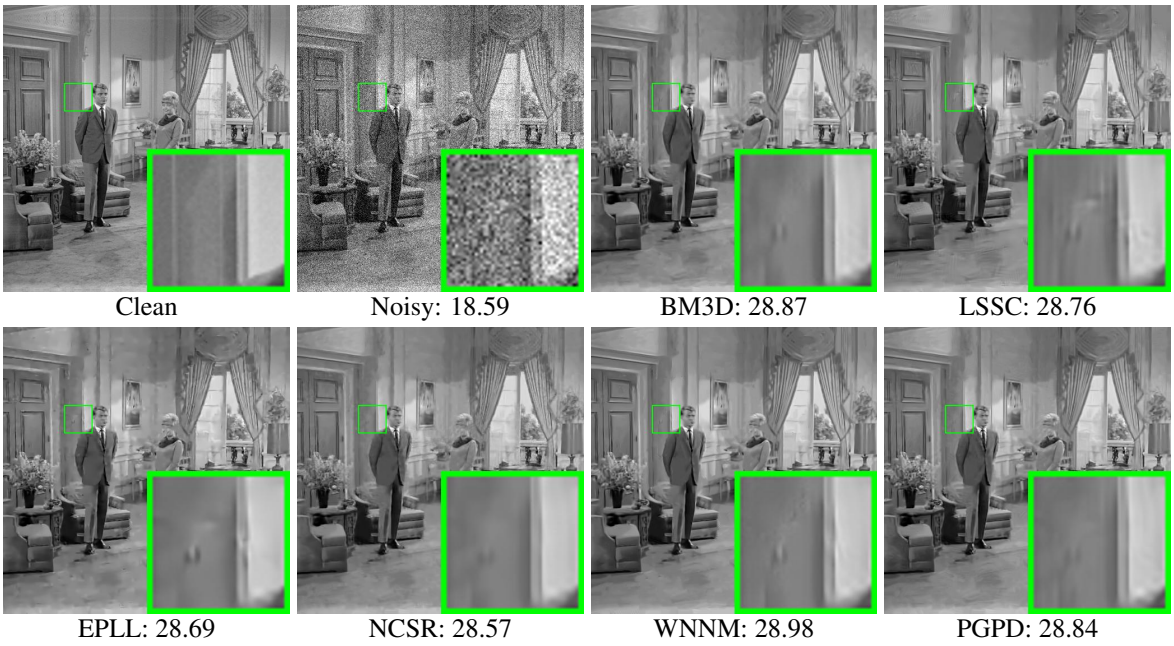

Figure 2.10 Denoised images and PSNR (dB) results of *Couple* by different methods (the standard deviation of noise is $\sigma = 30$).

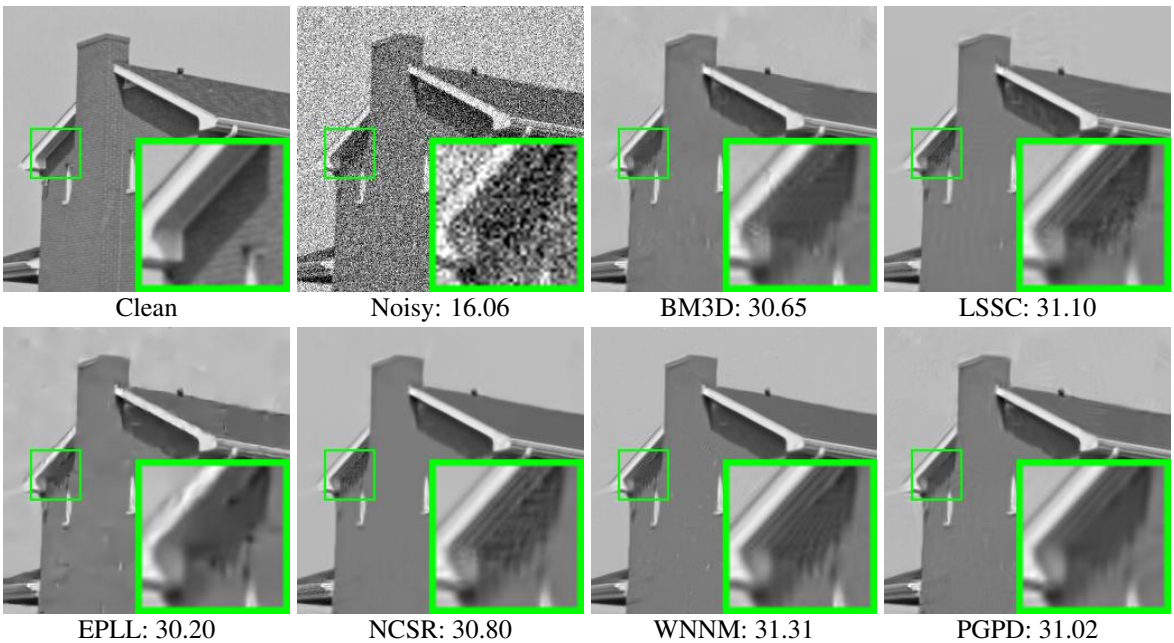

Figure 2.11 Denoised images and PSNR (dB) results of *House* by different methods (the standard deviation of noise is $\sigma = 40$).

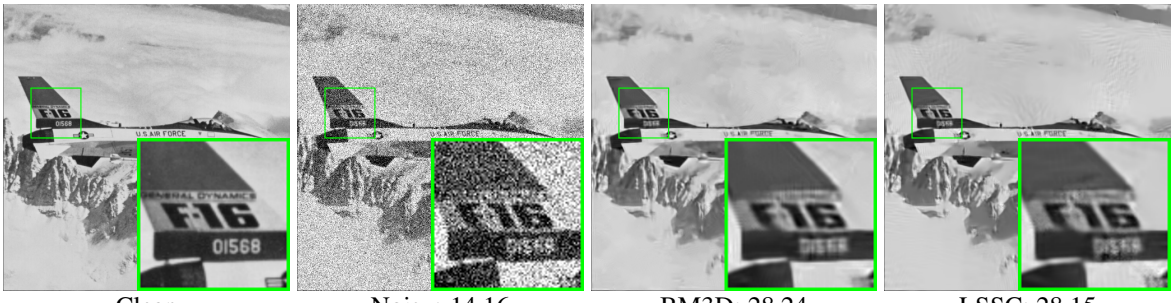

Figure 2.12 Denoised images and PSNR (dB) results of *Airplane* by different methods (the standard deviation of noise is $\sigma = 50$).

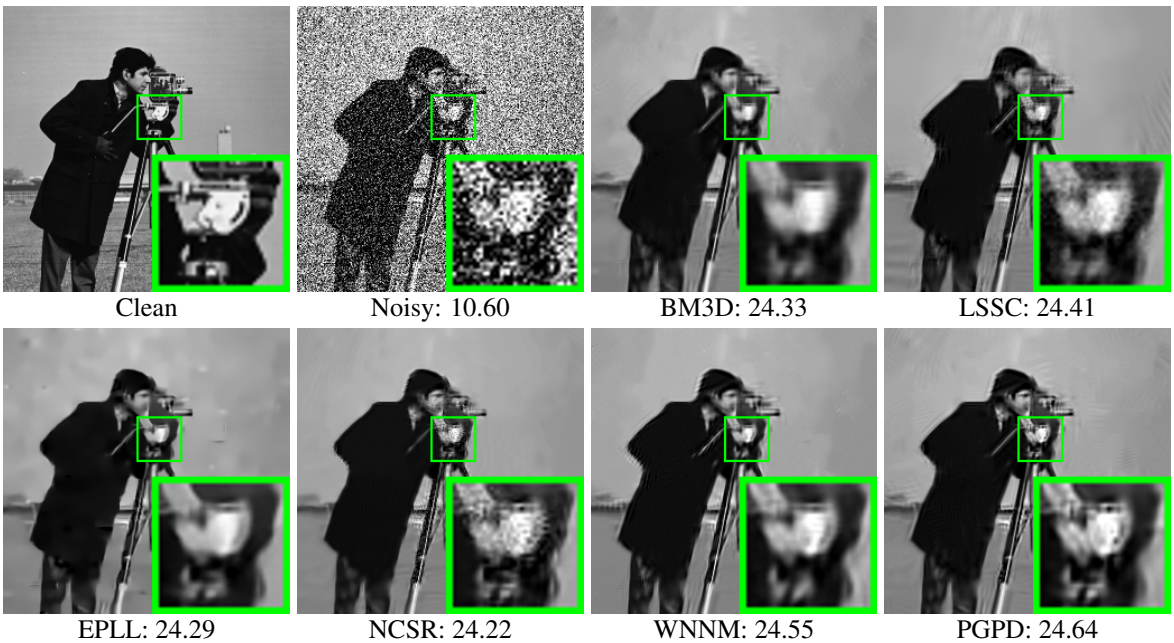

Figure 2.13 Denoised images and PSNR (dB) results of *Cameraman* by different methods (the standard deviation of noise is $\sigma = 75$).

Table 2.6 Average PSNR(dB) results of different denoising algorithms on the 200 test images of the Berkeley Segmentation Data Set.

Noise	**BM3D**	**LSSC**	**EPLL**	**NCSR**	**WNNM**	**PGPD**
$\sigma = 10$	33.62	33.75	33.64	33.68	33.88	33.60
$\sigma = 20$	29.86	30.02	29.96	29.89	30.11	29.89
$\sigma = 30$	27.93	28.05	28.00	27.92	28.17	27.96
$\sigma = 40$	26.58	26.75	26.71	26.58	26.88	26.73
$\sigma = 50$	25.71	25.80	25.77	25.65	25.96	25.82
$\sigma = 75$	24.22	24.18	24.18	24.04	24.42	24.30
$\sigma = 100$	23.21	23.12	23.15	23.00	23.37	23.29

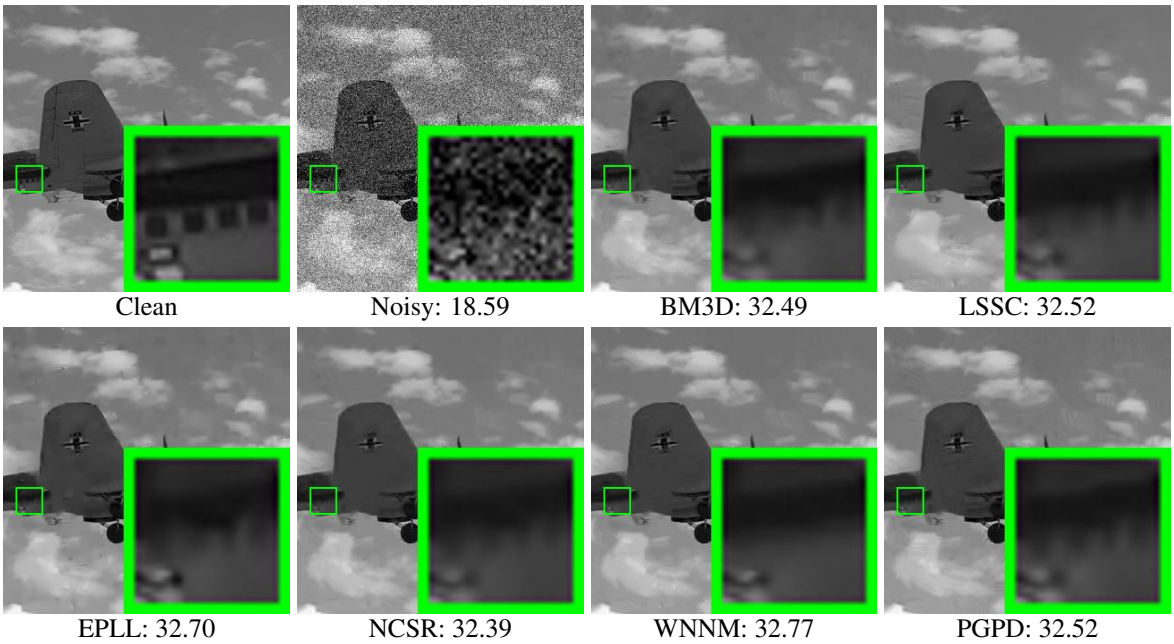

Figure 2.14 Denoised images and PSNR (dB) results of *3063* by different methods (the standard deviation of noise is $\sigma = 30$).

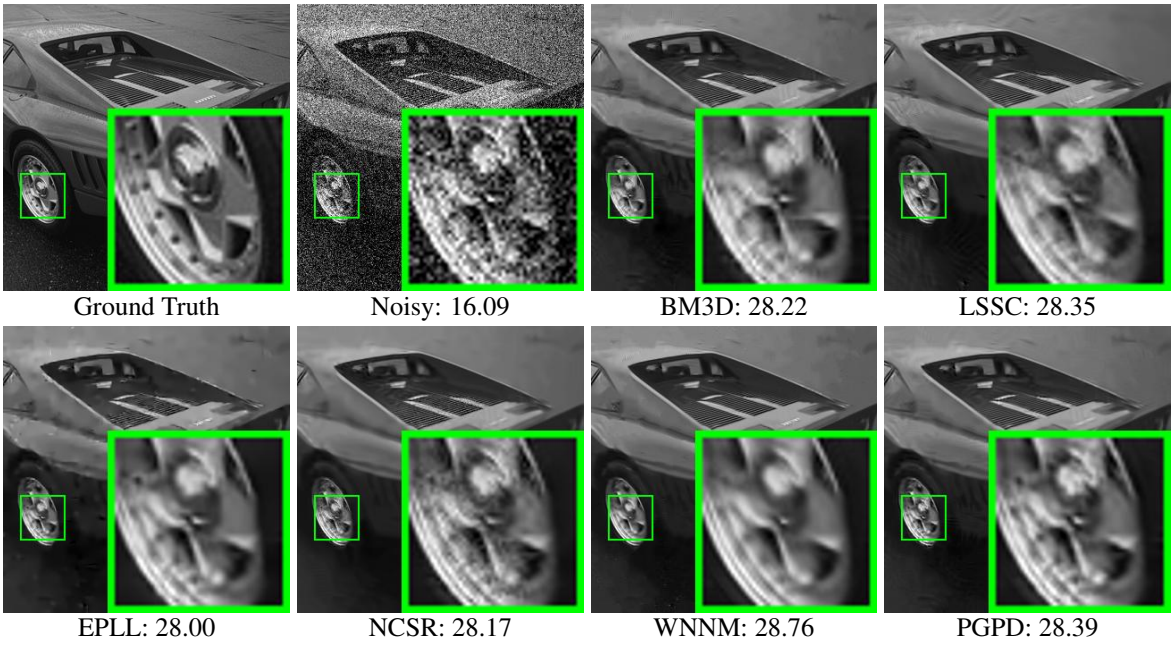

Figure 2.15 Denoised images and PSNR (dB) results of *29030* by different methods (the standard deviation of noise is $\sigma = 40$).

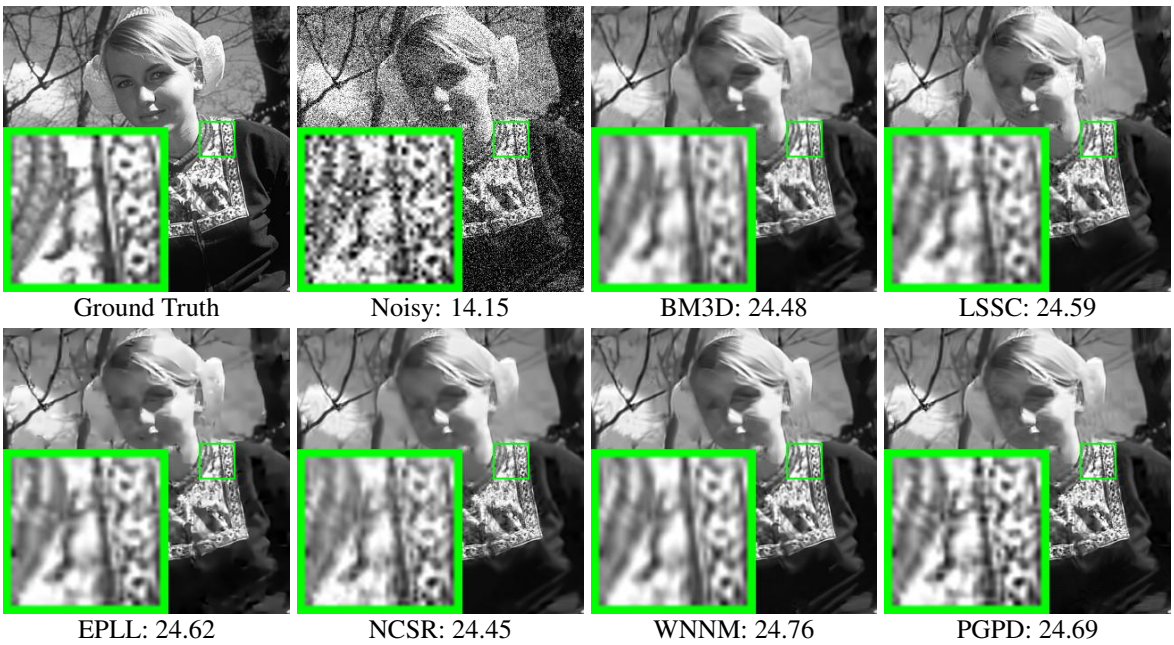

Figure 2.16 Denoised images and PSNR (dB) results of *258089* by different methods (the standard deviation of noise is $\sigma = 50$).

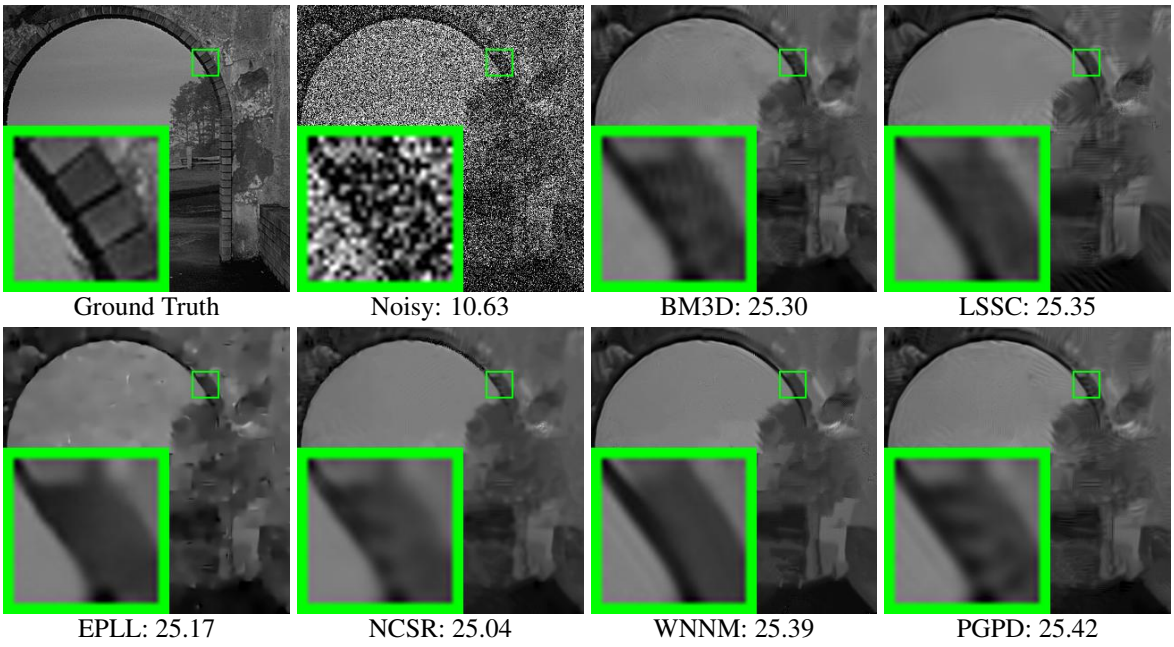

Figure 2.17 Denoised images and PSNR (dB) results of *5096* by different methods (the standard deviation of noise is $\sigma = 75$).

Chapter 3

External Prior Guided Internal Prior Learning for Real-world Image Denoising

3.1 Introduction

Image denoising is a crucial and indispensable step to improve image quality in digital imaging systems. In particular, with the decrease of size of CMOS/CCD sensors, image is more easily to be corrupted by noise and hence denoising is becoming increasingly important for high resolution imaging. The problem of image denoising has been extensively studied in literature and numerous image denoising methods [2, 7, 12, 13, 16, 17, 19, 21, 22, 24, 30, 32, 34, 36, 40, 43, 49–51, 53, 56–58, 62, 65, 67, 68, 76–79, 82, 83, 86, 89, 98, 99, 103, 106, 107, 109–111] have been proposed in the past decades. Most of existing denoising methods focus on the scenario of additive white Gaussian noise (AWGN) [7, 12, 13, 16, 19, 21, 22, 24, 30, 36, 49, 58, 77, 79, 83, 86, 89, 98, 103, 107, 109, 111], where the observed noisy image $\mathbf{y}$ is modeled as the addition of clean image $\mathbf{x}$ and AWGN $\mathbf{n}$, i.e., $\mathbf{y} = \mathbf{x} + \mathbf{n}$. There are also methods proposed for removing Poisson noise [82, 106], mixed Poisson and Gaussian noise [32, 56, 62, 65], mixed Gaussian and impulse noise [40, 43, 99], and real-world noise in real

photography [2, 34, 50, 51, 53, 68, 76, 78, 110].

Natural images have many priors, such as sparsity and nonlocal self-similarity, which can be employed as useful priors for designing image denoising methods. Based on the facts that natural images will be sparsely distributed in some transformed domain, wavelet [16] and curvelet [86] transforms have been widely adopted for image denoising. The sparse representation based methods [21, 22, 24, 30, 58, 109] encode image patches over a dictionary by using ℓ_1-norm minimization to enforce the sparsity. The well-known bilateral filters [89] employ the prior information that image pixels exhibit similarity in both spatial domain and intensity domain. Other image priors such as multiscale self-similarity [77] and nonlocal self-similarity [12, 49], or the combination of multiple image priors [36, 103] have also been successfully used in image denoising. For example, by using low-rank minimization to characterize the image nonlocal self-similarity, the WNNM [36] method achieves state-of-the-art performance for AWGN denoising.

Instead of using predefined image priors, methods have also been proposed to learn priors from natural images for denoising. The generative image prior learning methods usually learn prior models from a set of external clean images and apply the learned prior models to the given noisy image [79, 103, 111], or learn priors from the given noisy image to perform denoising [30]. Recently, the discriminative image prior learning methods [7, 13, 19, 83, 98, 107], which learn denoising models from pairs of clean and noisy images, have been becoming popular. The representative methods include the neural network based methods [13, 98, 107], random fields based methods [7, 83], and reaction diffusion based methods [19].

Learning natural image priors plays a key role in image denoising [7, 13, 17, 19, 24, 30, 57, 58, 67, 77, 79, 83, 98, 103, 107, 109, 111]. There are mainly four categories of prior learning based methods. 1) External prior learning methods [79, 103, 111] learn priors (e.g., dictionaries) from a set of external clean images, and the learned priors are used to recover the latent clean image from the given noisy image. 2) Internal prior learning methods

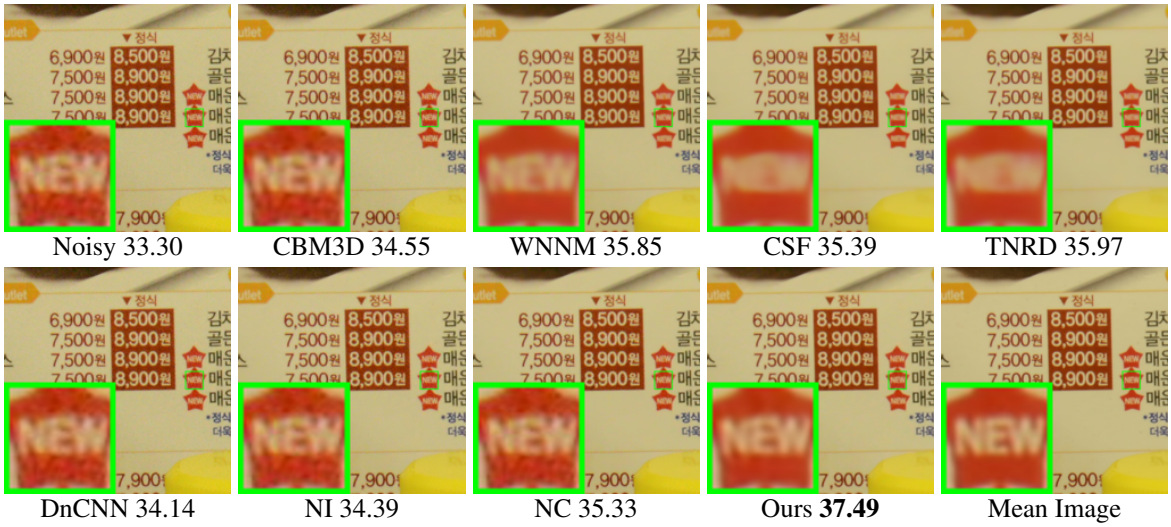

Figure 3.1 Denoised images and PSNR (dB) results of a region cropped from the real-world noisy image "Nikon D800 ISO 3200 A3" [68] by different methods. The scene was shot 500 times with the same camera and camera setting. The mean image of the 500 shots is roughly taken as the "ground truth", with which the PSNR index can be computed. The images are better viewed by zooming in on screen.

[24, 30, 58, 77, 109] directly learn priors from a given noisy image, and image denoising is often done simultaneously with the prior learning process. 3) Discriminative prior learning methods [7, 13, 19, 83, 98, 107] learn discriminative models or mapping functions from clean and noisy image pairs, and the learned models or mapping functions are applied to a noisy image for denoising. 4) Hybrid methods [17, 57, 67] combine the external and internal priors to denoise the given input image.

It has been shown [79, 103, 111] that the external priors learned from natural clean images are effective and efficient for universal image denoising problems, whereas they are not adaptive to the given noisy image and some fine-scale image structures may not be well recovered. By contrast, the internal priors learned from the given noisy image are adaptive to image content, but the learned priors can be much affected by noise and the learning processing is usually slow [24, 30, 58, 77, 109]. Besides, most of the internal prior learning methods [24, 30, 58, 77, 109] assume additive white Gaussian noise (AWGN), making the learned

priors less robust for real-world noisy images. In this work, we use external priors to guide the internal prior learning. Our method is not only much faster than the traditional internal learning methods, but also very robust to denoise real-world noisy images.

In [67], the authors employed external clean patches to denoise noisy patches with high individual Signal-to-Noise-Ratio (PatchSNR), and employed internal noisy patches to denoise noisy patches with low PatchSNR. This is essentially different from our work which employs the external patch group based prior to guide the clustering and dictionary learning of the internal noisy patch groups. In [17], the external priors are only used to guide the internal patch clustering for image denoising, while in our work, the learned external priors are employed to guide not only the internal clustering, but also the internal dictionary learning. Besides, the method of [17] follows a patch based framework for AWGN removal, while in our work we employ a patch group based framework for real-world noisy image denoising. In addition, some technical details are also different. For example, method in [17] utilizes low-rank minimization for denoising, while we use dictionary learning and sparse coding for denoising. In the Targeted Image Denoising (TID) method [57], targeted images are selected from a large dataset for each patch in the input noisy image for denoising, which is computationally expensive.

Most of the denoising methods in literature [7, 12, 13, 16, 19, 21, 22, 24, 30, 36, 49, 58, 77, 79, 83, 86, 89, 98, 103, 107, 109, 111] assume AWGN noise and use simulated noisy images for algorithm design and evaluation. However, the assumption of AWGN is too ideal to be true for real-world noisy images, where the noise is much more complex and varies with different scenes, cameras and camera settings (ISO, shutter speed, and aperture, etc.) [38, 68]. As a result, many denoising methods in literature, including those learning based methods, become less effective when applied to real-world noisy images. Fig. 3.1 shows an example, where we apply some representative and state-of-the-art denoising methods, including CBM3D [21], WNNM [36], DnCNN [107], CSF [83], and TNRD [19] to a real-world noisy image (captured

by a Nikon D800 camera with ISO is 3200) provided in [68]. One can see that these methods either remain much the noise or over-smooth the image details.

Recently, several denoising methods have been proposed to remove unknown noise from real-world noisy images [34, 50, 51, 53, 68, 76, 78, 110]. Portilla [76] employed a correlated Gaussian model to estimate the noise of each wavelet subband. Rabie [78] modeled the noisy pixels as outliers and performed denoising via Lorentzian robust estimator. Liu et al. [53] proposed the "noise level function" to estimate the noise and performed denoising by learning a Gaussian conditional random field. Gong et al. [34] proposed to model the data fitting term via weighted sum of ℓ_1 and ℓ_2 norms and performed denoising by a simple sparsity regularization term in the wavelet transform domain. The "Noise Clinic" [50, 51] estimates the noise distribution by using a multivariate Gaussian model and removes the noise by using a generalized version of nonlocal Bayesian model [49]. Zhu et al. [110] proposed a Bayesian method to approximate and remove the noise via a low-rank mixture of Gaussians (MoG) model. The method in [68] models the cross-channel noise in real-world noisy image as a multivariate Gaussian and the noise is removed by the Bayesian nonlocal means filter [46]. The commercial software Neat Image [2] estimates the noise parameters from a flat region of the given noisy image and filters the noise correspondingly.

There have been a few methods [34, 50, 51, 53, 68, 76, 78, 110] and software toolboxes [2] developed for real-world noisy image denoising. Almost all of these methods follow a two-stage framework: first estimate the parameters of the noise model (usually assumed to be Gaussian or mixture of Gaussians (MoG)), and then perform denoising with the estimated noise model. However, the noise in real-world noisy images is very complex and is hard to be modeled by explicit distributions such as Gaussian and MoG. According to [38], the noise corrupted in the in-camera imaging process [45, 47, 68, 90] is signal dependent and comes from five main sources: photon shot, fixed pattern, dark current, readout, and quantization noise. The existing methods [2, 34, 50, 51, 53, 68, 76, 78, 110] mentioned above may not

perform well on real-world noisy image denoising tasks. Fig. 3.1 also shows the denoising results of two real-world noisy image denoising methods, Noise Clinic [50, 51] and Neat Image [2]. One can see that these two methods still generate much noise caused artifacts.

This work aims to develop a new paradigm for real-world noisy image denoising. Different from existing real-world noisy image denoising methods [34, 50, 51, 53, 68, 76, 78, 110] which focus on noise modeling, we focus on image prior learning. We argue that with a strong and adaptive prior learning scheme, robust denoising performance on real-world noisy images can still be obtained. To achieve this goal, we propose to first learn image priors from external clean images, and then employ the learned external priors to guide the learning of internal priors from the given noisy image. The flowchart of the proposed method is illustrated in Fig. 3.2. We first extract millions of patch groups (PGs) from a set of high quality natural images, with which a Gaussian Mixture Model (GMM) is learned as the external image prior. The learned GMM prior model is used to cluster the PGs extracted from the given noisy image, and then an external-internal hybrid orthogonal dictionary is learned as the final prior for each cluster, with which the denoising can be readily performed by weighted sparse coding with closed form solution. Our proposed denoising method is simple and efficient, yet our extensive experiments on real-world noisy images demonstrate its better denoising performance than the current state-of-the-arts.

3.2 External Prior Guided Internal Prior Learning for Image Denoising

In this section, we first describe the learning of external prior, and then describe in detail the guided internal prior learning method, followed by the denoising algorithm.

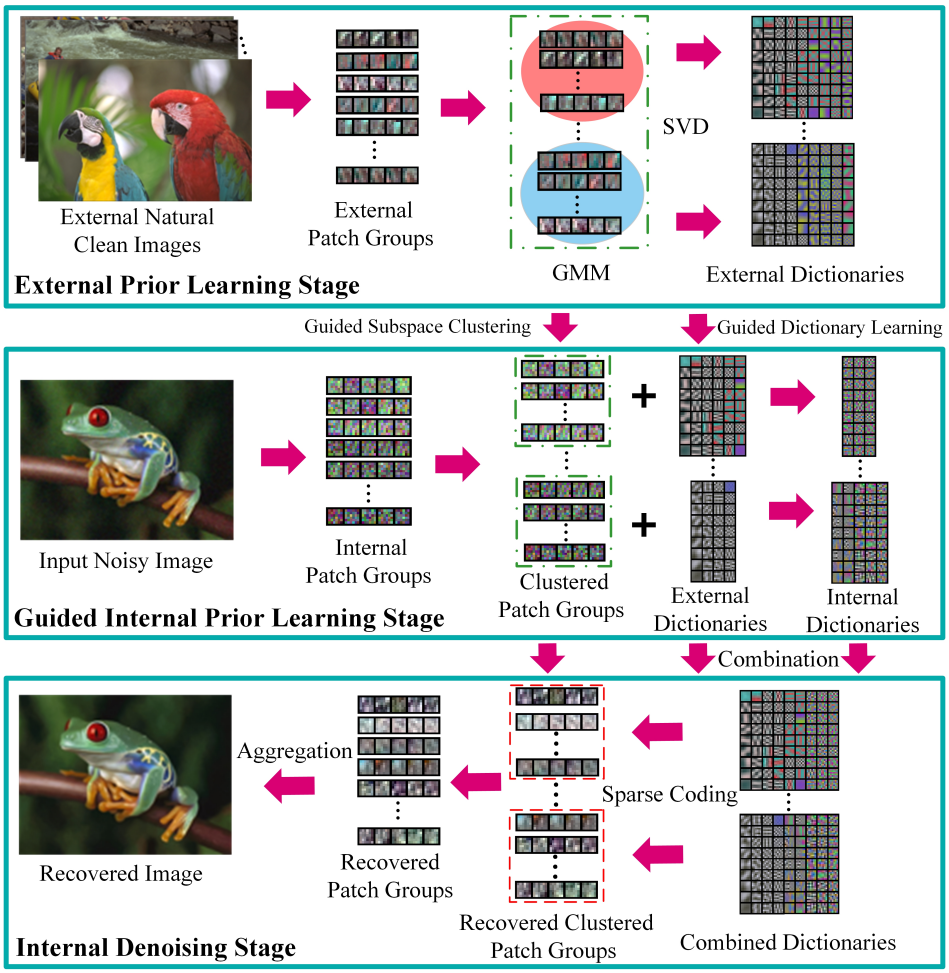

Figure 3.2 Flowchart of the proposed external prior guided internal prior learning and denoising framework.

3.2.1 Learn External Patch Group Priors

The nonlocal self-similarity based patch group (PG) prior learning [103] has proved to be very effective for image denosing. In this work, we extract PGs from natural clean images to learn external priors. A PG is a group of similar patches to a local patch. In our method, each local patch is extracted from a RGB image with patch size $p \times p \times 3$. We search the M most similar (i.e., smallest Euclidean distance) patches to this local patch (including the local patch itself) in a $W \times W$ region around it. Each patch is stretched to a patch vector $\mathbf{x}_m \in \mathbb{R}^{3p^2 \times 1}$ to form the

PG, denoted by $\{\mathbf{x}_m\}_{m=1}^M$. The mean vector of this PG is $\boldsymbol{\mu} = \frac{1}{M}\sum_{m=1}^M \mathbf{x}_m$, and the group mean subtracted PG is defined as $\overline{\mathbf{X}} \triangleq \{\overline{\mathbf{x}}_m = \mathbf{x}_m - \boldsymbol{\mu}\}_{m=1}^M$.

Assume that a number of L PGs are extracted from a set of external natural images, and the l-th PG is $\overline{\mathbf{X}}_l \triangleq \{\overline{\mathbf{x}}_{l,m}\}_{m=1}^M, l = 1, ..., L$. A Gaussian Mixture Model (GMM) is learned to model the PG prior. The overall log-likelihood function is

$$\ln \mathcal{L} = \sum_{l=1}^{L} \ln(\sum_{k=1}^{K} \pi_k \prod_{m=1}^{M} \mathcal{N}(\overline{\mathbf{x}}_{l,m}|\boldsymbol{\mu}_k, \boldsymbol{\Sigma}_k)). \tag{3.1}$$

The learning process is similar to the GMM learning in [103, 111]. Finally, a GMM model with K Gaussian components is learned, and the learned parameters include mixture weights $\{\pi_k\}_{k=1}^K$, mean vectors $\{\boldsymbol{\mu}_k\}_{k=1}^K$, and covariance matrices $\{\boldsymbol{\Sigma}_k\}_{k=1}^K$. Note that the mean vector of each cluster is naturally zero, i.e., $\boldsymbol{\mu}_k = \mathbf{0}$.

To better describe the subspace of each Gaussian component, we perform singular value decomposition (SVD) [28] on the covariance matrix:

$$\boldsymbol{\Sigma}_k = \boldsymbol{U}_k \boldsymbol{S}_k \boldsymbol{U}_k^\top. \tag{3.2}$$

The eigenvector matrices $\{\boldsymbol{U}_k\}_{k=1}^K$ will be employed as the external orthogonal dictionary to guide the internal sub-dictionary learning in next sub-section. The singular values in $\boldsymbol{S}_k$ reflect the significance of the singular vectors in $\boldsymbol{U}_k$. They will also be utilized as prior weights for weighted sparse coding in our denoising algorithm.

3.2.2 Guided Internal Prior Learning

After the external PG prior model is learned from external natural clean images, we employ it to guide the internal PG prior learning for a given real-world noisy image. The guidance lies in two aspects. First, the external prior will guide the subspace clustering of internal noisy PGs. Second, the external prior will guide the orthogonal dictionary learning of internal noisy PGs.

Internal Subspace Clustering

Given a real-world noisy image $\mathbf{y}$, we extract N (overlapped) local patches from it. Similar to the external prior learning stage, for the n-th ($n = 1, ..., N$) local patch we search its M most similar (by Euclidean distance) patches around it to form a noisy PG, denoted by $\boldsymbol{Y}_n = \{\mathbf{y}_{n,1}, ..., \mathbf{y}_{n,M}\}$. Then the group mean of $\boldsymbol{Y}_n$, denoted by $\boldsymbol{\mu}_n$, is subtracted from each patch by $\overline{\mathbf{y}}_{n,m} \triangleq \mathbf{y}_{n,m} - \boldsymbol{\mu}_n$, leading to the mean subtracted noisy PG $\overline{\boldsymbol{Y}}_n \triangleq \{\overline{\mathbf{y}}_{n,m}\}_{m=1}^{M}$.

The external GMM prior models $\{\mathcal{N}(\mathbf{0}, \boldsymbol{\Sigma}_k)\}_{k=1}^{K}$ basically characterize the subspaces of natural high quality PGs. Therefore, we project each noisy PG $\overline{\boldsymbol{Y}}_n$ into the subspaces of $\{\mathcal{N}(\mathbf{0}, \boldsymbol{\Sigma}_k)\}_{k=1}^{K}$ and assign it to the most suitable subspace based on the posterior probability:

$$P(k|\overline{\boldsymbol{Y}}_n) = \frac{\prod_{m=1}^{M} \mathcal{N}(\overline{\mathbf{y}}_{n,m}|\mathbf{0}, \boldsymbol{\Sigma}_k)}{\sum_{l=1}^{K} \prod_{m=1}^{M} \mathcal{N}(\overline{\mathbf{y}}_{n,m}|\mathbf{0}, \boldsymbol{\Sigma}_l)} \tag{3.3}$$

for $k = 1, ..., K$. Then $\overline{\boldsymbol{Y}}_n$ is assigned to the subspace with the maximum a-posteriori (MAP) probability $\max_k P(k|\overline{\boldsymbol{Y}}_n)$.

Guided Orthogonal Dictionary Learning

Assume that we have assigned all the internal noisy PGs $\{\overline{\boldsymbol{Y}}_n\}_{n=1}^{N}$ to their corresponding most suitable subspaces in $\{\mathcal{N}(\mathbf{0}, \boldsymbol{\Sigma}_k)\}_{k=1}^{K}$. For the k-th subspace, the noisy PGs assigned to it are $\{\overline{\boldsymbol{Y}}_{k_n}\}_{n=1}^{N_k}$, where $\overline{\boldsymbol{Y}}_{k_n} = [\overline{\mathbf{y}}_{k_n,1}, ..., \overline{\mathbf{y}}_{k_n,M}]$ and $\sum_{k=1}^{K} N_k = N$. We propose to learn an orthogonal dictionary $\boldsymbol{D}_k$ from each set of PGs $\overline{\boldsymbol{Y}}_{k_n}$ to characterize the internal PG prior with the guidance of the corresponding external orthogonal dictionary $\boldsymbol{U}_k$ (Eq. (3.2)). The reasons that we learn orthogonal dictionaries are two-fold. Firstly, the PGs $\{\overline{\boldsymbol{Y}}_{k_n}\}_{n=1}^{N_k}$ are in a subspace of the whole space of all PGs; therefore, there is no necessary to learn a redundant over-complete dictionary to characterize it, while an orthonormal dictionary has naturally zero *mutual incoherence* [27]. Secondly, the orthogonality of dictionary can make the patch encoding in the testing stage efficient, leading to an efficient denoising algorithm.

We let the orthogonal dictionary $\boldsymbol{D}_k$ be

$$\boldsymbol{D}_k \triangleq [\boldsymbol{D}_{k,\mathrm{E}}\ \boldsymbol{D}_{k,\mathrm{I}}] \in \mathbb{R}^{3p^2 \times 3p^2}, \tag{3.4}$$

where $\boldsymbol{D}_{k,\mathrm{E}} = \boldsymbol{U}_k(:, 1:r) \in \mathbb{R}^{3p^2 \times r}$ is the external sub-dictionary and it includes the first r most important eigenvectors of $\boldsymbol{U}_k$, and the internal sub-dictionary $\boldsymbol{D}_{k,\mathrm{I}} \in \mathbb{R}^{3p^2 \times (3p^2 - r)}$ is to be adaptively learned from the noisy PGs $\{\overline{\boldsymbol{Y}}_{k_n}\}_{n=1}^{N_k}$. The rationale to design $\boldsymbol{D}_k$ as a hybrid dictionary is as follows. The external sub-dictionary $\boldsymbol{D}_{k,\mathrm{E}}$ is pre-trained from external clean data, and it represents the k-th latent subspace of natural images, which is helpful to reconstruct the common latent structures of images. However, $\boldsymbol{D}_{k,\mathrm{E}}$ is general to all images but not adaptive to the given noisy image. Some fine-scale details specific to the given image may not be well characterized by $\boldsymbol{D}_{k,\mathrm{E}}$. Therefore, we learn an internal sub-dictionary $\boldsymbol{D}_{k,\mathrm{I}}$ to supplement $\boldsymbol{D}_{k,\mathrm{E}}$. In other words, $\boldsymbol{D}_{k,\mathrm{I}}$ is to reveal the latent subspace adaptive to the input noisy image, which cannot be effectively represented by $\boldsymbol{D}_{k,\mathrm{E}}$.

For notation simplicity, in the following development we ignore the subspace index k for $\overline{\boldsymbol{Y}}_{k_n}$ and $\boldsymbol{D}_k$, etc. The learning of hybrid orthogonal dictionary $\boldsymbol{D}$ is performed under the following weighted sparse coding framework:

$$\min_{\boldsymbol{D}_{\mathrm{I}}, \{\boldsymbol{\alpha}_{n,m}\}} \sum_{n=1}^{N} \sum_{m=1}^{M} (\|\overline{\boldsymbol{y}}_{n,m} - \boldsymbol{D}\boldsymbol{\alpha}_{n,m}\|_2^2 + \sum_{j=1}^{3p^2} \lambda_j |\boldsymbol{\alpha}_{n,m,j}|) \quad \text{s.t.} \quad \boldsymbol{D} = [\boldsymbol{D}_{\mathrm{E}}\ \boldsymbol{D}_{\mathrm{I}}],\ \boldsymbol{D}^{\top}\boldsymbol{D} = \boldsymbol{I}, \tag{3.5}$$

where $\boldsymbol{I}$ is the $3p^2$ dimensional identity matrix, $\boldsymbol{\alpha}_{n,m}$ is the sparse coding vector of the m-th patch $\overline{\boldsymbol{y}}_{n,m}$ in the n-th PG $\overline{\boldsymbol{Y}}_n$ and $\boldsymbol{\alpha}_{n,m,j}$ is the j-th element of $\boldsymbol{\alpha}_{n,m}$. λ_j is the j-th regularization parameter defined as

$$\lambda_j = \lambda / (\sqrt{\boldsymbol{S}_k(j)} + \varepsilon), \tag{3.6}$$

where $\boldsymbol{S}_k(j)$ is the j-th singular value of diagonal singular value matrix $\boldsymbol{S}_k$ (please refer to Eq. (3.2)) and ε is a small positive number to avoid zero denominator. Note that $\boldsymbol{D}_{\mathrm{E}} = \boldsymbol{U}_k$ if $r = 3p^2$ and $\boldsymbol{D}_{\mathrm{E}} = \emptyset$ if $r = 0$.

In the dictionary learning model (3.5), we use the ℓ_2 norm to model the representation residual of PGs. This is because the patches in those PGs have similar content, and we assume that the noise therein will have similar statistics, which can be roughly modeled as locally Gaussian. On the other hand, this will make the dictionary learning much easier to solve. We employ an alternating iterative approach to solve the optimization problem (3.5). Specifically,

we initialize the orthogonal dictionary as $\boldsymbol{D}^{(0)} = \boldsymbol{U}_k$ and for $t = 0, 1, ..., T-1$, and alternatively update $\boldsymbol{\alpha}_{n,m}$ and $\boldsymbol{D}_{\mathrm{I}}$ as follows.

Updating Sparse Coding Coefficients: Given the orthogonal dictionary $\boldsymbol{D}^{(t)}$, we update each sparse coding vector $\boldsymbol{\alpha}_{n,m}$ by solving

$$\boldsymbol{\alpha}_{n,m}^{(t+1)} := \arg\min_{\boldsymbol{\alpha}_{n,m}} \|\overline{\boldsymbol{y}}_{n,m} - \boldsymbol{D}^{(t)}\boldsymbol{\alpha}_{n,m}\|_2^2 + \sum_{j=1}^{3p^2} \lambda_j |\boldsymbol{\alpha}_{n,m,j}|. \tag{3.7}$$

Since dictionary $\boldsymbol{D}^{(t)}$ is orthogonal, the problems (3.7) has a closed-form solution

$$\boldsymbol{\alpha}_{n,m}^{(t+1)} = \mathrm{sgn}((\boldsymbol{D}^{(t)})^\top \overline{\boldsymbol{y}}_{n,m}) \odot \max(|(\boldsymbol{D}^{(t)})^\top \overline{\boldsymbol{y}}_{n,m}| - \boldsymbol{\lambda}, \boldsymbol{0}), \tag{3.8}$$

where $\boldsymbol{\lambda} = \frac{1}{2}[\lambda_1, \lambda_2, ..., \lambda_{3p^2}]^\top$ is the vector of regularization parameter, sgn(•) is the sign function and $\odot$ means element-wise multiplication. The detailed derivation of Eq. (3.8) can be found in Appendix A.

Updating Internal Sub-dictionary: Given the sparse coding vectors $\{\boldsymbol{\alpha}_{n,m}^{(t+1)}\}$, we update the internal sub-dictionary by solving

$$\begin{aligned} &\boldsymbol{D}_{\mathrm{I}}^{(t+1)} := \arg\min_{\mathbf{D}_{\mathrm{I}}} \sum_{n=1}^{N}\sum_{m=1}^{M} \|\overline{\boldsymbol{y}}_{n,m} - \boldsymbol{D}\boldsymbol{\alpha}_{n,m}^{(t+1)}\|_2^2 = \arg\min_{\mathbf{D}_{\mathrm{I}}} \|\overline{\boldsymbol{Y}}_n - \boldsymbol{D}\boldsymbol{A}^{(t+1)}\|_F^2 \\ &\text{s.t.} \quad \boldsymbol{D} = [\boldsymbol{D}_{\mathrm{E}}\ \boldsymbol{D}_{\mathrm{I}}],\ \boldsymbol{D}_{\mathrm{I}}^\top \boldsymbol{D}_{\mathrm{I}} = \boldsymbol{I}_{(3p^2-r)},\ \boldsymbol{D}_{\mathrm{E}}^\top \boldsymbol{D}_{\mathrm{I}} = \boldsymbol{0}, \end{aligned} \tag{3.9}$$

where $\mathbf{A}^{(t+1)} = [\boldsymbol{\alpha}_{1,1}^{(t+1)}, ..., \boldsymbol{\alpha}_{1,M}^{(t)}, ..., \boldsymbol{\alpha}_{N,1}^{(t+1)}, ..., \boldsymbol{\alpha}_{N,M}^{(t+1)}]$ and $\boldsymbol{I}_{(3p^2-r)}$ is the $(3p^2-r)$ dimensional identity matrix. The sparse coefficients matrix can be written as $\boldsymbol{A}^{(t+1)} = [(\boldsymbol{A}_{\mathrm{E}}^{(t+1)})^\top\ (\boldsymbol{A}_{\mathrm{I}}^{(t+1)})^\top]^\top$ where the external part $\boldsymbol{A}_{\mathrm{E}}^{(t+1)} \in \mathbb{R}^{r\times NM}$ and the internal part $\boldsymbol{A}_{\mathrm{I}}^{(t+1)} \in \mathbb{R}^{(3p^2-r)\times NM}$ represent the coding coefficients of $\boldsymbol{Y}$ over external sub-dictionary $\boldsymbol{D}_{\mathrm{E}}$ and internal sub-dictionary $\boldsymbol{D}_{\mathrm{I}}^{(t)}$, respectively. According to the following Theorem 3.2.1, by setting $\mathcal{Y} = \overline{\boldsymbol{Y}}_n - \boldsymbol{D}_{\mathrm{E}}\boldsymbol{A}_{\mathrm{E}}^{(t+1)}, \mathcal{E} = \boldsymbol{D}_{\mathrm{E}}, \mathcal{D} = \boldsymbol{D}_{\mathrm{I}}, \mathcal{A} = \boldsymbol{A}_{\mathrm{I}}$, the problem (3.9) has a closed-form solution $\boldsymbol{D}_{\mathrm{I}}^{(t+1)} = \boldsymbol{U}_{\mathrm{I}}\boldsymbol{V}_{\mathrm{I}}^\top$, where $\boldsymbol{U}_{\mathrm{I}} \in \mathbb{R}^{3p^2\times(3p^2-r)}$ and $\boldsymbol{V}_{\mathrm{I}} \in \mathbb{R}^{(3p^2-r)\times(3p^2-r)}$ are the orthogonal matrices obtained by the following SVD [28]

$$(\boldsymbol{I} - \boldsymbol{D}_{\mathrm{E}}\boldsymbol{D}_{\mathrm{E}}^\top)\boldsymbol{Y}(\boldsymbol{A}_{\mathrm{I}}^{(t+1)})^\top = \boldsymbol{U}_{\mathrm{I}}\boldsymbol{S}_{\mathrm{I}}\boldsymbol{V}_{\mathrm{I}}^\top. \tag{3.10}$$

The orthogonality of internal sub-dictionary $\boldsymbol{D}_{\mathrm{I}}^{(t+1)}$ can be shown by checking that $(\boldsymbol{D}_{\mathrm{I}}^{(t+1)})^{\top}(\boldsymbol{D}_{\mathrm{I}}^{(t+1)}) = \boldsymbol{V}_{\mathrm{I}}\boldsymbol{U}_{\mathrm{I}}^{\top}\boldsymbol{U}_{\mathrm{I}}\boldsymbol{V}_{\mathrm{I}}^{\top} = \boldsymbol{I}_{(3p^2-r)}$. In fact, the Theorem 3.2.1 provides a sufficient and necessary condition to guarantee the existence of the closed-form solution for the internal sub-dictionary of the problem (3.9).

Theorem 3.2.1 *Let $\mathcal{A} \in \mathbb{R}^{(3p^2-r)\times M}$, $\mathcal{Y} \in \mathbb{R}^{3p^2\times M}$ be two given data matrices. $\mathcal{E} \in \mathbb{R}^{3p^2\times r}$ is a given matrix satisfying $\mathcal{E}^{\top}\mathcal{E} = \boldsymbol{I}_{r\times r}$, then $\hat{\mathcal{D}} = \mathcal{U}\mathcal{V}^{\top}$ is the necessary condition of*

$$\hat{\mathcal{D}} = \arg\min_{\mathcal{D}} \|\mathcal{Y} - \mathcal{D}\mathcal{A}\|_F^2 \quad s.t. \quad \mathcal{D}^{\top}\mathcal{D} = \boldsymbol{I}_{(3p^2-r)\times(3p^2-r)}, \mathcal{E}^{\top}\mathcal{D} = \boldsymbol{0}_{r\times(3p^2-r)}, \tag{3.11}$$

where $\mathcal{U} \in \mathbb{R}^{3p^2\times(3p^2-r)}$ and $\mathcal{V} \in \mathbb{R}^{(3p^2-r)\times(3p^2-r)}$ are the orthogonal matrices obtained by performing economy (a.k.a. reduced) SVD [28]:

$$(\boldsymbol{I}_{3p^2\times 3p^2} - \mathcal{E}\mathcal{E}^{\top})\mathcal{Y}\mathcal{A}^{\top} = \mathcal{U}\Sigma\mathcal{V}^{\top} \tag{3.12}$$

Besides, if $rank(\Sigma) = 3p^2 - r$, $\hat{\mathcal{D}} = \mathcal{U}\mathcal{V}^{\top}$ is also the sufficient condition of problem (3.11).

The proof of the Theorem 3.2.1 can be found in Appendix B. Though the problem (3.9) has a closed-form solution by SVD [28], the uniqueness of solution cannot be guaranteed since the matrices $(\boldsymbol{I}_{3p^2\times 3p^2} - \mathcal{E}\mathcal{E}^{\top})\mathcal{Y}\mathcal{A}^{\top}$ as well as $\mathcal{U}$ and $\mathcal{V}$ may be reduced to matrices of lower rank. Hence, we also analyze the uniqueness of the solution $\hat{\mathcal{D}}$ by the following Theorem 3.2.2, whose proof can be found in Appendix C.

Theorem 3.2.2 *(a) If $(\boldsymbol{I}_{3p^2\times 3p^2} - \mathcal{E}\mathcal{E}^{\top})\mathcal{Y}\mathcal{A}^{\top} \in \mathbb{R}^{3p^2\times(3p^2-r)}$ is nonsingular, i.e., $rank(\Sigma) = 3p^2 - r$, then the solution of $\hat{\mathcal{D}} = \mathcal{U}\mathcal{V}^{\top}$ is unique; (b) If $(\boldsymbol{I}_{3p^2\times 3p^2} - \mathcal{E}\mathcal{E}^{\top})\mathcal{Y}\mathcal{A}^{\top}$ is singular, i.e., $0 \leq rank(\boldsymbol{\Sigma}) < 3p^2 - r$, then the number of possible solutions of $\hat{\mathcal{D}}$ is $2^{3p^2-r-rank(\boldsymbol{\Sigma})}$ for fixed $\mathcal{U}$, $\mathcal{V}$.*

The above alternative updating steps are repeated until the number of iterations exceeds a preset threshold. In each step, the energy value of the objective function (3.5) is decreased and we empirically found that the proposed model usually converges in 10 iterations. We summarize the procedures in Algorithm 1.

Algorithm 1: External Prior Guided Internal Prior Learning

Input: Matrices $\overline{\boldsymbol{Y}}_n$, external sub-dictionary $\boldsymbol{D}_{\mathrm{E}}$, parameter vector $\boldsymbol{\lambda}$

Initialization: initialize $\boldsymbol{D}^{(0)} = \boldsymbol{U}_k$ by Eq. (3.2);

for $t = 0, 1, ..., T-1$ **do**

1. Update $\boldsymbol{\alpha}_{n,m}^{(t+1)}$ by Eq. (3.7);

2. Update $\boldsymbol{D}_{\mathrm{I}}^{(t+1)}$ by Eq. (3.9);

end for

Output: Internal orthogonal dictionary $\boldsymbol{D}_{\mathrm{I}}^{(T)}$ and sparse codes $\mathbf{A}^{(T)}$.

3.2.3 The Denoising Algorithm

The denoising of the given noisy image $\mathbf{y}$ can be simultaneously done with the guided internal sub-dictionary learning process. Once we obtain the solutions of sparse coding vectors $\{\hat{\boldsymbol{\alpha}}_{n,m}^{(T)}\}$ in Eq. (3.8) and the orthogonal dictionary $\boldsymbol{D}^{(T)} = [\boldsymbol{D}_{\mathrm{E}}\ \boldsymbol{D}_{\mathrm{I}}^{(T)}]$ in Eq. (3.9), the latent clean patch $\hat{\mathbf{y}}_{n,m}$ of the m-th noisy patch in PG $\boldsymbol{Y}_n$ is reconstructed as

$$\hat{\mathbf{y}}_{n,m} = \boldsymbol{D}^{(T)}\hat{\boldsymbol{\alpha}}_{n,m}^{(T)} + \boldsymbol{\mu}_n, \tag{3.13}$$

where $\boldsymbol{\mu}_n$ is the group mean of $\boldsymbol{Y}_n$. The latent clean image is then reconstructed by aggregating all the reconstructed patches in all PGs. We perform the above denoising procedures for several iterations for better denoising outputs. The proposed denoising algorithm is summarized in Algorithm 2.

3.3 Experiments

3.3.1 Implementation Details

Our proposed method has two main stages: the external prior learning stage and the external prior guided internal prior learning stage. In the first stage, we set $p = 6$ (the patch size),

Algorithm 2: External Prior Guided Internal Prior Learning for Real Noisy Image Denoising

Input: Noisy image $\mathbf{y}$, external PG prior GMM model

Initialization: $\hat{\mathbf{x}}^{(0)} = \mathbf{y}$;

for $Ite = 1 : IteNum$ **do**

1. Extracting internal PGs $\{\boldsymbol{Y}_n\}_{n=1}^{N}$ from $\hat{\mathbf{x}}^{(Ite-1)}$;

Guided Internal Subspace Clustering:

for each PG $\boldsymbol{Y}_n$ **do**

2. Calculate group mean $\boldsymbol{\mu}_n$ and form mean subtracted PG $\overline{\boldsymbol{Y}}_n$;
3. Subspace clustering via Eq. (3.3);

end for

Guided Internal Orthogonal Dictionary Learning:

for the PGs in each subspace **do**

4. External PG prior guided internal orthogonal dictionary learning by solving Eq. (3.5);
5. Recover each patch in all PGs via Eq. (3.13);

end for

6. Aggregate the recovered PGs of all subspaces to form the recovered image $\hat{\mathbf{x}}^{(Ite)}$;

end for

Output: The denoised image $\hat{\mathbf{x}}$.

$M = 10$ (the number of similar patches in a PG), $W = 31$ (the window size for PG searching) and $K = 32$ (the number of Gaussian components in GMM). We learn the external GMM prior with 3.6 million PGs extracted from the Kodak PhotoCD Dataset (http://r0k.us/graphics/kodak/), which includes 24 high quality color images.

In the second stage, we set $r = 54$ (the number of atoms in the external sub-dictionaries); that is, we let the external sub-dictionaries have the same number of atoms as the internal sub-dictionaries to be learned. Our experiments show that setting r between 27 and 81 will lead to very similar results. For other parameters, we set $\lambda = 0.001$ (the sparse regularization

parameter), $T = 2$ (the number of iterations for solving problem (3.5)), and $IteNum = 4$ (the number of iterations for Alg. 2). All parameters of our method are fixed to all experiments, which are run under the Matlab2014b environment on a machine with Intel(R) Core(TM) i7-5930K CPU of 3.5GHz and 32GB RAM.

3.3.2 The Testing Datasets

We evaluate the proposed method on three real-world noisy image datasets, where the images were captured under indoor or outdoor lighting conditions by different types of cameras and camera settings.

Dataset 1. The first dataset is provided in [50], which includes 20 real-world noisy images collected under uncontrolled outdoor environment. Fig. 3.3 shows some sample images of this dataset. Since there is no "ground truth" of the noisy images, the objective measures such as PSNR cannot be computed on this dataset.

Dataset 2. The second dataset is provided in [68], which includes noisy images of 11 static scenes. The noisy images were collected under controlled indoor environment. Each scene was shot 500 times under the same camera and camera setting. The mean image of the 500 shots is roughly taken as the "ground truth", with which the PSNR can be computed. Fig. 3.4 shows some sample images of this dataset.

Since the image size is very large (about 7000×5000) and the 11 scenes share repetitive contents, the authors of [68] cropped 15 smaller images (of size 512×512) to perform experiments. In order to evaluate the proposed methods more comprehensively, we cropped 60 images of size 500×500 from the dataset for experiments. Some samples are shown in Fig. 3.5. Note that our cropped 60 images and the 15 cropped images by the authors of [68] are from different shots.

Dataset 3. The scenes of dataset 2 are mostly printed photos, and they cannot represent real-world objects and scenes with different reflectance properties. To remedy the limitation of

Figure 3.3 Some samples cropped from real-world noisy images of Dataset 1 [50].

dataset 2, we construct another dataset which contains images of 10 different scenes captured by Canon 80D and Sony A7II cameras under more ISO settings. The ISO settings in our dataset are 800, 1600, 3200, 6400, 12800 while those of dataset 2 are 1600, 3200, 6400. Similar to dataset 2, each scene was captured 500 shots, and the mean image of these 500 shots can be used a kind of ground-truth to evaluate the denoising algorithms. Fig. 3.6 shows some cropped images of the scenes in our dataset. One can see that the images contain a lot of different real-world objects with varying colors, shapes, materials, etc.

Our dataset provides real-world noisy images of real-world objects with different ISO settings. It can be used to more fairly evaluate the performance of different real-world noisy image denoising methods. Consider that the image resolution is very high (about 4000×4000), for the convenience of experimental studies, we cropped 100 (10 for each scene) smaller images (of size 512×512) from it to perform experiments. The whole dataset will be made publically available with the publication of this work.

Figure 3.4 The 15 cropped real-world noisy images used in [68].

Figure 3.5 Some samples cropped from real-world noisy images of Dataset 2 [68].

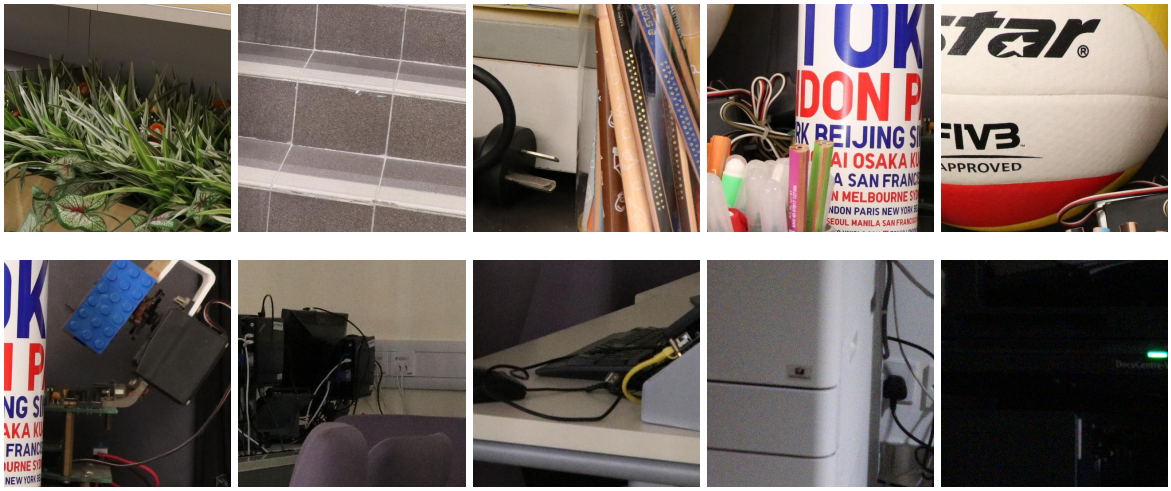

Figure 3.6 Some samples cropped from our dataset (Dataset 3).

Noisy 35.89 External 39.05 Internal 38.75 Guided **39.39** Mean Image

Figure 3.7 Denoised images and PSNR(dB) results of a region cropped from the real-world noisy image "Nikon D600 ISO 3200 C1" [68] by different methods. The images are better to be zoomed in on screen.

3.3.3 Comparison among external, internal and guided internal priors

To demonstrate the advantages of external prior guided internal prior learning, we perform real-world noisy image denoising by using external priors only (denoted by "External"), internal priors only (denoted by "Internal"), and the proposed guided internal priors (denoted by "Guided"), respectively. For the "External" method, we utilize the full external dictionaries (i.e., $r = 108$ in Eq. (3.5)) for denoising. For the "Internal" method, the overall framework is similar to the method of [24]. A GMM model (with $K = 32$ Gaussians) is directly learned from the PGs extracted from the given noisy image without using any external data, and then the internal orthogonal dictionaries are obtained via Eq. (3.2) to perform denoising. All parameters

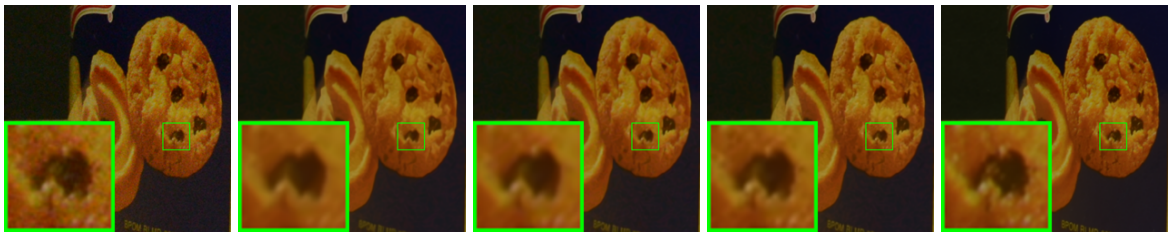

Noisy 33.77 External 36.97 Internal 37.40 Guided **38.01** Mean Image

Figure 3.8 Denoised images and PSNR(dB) results of a region cropped from the real-world noisy image "Nikon D600 ISO 3200 C1" [68] by different methods. The images are better to be zoomed in on screen.

of the "External" and "Internal" methods are tuned to achieve their best performance.

We compare the three methods on the 60 cropped images from [68]. The average PSNR and run time are listed in Table 3.1. The best results are highlighted in bold. It can be seen that "Guided" method achieves better PSNR than both "External" and "Internal" methods. In addition, the "Internal" method is very slow because it involves online GMM learning, while the "Guided" method is only a little slower than the "External" method. Figs. 3.7 and 3.8 show the denoised images of two noisy images by the three methods. One can see that the "External" method is good at recovering large-scale structures (see Fig. 3.7) while the "Internal" method is good at recovering fine-scale textures (see Fig. 3.8). By utilizing external priors to guide the internal prior learning, our proposed method can effectively recover both the large-scale structures and fine-scale textures.

3.3.4 Comparison with State-of-the-Art Denoising Methods

Comparison methods. We compare the proposed method with state-of-the-art image denoising methods, including GAT-BM3D [62], CBM3D [21], WNNM [36], MLP [13], DnCNN [107], CSF [83], TNRD [19], Noise Clinic (NC) [50, 51], Cross-Channel (CC) [68], and Neat Image (NI) [2]. Among these methods, GAT-BM3D [62] is a state-of-the-art Poisson noise reduction method. The method CBM3D [21] is a state-of-the-art method for color image denoising and the noise on color images is assumed to be additive white Gaussian. The methods

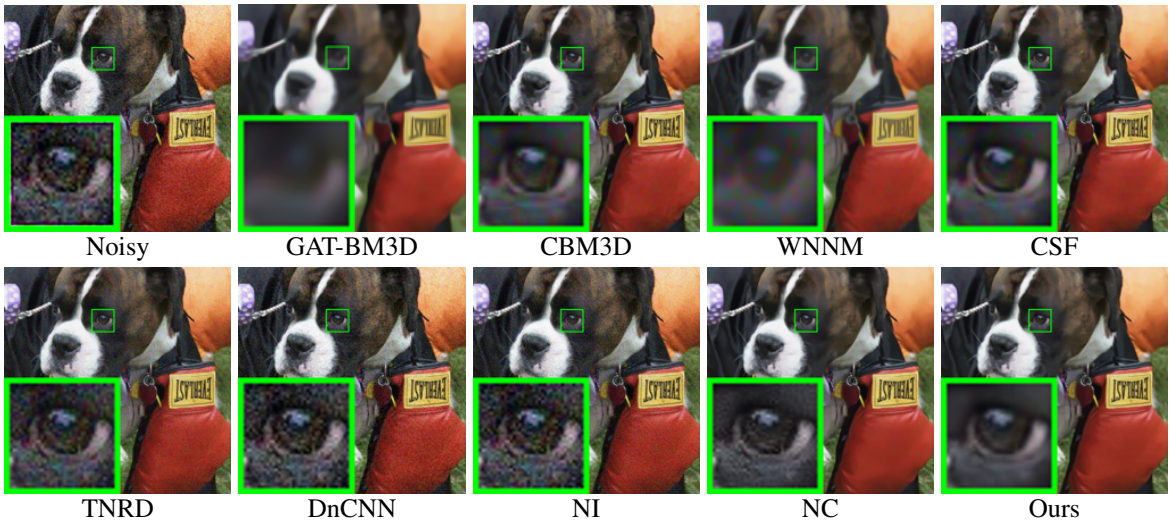

Figure 3.9 Denoised images of the real-world noisy image "Dog" [50] by different methods. The images are better to be zoomed in on screen.

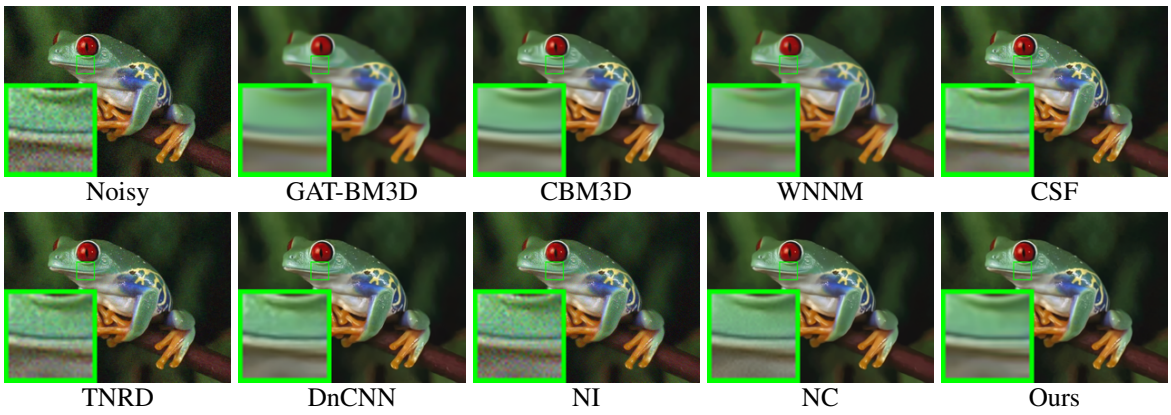

Figure 3.10 Denoised images of the real-world noisy image "Frog" [50] by different methods. The images are better to be zoomed in on screen.

of WNNM, MLP, DnCNN, CSF, and TNRD are state-of-the-art Gaussian noise removal methods for grayscale images, and we apply them to each channel of color images for denoising. NC is a blind image denoising method, and NI is a set of commercial software for image denoising, which has been embedded into Photoshop and Corel PaintShop. The code of CC is not released but its results on the 15 cropped images are available at [68]. Therefore, we only compare with it on the 15 cropped images in dataset 2 from [68].

Noise level of comparison methods. For the CBM3D method, the standard deviation of

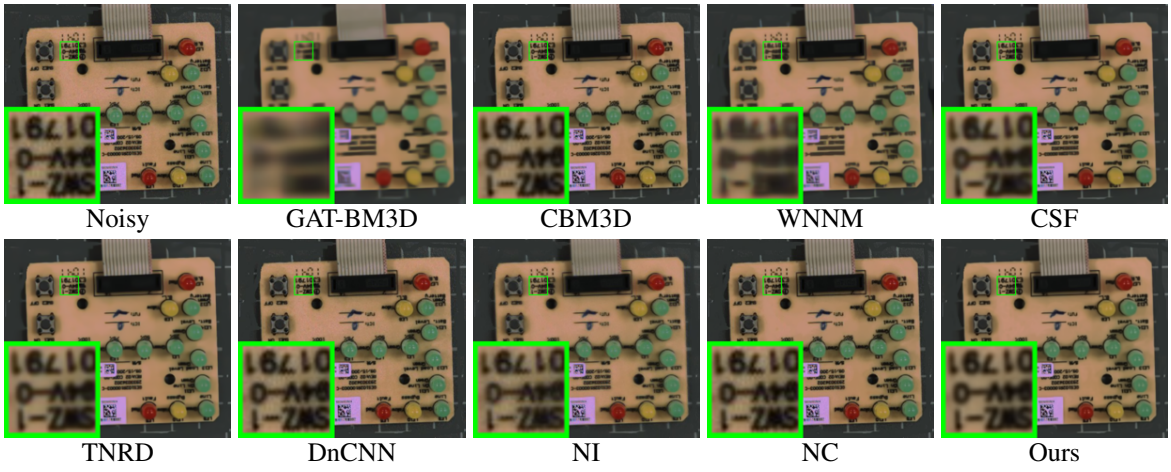

Figure 3.11 Denoised images of the real-world noisy image "Circuit" [50] by different methods. The images are better to be zoomed in on screen.

Table 3.1 Average PSNR (dB) and Run Time (seconds) of the "External", "Internal", and "Guided Internal" methods on 60 real-world noisy images (of size $500 \times 500 \times 3$) cropped from [68].

	Noisy	**External**	**Internal**	**Guided Internal**
PSNR	34.51	38.21	38.07	**38.75**
Time	—	**21.19**	312.67	22.26

noise on color images should be given as a parameter. For methods of WNNM, MLP, CSF, and TNRD, the noise level in each color channel should be input. For the DnCNN method, it is trained to deal with noise in a range of levels $0 \sim 55$. We retrain the models of discriminative denoising methods MLP, CSF, and TNRD (using the released codes by the authors) at different noise levels from $\sigma = 5$ to $\sigma = 50$ with a gap of 5. The denoising is performed by processing each channel with the model trained at the same (or nearest) noise level. The noise levels $(\sigma_r, \sigma_g, \sigma_b)$ in R, G ,B channels are assumed to be Gaussian and can be estimated via some noise estimation methods [18, 54]. In this work, we employ the method [18] to estimate the noise level for each color channel.

Results on dataset 1. Since there is no "ground truth" for the real-world noisy images

Table 3.2 PSNR(dB) results of different methods on 15 cropped real-world noisy images used in [68].

Camera Settings	**GAT-BM3D**	**CBM3D**	**WNNM**	**MLP**	**CSF**	**TNRD**	**DnCNN**	**NI**	**NC**	**CC**	**Ours**
	31.23	39.76	37.51	39.00	35.68	39.51	37.26	37.68	38.76	38.37	**40.50**
Canon 5D	30.55	36.40	33.86	36.34	34.03	36.47	34.13	34.87	35.69	35.37	**37.05**
ISO = 3200	27.74	36.37	31.43	36.33	32.63	**36.45**	34.09	34.77	35.54	34.91	36.11
	28.55	34.18	33.46	34.70	31.78	34.79	33.62	34.12	**35.57**	34.98	34.88
Nikon D600	32.01	35.07	36.09	36.20	35.16	36.37	34.48	35.36	**36.70**	35.95	36.31
ISO = 3200	39.78	37.13	39.86	39.33	39.98	39.49	35.41	38.68	39.28	**41.15**	39.23
	32.24	36.81	36.35	37.95	34.84	38.11	35.79	37.34	38.01	37.99	**38.40**
Nikon D800	33.86	37.76	39.99	40.23	38.42	40.52	36.08	38.57	39.05	40.36	**40.92**
ISO = 1600	33.90	37.51	37.15	37.94	35.79	38.17	35.48	37.87	38.20	38.30	**38.97**
	36.49	35.05	38.60	37.55	38.36	37.69	34.08	36.95	38.07	**39.01**	38.66
Nikon D800	32.91	34.07	36.04	35.91	35.53	35.90	33.70	35.09	35.72	36.75	**37.07**
ISO = 3200	**40.20**	34.42	39.73	38.15	40.05	38.21	33.31	36.91	36.76	39.06	38.52
	29.84	31.13	33.29	32.69	34.08	32.81	29.83	31.28	33.49	**34.61**	33.76
Nikon D800	27.94	31.22	31.16	32.33	32.13	32.33	30.55	31.38	32.79	33.21	**33.43**
ISO = 6400	29.15	30.97	31.98	32.29	31.52	32.29	30.09	31.40	32.86	33.22	**33.58**
Average	32.43	35.19	35.77	36.46	35.33	36.61	33.86	35.49	36.43	36.88	**37.15**

in dataset 1 [50], we only compare the visual quality of the denoised images by different methods. (Note that method CC [68] is not compared since its code is not available. The result of MLP is not shown here due to the limit of space.) Fig. 3.9 show the denoised images of "Dog". It can be seen that CBM3D and WNNM tend to over-smooth much the image while remaining some noise caused color artifacts. DnCNN and TNRD are likely to remain many noise-caused color artifacts across the whole image. These results demonstrate that the methods designed with Gaussian noise model are not effective for real noise removal. Though NC and NI methods are specifically developed for real-world noisy images, their performance on noise removal is not very satisfactory. In comparison, our proposed method recovers much better the structures and textures (such as the eye area in "Dog") than the other competing methods. More visual comparisons can be found in Figures 3.10 and 3.11.

In this section, we provide more comparisons of the proposed method with the state-of-the-art denoising methods on the 15 cropped real-world noisy images used in [68]. In this

Table 3.3 SSIM [92] results of different methods on 15 cropped real-world noisy images used in [68].

Camera Settings	GAT-BM3D	CBM3D	WNNM	MLP	CSF	TNRD	DnCNN	NI	NC	CC	Ours
	0.9126	0.9778	0.9673	0.9695	0.9434	0.9742	0.9389	0.9600	0.9689	0.9678	**0.9813**
Canon 5D	0.8427	0.9552	0.9210	0.9458	0.9011	0.9491	0.8989	0.9308	0.9427	0.9359	**0.9572**
ISO = 3200	0.8017	**0.9660**	0.9110	0.9599	0.9037	0.9617	0.9182	0.9463	0.9476	0.9478	0.9643
	0.7845	0.9330	0.9281	0.9481	0.8792	0.9494	0.9123	0.9413	0.9497	0.9484	**0.9535**
Nikon D600	0.9028	0.9168	0.9432	0.9469	0.9261	**0.9499**	0.8932	0.9251	0.9398	0.9293	0.9461
ISO = 3200	**0.9806**	0.9313	0.9737	0.9726	0.9763	0.9742	0.8708	0.9481	0.9588	0.9799	0.9683
	0.8791	0.9339	0.9417	0.9543	0.9148	0.9572	0.9060	0.9506	0.9533	0.9575	**0.9620**
Nikon D800	0.9534	0.9383	0.9748	0.9743	0.9674	0.9774	0.8943	0.9615	0.9591	0.9767	**0.9779**
ISO = 1600	0.8795	0.9277	0.9311	0.9354	0.9035	0.9410	0.8735	0.9229	0.9406	0.9427	**0.9531**
	0.9526	0.8866	**0.9656**	0.9533	0.9654	0.9569	0.8463	0.9101	0.9466	0.9637	0.9613
Nikon D800	0.9078	0.8928	0.9416	0.9381	0.9354	0.9394	0.8755	0.9194	0.9309	0.9477	**0.9521**
ISO = 3200	0.9707	0.8430	0.9664	0.9548	**0.9712**	0.9576	0.7204	0.9001	0.9070	0.9544	0.9512
	0.8909	0.7952	0.9188	0.8914	**0.9259**	0.8966	0.7847	0.7781	0.9024	0.9206	0.8958
Nikon D800	0.8328	0.8613	0.9050	0.9137	0.9127	0.9142	0.8259	0.8649	0.9141	**0.9369**	0.9238
ISO = 6400	0.7773	0.8363	0.8818	0.8958	0.8494	0.8960	0.7936	0.8295	0.8847	**0.9118**	0.9089
Average	0.8846	0.9063	0.9381	0.9436	0.9250	0.9463	0.8635	0.9126	0.9364	0.9481	**0.9504**

dataset, each scene was shot 500 times under the same camera and camera setting. The mean image of the 500 shots is roughly taken as the "ground truth", with which the PSNR and SSIM [92] can be computed. The average SSIM results of GAT-BM3D [62], CBM3D [22], WNNM [36], MLP [13], CSF [83], TNRD [19], DnCNN [107], NI [2], NC [50, 51], CC [68], and the proposed method are listed in Table 3.1. As can be seen from Figures 3.3-3.5, our proposed method achieves better performance than the the competing methods.

Results on dataset 2. As described in section 3.4.2, there is a mean image for each of the 11 scenes used in dataset 2 [68], and those mean images can be roughly taken as "ground truth" images for quantitative evaluation of denoising algorithms. We firstly perform quantitative comparison on the 15 cropped images used in [68]. The PSNR results of GAT-BM3D, CBM3D, WNNM, MLP, CSF, TNRD, DnCNN, NC, NI and CC are listed in Table II (The results of CC are copied from the original paper [68]). The best PSNR results of each image are highlighted in bold. One can see that on 8 out of the 15 images, our method achieves the

best PSNR values. CC achieves the best PSNR on 3 of the 15 images. It should be noted that in the CC method, a specific model is trained for each camera and camera setting, while our method uses the same model for all images. On average, our proposed method has 0.27dB PSNR improvements over the second best method CC and much higher PSNR gains over other competing methods. The method GAT-BM3D does not work well on most images. This is because real world noise is much more complex than Poisson.

Fig. 3.12 shows the denoised images of one scene captured by Canon 5D Mark 3 at ISO = 3200. We can see that GAT-BM3D, CBM3D, WNNM, DnCNN, NC, NI and CC would either remain noise or generate artifacts, while TNRD over-smooths much the image. By using the external prior guided internal priors, our proposed method preserves edges and textures better than other methods, leading to visually pleasant outputs. More comparisons on visual quality and SSIM [92] index can be found in the Figures 3.13 and 3.14.

We then perform denoising experiments on the 60 images we cropped from [68]. The average PSNR results are listed in Table III (CC is not compared since the code is not available). Again, our proposed method achieves much better PSNR results than the other methods. The improvements of our method over the second best method (TNRD) are 0.43dB on PSNR. Fig. 3.15 shows the denoised images of one scene captured by Nikon D800 at ISO = 3200. We can see again that the proposed method obtain better visual quality than other competing methods. More comparisons on visual quality and SSIM can be found in the Figures 3.16 and 3.17.

Results on dataset 3. Similar to dataset 2 [68], there is a "ground truth" image for each of the 10 scenes used in our constructed dataset 3. We perform quantitative comparison on the 100 cropped images. The average PSNR results of competing methods are listed in Table IV. We can see that our proposed method achieves much better PSNR results than the other methods. The improvements of our method over the second best method (TNRD) is 0.16dB on PSNR. Fig. 3.18 shows the denoised images of one scene captured by Canon 80D at ISO = 12800. We can see again that the proposed method removes the noise while maintains

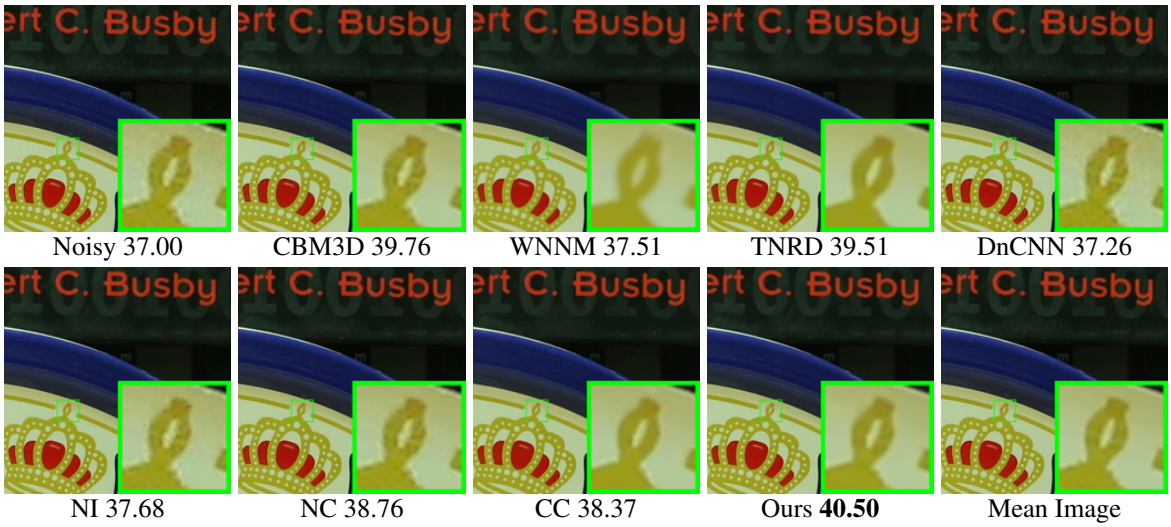

Figure 3.12 Denoised images and PSNR(dB) results of a region cropped from the real-world noisy image "Canon 5D Mark 3 ISO 3200 1" [68] by different methods. The images are better to be zoomed in on screen.

better details (such as the vertical black shadow area) than other competing methods. More comparisons on visual quality and SSIM can be found in the Figures 3.19 and 3.20.

Comparison on speed. Efficiency is an important aspect to evaluate the efficiency of algorithms. We compare the speed of all competing methods except for CC. All experiments are run under the Matlab2014b environment on a machine with Intel(R) Core(TM) i7-5930K CPU of 3.5GHz and 32GB RAM. The average running time (second) of the compared methods on the 100 real-world noisy images is shown in Table 3.5. The least average running time are highlighted in bold. One can easily see that the commercial software Neat Image (NI) is the fastest method with highly optimized code. For a 512×512 image, NI costs about 0.6 second. The other methods cost from 5.2 (TNRD) to 152.2 (WNNM) seconds, while the proposed method costs about 24.1 seconds. It should be noted that GAT-BM3D, CBM3D, TNRD, and NC are implemented with compiled C++ mex-function and with parallelization, while WNNM, MLP, CSF, DnCNN, and the proposed method are implemented purely in Matlab.

In this section, we provide more comparisons of the proposed method with the state-of-the-art denoising methods on the 60 real-world noisy images cropped from [68]. In this dataset,

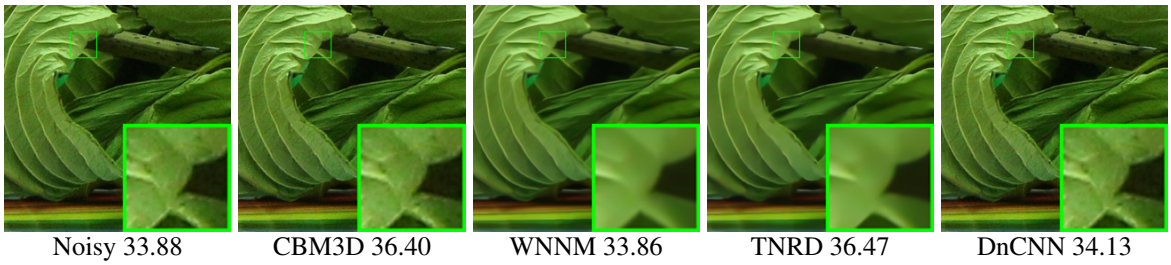

Noisy 33.88 | CBM3D 36.40 | WNNM 33.86 | TNRD 36.47 | DnCNN 34.13

NI 34.87 | NC 35.69 | CC 35.37 | Ours **37.05** | Mean Image

Figure 3.13 Denoised images and PSNR(dB) results of a region cropped from the real-world noisy image "Canon 5D Mark 3 ISO 3200 2" [68] by different methods. The images are better to be zoomed in on screen.

Noisy 33.77 | CBM3D 35.07 | WNNM 36.09 | TNRD 36.37 | DnCNN 34.48

NI 35.36 | NC **36.70** | CC 35.95 | Ours 36.31 | Mean Image

Figure 3.14 Denoised images and PSNR(dB) results of a region cropped from the real-world noisy image "Nikon D600 ISO 3200 2" [68] by different methods. The images are better to be zoomed in on screen.

each scene was shot 500 times under the same camera and camera setting. The mean image of the 500 shots is roughly taken as the "ground truth", with which the PSNR and SSIM can be computed. The average SSIM results of GAT-BM3D [62], CBM3D [22], WNNM [36], MLP

Table 3.4 Average PSNR(dB) results of different methods on 60 real-world noisy images cropped from [68].

Methods	**GAT-BM3D**	**CBM3D**	**WNNM**	**MLP**	**CSF**	**TNRD**	**DnCNN**	**NI**	**NC**	**Ours**
PSNR	34.33	36.34	37.67	38.13	37.40	38.32	34.99	36.53	37.57	**38.75**

Table 3.5 Average SSIM [92] results of different methods on 60 real-world noisy images cropped from [68].

Methods	**GAT-BM3D**	**CBM3D**	**WNNM**	**MLP**	**CSF**	**TNRD**	**DnCNN**	**NI**	**NC**	**Ours**
SSIM	0.9331	0.9251	0.9633	0.9653	0.9598	0.9670	0.8873	0.9241	0.9514	**0.9691**

Table 3.6 Average PSNR(dB) results of different methods on 100 real-world noisy images cropped from our new dataset.

Methods	**GAT-BM3D**	**CBM3D**	**WNNM**	**MLP**	**CSF**	**TNRD**	**DnCNN**	**NI**	**NC**	**Ours**
PSNR	33.54	37.14	35.18	37.34	37.07	37.48	34.74	35.70	36.76	**37.64**

[13], CSF [83], TNRD [19], DnCNN [107], NI [2], NC [50, 51], and the proposed method are listed in Table 3.4 (CC is not compared since the code of [68] is not available). As can be seen from Figures 3.6-3.7, our proposed method achieves better performance than the competing methods.

In this section, we provide more comparisons of the proposed method with the state-of-the-art denoising methods on the 100 real-world noisy images cropped from the new dataset we constructed. In this dataset, each scene was shot 500 times under the same camera and camera setting. The mean image of the 500 shots is roughly taken as the "ground truth", with which the PSNR and SSIM can be computed. The average SSIM results of GAT-BM3D [62], CBM3D [22], WNNM [36], MLP [13], CSF [83], TNRD [19], DnCNN [107], NI [2], NC [50, 51], and the proposed method are listed in Table 3.7 (CC is not compared since the code of [68] is not available). As can be seen from Figure 3.12, our proposed method achieves better performance than the competing methods.

Table 3.7 Average SSIM [92] results of different methods on 100 real-world noisy images cropped from our new dataset.

Methods	**GAT-BM3D**	**CBM3D**	**WNNM**	**MLP**	**CSF**	**TNRD**	**DnCNN**	**NI**	**NC**	**Ours**
SSIM	0.8881	0.9494	0.9290	0.9453	0.9398	0.9486	0.8852	0.9190	0.9356	**0.9529**

Table 3.8 Average Speed (sec.) results of different methods on 100 real-world noisy images cropped from our new dataset.

Methods	**GAT-BM3D**	**CBM3D**	**WNNM**	**MLP**	**CSF**	**TNRD**	**DnCNN**	**NI**	**NC**	**Ours**
Time	11.1	6.9	152.2	17.1	19.5	5.2	79.5	**0.6**	15.6	24.1

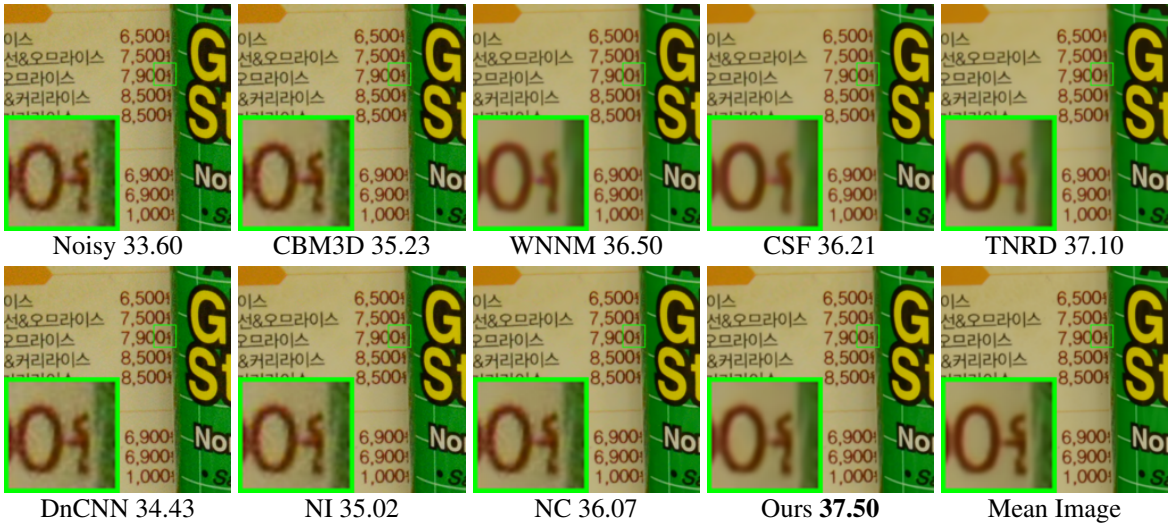

Noisy 33.60 | CBM3D 35.23 | WNNM 36.50 | CSF 36.21 | TNRD 37.10

DnCNN 34.43 | NI 35.02 | NC 36.07 | Ours **37.50** | Mean Image

Figure 3.15 Denoised images and PSNR(dB) results of a region cropped from the real-world noisy image "Nikon D800 ISO 3200 A3" [68] by different methods. The images are better to be zoomed in on screen.

3.4 Conclusion

We proposed a new prior learning method for the real-world noisy image denoising problem by exploiting the useful information in both external and internal data. We first learned Gaussian Mixture Models (GMMs) from a set of clean external images as general image prior, and then employed the learned GMM model to guide the learning of adaptive internal prior from the given noisy image. Finally, a set of orthogonal dictionaries were output as the external-internal hybrid prior models for image denoising. Extensive experiments on three real-world

Figure 3.16 Denoised images and PSNR(dB) results of a region cropped from the real-world noisy image "Nikon D800 ISO 1600 B2" [68] by different methods. The images are better to be zoomed in on screen.

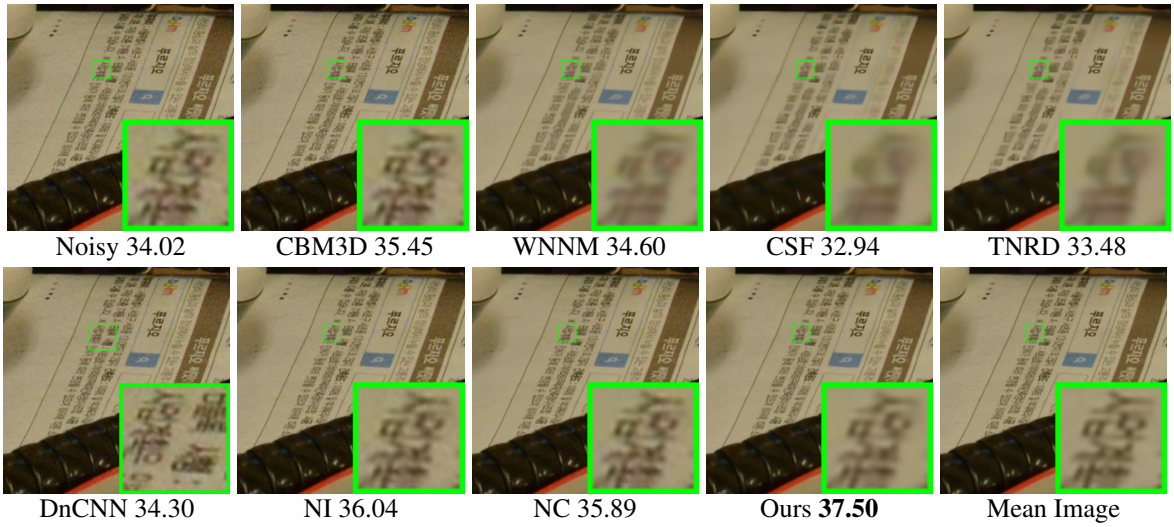

Figure 3.17 Denoised images and PSNR(dB) results of a region cropped from the real-world noisy image "Nikon D800 ISO 3200 A1" [68] by different methods. The images are better to be zoomed in on screen.

noisy image datasets, including a new dataset constructed by us by different types of cameras and camera settings, demonstrated that our proposed method achieves much better performance than state-of-the-art image denoising methods in terms of both quantitative measure and perceptual quality.

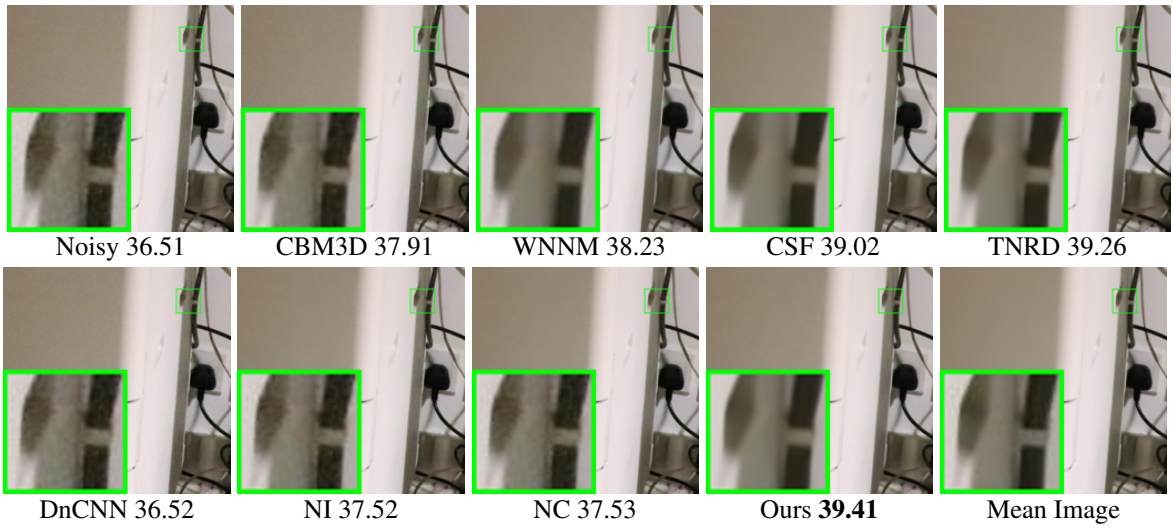

Figure 3.18 Denoised images and PSNR(dB) results of a region cropped from the real-world noisy image "Canon 80D ISO 12800 IMG 2321" in our new dataset by different methods.. The images are better to be zoomed in on screen.

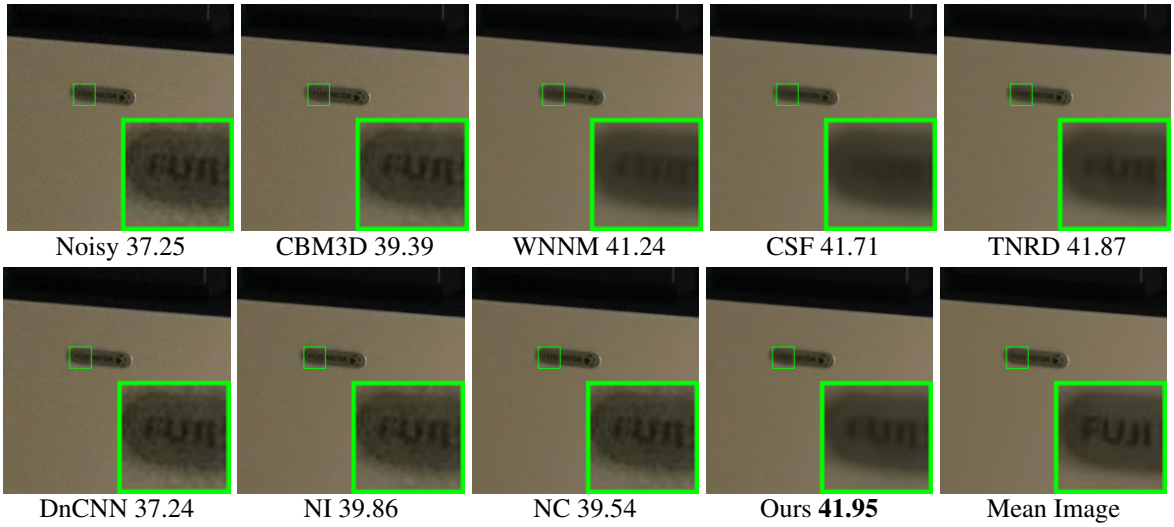

Figure 3.19 Denoised images and PSNR(dB) results of a region cropped from the real-world noisy image "Canon 80D ISO 12800 IMG2360" in our new dataset by different methods.. The images are better to be zoomed in on screen.

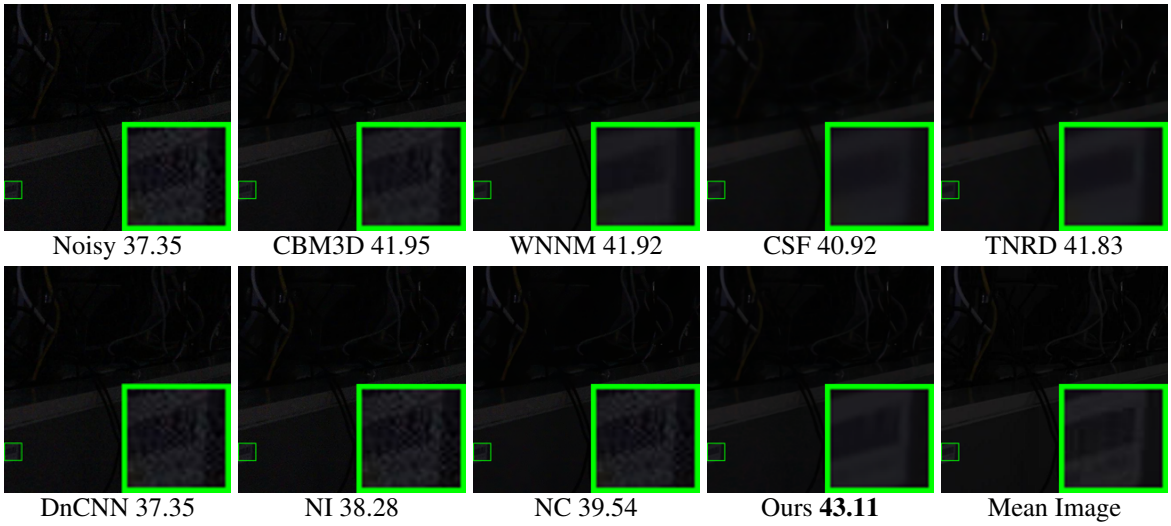

Figure 3.20 Denoised images and PSNR(dB) results of a region cropped from the real-world noisy image "SONY A7II ISO 6400 DSC03017" in our new dataset by different methods.. The images are better to be zoomed in on screen.

Chapter 4

Multi-channel Weighted Nuclear Norm Minimization for Real-world Image Denoising

4.1 Introduction

Image denoising is a classical yet fundamental problem for image quality enhancement in computer vision and photography systems. Most of existing denoising algorithms are designed for grayscale images, aiming to recover the clean image $\mathbf{x}$ from its noisy observation $\mathbf{y} = \mathbf{x} + \mathbf{n}$, where $\mathbf{n}$ is generally assumed to be additive white Gaussian noise (AWGN). State-of-the-art image denoising methods include sparse representation [22], dictionary learning [30], low-rank approximation [36], non-local self-similarity (NSS) [12] based methods, and the combination of those techniques [22, 24, 30, 36, 58, 103, 111]. Recently, some discriminative denoising methods have also been developed by learning discriminative priors from pairs of clean and noisy images [13, 19, 83, 107].

During the last decade, a few methods have been proposed for real-world color image

denoising. Among them, the CBM3D method [21] is a representative one, which first transforms the RGB image into a luminance-chrominance space (e.g., YCbCr) and then applies the benchmark BM3D method [22] to each channel separately. The non-local similar patches are grouped by the luminance channel. In [53], Liu et al. proposed the "Noise Level Function" to estimate and remove the noise for each channel in natural images. However, processing each channel separately would often achieve inferior performance to processing the color channels jointly [60]. Therefore, the methods [50, 51, 110] perform real color image denoising by concatenating the patches of RGB channels into a long vector. However, the concatenation treats each channel equally and ignores the different noise statistics among these channels. The method in [68] models the cross-channel noise in real-world noisy images as multivariate Gaussian and the noise is removed by the Bayesian non-local means filter [46]. The commercial software Neat Image [2] estimates the noise parameters from a flat region of the given noisy image and filters the noise accordingly. The methods in [2, 68] ignore the non-local self-similarity of natural images [22, 36].

When the input is a noisy RGB color image, there are mainly three strategies for color image denoising. (1) The first strategy is to apply the grayscale image denoising algorithm to each channel. However, such a straightforward solution will not exploit the spectral correlation among RGB channels, and the denoising performance may not be very satisfying. (2) The second strategy is to transform the RGB image into a less correlated color space, such as YCbCr, and perform denoising in each channel of the transformed space [21, 79]. One representative work along this line is the CBM3D algorithm [21]. However, the color transform will complicate the noise distribution, and the correlation among color channels is not fully exploited. (3) The third strategy is to perform joint denoising on the RGB channels simultaneously for better use of the spectral correlation. For example, the patches from RGB channels are concatenated as a long vector for processing [60, 110].

Though joint denoising of RGB channels is a more promising way for color image denois-

ing, it is not a trivial extension from single channel (grayscale image) to multiple channels (color image). The noise in standard RGB (sRGB) space can be approximately modeled as AWGN, but it has different variances for different channels [52, 53, 68] due to the sensor characteristics and on-board processing steps in digital camera pipelines [45, 68]. This makes the real color image denoising problem much more complex. If the three channels are treated equally in the joint denoising process, false colors or artifacts can be generated [60]. How to account for the different noise characteristics in color channels, and how to effectively exploit the within and cross channel correlation are the key issues for designing a good color image denoising method.

During the last decade, a few methods have been proposed for real color image denoising. Among them, the CBM3D method [21] is a representative one, which first transforms the RGB image into a luminance-chrominance space (e.g., YCbCr) and then applies the benchmark BM3D method [22] to each channel separately. The non-local similar patches are grouped by the luminance channel. In [53], Liu et al. proposed the "Noise Level Function" to estimate and remove the noise for each channel in natural images. However, processing each channel separately would often achieve inferior performance to processing the color channels jointly [60]. Therefore, the methods [50, 51, 110] perform real color image denoising by concatenating the patches of RGB channels into a long vector. However, the concatenation treats each channel equally and ignores the different noise statistics among these channels. The method in [68] models the cross-channel noise in real-world noisy images as multivariate Gaussian and the noise is removed by the Bayesian non-local means filter [46]. The commercial software Neat Image [2] estimates the noise parameters from a flat region of the given noisy image and filters the noise accordingly. The methods in [2, 68] ignore the non-local self-similarity of natural images [22, 36]. This work presents a new color image denoising algorithm. Considering that the weighted nuclear norm minimization (WNNM) method [35, 36], which exploits the image NSS property via low rank regularization, has achieved excellent denoising performance on

grayscale images. As a generalization to the nuclear norm minimization (NNM) model [14], the weighted nuclear norm minimization (WNNM) model [35, 36] is described as

$$\min_{\mathbf{X}} \|\mathbf{Y}-\mathbf{X}\|_F^2 + \|\mathbf{X}\|_{\boldsymbol{w},*}, \tag{4.1}$$

where $\|\mathbf{X}\|_{\boldsymbol{w},*} = \sum_i w_i\sigma_i(\mathbf{X})$ is the weighted nuclear norm of matrix $\mathbf{X}$, $\boldsymbol{w} = [w_1, ..., w_n]^\top$ ($w_i \geq 0$) is the weight vector, and $\sigma_i(\mathbf{X})$ is the ith singular value of $\mathbf{X}$. According to the Corollary 1 of [35], if the weights are non-decreasing, the problem (4.1) has a closed-form solution:

$$\hat{\mathbf{X}} = \mathbf{U}\mathcal{S}_{\boldsymbol{w}/2}(\boldsymbol{\Sigma})\mathbf{V}^\top, \tag{4.2}$$

where $\mathbf{Y} = \mathbf{U}\boldsymbol{\Sigma}\mathbf{V}^\top$ is the singular value decomposition (SVD) [28] of $\mathbf{Y}$ and $\mathcal{S}_{\boldsymbol{w}/2}(\bullet)$ is the generalized soft-thresholding operator with weight vector $\boldsymbol{w}$:

$$\mathcal{S}_{\boldsymbol{w}/2}(\boldsymbol{\Sigma}_{ii}) = \max(\boldsymbol{\Sigma}_{ii} - w_i/2, 0). \tag{4.3}$$

WNNM has demonstrated highly competitive denoising performance on grayscale images. However, if we directly extend it to color image denoising by concatenating the patches from RGB channels, denoising artifacts may happen (please refer to Fig. 4.1 and the section of experimental results). In this work, we propose a multi-channel WNNM (MC-WNNM) model for color image denoising, which preserves the power of WNNM and is able to address the noise differences among different channels.

In this work, we propose to extend WNNM to real color image denoising. More specifically, we propose a multi-channel WNNM (MC-WNNM) model, which concatenates the patches from RGB channels for rank minimization but introduces a weight matrix to adjust the contributions of the three channels based on their noise levels. The proposed MC-WNNM model no longer has a closed-form solution as in the original WNNM model [35]. We reformulate it into a linear equality-constrained problem with two variables, and solve the relaxed problem under the alternating direction method of multipliers [11] framework. Each variable can be updated with closed-form solutions, and the convergence analysis is given to

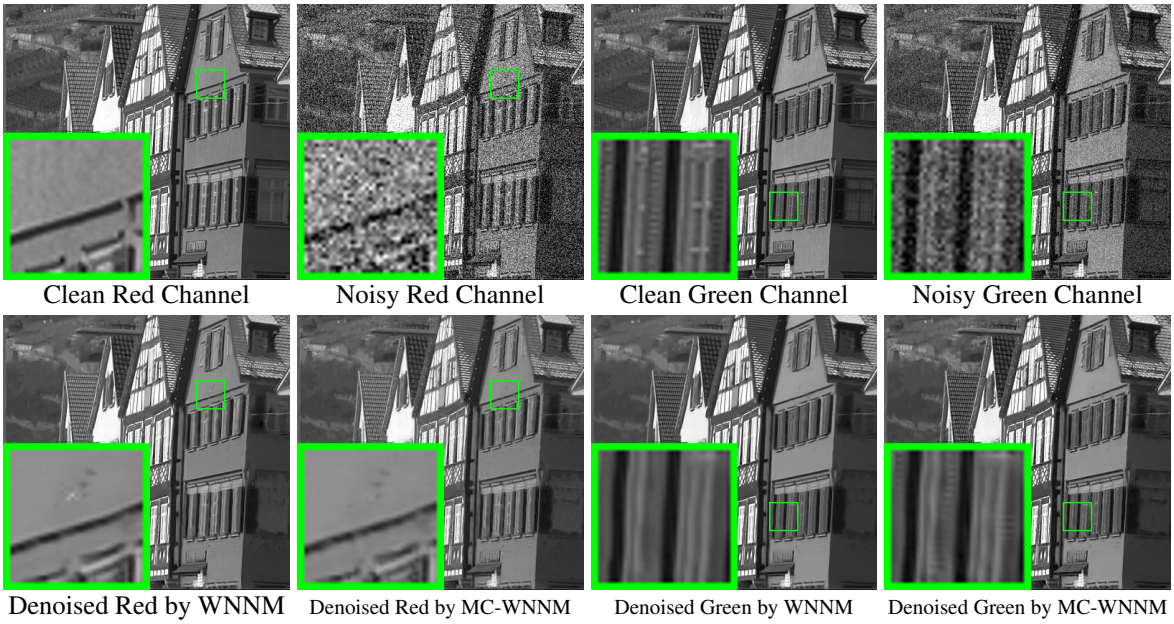

Figure 4.1 The Red and Green channels of the image "kodim08" from the Kodak PhotoCD Dataset, its synthetic noisy version, and the images recovered by the concatenated WNNM and the proposed MC-WNNM methods.

guarantee a rational termination of the proposed algorithm. Besides, we present an effective multi-channel image denoising algorithm, which utilizes the strong low-rank prior of image non-local similar patches, and introduces a weight matrix to balance the multi-channels based on their different noise levels.

4.2 The Proposed Color Image Denoising Algorithm

4.2.1 The Multi-channel Weighted Nuclear Norm Minimization Model

The color image denoising problem is to recover the clean image $\mathbf{x}_c$ from its noisy version $\mathbf{y}_c = \mathbf{x}_c + \mathbf{n}_c$, where $c = \{r, g, b\}$ is the index of R, G, B channels and $\mathbf{n}_c$ is the noise in the c channel. Patch based image denoising [13, 19, 22, 24, 30, 36, 58, 79, 83, 103, 107, 111] has achieved a great success in the last decade. Given a noisy color image $\mathbf{y}_c$, each local patch of size $p \times p \times 3$ is extracted and stretched to a patch vector, denoted by $\mathbf{y} = [\mathbf{y}_r^\top \ \mathbf{y}_g^\top \ \mathbf{y}_b^\top]^\top \in \mathbb{R}^{3p^2}$,

where $\mathbf{y}_r, \mathbf{y}_g, \mathbf{y}_b \in \mathbb{R}^{p^2}$ are the corresponding patches in R, G, B channels. For each local patch $\mathbf{y}$, we search the M most similar patches to it (including $\mathbf{y}$ itself) by Euclidean distance in a relatively large local window around it. By stacking the M similar patches column by column, we form a noisy patch matrix $\mathbf{Y} = \mathbf{X} + \mathbf{N} \in \mathbb{R}^{3p^2 \times M}$, where $\mathbf{X}$ and $\mathbf{N}$ are the corresponding clean and noise patch matrices.

The noise in standard RGB (sRGB) space could be approximately modeled as additive white Gaussian (AWGN), but noise in different channels has different variances [52, 53, 68]. Therefore, it is problematic to directly apply some grayscale denoising methods to the concatenated vectors $\mathbf{y}$ or matrices $\mathbf{Y}$. To better illustrate this point, in Fig. 4.1, we show a clean image "kodim08" (only the R and G channels are shown due to limit of space), its noisy version generated by adding AWGN to each channel, and the denoised image by applying WNNM [35] to the concatenated patch matrix $\mathbf{Y}$. The standard deviations of AWGN added to the R, G, B channels are $\sigma_r = 40$, $\sigma_g = 20$, $\sigma_b = 30$, respectively. To make WNNM applicable to color image denoising, we set the noise standard deviation as the average deviation of the whole noisy image, i.e., $\sigma = \sqrt{(\sigma_r^2 + \sigma_g^2 + \sigma_b^2)/3} \approx 31.1$. From Fig. 4.1, one can see that the concatenated WNNM remains some noise in the R channel while over-smoothing the G channel. This is because it processes R and G channels equally without considering their differences in noise corruption.

Clearly, a more effective color image denoising algorithm should consider the different noise strength in color channels. To this end, we introduce a weight matrix $\mathbf{W}$ to balance the noise in the RGB channels, and present the following multi-channel WNNM (MC-WNNM) model:

$$\min_{\mathbf{X}} \|\mathbf{W}(\mathbf{Y} - \mathbf{X})\|_F^2 + \|\mathbf{X}\|_{\boldsymbol{w},*}. \tag{4.4}$$

We follow the method in [35] to set the weight vector $\boldsymbol{w}$ on nuclear norm as $w_i^{k+1} = C/(|\sigma_i(\mathbf{X}_k)| + \epsilon)$, where $\epsilon > 0$ is a small number to avoid zero numerator and $\sigma_i(\mathbf{X}_k)$ is the ith singular value of the estimated data matrix $\mathbf{X}$ at the kth iteration. Note that if $\sigma_r = \sigma_g = \sigma_b$, the proposed

MC-WNNM model will be reduced to the concatenated WNNM model. With an appropriate setting of the weight matrix $\mathbf{W}$ and a good optimization algorithm, the proposed MC-WNNM model will lead to much better color image denoising results. As shown in Figs. 4.1(f) and 4.1(h), MC-WNNM removes clearly the noise in the R channel while preserving textures effectively in the G channel.

4.2.2 The Setting of Weight Matrix W

Let's denote the noisy patch matrix by $\mathbf{Y} = [\mathbf{Y}_r^\top\ \mathbf{Y}_g^\top\ \mathbf{Y}_b^\top]^\top$, where $\mathbf{Y}_r, \mathbf{Y}_g, \mathbf{Y}_b$ are sub-matrices of similar patches in R, G, B channels, respectively. The corresponding clean matrix is $\mathbf{X} = [\mathbf{X}_r^\top\ \mathbf{X}_g^\top\ \mathbf{X}_b^\top]^\top$, where $\mathbf{X}_r, \mathbf{X}_g, \mathbf{X}_b$ are similarly defined. The weight matrix $\mathbf{W}$ can be determined under the *maximum a-posterior* (MAP) estimation framework:

$$\hat{\mathbf{X}} = \arg\max_{\mathbf{X}} \ln P(\mathbf{X}|\mathbf{Y}, \boldsymbol{w}) = \arg\max_{\mathbf{X}} \{\ln P(\mathbf{Y}|\mathbf{X}) + \ln P(\mathbf{X}|\boldsymbol{w})\}. \tag{4.5}$$

The log-likelihood term $\ln P(\mathbf{Y}|\mathbf{X})$ is characterized by the statistics of noise. According to [52], we assume that the noise is independent among RGB channels and independently and identically distributed (i.i.d.) in each channel with Gaussian distribution and standard deviations $\{\sigma_r, \sigma_g, \sigma_b\}$. There is:

$$P(\mathbf{Y}|\mathbf{X}) = \prod_{c\in\{r,g,b\}} (2\pi\sigma_c^2)^{-\frac{3p^2}{2}} \exp(-\frac{1}{2\sigma_c^2}\|\mathbf{Y}_c - \mathbf{X}_c\|_F^2). \tag{4.6}$$

For the latent data $\mathbf{X}$, the small weighted nuclear norm prior is imposed on it, i.e., $\|\mathbf{X}\|_{\boldsymbol{w},*} = \sum_i w_i\sigma_i(\mathbf{X})$ should be sparsely distributed. We let it be:

$$P(\mathbf{X}|\boldsymbol{w}) \propto \exp(-\frac{1}{2}\|\mathbf{X}\|_{\boldsymbol{w},*}). \tag{4.7}$$

Putting (4.7) and (4.6) into (4.5), we have

$$\hat{\mathbf{X}} = \arg\min_{\mathbf{X}} \sum_{c\in\{r,g,b\}} \frac{1}{\sigma_c^2}\|(\mathbf{Y}_c - \mathbf{X}_c)\|_F^2 + \|\mathbf{X}\|_{\boldsymbol{w},*} = \arg\min_{\mathbf{X}} \|\mathbf{W}(\mathbf{Y} - \mathbf{X})\|_F^2 + \|\mathbf{X}\|_{\boldsymbol{w},*}, \tag{4.8}$$

with

$$\mathbf{W} = \begin{pmatrix} \sigma_r^{-1}\mathbf{I} & \mathbf{0} & \mathbf{0} \\ \mathbf{0} & \sigma_g^{-1}\mathbf{I} & \mathbf{0} \\ \mathbf{0} & \mathbf{0} & \sigma_b^{-1}\mathbf{I} \end{pmatrix}, \tag{4.9}$$

where $\mathbf{I} \in \mathbb{R}^{p^2 \times p^2}$ is the identity matrix.

Clearly, the weight matrix $\mathbf{W}$ is diagonal and determined by the noise standard deviation in each channel. The stronger the noise in a channel, the less the contribution that channel should make to the estimation of $\mathbf{X}$. Our experimental results (refer to Section 4 please) on synthetic and real-world noisy images clearly demonstrate the advantages of MC-WNM over WNNM and other methods in color image denoising.

4.2.3 Model Optimization

The proposed MC-WNNM model does not have an analytical solution. In the WNNM model [35], when the weights assigned on singular values are in a non-descending order, the weighted nuclear norm proximal operator can have a global optimum with closed-form solution. Unfortunately, such a property is not valid for the MC-WNNM model because a weight matrix $\mathbf{W}$ is assigned to the rows of data matrix $\mathbf{X}$. This makes the proposed model more difficult to solve than the original WNNM model.

We employ the variable splitting method [20, 29] to solve the MC-WNNM model. By introducing an augmented variable $\mathbf{Z}$, the MC-WNNM model can be reformulated as a linear equality-constrained problem with two variables $\mathbf{X}$ and $\mathbf{Z}$:

$$\min_{\mathbf{X},\mathbf{Z}} \|\mathbf{W}(\mathbf{Y}-\mathbf{X})\|_F^2 + \|\mathbf{Z}\|_{\boldsymbol{w},*} \quad \text{s.t.} \quad \mathbf{X} = \mathbf{Z}. \tag{4.10}$$

Since the objective function is separable w.r.t. the two variables, the problem (4.10) can be solved under the alternating direction method of multipliers (ADMM) [11] framework. The augmented Lagrangian function is:

$$\mathcal{L}(\mathbf{X},\mathbf{Z},\mathbf{A},\rho) = \|\mathbf{W}(\mathbf{Y}-\mathbf{X})\|_F^2 + \|\mathbf{Z}\|_{\boldsymbol{w},*} + \langle \mathbf{A}, \mathbf{X}-\mathbf{Z}\rangle + \frac{\rho}{2}\|\mathbf{X}-\mathbf{Z}\|_F^2, \tag{4.11}$$

where $\mathbf{A}$ is the augmented Lagrangian multiplier and $\rho > 0$ is the penalty parameter. We initialize the matrix variables $\mathbf{X}_0$, $\mathbf{Z}_0$, and $\mathbf{A}_0$ to be zero matrix and $\rho_0 > 0$ to be a suitable value. Denote by $(\mathbf{X}_k, \mathbf{Z}_k)$ and $\mathbf{A}_k$ the optimization variables and Lagrange multiplier at iteration k ($k = 0, 1, 2, ...$), respectively. By taking derivatives of the Lagrangian function $\mathcal{L}$ w.r.t. $\mathbf{X}$ and $\mathbf{Z}$ and setting the derivative function to be zero, we can alternatively update the variables as follows:

(1) **Update X while fixing Z and A**:

$$\mathbf{X}_{k+1} = \arg\min_{\mathbf{X}} \|\mathbf{W}(\mathbf{Y} - \mathbf{X})\|_F^2 + \frac{\rho_k}{2}\|\mathbf{X} - \mathbf{Z}_k + \rho_k^{-1}\mathbf{A}_k\|_F^2. \tag{4.12}$$

This is a standard least squares regression problem with closed-form solution:

$$\mathbf{X}_{k+1} = (\mathbf{W}^\top\mathbf{W} + \frac{\rho_k}{2}\mathbf{I})^{-1}(\mathbf{W}^\top\mathbf{W}\mathbf{Y} + \frac{\rho_k}{2}\mathbf{Z}_k - \frac{1}{2}\mathbf{A}_k). \tag{4.13}$$

(2) **Update Z while fixing X and A**:

$$\mathbf{Z}_{k+1} = \arg\min_{\mathbf{Z}} \frac{\rho_k}{2}\|\mathbf{Z} - (\mathbf{X}_{k+1} + \rho_k^{-1}\mathbf{A}_k)\|_F^2 + \|\mathbf{Z}\|_{w,*}. \tag{4.14}$$

According to the Theorem 1 in [35], given the SVD of $\mathbf{X}_{k+1} + \rho_k^{-1}\mathbf{A}_k$, i.e., $\mathbf{X}_{k+1} + \rho_k^{-1}\mathbf{A}_k = \mathbf{U}_k\mathbf{\Sigma}_k\mathbf{V}_k^\top$, where $\mathbf{\Sigma}_k = \begin{pmatrix} \mathrm{diag}(\sigma_1, \sigma_2, ..., \sigma_M) \\ \mathbf{0} \end{pmatrix} \in \mathbb{R}^{3p^2 \times M}$ (without loss of generality, we assume that $3p^2 \geq M$), the global optimum of the above problem is $\hat{\mathbf{Z}}_{k+1} = \mathbf{U}_k\hat{\mathbf{\Sigma}}_k\mathbf{V}_k^\top$, where $\hat{\mathbf{\Sigma}}_k = \begin{pmatrix} \mathrm{diag}(\hat{\sigma}_1, \hat{\sigma}_2, ..., \hat{\sigma}_M) \\ \mathbf{0} \end{pmatrix} \in \mathbb{R}^{3p^2 \times M}$ and $(\hat{\sigma}_1, \hat{\sigma}_2, ..., \hat{\sigma}_M)$ is the solution to the following convex optimization problem:

$$\min_{\hat{\sigma}_1, \hat{\sigma}_2, ..., \hat{\sigma}_M} \sum_{i=1}^{M} (\sigma_i - \hat{\sigma}_i)^2 + \frac{2w_i}{\rho_k}\hat{\sigma}_i \quad \text{s.t.} \quad \hat{\sigma}_1 \geq \hat{\sigma}_2 \geq ... \geq \hat{\sigma}_M \geq 0. \tag{4.15}$$

According to the Remark 1 in [35], the problem above has closed-form solution ($i = 1, 2, ..., M$):

$$\hat{\sigma}_i = \begin{cases} 0 & \text{if } c_2 < 0 \\ \frac{c_1 + \sqrt{c_2}}{2} & \text{if } c_2 \geq 0 \end{cases}, \tag{4.16}$$

where $c_1 = \sigma_i - \epsilon$, $c_2 = (\sigma_i - \epsilon)^2 - \frac{8C}{\rho_k}$, $\epsilon > 0$ is a small number, and C is set as $\sqrt{2M}$ by experience in [35].

(3) **Update A while fixing X and Z**:

$$\mathbf{A}_{k+1} = \mathbf{A}_k + \rho_k(\mathbf{X}_{k+1} - \mathbf{Z}_{k+1}). \tag{4.17}$$

(4) **Update** ρ_k: $\rho_{k+1} = \mu * \rho_k$, where $\mu > 1$.

The above alternative updating steps are repeated until the convergence condition is satisfied or the number of iterations exceeds a preset threshold. The convergence condition of the ADMM algorithm is: $\|\mathbf{X}_{k+1} - \mathbf{Z}_{k+1}\|_F \leq \text{Tol}$, $\|\mathbf{X}_{k+1} - \mathbf{X}_k\|_F \leq \text{Tol}$, and $\|\mathbf{Z}_{k+1} - \mathbf{Z}_k\|_F \leq \text{Tol}$ are simultaneously satisfied, where $\text{Tol} > 0$ is a small tolerance number. We summarize the updating procedures in Algorithm 1. The convergence analysis of the proposed Algorithm 1 is given in Theorem 4.2.1. Note that since the weighted nuclear norm is non-convex in general, we employ an unbounded sequence of $\{\rho_k\}$ here to make sure that Algorithm 1 converges.

Theorem 4.2.1 *Assume that the weights in* $\boldsymbol{w}$ *are in a non-descending order, the sequences* $\{\mathbf{X}_k\}$, $\{\mathbf{Z}_k\}$, *and* $\{\mathbf{A}_k\}$ *generated in Algorithm 1 satisfy:*

$$(a) \lim_{k\to\infty} \|\mathbf{X}_{k+1} - \mathbf{Z}_{k+1}\|_F = 0; \tag{4.18}$$

$$(b) \lim_{k\to\infty} \|\mathbf{X}_{k+1} - \mathbf{X}_k\|_F = 0; \tag{4.19}$$

$$(c) \lim_{k\to\infty} \|\mathbf{Z}_{k+1} - \mathbf{Z}_k\|_F = 0. \tag{4.20}$$

Proof We give a sketch proof here and detailed proof of this theorem can be found in the supplementary file.

We first prove that the sequence $\{\mathbf{A}_k\}$ generated by Algorithm 1 is upper bounded. Since $\{\rho_k\}$ is unbounded, i.e., $\lim_{k\to\infty} \rho_k = +\infty$, we can prove that the sequence of Lagrangian function $\{\mathcal{L}(\mathbf{X}_{k+1}, \mathbf{Z}_{k+1}, \mathbf{A}_k, \rho_k)\}$ is also upper bounded. Hence, both $\{\mathbf{W}(\mathbf{Y} - \mathbf{X}_k)\}$ and $\{\mathbf{Z}_k\}$ are upper bounded. Then $\{\mathbf{X}_k\}$ is also upper bounded. According to Eq. (4.17), we can prove that

Algorithm 1: Solve MC-WNNM via ADMM

Input: Matrices $\mathbf{Y}$ and $\mathbf{W}$, $\mu > 1$, Tol > 0, K_1;

Initialization: $\mathbf{X}_0 = \mathbf{Z}_0 = \mathbf{A}_0 = \mathbf{0}$, $\rho_0 > 0$, T = False, $k = 0$;

While (T == false) **do**

1. Update $\mathbf{X}_{k+1}$ as

   $\mathbf{X}_{k+1} = (\mathbf{W}^\top\mathbf{W} + \frac{\rho_k}{2}\mathbf{I})^{-1}(\mathbf{W}^\top\mathbf{W}\mathbf{Y} + \frac{\rho_k}{2}\mathbf{Z}_k - \frac{1}{2}\mathbf{A}_k)$

2. Update $\mathbf{Z}_{k+1}$ by solving the problem

   $\min_{\mathbf{Z}} \frac{\rho_k}{2}\|\mathbf{Z} - (\mathbf{X}_{k+1} + \rho_k^{-1}\mathbf{A}_k)\|_F^2 + \|\mathbf{Z}\|_{\boldsymbol{w},*}$

3. Update $\mathbf{A}_{k+1}$ as $\mathbf{A}_{k+1} = \mathbf{A}_k + \rho_k(\mathbf{X}_{k+1} - \mathbf{Z}_{k+1})$

4. Update $\rho_{k+1} = \mu * \rho_k$;

5. $k \leftarrow k + 1$;

   if (Convergence condition is satisfied) or ($k \geq K_1$)

6. T $\leftarrow$ True

   end if

end while

Output: Matrices $\mathbf{X}$ and $\mathbf{Z}$.

$\lim_{k\to\infty} \|\mathbf{X}_{k+1} - \mathbf{Z}_{k+1}\|_F = \lim_{k\to\infty} \rho_k^{-1}\|\mathbf{A}_{k+1} - \mathbf{A}_k\|_F = 0$, and (a) is proved. Then we can prove that $\lim_{k\to\infty} \|\mathbf{X}_{k+1} - \mathbf{X}_k\|_F \leq \lim_{k\to\infty}(\|(\mathbf{W}^\top\mathbf{W} + \frac{\rho_k}{2}\mathbf{I})^{-1}(\mathbf{W}^\top\mathbf{W}\mathbf{Y} - \mathbf{W}^\top\mathbf{W}\mathbf{Z}_k - \frac{1}{2}\mathbf{A}_k)\|_F + \rho_k^{-1}\|\mathbf{A}_k - \mathbf{A}_{k-1}\|_F) = 0$ and hence (b) is proved. Finally, (c) can be proved by checking that $\lim_{k\to\infty} \|\mathbf{Z}_{k+1} - \mathbf{Z}_k\| \leq \lim_{k\to\infty}(\|\mathbf{\Sigma}_{k-1} - \mathcal{S}_{\boldsymbol{w}/\rho_{k-1}}(\mathbf{\Sigma}_{k-1})\|_F + \|\mathbf{X}_{k+1} - \mathbf{X}_k\|_F + \|\rho_{k-1}^{-1}\mathbf{A}_{k-1} + \rho_k^{-1}\mathbf{A}_{k+1} - \rho_k^{-1}\mathbf{A}_k\|_F) = 0$, where $\mathbf{U}_{k-1}\mathbf{\Sigma}_{k-1}\mathbf{V}_{k-1}^\top$ is the SVD of $\mathbf{X}_k + \rho_{k-1}^{-1}\mathbf{A}_{k-1}$.

4.2.4 The Denoising Algorithm

Given a noisy color image $\mathbf{y}_c$, suppose that we have extracted N local patches $\{\mathbf{y}_j\}_{j=1}^N$ and their similar patches. N noisy patch matrices $\{\mathbf{Y}_j\}_{j=1}^N$ can be formed to estimate the clean

Algorithm 2: Color Image Denoising by MC-WNNM

Input: Noisy image $\mathbf{y}_c$, noise levels $\{\sigma_r, \sigma_g, \sigma_b\}$, K_2;

Initialization: $\hat{\mathbf{x}}_c^{(0)} = \mathbf{y}_c$, $\mathbf{y}_c^{(0)} = \mathbf{y}_c$;

for $k = 1 : K_2$ **do**

1. Set $\mathbf{y}_c^{(k)} = \hat{\mathbf{x}}_c^{(k-1)}$;
2. Extract local patches $\{\mathbf{y}_j\}_{j=1}^N$ from $\mathbf{y}_c^{(k)}$;

   for each patch $\mathbf{y}_j$ **do**

3. Search non-local similar patches $\mathbf{Y}_j$;
4. Apply the MC-WNNM model (4.10) to $\mathbf{Y}_j$ and obtain the estimated $\mathbf{X}_j$;

   end for

5. Aggregate $\{\mathbf{X}_j\}_{j=1}^N$ to form the image $\hat{\mathbf{x}}_c^{(k)}$;

end for

Output: Denoised image $\hat{\mathbf{x}}_c^{(K_2)}$.

matrices $\{\mathbf{X}_j\}_{j=1}^N$. The patches in matrices $\{\mathbf{X}_j\}_{j=1}^N$ are aggregated to form the denoised image $\hat{\mathbf{x}}_c$. To obtain better denoising results, we perform the above denoising procedures for several rounds. The proposed MC-WNNM based color image denoising algorithm is summarized in Algorithm 2.

4.2.5 Complexity Analysis

In Algorithm 1 for solving the MC-WNNM model via ADMM, the cost for updating $\boldsymbol{X}$ is $O(\max(p^4M, M^3))$, while the cost for updating $\boldsymbol{Z}$ is $O(p^4M + M^3)$. The costs for updating $\boldsymbol{A}$ and ρ can be ignored. So the overall complexity is $O((p^4M + M^3)K_1)$, where K_1 is the number of iterations. In Algorithm 2 for image denoising, we consider the number of patches N extracted from the input noisy image and the number of itertations K_2 and ignore the cost for searching similar patches. The overall cost is $O((p^4M + M^3)K_1K_2N)$.

4.3 Experiments

We evaluate the proposed MC-WNNM method on synthetic and real-world noisy color images. We compare the proposed method with state-of-the-art denoising methods, including CBM3D [21], MLP [13], WNNM [36], TNRD [19], DnCNN [107] "Noise Clinic" (NC) [50, 51], CC [68], and the commercial software Neat Image (NI) [2]. The Matlab source code of our MC-WNNM algorithm can be downloaded at http://www4.comp.polyu.edu.hk/~cslzhang/code/MCWNNM.zip.

4.3.1 Experimental Settings

Noise level estimation. For most of the competing denoising algorithms, the standard deviation of noise should be given as a parameter. In synthetic experiments, the noise levels $(\sigma_r, \sigma_g, \sigma_b)$ in R, G ,B channels are assumed to be known. In the case of real-world noisy images, the noise levels can be estimated via some noise estimation methods [18, 54]. In this work, we employ the method [18] to estimate the noise level for each color channel.

Noise level of comparison methods. For the CBM3D method [21], a single parameter of noise level should be input. We set the noise level as

$$\sigma = \sqrt{(\sigma_r^2 + \sigma_g^2 + \sigma_b^2)/3}. \tag{4.21}$$

The methods of MLP [13] and TNRD [19] are originally designed for grayscale images. We retrain their models (using the released codes by the authors) at different noise levels from $\sigma = 5$ to $\sigma = 75$ with a gap of 5. The denoising on color images is performed by processing each channel with the model trained at the same (or nearest) noise level.

Comparison with WNNM. In order to make a full and fair comparison with the original WNNM method [35], we implement WNNM for color image denoising in three ways. 1) We apply WNNM to each color channel separately with the corresponding noise levels

$\sigma_r, \sigma_g, \sigma_b$. We call this method "WNNM-1". 2) We perform WNNM on the concatenated matrix $\mathbf{Y}$ formed by the patches in RGB channels, while the input noise level σ is computed by Eq. (4.21). We call this method "WNNM-2". 3) We set the weight matrix $\mathbf{W}$ as $\mathbf{W} = \sigma^{-1}\mathbf{I}$ in the proposed MC-WNNM model, and use our developed algorithm for denoising. We call this method "WNNM-3".

For a fair comparison, we tune the parameters of WNNM-1, WNNM-2, WNNM-3 and MC-WNNM to achieve their best denoising performance. The detailed parameters are as follows: we set the patch size as $p = 6$, the number of non-local similar patches as $M = 70$, the window size for searching similar patches as 40×40. For WNNM-3 and MC-WNNM, the updating parameter is set as $\mu = 1.001$. The number of iterations in Algorithm 1 is set as $K_1 = 10$. The number of iterations K_2 in Algorithm 2 and the initial penalty parameter ρ_0 will be given in the following sub-sections.

4.3.2 Experiments on Synthetic Noisy Color Images

We first compare MC-WNNM with the competing denoising methods [2, 13, 19, 21, 51, 107] on the 24 color images from the Kodak PhotoCD Dataset (http://r0k.us/graphics/kodak/). The noisy images are generated by adding AWGN to each of the R, G, B channels, respectively. For WNNM-3 and MC-WNNM, the initial penalty parameter is set as $\rho_0 = 10$ and $\rho_0 = 3$, respectively. The number of iterations in Algorithm 2 is set as $K_2 = 8$.

The PSNR results by competing methods are listed in Tables 4.1-4.3 on these images when the noise standard deviations are $\sigma_r = 40, \sigma_g = 20, \sigma_b = 30$ in Table 4.1, $\sigma_r = 30, \sigma_g = 10, \sigma_b = 50$ in Table 4.2 and $\sigma_r = 5, \sigma_g = 30, \sigma_b = 15$ in Table 4.3, respectively. While the best PSNR result for each image is highlighted in bold, one can see that on all the 24 images, our method achieves the highest PSNR values among the competing methods. We can see that in all these cases, the proposed MC-WNNM achieves better performance than the other competing methods. For example, in Table 4.1, the proposed MC-WNNM achieves on

Table 4.1 PSNR(dB) results of different denoising methods on the Kodak PhotoCD dataset.

	$\sigma_r = 40, \sigma_g = 20, \sigma_b = 30$									
Image#	**CBM3D**	**MLP**	**TNRD**	**DnCNN**	**NI**	**NC**	**WNNM-1**	**WNNM-2**	**WNNM-3**	**MC-WNNM**
1	25.24	25.70	25.74	20.47	23.85	24.90	26.01	25.95	25.58	**26.66**
2	28.27	30.12	30.21	20.47	25.90	25.87	30.08	30.11	29.80	**30.20**
3	28.81	31.19	31.49	20.53	26.00	28.58	31.58	31.61	31.20	**32.25**
4	27.95	29.88	29.86	20.47	25.82	25.67	30.13	30.16	29.84	**30.49**
5	25.03	26.00	26.18	20.52	24.38	25.15	26.44	26.39	25.32	**26.82**
6	26.24	26.84	26.90	20.66	24.65	24.74	27.39	27.30	26.88	**27.98**
7	27.88	30.28	30.40	20.52	25.63	27.69	30.47	30.54	29.70	**30.98**
8	25.05	25.59	25.83	20.57	24.02	25.30	26.71	26.75	25.26	**26.90**
9	28.44	30.75	30.81	20.50	25.94	27.44	30.86	30.92	30.29	**31.49**
10	28.27	30.38	30.57	20.52	25.87	28.42	30.65	30.68	29.95	**31.26**
11	26.95	28.00	28.14	20.52	25.32	24.67	28.19	28.16	27.61	**28.63**
12	28.76	30.87	31.05	20.60	26.01	28.37	30.97	31.06	30.58	**31.48**
13	23.76	23.95	23.99	20.52	23.53	22.76	24.27	24.15	23.52	**24.89**
14	26.02	26.97	27.11	20.51	24.94	25.68	27.20	27.15	26.55	**27.57**
15	28.38	30.15	30.44	20.71	26.06	28.21	30.52	30.60	30.13	**30.81**
16	27.75	28.82	28.87	20.52	25.69	26.66	29.27	29.21	29.02	**29.96**
17	27.90	29.57	29.80	20.56	25.85	28.32	29.78	29.79	29.16	**30.40**
18	25.77	26.40	26.41	20.53	24.74	25.70	26.63	26.56	26.01	**27.22**
19	27.30	28.67	28.81	20.53	25.40	26.52	29.19	29.22	28.67	**29.57**
20	28.96	30.40	30.76	21.44	24.95	25.90	30.79	30.83	29.97	**31.07**
21	26.54	27.53	27.60	20.51	25.06	26.48	27.80	27.75	27.12	**28.34**
22	27.05	28.17	28.27	20.51	25.36	26.60	28.21	28.16	27.81	**28.64**
23	29.14	32.31	32.51	20.54	26.13	23.24	31.89	31.97	31.21	**32.34**
24	25.75	26.41	26.53	20.59	24.55	25.73	27.10	27.03	26.18	**27.59**
Average	27.13	28.54	28.68	20.58	25.24	26.19	28.84	28.83	28.22	**29.31**

average 0.47dB, 0.48dB and 1.09dB improvements over WNNM-1, WNNM-2 and WNNM-3, respectively. In Figures 4.2-4.7, we give the visual comparisons of the denoised images by different methods.

Table 4.2 PSNR(dB) results of different denoising methods on the Kodak PhotoCD dataset.

	$\sigma_r = 30, \sigma_g = 10, \sigma_b = 50$									
Image#	**CBM3D**	**MLP**	**TNRD**	**DnCNN**	**NI**	**NC**	**WNNM-1**	**WNNM-2**	**WNNM-3**	**MC-WNNM**
1	23.38	26.49	26.50	20.21	24.82	23.59	26.40	25.60	24.76	**27.81**
2	25.19	30.94	30.90	20.43	26.82	27.79	30.89	29.75	29.21	**30.96**
3	25.39	32.03	32.09	20.47	27.52	27.41	32.20	31.17	30.39	**32.89**
4	24.96	30.55	30.47	20.34	27.34	27.00	30.74	29.71	29.10	**31.19**
5	23.29	26.65	26.73	20.34	25.72	26.67	26.74	25.98	24.68	**27.60**
6	24.09	27.76	27.70	20.45	26.10	26.12	27.85	26.96	26.01	**29.15**
7	24.89	30.70	30.72	20.40	27.17	28.07	30.91	29.94	28.87	**31.37**
8	23.30	26.12	26.27	20.32	25.59	26.11	26.87	26.33	24.74	**27.44**
9	25.20	31.35	31.31	20.36	27.74	28.33	31.30	30.45	29.44	**32.08**
10	25.13	31.01	31.05	20.38	27.60	28.53	31.12	30.17	29.21	**31.83**
11	24.54	28.79	28.82	20.40	26.72	24.40	28.73	27.79	26.94	**29.60**
12	25.43	31.60	31.60	20.44	27.82	29.01	31.59	30.62	29.91	**32.11**
13	22.50	24.71	24.73	20.17	24.96	23.36	24.70	23.85	22.86	**25.96**
14	23.91	27.69	27.72	20.34	26.26	23.08	27.62	26.81	25.91	**28.57**
15	25.45	31.09	31.05	20.68	27.36	28.49	31.29	30.21	29.46	**31.39**
16	24.89	29.79	29.73	20.39	27.35	27.10	29.84	28.85	28.13	**31.10**
17	25.12	30.26	30.24	20.52	27.15	27.54	30.11	29.35	28.43	**31.08**
18	23.83	27.26	27.26	20.39	26.05	26.15	27.32	26.18	25.28	**28.32**
19	24.63	29.40	29.39	20.39	27.06	27.41	29.78	28.87	28.05	**30.53**
20	26.43	31.16	31.27	21.39	26.43	26.92	31.25	30.43	29.41	**31.55**
21	24.24	28.26	28.27	20.33	26.66	27.18	28.22	27.45	26.40	**29.29**
22	24.51	29.03	29.06	20.33	26.83	27.64	29.02	27.81	27.18	**29.57**
23	25.55	32.87	32.75	20.46	27.60	23.75	32.58	31.46	30.50	**32.34**
24	23.85	27.06	27.13	20.37	25.86	27.05	27.50	26.63	25.55	**28.32**
Average	24.57	29.27	29.28	20.43	26.69	26.61	29.36	28.43	27.52	**30.09**

4.3.3 Experiments on Real-world Noisy Images

We evaluate the proposed method on two real-world noisy color image datasets, where the images were captured under indoor or outdoor lighting conditions by different types of cameras and camera settings. For WNNM-3 and MC-WNNM, the initial penalty parameter is set as $\rho_0 = 8$ and $\rho_0 = 6$, respectively. The number of iterations in Algorithm 2 is set as $K_2 = 2$.

Table 4.3 PSNR(dB) results of different denoising methods on the Kodak PhotoCD dataset.

	$\sigma_r = 5, \sigma_g = 30, \sigma_b = 15$									
Image#	**CBM3D**	**MLP**	**TNRD**	**DnCNN**	**NI**	**NC**	**WNNM-1**	**WNNM-2**	**WNNM-3**	**MC-WNNM**
1	27.25	28.06	28.62	24.99	25.00	29.55	28.16	27.95	28.15	**30.20**
2	29.70	31.30	32.70	25.09	27.80	29.69	32.54	31.60	31.73	**34.04**
3	30.34	31.98	34.07	25.37	28.02	31.93	33.91	33.68	33.52	**35.55**
4	29.47	31.10	32.56	25.14	27.70	32.56	32.68	31.85	31.90	**34.06**
5	27.31	28.59	29.35	25.18	26.14	30.00	28.83	29.00	28.91	**30.05**
6	28.20	29.10	29.90	25.27	26.15	28.81	29.55	29.46	29.62	**31.64**
7	29.73	31.60	33.46	25.40	27.22	31.63	33.09	33.29	32.86	**34.24**
8	27.47	28.16	28.91	25.12	25.34	30.16	29.15	29.24	29.03	**29.91**
9	30.07	31.63	33.55	25.33	27.86	31.54	33.19	33.20	32.95	**34.53**
10	29.96	31.37	33.20	25.33	27.74	33.44	32.98	33.02	32.74	**34.38**
11	28.73	29.85	30.87	25.23	26.98	30.16	30.45	30.14	30.21	**32.10**
12	30.20	31.50	33.31	25.40	27.97	31.69	33.22	32.71	32.65	**34.64**
13	26.18	26.69	26.98	24.81	25.14	27.97	26.49	26.42	26.62	**28.30**
14	27.86	29.07	29.87	25.16	26.67	29.21	29.36	29.14	29.30	**31.18**
15	29.91	31.58	33.13	25.47	28.04	31.17	33.22	32.34	32.36	**34.27**
16	29.29	30.35	31.54	25.26	27.46	32.18	31.34	31.05	31.21	**33.72**
17	29.50	31.09	32.52	25.37	27.81	32.80	32.09	32.00	31.85	**33.61**
18	27.72	28.74	29.36	25.10	26.57	28.63	28.88	28.76	28.89	**30.56**
19	28.98	30.18	31.35	25.24	27.25	29.79	31.34	30.77	30.95	**33.10**
20	30.63	31.78	33.27	26.08	27.89	29.52	33.00	32.55	32.58	**34.18**
21	28.50	29.58	30.54	25.18	26.86	30.99	30.02	30.03	30.03	**31.69**
22	28.61	29.78	30.82	25.14	27.19	30.50	30.47	29.82	30.10	**32.08**
23	30.60	32.66	35.06	25.33	28.17	32.82	34.72	34.37	33.94	**35.16**
24	27.97	28.81	29.61	25.12	26.01	30.75	29.47	29.35	29.39	**30.93**
Average	28.92	30.19	31.44	25.26	27.04	30.73	31.17	30.91	30.89	**32.67**

The first dataset is provided in [50], which includes 20 real-world noisy images collected under uncontrolled outdoor environment. Since there is no "ground truth" of the noisy images, the objective measures such as PSNR cannot be computed on this dataset.

The second dataset is provided in [68], which includes noisy images of 11 static scenes. The noisy images were collected under controlled indoor environment. Each scene was shot 500 times under the same camera and camera setting. The mean image of the 500 shots is

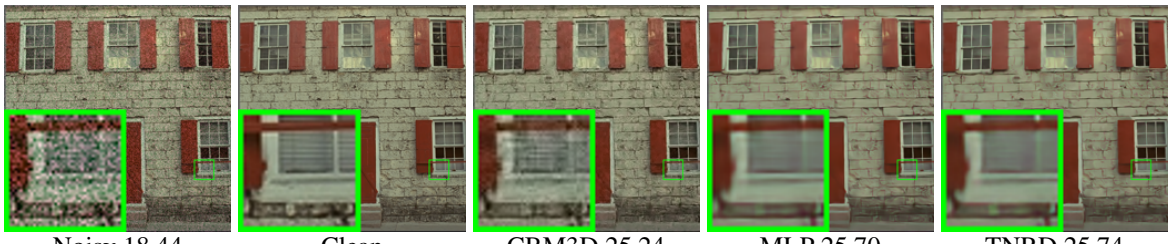

Figure 4.2 Denoised images and PSNR (dB) results of different methods on the image "kodim01" degraded by AWGN with different standard deviations of $\sigma_r = 40, \sigma_g = 20, \sigma_b = 30$ on R, G, B channels, respectively. The images are better to be zoomed in on screen.

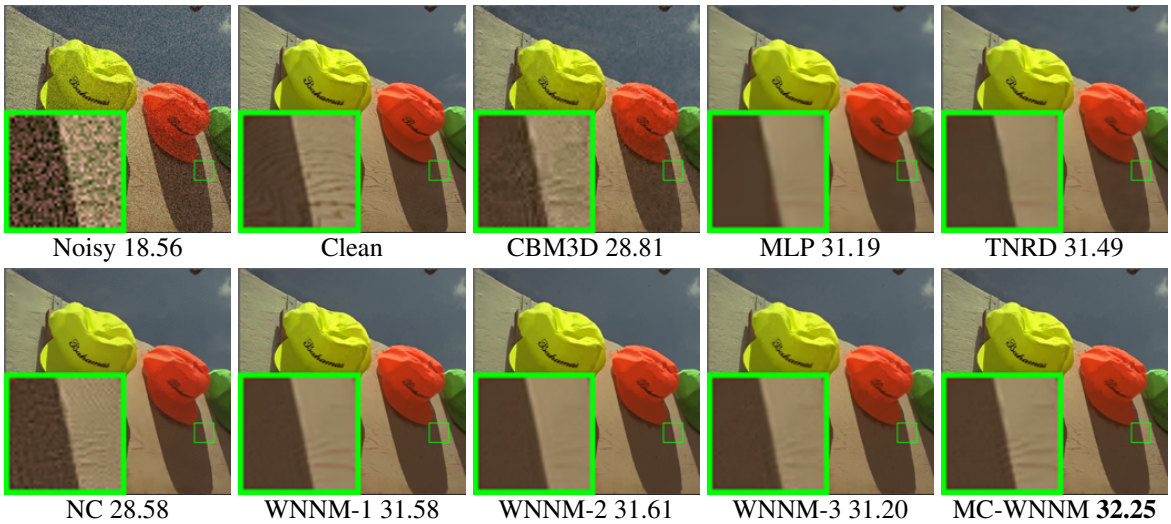

Figure 4.3 Denoised images and PSNR (dB) results of different methods on the image "kodim03" degraded by AWGN with different standard deviations of $\sigma_r = 40, \sigma_g = 20, \sigma_b = 30$ on R, G, B channels, respectively. The images are better to be zoomed in on screen.

roughly taken as the "ground truth", with which the PSNR can be computed. Since the image size is very large (about 7000×5000) and the 11 scenes share repetitive contents, the authors of [68] cropped 15 smaller images of size 512×512 for experiments. Fig. 4.2 shows the contents

Figure 4.4 Denoised images and PSNR (dB) results of different methods on the image "kodim17" degraded by AWGN with different standard deviations of $\sigma_r = 30, \sigma_g = 10, \sigma_b = 20$ on R, G, B channels, respectively. The images are better to be zoomed in on screen.

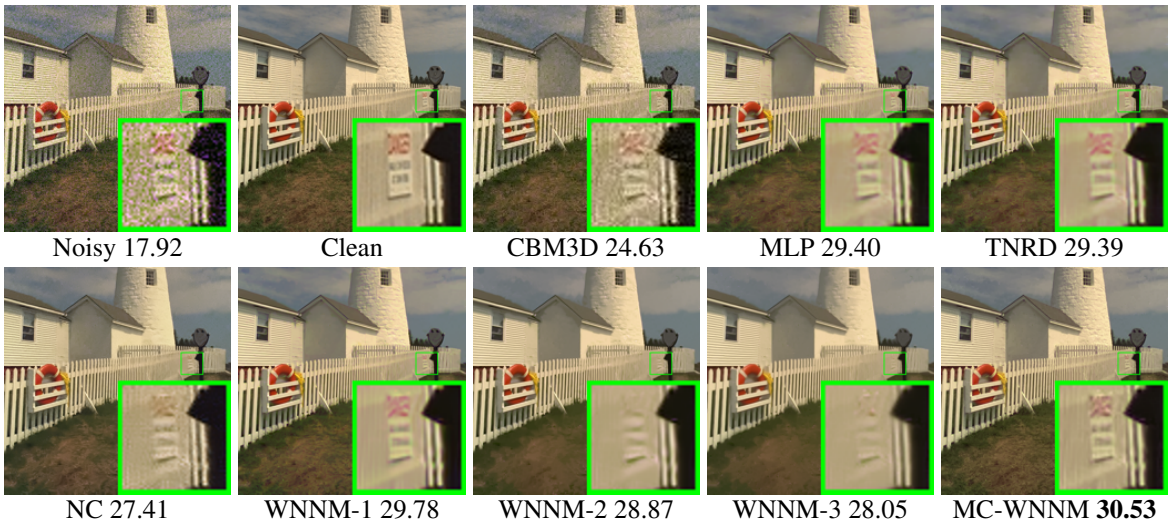

Figure 4.5 Denoised images and PSNR (dB) results of different methods on the image "kodim19" degraded by AWGN with different standard deviations of $\sigma_r = 30, \sigma_g = 10, \sigma_b = 50$ on R, G, B channels, respectively. The images are better to be zoomed in on screen.

of these images. Quantitative comparisons on the 15 cropped images will be reported.

Results on Dataset [50]. Since there is no "ground truth" for the real-world noisy images in dataset [50], we only compare the visual quality of the denoised images by the compared

Figure 4.6 Denoised images and PSNR (dB) results of different methods on the image "kodim09" degraded by AWGN with different standard deviations of $\sigma_r = 5, \sigma_g = 30, \sigma_b = 15$ on R, G, B channels, respectively. The images are better to be zoomed in on screen.

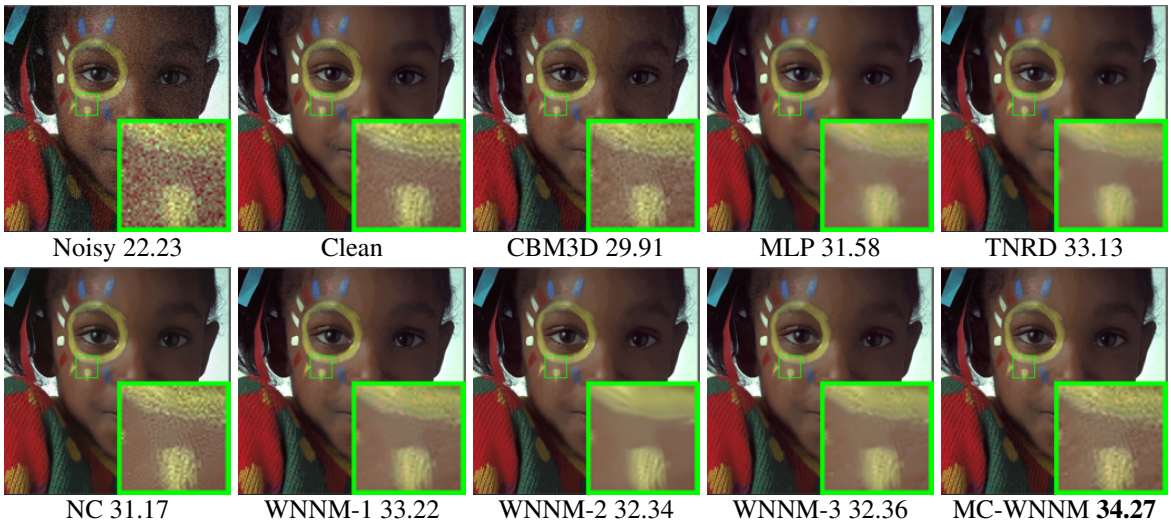

Figure 4.7 Denoised images and PSNR (dB) results of different methods on the image "kodim15" degraded by AWGN with different standard deviations of $\sigma_r = 5, \sigma_g = 30, \sigma_b = 15$ on R, G, B channels, respectively. The images are better to be zoomed in on screen.

methods. (Note that the method CC [68] is not compared here since its code is not publically available.)

Fig. 4.8 shows the denoised images of "Dog" by the competing methods. It can be seen

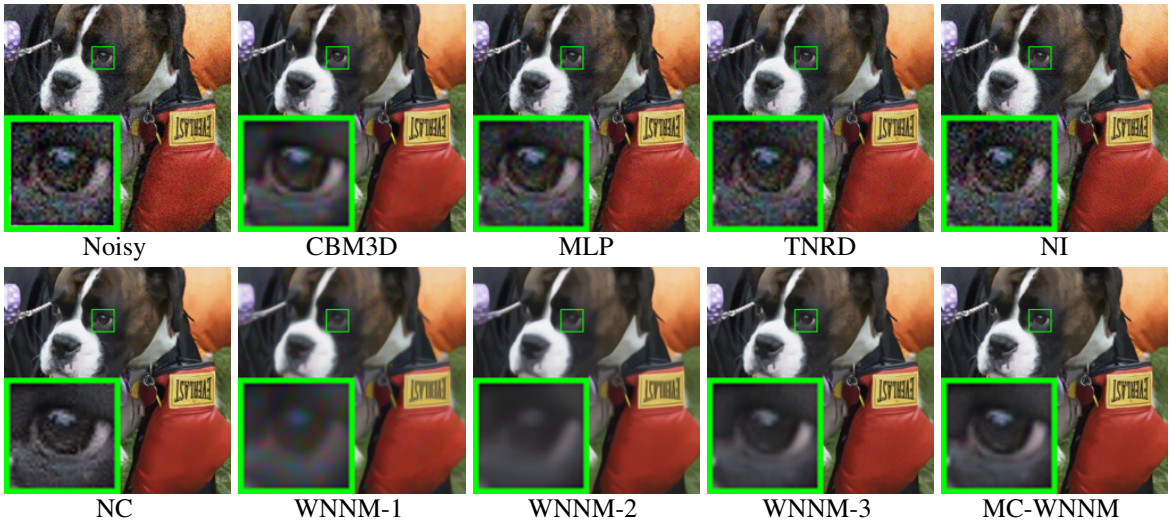

Figure 4.8 Denoised images of the real-world noisy image "Dog" [50] by different methods. The images are better to be zoomed in on screen.

that CBM3D, MLP, TRND and WNNM-1 tend to generate some noise caused color artifacts. Besides, WNNM-2 and WNNM-3 tend to over-smooth much the image. These results demonstrate that for color image denoising, neither processing each channel separately nor processing the three channels jointly but ignoring their noise difference is an effective solution. Though NC and NI methods are specifically developed for real color image denoising, their performance is not very satisfactory. In comparison, the proposed MC-WNNM recovers much better the structures and textures (such as the eye area) than the other competing methods. More visual comparisons on this dataset can be found in the Figures 4.9 to 4.12.

Results on Dataset [68]. As described at the beginning of Section 4.3, there is a mean image for each noisy image in dataset [68], and those mean images can be roughly taken as "ground truth" for quantitative evaluation of denoising algorithms.

The results on PSNR and averaged computational time by competing methods (including CC [68] whose results are copied from [68]) are listed in Table 4.4. For methods MLP [13] and TNRD [19], both of them achieve the best results when setting the noise level of the trained models at $\sigma = 10$. The highest PSNR results are highlighted in bold. On average, MC-WNNM achieves 1.94dB, 0.44dB, 0.59dB improvements over the three WNNM methods,

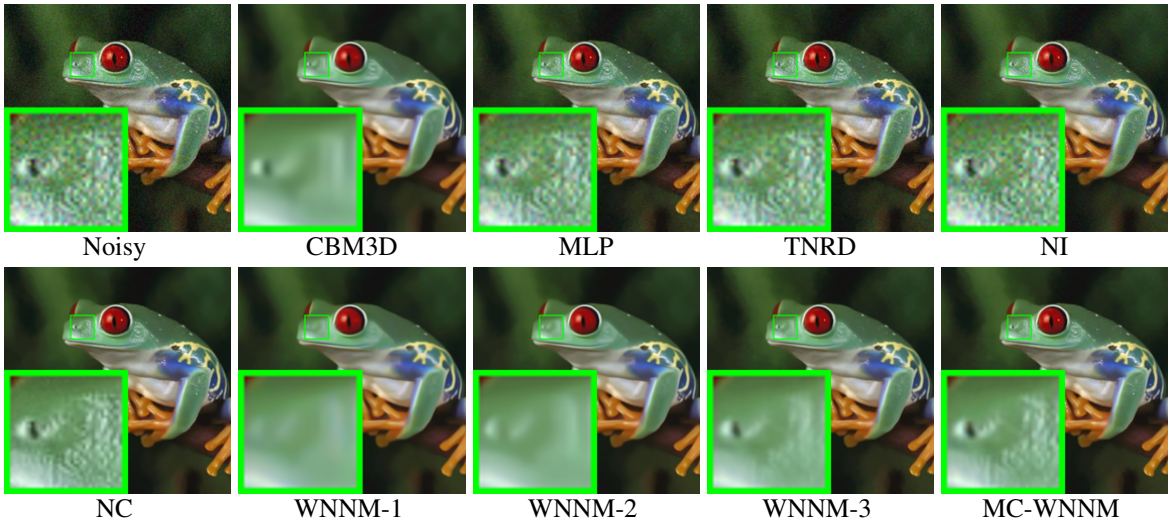

Figure 4.9 Denoised images of the real-world noisy image "Frog" [50] by different methods. The images are better to be zoomed in on screen.

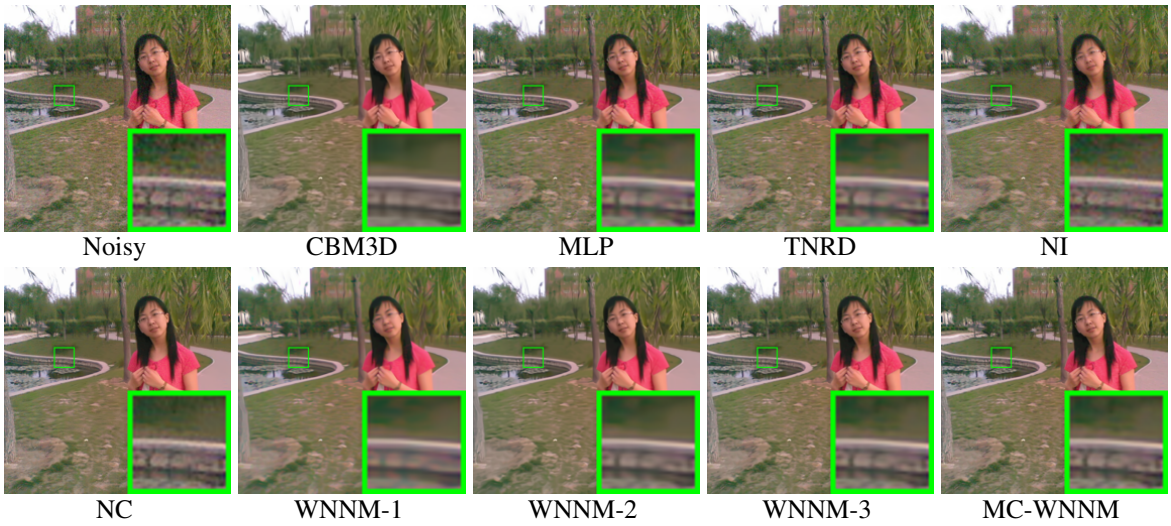

Figure 4.10 Denoised images of the real-world noisy image "Girl" [50] by different methods. The images are better to be zoomed in on screen.

and significantly outperforms other competing method, including CC [68]. On 10 out of the 15 images, the proposed MC-WNNM achieves the highest PSNR values, while WNNM-2 achieves the highest PSNR results on 3 of 15 images. It should be noted that in the CC method [68], a specific model is trained for each camera and camera setting, while the other methods uses the same model for all cases.

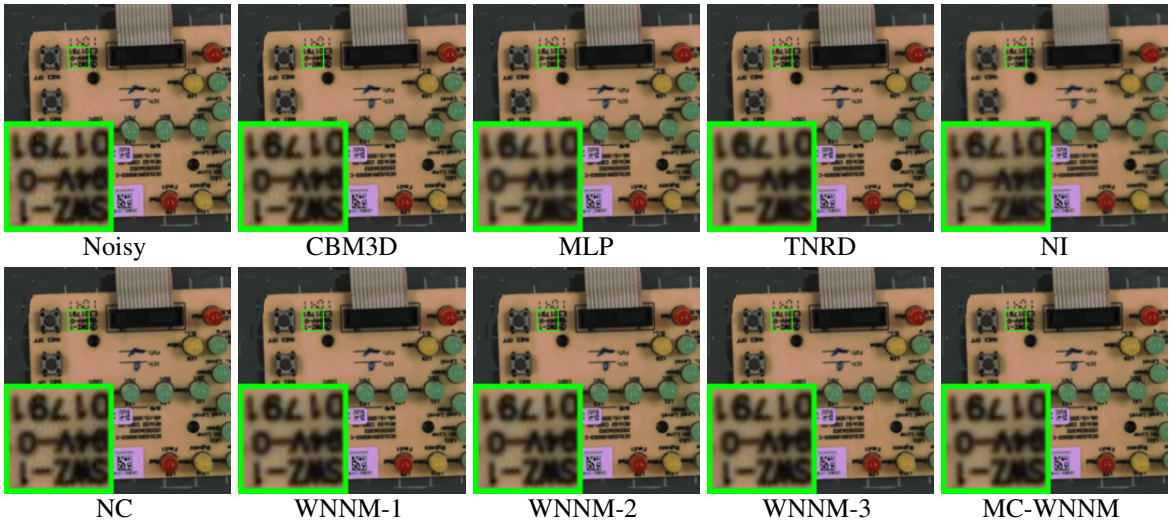

Figure 4.11 Denoised images of the real-world noisy image "Circuit" [50] by different methods. The images are better to be zoomed in on screen.

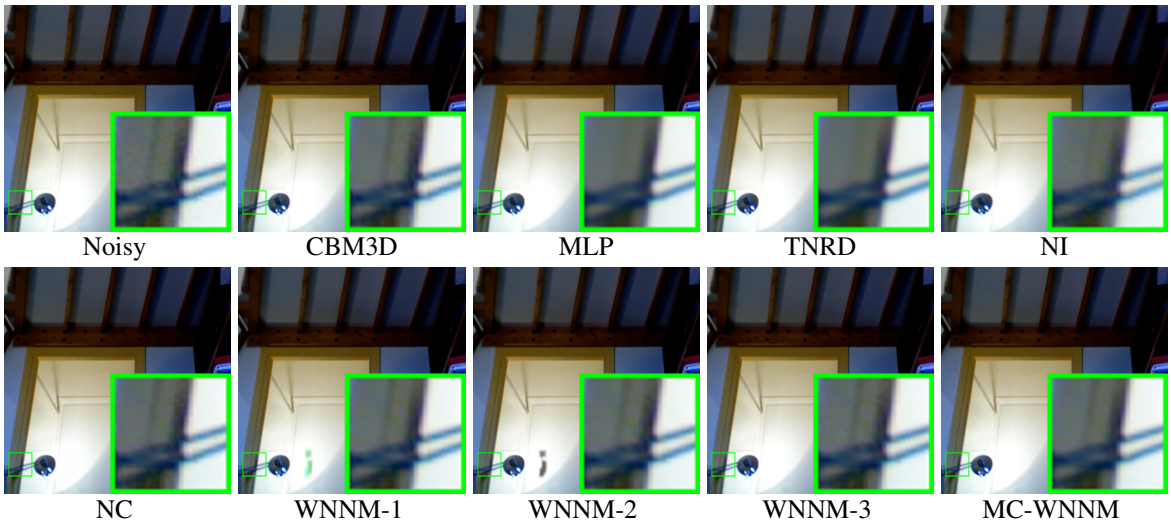

Figure 4.12 Denoised images of the real-world noisy image "Room" [50] by different methods. The images are better to be zoomed in on screen.

Fig. 4.13 shows the denoised images of a scene captured by Canon 5D Mark 3 ISO=3200. (The results of DnCNN and WNNM-1 are not shown here due to the limit of space.) We can see that CBM3D, NI, NC and CC will either remain noise or generate color artifacts, while TNRD, WNNM-2 and WNNM-3 over-smooth the image. In addition, due to treating each channel equally, both the denoised images (Fig. 4.13(g) and Fig. 4.13(h)) by WNNM-2

Table 4.4 PSNR(dB) results and averaged computational time (s) of different methods on 15 cropped real-world noisy images used in [68].

Camera Settings	CBM3D	MLP	TNRD	DnCNN	NI	NC	CC	WNNM-1	WNNM-2	WNNM-3	MC-WNNM
	39.76	39.00	39.51	37.26	35.68	36.20	38.37	37.51	39.74	39.98	**41.13**
Canon 5D	36.40	36.34	36.47	34.13	34.03	34.35	35.37	33.86	35.12	36.65	**37.28**
ISO = 3200	36.37	36.33	36.45	34.09	32.63	33.10	34.91	31.43	33.14	34.63	**36.52**
	34.18	34.70	34.79	33.62	31.78	32.28	34.98	33.46	35.08	35.08	**35.53**
Nikon D600	35.07	36.20	36.37	34.48	35.16	35.34	35.95	36.09	36.42	36.84	**37.02**
ISO = 3200	37.13	39.33	39.49	35.41	39.98	40.51	**41.15**	39.86	40.78	39.24	39.56
	36.81	37.95	38.11	35.79	34.84	35.09	37.99	36.35	38.28	38.61	**39.26**
Nikon D800	37.76	40.23	40.52	36.08	38.42	38.65	40.36	39.99	41.24	40.81	**41.43**
ISO = 1600	37.51	37.94	38.17	35.48	35.79	35.85	38.30	37.15	38.04	38.96	**39.55**
	35.05	37.55	37.69	34.08	38.36	38.56	39.01	38.60	**39.93**	37.97	38.91
Nikon D800	34.07	35.91	35.90	33.70	35.53	35.76	36.75	36.04	37.32	37.30	**37.41**
ISO = 3200	34.42	38.15	38.21	33.31	40.05	40.59	39.06	39.73	**41.52**	38.68	39.39
	31.13	32.69	32.81	29.83	34.08	34.25	34.61	33.29	**35.20**	34.57	34.80
Nikon D800	31.22	32.33	32.33	30.55	32.13	32.38	33.21	31.16	33.61	33.43	**33.95**
ISO = 6400	30.97	32.29	32.29	30.09	31.52	31.76	33.22	31.98	33.62	**34.02**	33.94
Average	35.19	36.46	36.61	33.86	35.33	35.65	36.88	35.77	37.27	37.12	**37.71**
Time	7.8	20.4	6.7	180.3	**0.9**	18.2	NA	689.1	465.3	198.6	202.9

and WNNM-3 have chromatic aberration compared to the mean image (Fig. 4.13(j)). MC-WNNM results in much better visual quality than other methods. More visual comparisons can be found in the Figures 4.14 to 4.17.

Comparison on speed. We compare the average computational time (second) of different methods (except CC), which is shown in Table 4.4. All experiments are run under the Matlab environment on a machine with 3.5GHz CPU and 32GB RAM. The fastest result is highlighted in bold. One can see that Neat Image (NI) is the fastest and costs about 0.9 second, while the proposed MC-WNNM needs 202.9 seconds. Noted that CBM3D, TNRD, and NC are implemented with compiled C++ mex-function and with parallelization, while WNNM, MLP, DnCNN, and the proposed MC-WNNM are implemented purely in Matlab.

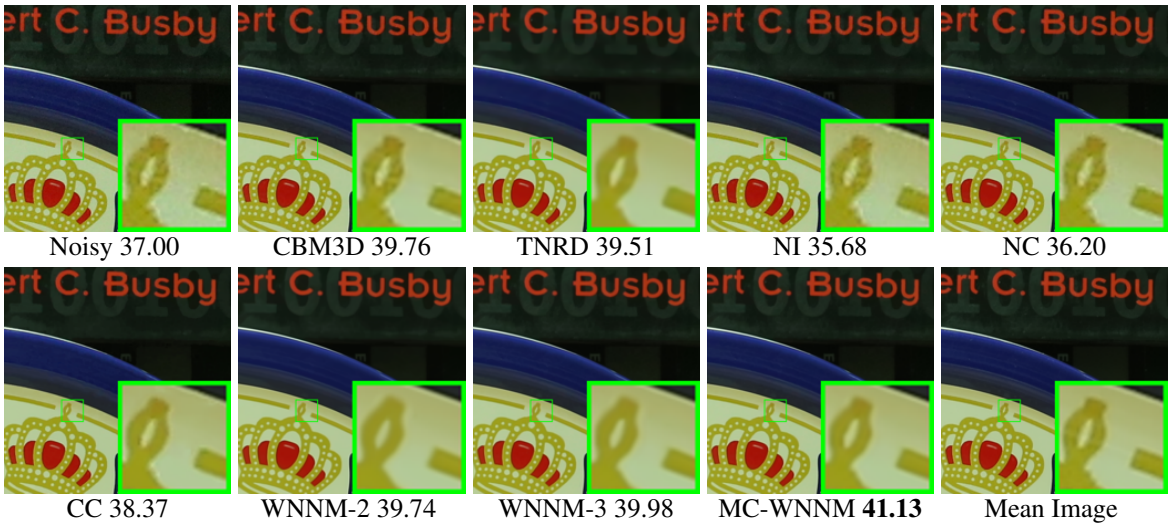

Figure 4.13 Denoised images and PSNR (dB) results of a region cropped from the real-world noisy image "Canon 5D Mark 3 ISO=3200 1" [68] by different methods. The images are better to be zoomed in on screen.

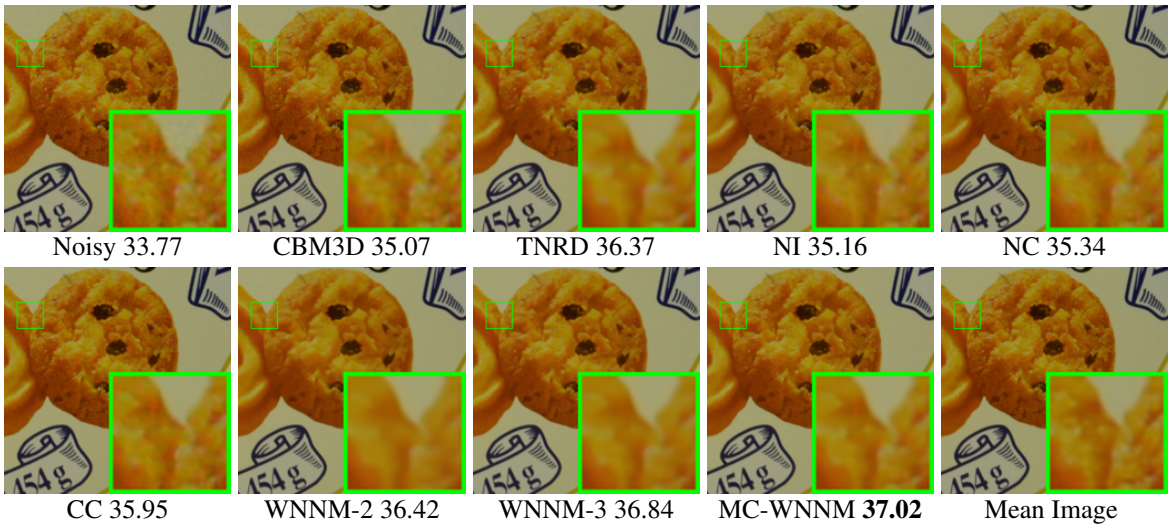

Figure 4.14 Denoised images and PSNR (dB) results of a region cropped from the real-world noisy image "Nikon D600 ISO=3200 2" [68] by different methods. The images are better to be zoomed in on screen.

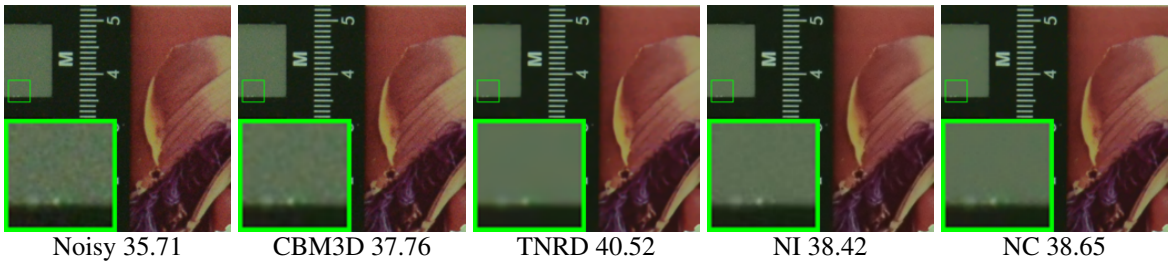

Figure 4.15 Denoised images and PSNR (dB) results of a region cropped from the real-world noisy image "Nikon D800 ISO=1600 2" [68] by different methods. The images are better to be zoomed in on screen.

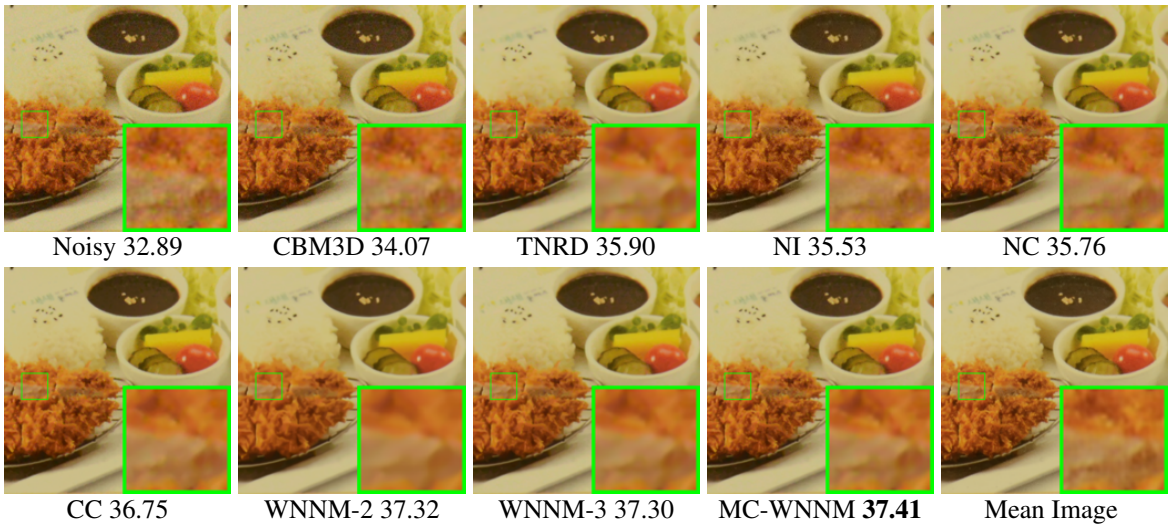

Figure 4.16 Denoised images and PSNR (dB) results of a region cropped from the real-world noisy image "Nikon D800 ISO=3200 2" [68] by different methods. The images are better to be zoomed in on screen.

4.4 Conclusion

The real-world noisy color images have different noise statistics across the R, G, B channels due to digital camera pipelines in CCD or CMOS sensors. This makes the real color

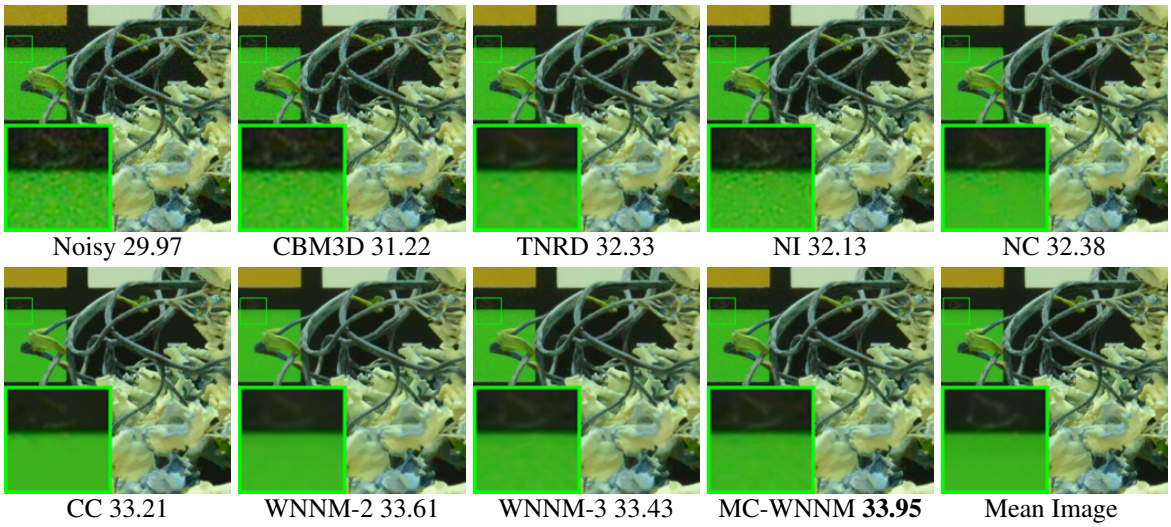

Figure 4.17 Denoised images and PSNR (dB) results of a region cropped from the real-world noisy image "Nikon D800 ISO=6400 2" [68] by different methods. The images are better to be zoomed in on screen.

image denoising problem more challenging than grayscale image denoising. In this work, we proposed a novel multi-channel (MC) denoising model to effectively exploit the redundancy across color channels while differentiating their different noise statistics. Specifically, we introduced a weight matrix to the data term in the RGB channel concatenated weighted nuclear norm minimization (WNNM) model, and the resulting MC-WNNM model can process adaptively the different noise in RGB channels. We solved the MC-WNNM model via an ADMM algorithm. Extensive experiments on synthetic and real datasets demonstrated that the proposed MC-WNNM method outperforms significantly the other competing denoising methods.

The proposed MC-WNNM model can be extended in at least two directions. Firstly, it is worthy to investigate new weight matrix beyond the diagonal form, such as the correlation form [39], to further improve the color image denoising performance. Secondly, the proposed MC-WNNM model can be extended for hyperspectral image analysis, which may contain hundreds of bands with complex noise statistics.

Chapter 5

A Trilateral Weighted Sparse Coding Scheme for Real-world Image Denoising

5.1 Introduction

Image denoising aims to recover the clean image $\boldsymbol{x}$ from its noisy observation $\boldsymbol{y} = \boldsymbol{x} + \boldsymbol{n}$, where $\boldsymbol{n}$ is the corrupted noise. The denoising problem has been extensively studied in computer vision and machine learning, and numerous statistical image modeling and learning methods have been proposed in the past decades [2, 13, 19, 21, 22, 24, 30, 36, 51, 53, 58, 68, 83, 103, 107, 110, 111]. Most of the existing methods [13, 19, 21, 22, 24, 30, 36, 58, 83, 103, 107, 111] focus on additive white Gaussian noise (AWGN), which can be categorized into dictionary learning based methods [30], nonlocal self-similarity based methods [21, 22, 24, 36, 58], sparsity based methods [21, 22, 24, 30, 58], low-rankness based methods [36], generative learning based methods [103, 111], and discriminative learning based methods [13, 19, 83, 107]. However, the real-world noise in real-world images is much more complex than AWGN [68] and varies with different cameras and camera settings (such as ISO, shutter speed, and aperture, etc.). Though have shown promising performance on AWGN noise removal, the

above methods [13, 19, 21, 22, 24, 30, 36, 58, 83, 103, 107, 111] will become much less effective when dealing with complex real-world noise.

In the past decade, several denoising methods for real-world noisy images have been developed [2, 21, 51, 53, 68, 110]. Among them, CBM3D [21] is a representative method which applies the benchmark BM3D method [22] to each channel of the luminance-chrominance space of the noisy image. Liu et al. [53] proposed to estimate the noise via a "noise level function" and remove the noise for each channel of the real image. However, processing each channel separately would often achieve unsatisfactory performance and generate artifacts. The methods [51, 110] perform image denoising by concatenating the patches of RGB channels into a vector. However, the concatenation does not consider the different noise statistics among different channels. The method in [68] models the noise in a noisy image as multivariate Gaussian and performs denoising by the Non-local Bayes filter [51]. The commercial software Neat Image [2] estimates the global noise parameters from a flat region of the given noisy image and filters the noise accordingly. However, both the two methods [2, 68] ignore the local statistical property of the noise which is signal dependent and varies in different pixels. By far, real-world image denoising remains a challenging problem in low level vision.

Sparse coding (SC) [88] has been well studied in many computer vision and learning problems [96, 104], including image denoising [24, 30, 58]. Usually, the SC models employ an ℓ_2 (or Frobenious) norm to describe the residual in the data term, and minimize an energy function $\min_{\alpha} \|\boldsymbol{y} - \boldsymbol{D}\boldsymbol{\alpha}\|_2^2 + \mathcal{R}(\boldsymbol{\alpha})$, where $\boldsymbol{D}$ is the dictionary, $\boldsymbol{\alpha}$ is the sparse coefficients vector of signal $\boldsymbol{y}$, and $\mathcal{R}(\boldsymbol{\alpha})$ is usually the ℓ_0 or ℓ_1 norm of $\boldsymbol{\alpha}$ to enforce sparse regularization. Some representative SC based image denoising methods include K-SVD [30], LSSC [58], and NCSR [24]. Though being effective on dealing with AWGN, SC based denoising methods are essentially limited by the ℓ_2 (or Frobenious) norm based data term, which actually assumes white Gaussian noise and is not able to characterize the complex real-world noise. Recently, there are several methods [108, 110] modeling complex noise via mixture of Gaus-

sian distribution. However, these methods [108, 110] are time-consuming due to employing variational Bayesian inference techniques.

In this work, we propose to lift the SC model to a robust denoiser for real noisy images by utilizing the channel-wise statistics and locally signal dependent property of the real-world noise. Specifically, we propose a trilateral weighted sparse coding (TWSC) scheme for real-world image denoising. Two weight matrices are introduced into the data term of the SC model to characterize the real-world noise property, and another weight matrix is introduced into the regularization term to characterize the sparsity priors of natural images. To solve the proposed TWSC model, we reformulate it into a linear equality-constrained optimization program, which can be minimized under the alternating direction method of multipliers [11] framework. Theoretical analysis on the existence and uniqueness of the solution of the TWSC model, as well as the convergence of the algorithm, are presented. Experiments on real noisy image datasets demonstrate that the proposed TWSC method achieves much more robust real-world denoising performance than the existing methods.

5.2 The Proposed Realistic Image Denoising Algorithm

5.2.1 The Trilateral Weighted Sparse Coding Model

Denote by $\boldsymbol{y}_c = \boldsymbol{x}_c + \boldsymbol{n}_c$ the noisy observation of the clean color image $\boldsymbol{x}_c$, where $c \in \{r, g, b\}$ is the index of R, G, B channels and $\boldsymbol{n}_c$ is the noise in channel c. A local patch of size $p \times p \times 3$ is extracted from the image and stretched to a vector, denoted by $\boldsymbol{y} = [\boldsymbol{y}_r^\top \ \boldsymbol{y}_g^\top \ \boldsymbol{y}_b^\top]^\top \in \mathbb{R}^{3p^2}$, where $\boldsymbol{y}_c \in \mathbb{R}^{p^2}$ is the corresponding patch in channel c. For each local patch $\boldsymbol{y}$, we search the M most similar patches to it (including $\boldsymbol{y}$ itself) by Euclidean distance in a local window around it. By stacking the M similar patches column by column, we form a noisy patch matrix $\boldsymbol{Y} = \boldsymbol{X} + \boldsymbol{N} \in \mathbb{R}^{3p^2 \times M}$, where $\boldsymbol{X}$ and $\boldsymbol{N}$ are the corresponding clean and noise patch matrices, respectively. The noisy patch matrix can be written as $\boldsymbol{Y} = [\boldsymbol{Y}_r^\top \ \boldsymbol{Y}_g^\top \ \boldsymbol{Y}_b^\top]^\top$, where $\boldsymbol{Y}_c$ is the

sub-matrix of channel c.

Suppose that we have a dictionary $\boldsymbol{D} = [\boldsymbol{D}_r^\top \ \boldsymbol{D}_g^\top \ \boldsymbol{D}_b^\top]^\top$, where $\boldsymbol{D}_c$ is the sub-dictionary corresponding to channel c. Under the sparse coding (SC) framework [88], the sparse code matrix of $\boldsymbol{Y}$ over $\boldsymbol{D}$ can be obtained by

$$\hat{\boldsymbol{C}} = \arg\min_{\boldsymbol{C}} \|\boldsymbol{Y} - \boldsymbol{D}\boldsymbol{C}\|_F^2 + \lambda\|\boldsymbol{C}\|_1, \tag{5.1}$$

where λ is the regularization parameter. Once $\hat{\boldsymbol{C}}$ is computed, the latent clean patch matrix $\hat{\boldsymbol{X}}$ can be estimated as $\hat{\boldsymbol{X}} = \boldsymbol{D}\hat{\boldsymbol{C}}$. In this work, we use an adaptive dictionary to the given data matrix $\boldsymbol{Y}$. The dictionary $\boldsymbol{D}$ can be obtained by applying SVD to $\boldsymbol{Y}$ as

$$\boldsymbol{Y} = \boldsymbol{D}\boldsymbol{S}\boldsymbol{V}^\top. \tag{5.2}$$

Though SC based methods [24, 30, 58] have achieved promising performance in removing additive white Gaussian noise (AWGN), their performance is very limited when dealing with real-world noise in real-world images. The reason is that the real-world noise is non-Gaussian, varies locally and across channels, which cannot be characterized well by the Frobenious norm in model (5.1).

To account for the varying statistics of the real-world noise in different channels and different patches, we introduce two weight matrices $\boldsymbol{W}_1 \in \mathbb{R}^{3p^2\times 3p^2}$ and $\boldsymbol{W}_2 \in \mathbb{R}^{M\times M}$ to characterize the SC residual ($\boldsymbol{Y}-\boldsymbol{D}\boldsymbol{C}$) in the data term of Eq. (5.1). Besides, to better characterize the sparse priors of the natural images, we introduce a third weight matrix $\boldsymbol{W}_3$, which is related to the distribution of the sparse coefficients matrix $\boldsymbol{C}$, into the regularization term of Eq. (5.1). Finally, the proposed trilateral weighted sparse coding (TWSC) model is formulated as follows:

$$\min_{\boldsymbol{C}} \|\boldsymbol{W}_1(\boldsymbol{Y} - \boldsymbol{D}\boldsymbol{C})\boldsymbol{W}_2\|_F^2 + \|\boldsymbol{W}_3^{-1}\boldsymbol{C}\|_1. \tag{5.3}$$

All the three weight matrices are diagonal matrices and have clear physical meanings. $\boldsymbol{W}_1$ is a block diagonal matrix. Each block of $\boldsymbol{W}_1$ has the same diagonal elements to describe the noise properties in each RGB channel. The real-world noise in a local region could be approximately

modeled as Gaussian [52], and each diagonal element of weight matrix $\boldsymbol{W}_2$ is used to describe the noise variance in each patch $\boldsymbol{y}$. Geometrically speaking, $\boldsymbol{W}_1$ is employed to regularize the row discrepancy of residual matrix $(\boldsymbol{Y} - \boldsymbol{DC})$, while $\boldsymbol{W}_2$ is employed to regularize the column discrepancy of $(\boldsymbol{Y} - \boldsymbol{DC})$. For matrix $\boldsymbol{W}_3$, each diagonal element will be set based on the prior information on $\boldsymbol{C}$. All the three weight matrices $\boldsymbol{W}_1, \boldsymbol{W}_2, \boldsymbol{W}_3$ can be determined under the *maximum a-posterior* (MAP) estimation framework, as described in detail in the next subsection.

5.2.2 The Setting of Weight Matrices

We determine the weight matrices $\boldsymbol{W}_1, \boldsymbol{W}_2, \boldsymbol{W}_3$ by employing the MAP estimation:

$$\hat{\boldsymbol{C}} = \arg\max_{\boldsymbol{C}} \ln P(\boldsymbol{C}|\boldsymbol{Y}) = \arg\max_{\boldsymbol{C}} \{\ln P(\boldsymbol{Y}|\boldsymbol{C}) + \ln P(\boldsymbol{C})\}. \tag{5.4}$$

The log-likelihood term $\ln P(\boldsymbol{Y}|\boldsymbol{C})$ is characterized by the statistics of noise or residual. According to [52], it can be assumed that the noise is independently and identically distributed (i.i.d.) in each channel and each patch with Gaussian distribution. We denote by σ_c the standard deviation (std) of noise in channel c, $c \in \{r, g, b\}$, and denote by σ_m the std of noise in a color patch m, $m \in \{1, ..., M\}$. Denote by σ_{cm} the noise std of sub-patch m in channel c. Then we have:

$$P(\boldsymbol{Y}|\boldsymbol{C}) = \prod\nolimits_{c\in\{r,g,b\}} \prod\nolimits_{m=1}^{M} (\pi\sigma_{cm})^{-p^2} \exp(-\sigma_{cm}^{-2} \|\boldsymbol{y}_{cm} - \boldsymbol{D}_c \boldsymbol{c}_m\|_2^2), \tag{5.5}$$

where $\boldsymbol{y}_{cm}, \boldsymbol{c}_m$ are the mth column of the matrices $\boldsymbol{Y}_c$ and $\boldsymbol{C}$, respectively. From the perspective of statistics [63], the set of $\{\sigma_{cm}\}$ can be viewed as a $3 \times M$ contingency table created by two variables σ_c and σ_m, and their relationship could be modeled by a log-linear model $\sigma_{cm} = \sigma_c^{l_1} \sigma_m^{l_2}$, where $l_1 + l_2 = 1$. The estimation of $\{\sigma_{cm}\}$ can be reduced to the estimation of $\{\sigma_c\}$ and $\{\sigma_m\}$. Specifically, the noise std σ_c of channel c can be estimated by some noise estimation methods [18]. The noise std for the mth patch of $\boldsymbol{Y}$ can be initialized as

$\sigma_m = \sigma \triangleq \sqrt{(\sigma_r^2 + \sigma_g^2 + \sigma_b^2)/3}$ and updated as $\sigma_m = \sqrt{\sigma^2 - \|\boldsymbol{y}_m - \boldsymbol{x}_m\|_2^2}$, where $\boldsymbol{y}_m$ is the mth image patch in $\boldsymbol{Y}$, and $\boldsymbol{x}_m = \boldsymbol{D}\boldsymbol{c}_m$ is the mth image patch recovered in previous iteration (refer to Algorithm 2 in next section).

We assume that each column $\boldsymbol{c}_m$ of coefficients matrix $\boldsymbol{C}$ follows i.i.d. Laplacian distribution. Specifically, for each entry $\boldsymbol{c}_m^i$, which is the coding coefficient of the mth patch over the ith atom of dictionary $\boldsymbol{D}$, we assume that it follows distribution $(2\boldsymbol{S}_i)^{-1}\exp(-\boldsymbol{S}_i^{-1}|\boldsymbol{c}_m^i|)$, where $\boldsymbol{S}_i$ is the ith element of the diagonal singular value matrix $\boldsymbol{S}$ in Eq. (5.2). Note that we set the scale factor of the distribution as the inverse of the ith singular value $\boldsymbol{S}_i$. This is because the larger the singular value $\boldsymbol{S}_i$ is, the more important the ith singular vector in $\boldsymbol{D}$ should be, and hence the distribution of the coding coefficients over this singular vector should have stronger regularization with less sparse distribution. The prior term in Eq. (5.4) becomes

$$P(\boldsymbol{C}) = \prod_{m=1}^{M}\prod_{i=1}^{3p^2}(2\boldsymbol{S}_i)^{-1}\exp(-\boldsymbol{S}_i^{-1}|\boldsymbol{c}_m^i|). \tag{5.6}$$

Put (5.6) and (5.5) into (5.4) and consider the log-linear model $\sigma_{cm} = \sigma_c^{l_1}\sigma_m^{l_2}$, we have

$$\begin{aligned}
\hat{\boldsymbol{C}} &= \arg\min_{\boldsymbol{C}} \sum_{c\in\{r,g,b\}}\sum_{m=1}^{M}\sigma_{cm}^{-2}\|(\boldsymbol{y}_{cm} - \boldsymbol{D}_c\boldsymbol{c}_m)\|_2^2 + \sum_{m=1}^{M}\|\boldsymbol{S}^{-1}\boldsymbol{c}_m\|_1 \\
&= \arg\min_{\boldsymbol{C}} \sum_{c\in\{r,g,b\}}\sigma_c^{-2l_1}\|(\boldsymbol{Y}_c - \boldsymbol{D}_c\boldsymbol{C})\boldsymbol{W}_2\|_F^2 + \|\boldsymbol{S}^{-1}\boldsymbol{C}\|_1 \\
&= \arg\min_{\boldsymbol{C}} \|\boldsymbol{W}_1(\boldsymbol{Y} - \boldsymbol{D}\boldsymbol{C})\boldsymbol{W}_2\|_F^2 + \|\boldsymbol{W}_3^{-1}\boldsymbol{C}\|_1,
\end{aligned} \tag{5.7}$$

where

$$\boldsymbol{W}_1 = \mathrm{diag}(\sigma_r^{-l_1}\boldsymbol{I}_{p^2}, \sigma_g^{-l_1}\boldsymbol{I}_{p^2}, \sigma_b^{-l_1}\boldsymbol{I}_{p^2}), \boldsymbol{W}_2 = \mathrm{diag}(\sigma_1^{-l_2}, ..., \sigma_M^{-l_2}), \boldsymbol{W}_3 = \boldsymbol{S}, \tag{5.8}$$

and $\boldsymbol{I}_{p^2}$ is the p^2 dimensional identity matrix. We can see that the diagonal elements of $\boldsymbol{W}_1$ and $\boldsymbol{W}_2$ are determined by the noise standard deviation in each channel and each patch, respectively. The stronger the noise in a channel and a patch, the less the contribution that channel and patch will make to the denoising output. In our experiments, we consider $\{\sigma_c\}, \{\sigma_m\}$ of equal importance and empirically set $l_1 = l_2 = 0.5$.

5.2.3 Model Optimization

Letting $\boldsymbol{C}^* = \boldsymbol{W}_3^{-1}\boldsymbol{C}$, we can transfer the weight matrix $\boldsymbol{W}_3$ into the data term of (5.3). Thus, the TWSC model (5.3) is reformulated as

$$\min_{\boldsymbol{C}^*} \|\boldsymbol{W}_1(\boldsymbol{Y} - \boldsymbol{D}\boldsymbol{W}_3\boldsymbol{C}^*)\boldsymbol{W}_2\|_F^2 + \|\boldsymbol{C}^*\|_1. \tag{5.9}$$

To make the notation simple, we remove the superscript $*$ in $\boldsymbol{C}^*$ and still use $\boldsymbol{C}$ in the following development.

Since the problem (5.9) is convex, we can obtain its globally optimal solution. We employ the variable splitting method [29] to solve it. By introducing an augmented variable $\boldsymbol{Z}$, the problem (5.9) is reformulated as a linear equality-constrained problem with two variables $\boldsymbol{C}$ and $\boldsymbol{Z}$:

$$\min_{\boldsymbol{C},\boldsymbol{Z}} \|\boldsymbol{W}_1(\boldsymbol{Y} - \boldsymbol{D}\boldsymbol{W}_3\boldsymbol{C})\boldsymbol{W}_2\|_F^2 + \|\boldsymbol{Z}\|_1 \quad \text{s.t.} \quad \boldsymbol{C} = \boldsymbol{Z}. \tag{5.10}$$

Since the objective function is separable w.r.t. the two variables, the problem (5.10) can be solved under the alternating direction method of multipliers (ADMM) [11] framework. The augmented Lagrangian function is:

$$\mathcal{L}(\boldsymbol{C}, \boldsymbol{Z}, \boldsymbol{\Delta}, \rho) = \|\boldsymbol{W}_1(\boldsymbol{Y} - \boldsymbol{D}\boldsymbol{W}_3\boldsymbol{C})\boldsymbol{W}_2\|_F^2 + \|\boldsymbol{Z}\|_1 + \langle \boldsymbol{\Delta}, \boldsymbol{C} - \boldsymbol{Z}\rangle + \frac{\rho}{2}\|\boldsymbol{C} - \boldsymbol{Z}\|_F^2, \tag{5.11}$$

where $\boldsymbol{\Delta}$ is the augmented Lagrangian multiplier and $\rho > 0$ is the penalty parameter. We initialize the matrix variables $\boldsymbol{C}_0$, $\boldsymbol{Z}_0$, and $\boldsymbol{\Delta}_0$ to be comfortable zero matrix and $\rho_0 > 0$. Denote by $(\boldsymbol{C}_k, \boldsymbol{Z}_k)$ and $\boldsymbol{\Delta}_k$ the optimization variables and Lagrange multiplier at iteration k ($k = 0, 1, 2, ...$), respectively. By taking derivatives of the Lagrangian function $\mathcal{L}$ w.r.t. $\boldsymbol{C}$ and $\boldsymbol{Z}$ and setting the derivatives to be zeros, we can alternatively update the variables as follows:
(1) **Update $\boldsymbol{C}$ by fixing $\boldsymbol{Z}$ and $\boldsymbol{\Delta}$**:

$$\boldsymbol{C}_{k+1} = \arg\min_{\boldsymbol{C}} \|\boldsymbol{W}_1(\boldsymbol{Y} - \boldsymbol{D}\boldsymbol{W}_3\boldsymbol{C})\boldsymbol{W}_2\|_F^2 + \frac{\rho_k}{2}\|\boldsymbol{C} - \boldsymbol{Z}_k + \rho_k^{-1}\boldsymbol{\Delta}_k\|_F^2. \tag{5.12}$$

This is a two-sided weighted least squares regression problem with the solution satisfying that

$$\boldsymbol{A}\boldsymbol{C}_{k+1} + \boldsymbol{C}_{k+1}\boldsymbol{B}_k = \boldsymbol{E}_k, \tag{5.13}$$

where $\boldsymbol{A} = \boldsymbol{W}_3^\top \boldsymbol{D}^\top \boldsymbol{W}_1^\top \boldsymbol{W}_1 \boldsymbol{D} \boldsymbol{W}_3$, $\boldsymbol{B}_k = \frac{\rho_k}{2}(\boldsymbol{W}_2 \boldsymbol{W}_2^\top)^{-1}$, and $\boldsymbol{E}_k = \boldsymbol{W}_3^\top \boldsymbol{D}^\top \boldsymbol{W}_1^\top \boldsymbol{W}_1 \boldsymbol{Y} + (\frac{\rho_k}{2}\boldsymbol{Z}_k - \frac{1}{2}\boldsymbol{\Delta}_k)(\boldsymbol{W}_2 \boldsymbol{W}_2^\top)^{-1}$. Eq. (5.13) is a standard Sylvester equation (SE) which has a unique solution if and only if $\sigma(\boldsymbol{A}) \cap \sigma(-\boldsymbol{B}_k) = \emptyset$, where $\sigma(\boldsymbol{F})$ denotes the spectrum, i.e., the set of eigenvalues, of the matrix $\boldsymbol{F}$ [85]. We can rewrite the SE (5.13) as

$$(\boldsymbol{I}_M \otimes \boldsymbol{A} + \boldsymbol{B}_k^\top \otimes \boldsymbol{I}_{3p^2})\mathrm{vec}(\boldsymbol{C}_{k+1}) = \mathrm{vec}(\boldsymbol{E}_k), \tag{5.14}$$

and the solution $\boldsymbol{C}_{k+1}$ (if existed) can be obtained via $\boldsymbol{C}_{k+1} = \mathrm{vec}^{-1}(\mathrm{vec}(\boldsymbol{C}_{k+1}))$, where $\mathrm{vec}^{-1}(\bullet)$ is the inverse of the vec-operator $\mathrm{vec}(\bullet)$. Detailed theoretical analysis on the existence of the unique solution is given in Section 3.

(2) **Update $\boldsymbol{Z}$ by fixing $\boldsymbol{C}$ and $\boldsymbol{\Delta}$**:

$$\boldsymbol{Z}_{k+1} = \arg\min_{\boldsymbol{Z}} \frac{\rho_k}{2}\|\boldsymbol{Z} - (\boldsymbol{C}_{k+1} + \rho_k^{-1}\boldsymbol{\Delta}_k)\|_F^2 + \|\boldsymbol{Z}\|_1. \tag{5.15}$$

This problem has a closed-form solution as

$$\boldsymbol{Z}_{k+1} = \mathcal{S}_{\rho_k^{-1}}(\boldsymbol{C}_{k+1} + \rho_k^{-1}\boldsymbol{\Delta}_k), \tag{5.16}$$

where $\mathcal{S}_\lambda(x) = \mathrm{sign}(x)\max(x - \lambda, 0)$ is the soft-thresholding operator.

(3) **Update $\boldsymbol{\Delta}$ by fixing $\boldsymbol{X}$ and $\boldsymbol{Z}$**:

$$\boldsymbol{\Delta}_{k+1} = \boldsymbol{\Delta}_k + \rho_k(\boldsymbol{C}_{k+1} - \boldsymbol{Z}_{k+1}). \tag{5.17}$$

(4) **Update** ρ: $\rho_{k+1} = \mu\rho_k$, where $\mu > 1$.

The above alternative updating steps are repeated until the convergence condition is satisfied or the number of iterations exceeds a preset threshold K_1. The ADMM algorithm converges when $\|\boldsymbol{C}_{k+1} - \boldsymbol{Z}_{k+1}\|_F \leq \mathrm{Tol}$, $\|\boldsymbol{C}_{k+1} - \boldsymbol{C}_k\|_F \leq \mathrm{Tol}$, and $\|\boldsymbol{Z}_{k+1} - \boldsymbol{Z}_k\|_F \leq \mathrm{Tol}$ are simultaneously satisfied, where $\mathrm{Tol} > 0$ is a small tolerance number. We summarize the updating procedures in Algorithm 1. The convergence analysis of Algorithm 1 is given in Theorem 5.2.1. Note that here we employ an unbounded sequence of $\{\rho_k\}$, i.e., $\lim_{k\to\infty}\rho_k = +\infty$, to make sure that Algorithm 1 converges. In fact, since the optimization problem (5.10) is convex, it is naturally convergent under the ADMM [11] framework.

5.2.4 Convergence Analysis

Theorem 5.2.1 *Given $\rho_{k+1} = \mu\rho_k$ $(\rho_0 > 0)$ for $k \geq 0$ and $\mu > 1$, the sequences $\{\boldsymbol{C}_k\}$ and $\{\boldsymbol{Z}_k\}$ generated in Algorithm 1 satisfy:*

$$(a)\ \|\boldsymbol{C}_{k+1} - \boldsymbol{Z}_{k+1}\|_F = O(\rho_k^{-1})\ as\ k \to +\infty,\ i.e.,\ \lim_{k\to+\infty} \|\boldsymbol{C}_{k+1} - \boldsymbol{Z}_{k+1}\|_F = 0; \tag{5.18}$$

$$(b)\ If\ \|\boldsymbol{Z}_{k+1} - \boldsymbol{Z}_k\|_F = O(\rho_k^{-1})\ as\ k \to +\infty,\ then\ \lim_{k\to+\infty} \|\boldsymbol{C}_{k+1} - \boldsymbol{C}_k\|_F = 0; \tag{5.19}$$

$$(c)\ If\ \lim_{k\to+\infty} \|\boldsymbol{C}_{k+1} - \boldsymbol{C}_k\|_F = 0,\ then\ \lim_{k\to+\infty} \|\boldsymbol{Z}_{k+1} - \boldsymbol{Z}_k\|_F = 0. \tag{5.20}$$

The proof of Theorem 5.2.1 can be found in the Appendix 8. Though Theorem 5.2.1 could not directly guarantee $\lim_{k\to+\infty} \|\boldsymbol{C}_{k+1} - \boldsymbol{C}_k\|_F = 0$ and $\lim_{k\to+\infty} \|\boldsymbol{Z}_{k+1} - \boldsymbol{Z}_k\|_F = 0$, it is empirically found that both $\|\boldsymbol{C}_{k+1} - \boldsymbol{C}_k\|_F$ and $\|\boldsymbol{Z}_{k+1} - \boldsymbol{Z}_k\|_F$ will approach to 0 simultaneously in all our tests. In Figure 5.1, we can see that the maximal errors in $|\boldsymbol{C}_{k+1} - \boldsymbol{Z}_{k+1}|, |\boldsymbol{C}_{k+1} - \boldsymbol{C}_k|, |\boldsymbol{Z}_{k+1} - \boldsymbol{Z}_k|$ approach to 0 simultaneously in 50 iterations.

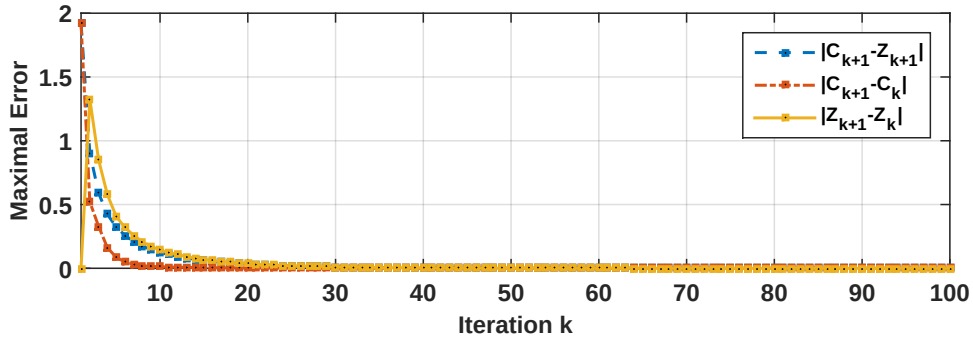

Figure 5.1 The convergence curves of maximal errors in entries of $|\boldsymbol{C}_{k+1} - \boldsymbol{Z}_{k+1}|$ (blue line), $|\boldsymbol{C}_{k+1} - \boldsymbol{C}_k|$ (red line), and $|\boldsymbol{Z}_{k+1} - \boldsymbol{Z}_k|$ (yellow line). The test image is "Barbara".

Algorithm 1: Solve Eq. (5.10) via ADMM

Input: $\boldsymbol{Y}, \boldsymbol{W}_1, \boldsymbol{W}_2, \boldsymbol{W}_3, \mu$, Tol, K_1;

Initialization: $\boldsymbol{C}_0 = \boldsymbol{Z}_0 = \boldsymbol{\Delta}_0 = \boldsymbol{0}$, $\rho_0 > 0$, T = False, $k = 0$;

While (T == false) **do**

1. Update $\boldsymbol{C}_{k+1}$ by solving Eq. (5.13);

2. Update $\boldsymbol{Z}_{k+1}$ by soft thresholding (5.16);

3. Update $\boldsymbol{\Delta}_{k+1}$ as $\boldsymbol{\Delta}_{k+1} = \boldsymbol{\Delta}_k + \rho_k(\boldsymbol{C}_{k+1} - \boldsymbol{Z}_{k+1})$;

4. Update $\rho_{k+1} = \mu\rho_k$;

5. $k \leftarrow k + 1$;

   if (Converged) or ($k \geq K_1$)

6. T $\leftarrow$ True

   end if

end while

Output: Matrices $\boldsymbol{C}$ and $\boldsymbol{Z}$.

5.2.5 The Denoising Algorithm

Given a noisy image $\boldsymbol{y}_c$, suppose that we have extracted N local patches $\{\boldsymbol{y}_j\}_{j=1}^N$ and their similar patches. Then N noisy patch matrices $\{\boldsymbol{Y}_j\}_{j=1}^N$ can be formed to estimate the clean matrices $\{\boldsymbol{X}_j\}_{j=1}^N$. The patches in matrices $\{\boldsymbol{X}_j\}_{j=1}^N$ are aggregated to form the denoised image $\hat{\boldsymbol{x}}_c$. To obtain better denoising results, we perform the above denoising procedures for several iterations. The proposed TWSC based robust image denoising algorithm is summarized in Algorithm 2.

Algorithm 2: Image Denoising by TWSC

Input: Noisy image $\boldsymbol{y}_c$, $\{\sigma_r, \sigma_g, \sigma_b\}$, K_2;

Initialization: $\hat{\boldsymbol{x}}_c^{(0)} = \boldsymbol{y}_c$, $\boldsymbol{y}_c^{(0)} = \boldsymbol{y}_c$;

for $k = 1 : K_2$ **do**

1. Set $\boldsymbol{y}_c^{(k)} = \hat{\boldsymbol{x}}_c^{(k-1)}$;
2. Extract local patches $\{\boldsymbol{y}_j\}_{j=1}^N$ from $\boldsymbol{y}_c^{(k)}$;

   for each patch $\boldsymbol{y}_j$ **do**

3. Search nonlocal similar patches $\boldsymbol{Y}_j$;
4. Apply the TWSC model (5.3) to $\boldsymbol{Y}_j$ and obtain the estimated $\boldsymbol{X}_j = \boldsymbol{DC}$;

   end for

5. Aggregate $\{\boldsymbol{X}_j\}_{j=1}^N$ to form the image $\hat{\boldsymbol{x}}_c^{(k)}$;

end for

Output: Denoised image $\hat{\boldsymbol{x}}_c^{(K_2)}$.

5.3 Existence and Faster Solution of Sylvester Equation (5.13)

The solution of the Sylvester equation (SE) (5.13) does not always exist, though the solution is unique if it exists. Besides, solving SE (5.13) is usually computationally expensive in high dimensional cases. In this section, we provide a sufficient condition to guarantee the existence of the solution to SE (5.13), as well as a faster solution of (5.13) to save the computational cost of Algorithms 1 and 2.

5.3.1 Existence of the Unique Solution

Before we prove the existence of unique solution of Eq. (5.13), we first introduce the following theorem.

Theorem 5.3.1 *Assume that* $\boldsymbol{A} \in \mathbb{R}^{3p^2 \times 3p^2}$, $\boldsymbol{B} \in \mathbb{R}^{M \times M}$ *are both symmetric and positive semi-*

definite matrices. If at least one of $\boldsymbol{A}, \boldsymbol{B}$ *is positive definite, the Sylvester equation* $\boldsymbol{AC} + \boldsymbol{CB} = \boldsymbol{E}$ *has a unique solution for* $\boldsymbol{C} \in \mathbb{R}^{3p^2 \times M}$.

The proof of Theorem 5.3.1 can be found in the Appendix 8. We then have the following corollary.

Corollary 5.3.2 *The Sylvester equation (5.13) has a unique solution.*

Proof Since $\boldsymbol{A}, \boldsymbol{B}_k$ in (5.13) are both symmetric and positive definite matrices, according to Theorem 5.3.1, the SE (5.13) has a unique solution.

5.3.2 Faster Solution of the Sylvester Equation (5.13)

The solution (5.14) of the SE (5.13) is typically obtained by the Bartels-Stewart algorithm [9]. This algorithm firstly employs a QR factorization [33], implemented via Gram-Schmidt process, to decompose the matrices $\boldsymbol{A}$ and $\boldsymbol{B}_k$ into Schur forms, and then solves the obtained triangular system by the back-substitution method [8]. However, since the matrices $\boldsymbol{I}_M \otimes \boldsymbol{A}$ and $\boldsymbol{B}_k^\top \otimes \boldsymbol{I}_{3p^2}$ are of $3p^2M \times 3p^2M$ dimensions, it is very computationally expensive ($O(p^6M^3)$) to calculate their QR factorization to obtain the Schur forms. By exploiting the specific properties of our problem, we provide a faster while exact solution for the SE (5.13).

Since the matrices $\boldsymbol{A}, \boldsymbol{B}_k$ in (5.13) are symmetric and positive definite, the matrix $\boldsymbol{A}$ can be eigen-decomposed as $\boldsymbol{A} = \boldsymbol{U}_A \boldsymbol{\Sigma}_A \boldsymbol{U}_A^\top$, with computational cost of $O(p^6)$. Left multiply both sides of the SE (5.13) by $\boldsymbol{U}_A^\top$, we can get $\boldsymbol{\Sigma}_A \boldsymbol{U}_A^\top \boldsymbol{C}_{k+1} + \boldsymbol{U}_A^\top \boldsymbol{C}_{k+1} \boldsymbol{B}_k = \boldsymbol{U}_A^\top \boldsymbol{E}_k$. This can be viewed as an SE w.r.t. the matrix $\boldsymbol{U}_A^\top \boldsymbol{C}_{k+1}$, with a unique solution $\text{vec}(\boldsymbol{U}_A^\top \boldsymbol{C}_{k+1}) = (\boldsymbol{I}_M \otimes \boldsymbol{\Sigma}_A + \boldsymbol{B}_k^\top \otimes \boldsymbol{I}_{3p^2})^{-1} \text{vec}(\boldsymbol{U}_A^\top \boldsymbol{E}_k)$. Since the matrix $(\boldsymbol{I}_M \otimes \boldsymbol{\Sigma}_A + \boldsymbol{B}_k^\top \otimes \boldsymbol{I}_{3p^2})$ is diagonal and positive definite, its inverse can be calculated on each diagonal element of $(\boldsymbol{I}_M \otimes \boldsymbol{\Sigma}_A + \boldsymbol{B}_k^\top \otimes \boldsymbol{I}_{3p^2})$. The computational cost for this step is $O(p^2M)$. Finally, the solution $\boldsymbol{C}_{k+1}$ can be obtained via $\boldsymbol{C}_{k+1} = \boldsymbol{U}_A \text{vec}^{-1}(\text{vec}(\boldsymbol{U}_A^\top \boldsymbol{C}_{k+1}))$. By this way, the complexity for solving the SE (5.13) is reduced from $O(p^6M^3)$ to $O(\max(p^6, p^2M))$, which is a huge computational saving.

5.4 Experiments

To validate the effectiveness of our proposed TWSC scheme, we apply it to both synthetic AWGN corrupted images and real-world noisy images. To better demonstrate the roles of the weights in our model, we compare with a baseline method, in which the weights $\boldsymbol{W}_1, \boldsymbol{W}_2$ are set to comfortable identity matrices, while the matrix $\boldsymbol{W}_3$ is set as in (5.8). We call this baseline the weighted sparse coding (WSC) method.

Implementation Details. We empirically set the parameter $\rho_0 = 0.5$ and $\mu = 1.1$. The maximum number of iteration is set as $K_1 = 100$. The window size for similar patch searching is set as 60×60. For parameters p, M, K_2, we set $p = 7, M = 70, K_2 = 8$ for $0 < \sigma \leq 20$; $p = 8, M = 90, K_2 = 12$ for $20 < \sigma \leq 40$; $p = 8, M = 120, K_2 = 12$ for $40 < \sigma \leq 60$; $p = 9, M = 140, K_2 = 14$ for $60 < \sigma \leq 100$. All parameters are fixed in our experiments, which are run under the Matlab2014b environment on a machine with Intel(R) Core(TM) i7-5930K CPU of 3.5GHz and 32GB RAM. It takes about 240 seconds to process a real noisy image of size $512 \times 512 \times 3$.

5.4.1 Results on Additive White Gaussian Noise Removal

We first compare the proposed TWSC with the state-of-the-art AWGN denoising methods such as BM3D [22], LSSC [58], NCSR [24], WNNM [36], TNRD [19], and DnCNN [107] on 20 gray level images commonly used in [22]. Since TNRD and DnCNN are discriminative learning based methods, we retrain the two methods for noise standard deviations $5 \sim 100$ with a gap of 5 by using the source codes provided by the authors. The noisy images are generated by adding AWGN to each image with $\sigma = 20, 40, 60, 80, 100$, respectively. Note that in this experiment the weight matrix $\boldsymbol{W}_1 = \boldsymbol{I}_{p^2}$ is an identity matrix because the input images are gray level.

The averaged PSNR and SSIM [92] results are listed in Table 5.1. One can see that the

Table 5.1 Average results on PSNR(dB) and SSIM of different denoising algorithms on 20 gray level images corrupted by AWGN noise.

σ_n	Metric	**BM3D**	**LSSC**	**NCSR**	**WNNM**	**TNRD**	**DnCNN**	**WSC**	**TWSC**
20	PSNR	30.95	30.95	30.95	31.20	31.30	31.36	30.90	31.15
	SSIM	0.8552	0.8561	0.8536	0.8580	0.8602	0.8631	0.8484	0.8581
40	PSNR	27.69	27.80	27.71	28.03	28.09	28.19	27.71	28.06
	SSIM	0.7726	0.7750	0.7717	0.7784	0.7824	0.7877	0.7682	0.7833
60	PSNR	26.02	25.83	25.82	26.25	26.14	26.35	25.93	26.28
	SSIM	0.7176	0.7086	0.7163	0.7249	0.7203	0.7307	0.7142	0.7309
80	PSNR	24.76	24.55	24.50	25.01	24.44	24.60	24.67	25.03
	SSIM	0.6716	0.6624	0.6738	0.6838	0.6528	0.6516	0.6727	0.6891
100	PSNR	23.78	23.59	23.49	24.03	22.56	17.07	23.62	24.06
	SSIM	0.6336	0.6299	0.6388	0.6455	0.4766	0.2367	0.6371	0.6538

proposed TWSC is only a little inferior to TNRD and DnCNN when $\sigma \leq 40$. Note that TNRD and DnCNN are trained on external and synthetic clean and noisy image pairs, which is unfair for comparison since TWSC only utilizes the tested noisy image. Besides, one can see that the proposed TWSC model works much better than the baseline method WSC, which proves that the weight matrix $\boldsymbol{W}_2$ can characterize better the noise statistics in local image patches.

In this section, we provide more comparisons of the competing methods on the 20 widely used images (listed in Fig. 2.5) in Figures 5.2–5.6. The compared methods include BM3D [22], LSSC [58], NCSR [24], WNNM [36], TNRD [19], DnCNN [107], and the baseline method WSC.

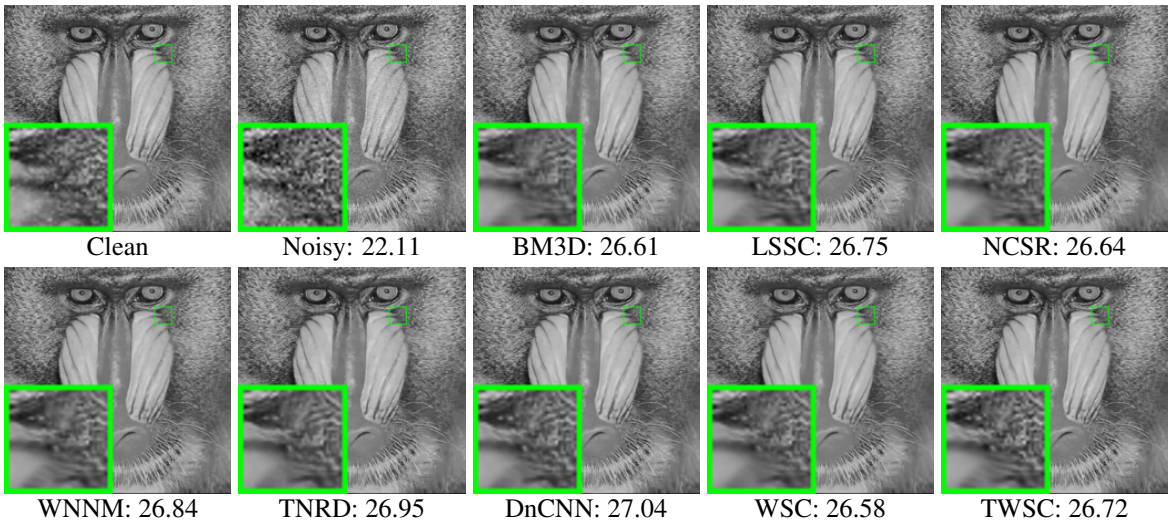

Figure 5.2 Denoised images and PSNR (dB) results of *Baboon* by different methods (the standard deviation of noise is $\sigma = 20$).

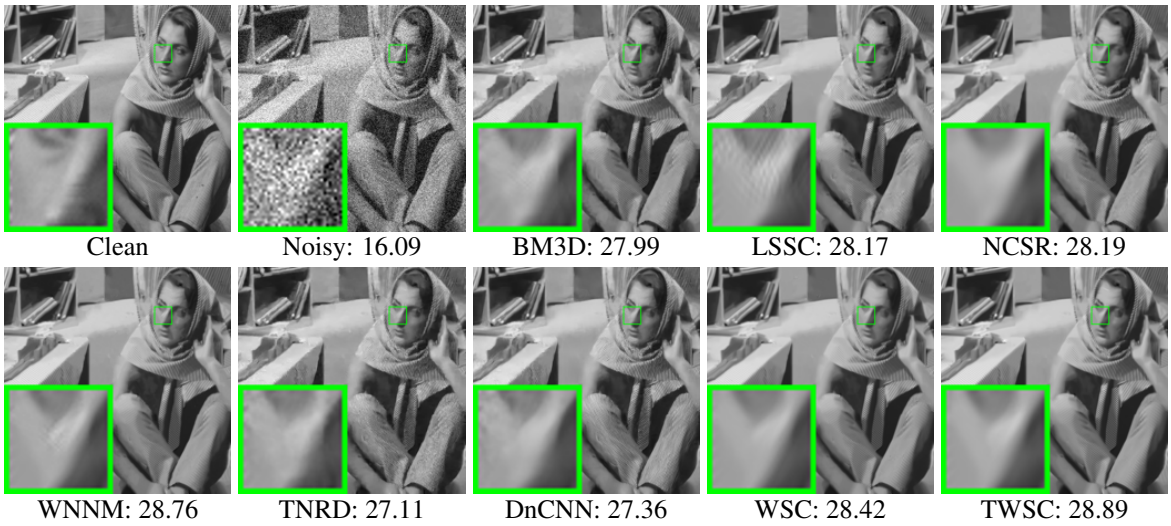

Figure 5.3 Denoised images and PSNR (dB) results of *Barbara* by different methods (the standard deviation of noise is $\sigma = 40$).

5.4.2 Results on Real-world Noise Removal

We evaluate the proposed method on two real noisy image datasets, where the images were captured under indoor and outdoor lighting conditions by different types of cameras and camera settings.

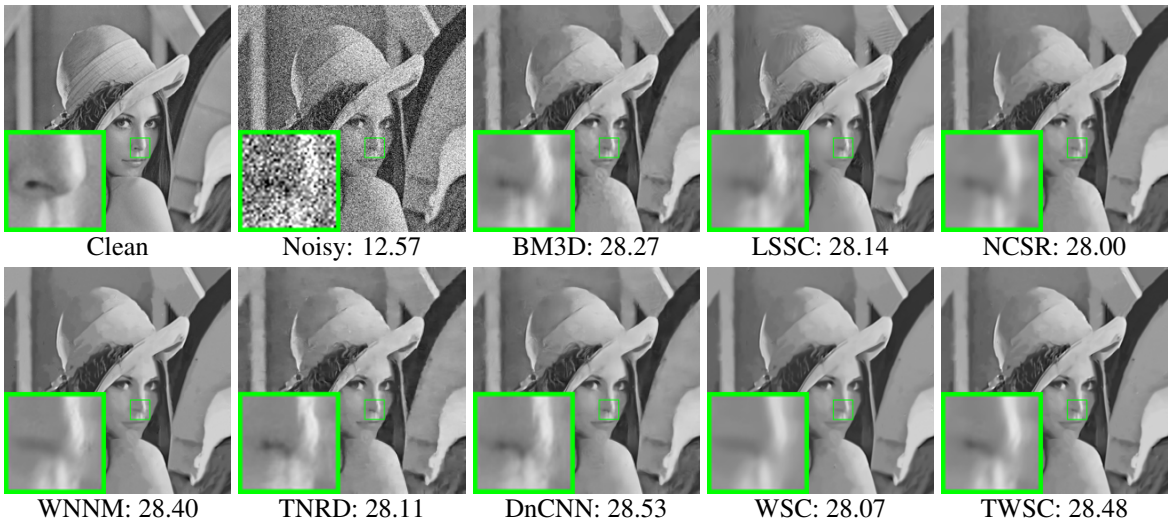

Figure 5.4 Denoised images and PSNR (dB) results of *Lena* by different methods (the standard deviation of noise is $\sigma = 60$).

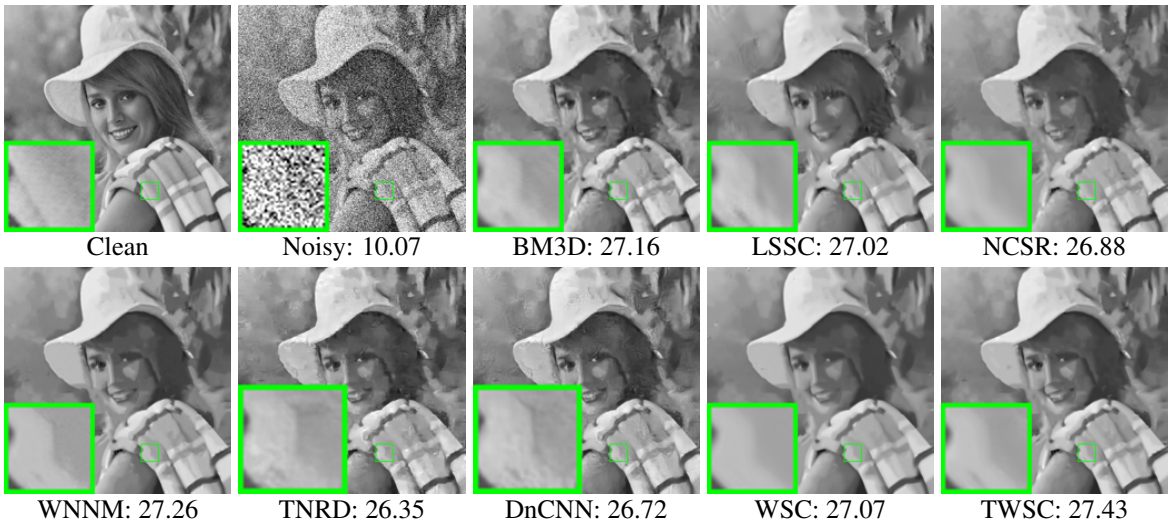

Figure 5.5 Denoised images and PSNR (dB) results of *Elaine* by different methods (the standard deviation of noise is $\sigma = 80$).

Dataset 1 is provided in [50], which includes 20 real noisy images collected under uncontrolled environment. Since there is no "ground truth" of the noisy images, we only compare the visual quality of the denoised images by different methods. Fig. 3.3 shows some sample images of this dataset.

Dataset 2 is provided in [68], which includes noisy images of 11 static scenes. The noisy

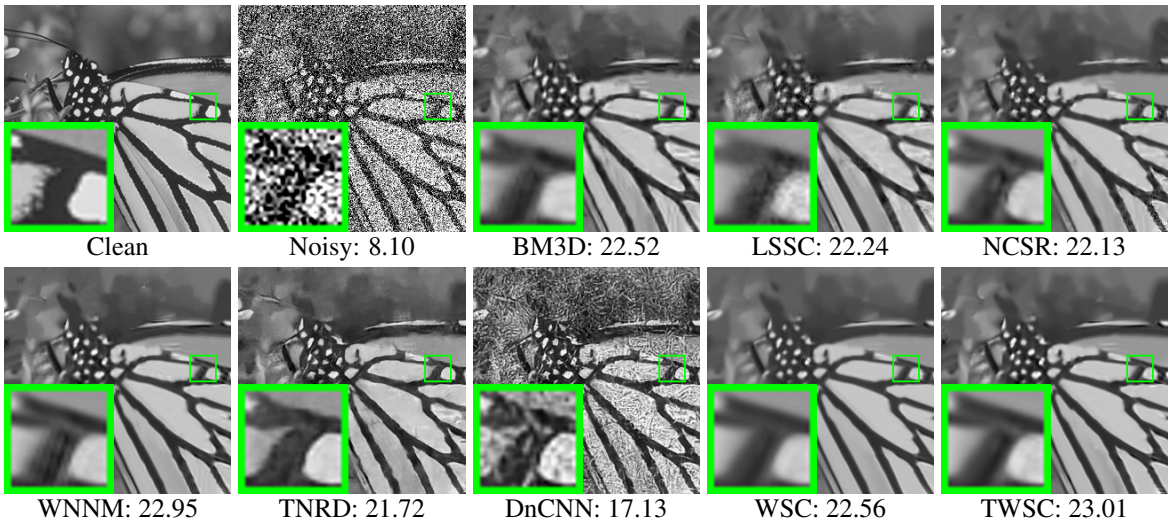

Figure 5.6 Denoised images and PSNR (dB) results of *Monarch* by different methods (the standard deviation of noise is $\sigma = 100$).

images were collected under controlled indoor environment. Each scene was shot 500 times under the same camera and camera setting. The mean image of the 500 shots is roughly taken as the "ground truth", with which the PSNR and SSIM [92] can be computed. 15 images of size 512×512 were cropped in [68] to evaluate the different denoising methods. Fig. 3.4 shows some sample images of this dataset.

We compare the proposed TWSC method with CBM3D [21], WNNM [36], TNRD [19], DnCNN [107], the commercial software Neat Image (NI) [2], the state-of-the-art real image denoising methods "Noise Clinic" (NC) [51] and CC [68]. Since WNNM and TNRD are designed for gray level images, we applied them to each channel of real noisy images. The input noise stds σ_c ($c \in \{r, g, b\}$) for WNNM are estimated by a noise estimation method [18]. TNRD achieves its best results when setting the noise std of the trained models at $\sigma_c = 10$. The methods of CBM3D and DnCNN can directly deal with color images, and the input noise std is set as $\sigma = \sqrt{(\sigma_r^2 + \sigma_g^2 + \sigma_b^2)/3}$. Due to limited space, we do not compare with the baseline method WSC on visual quality.

Results on Dataset 1. Fig. 5.7 show the denoised images of "Dog". (The method CC [68] is not compared since its code is not available.) One can see that CBM3D and WNNM tend

Table 5.2 Average results on PSNR(dB) and SSIM of different denoising methods on 15 cropped real noisy images used in [68].

Metric	**CBM3D**	**WNNM**	**TNRD**	**DnCNN**	**NI**	**NC**	**CC**	**WSC**	**TWSC**
PSNR	35.19	35.77	36.61	33.86	35.49	36.43	36.88	37.36	**37.81**
SSIM	0.9063	0.9381	0.9463	0.8635	0.9126	0.9364	0.9481	0.9516	**0.9586**

to over-smooth the image. DnCNN, TNRD and NI remain many noise-caused color artifacts across the whole image. NC is better than other methods except the proposed TWSC. These results demonstrate that the methods designed for AWGN are not effective for real-world noise removal. Though NC and NI methods are specifically developed for real noisy images, their performance is not satisfactory. In comparison, the proposed TWSC works much better in removing the noise while maintaining the details (see the zoom-in window in "Dog") than the other competing methods. More visual comparisons can be found in the Figures 5.8-5.10, in which we can see that our proposed method performs better than the competing methods.

Results on Dataset 2. The average PSNR and SSIM results on the 15 cropped images by competing methods are listed in Table 5.2. One can see that the proposed TWSC is much better than other competing methods, including CC and the baseline method WSC. Fig. 5.11 shows the denoised images of a scene captured by Canon 5D Mark 3 at ISO = 3200. One can see that the proposed TWSC method results in not only higher PSNR and SSIM measures, but also much better visual quality than the other denoising methods. More comparisons can be found in Figures 5.12–5.15, our proposed TWSC method achieves better performance than the the competing methods.

Figure 5.7 Denoised images of the real noisy image *Dog* [50] by different methods. The images are better to be zoomed in on screen.

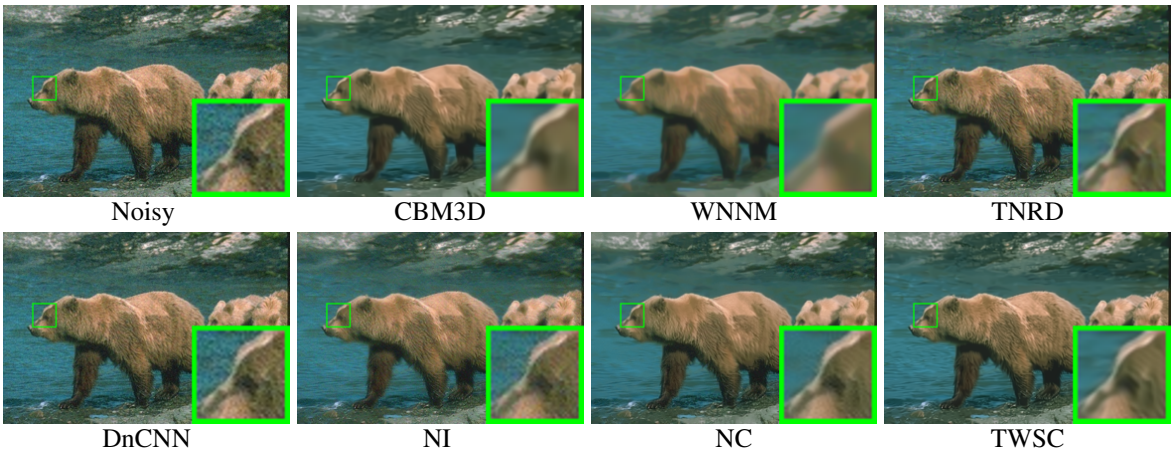

Figure 5.8 Denoised images of the real noisy image *Bears* [50] by different methods. The images are better to be zoomed in on screen.

5.5 Conclusion

The real-world noise in real-world noisy images is very complex due to the various factors in digital camera pipelines, making the real-world image denoising problem much more chal-

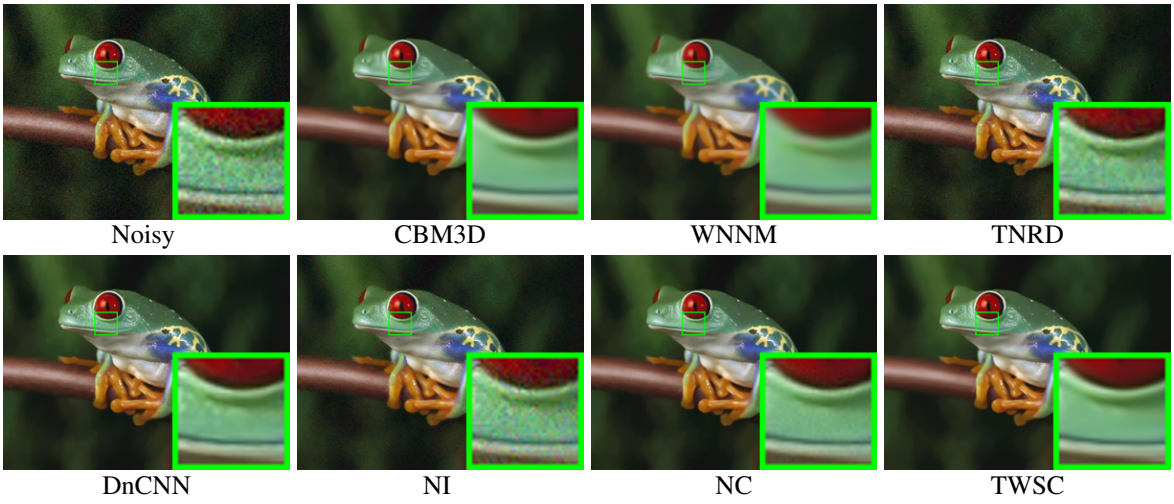

Figure 5.9 Denoised images of the real noisy image *Frog* [50] by different methods. The images are better to be zoomed in on screen.

Figure 5.10 Denoised images of the real noisy image *Girl* [50] by different methods. The images are better to be zoomed in on screen.

lenging than white Gaussian noise removal. We proposed a novel trilateral weighted sparse coding (TWSC) scheme to exploit the noise properties across different channels and patches. Specifically, we introduced two weight matrices into the data term of sparse coding model to adaptively process each patch in each channel, and a weight matrix to better model image priors. The proposed TWSC model was solved via the ADMM algorithm and the solution existence and convergence can be guaranteed. Experiments demonstrated the superior perfor-

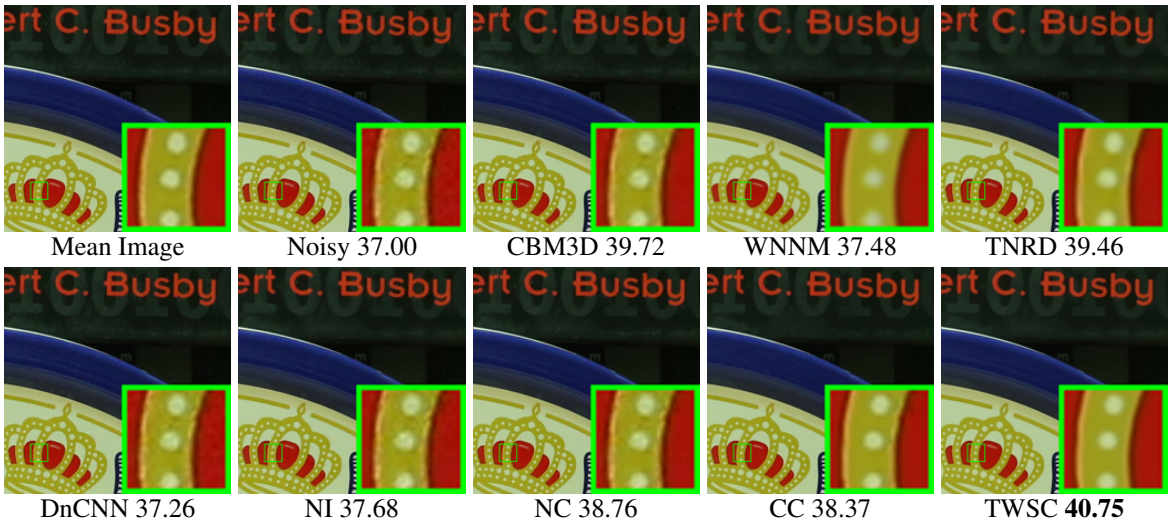

Figure 5.11 Denoised images and PSNR (dB) results of the real noisy image *Canon 5D Mark 3 ISO 3200 1* [68] by different methods. The images are better to be zoomed in on screen.

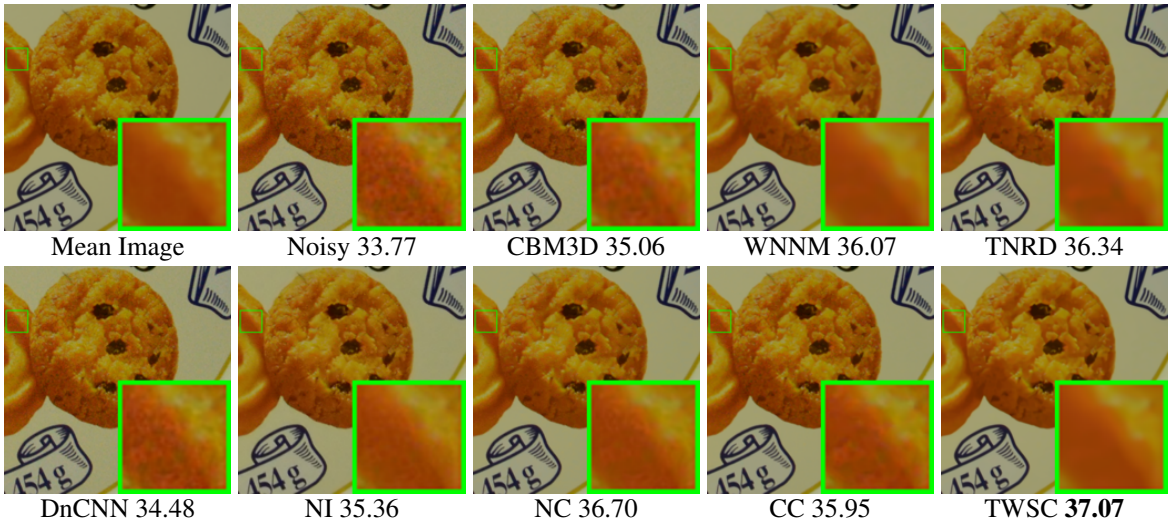

Figure 5.12 Denoised images and PSNR (dB) results of the real noisy image *Nikon D600 ISO 3200 2* [68] by different methods. The images are better to be zoomed in on screen.

mance of TWSC to the state-of-the-art denoising methods, including those methods designed for real-world noise.

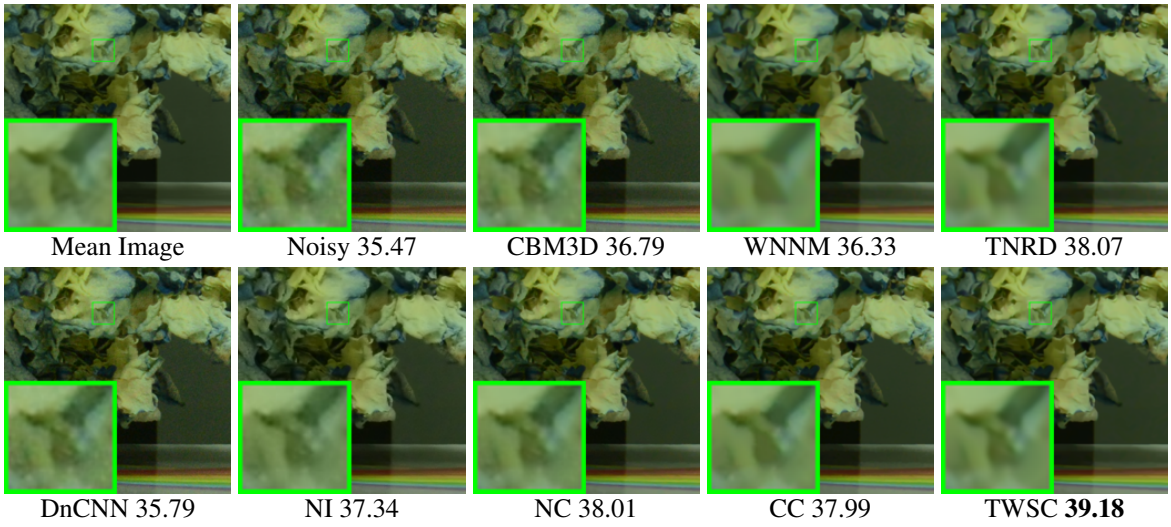

Figure 5.13 Denoised images and PSNR (dB) results of the real noisy image *Nikon D800 ISO 1600 1* [68] by different methods. The images are better to be zoomed in on screen.

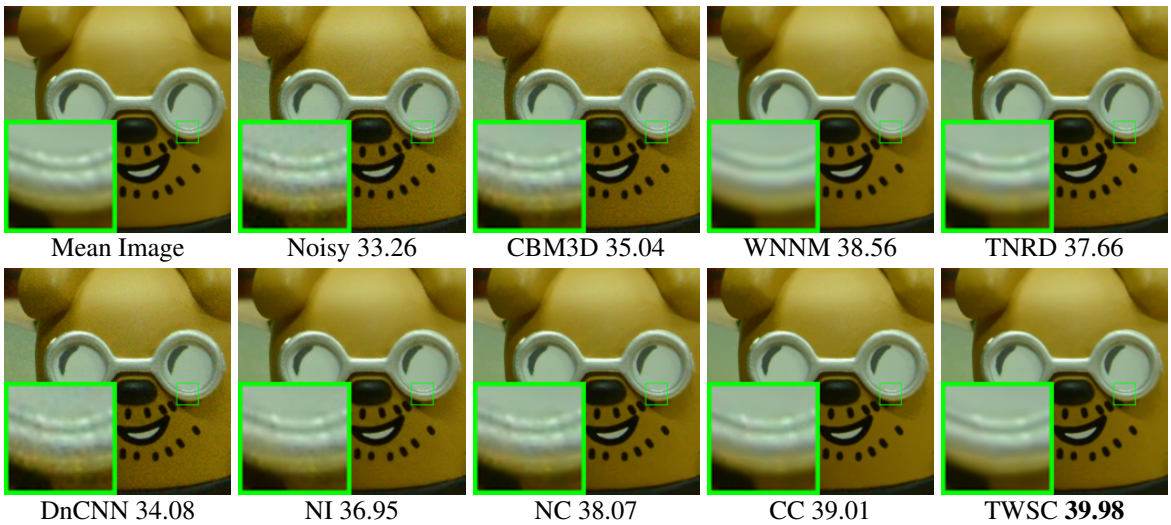

Figure 5.14 Denoised images and PSNR (dB) results of the real noisy image *Nikon D800 ISO 3200 1* [68] by different methods. The images are better to be zoomed in on screen.

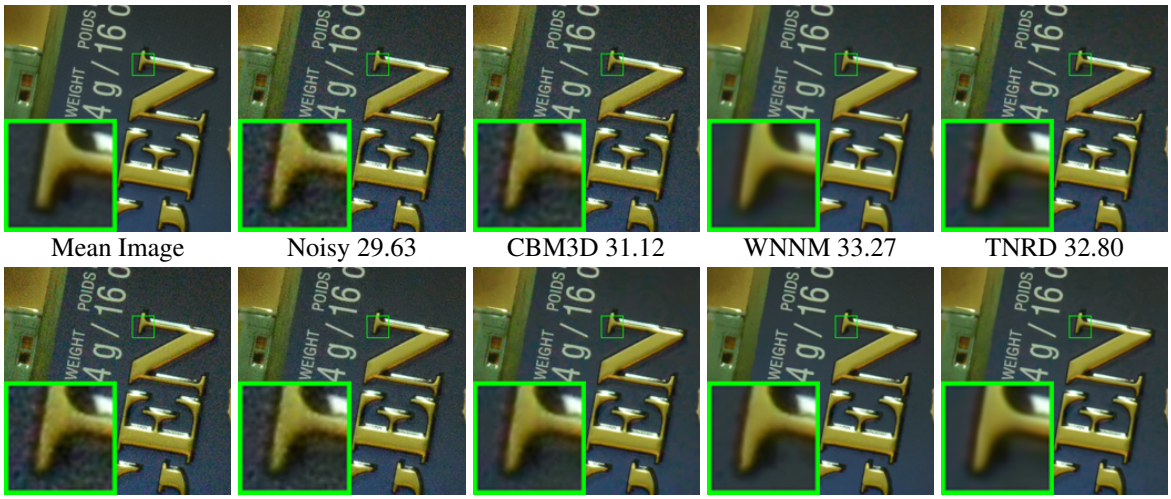

Figure 5.15 Denoised images and PSNR (dB) results of the real noisy image *Nikon D800 ISO 6400 1* [68] by different methods. The images are better to be zoomed in on screen.

Chapter 6

Real-world Noisy Image Dataset: A New Benchmark

6.1 Introduction

During the past decades, the statistical property of real-world noise has been studied for CCD and CMOS image sensors [4, 38, 68, 74, 90]. There are five major sources for real-world noise, including photon shot noise, fixed pattern noise, dark current, readout noise, and quantization noise, etc. The shot noise is one inevitable source of noise, which is induced by the stochastic arrival process of photons to the sensor. The arrival of photons can be modeled by a Possion process in which the number of photons arriving the sensor follows a Possion distribution. This type of noise is proportional to the mean intensity of the specific pixel and is not stationary across the whole image. The fixed pattern noise include pixel response non-uniformity (PRNU) noise and dark current non-uniformity (DCNU) noise. In PRNU noise, each pixel will have a slightly different output level or response for a fixed light level. The major cause of the PRNU noise is the loss of light and color mixture in the neighboring pixels. The DCNU noise comes from the electronics within the sensor chip, and it is generated due

to thermal agitation, even there is no light reaching the camera sensor. The readout noise and quantization noise come from the discretization of measured signals. The readout noise is generated during the process of charge-to-voltage conversion, which is inheretantly not accurate. The quantization noise is generated when the readout values are quantized to integers. The final pixel values are discretizations of the original raw pixel values. Other noise include CCD specific sources such as transfer efficiency, and CMOS specific sources such as column noise.

Different from additive white Gaussian noise (AWGN), the real-world noise is signal dependent, and cannot be modeled by an explicit distribution. It becomes much more complex after being processed in the camera imaging pipelines. Hence, removing noise from real-world noisy images is a more challenging task than its synthetic AWGN counterpart. Another issue about real-world image denoising is how to evaluate the quality of the denoised images. The image quality assessment by subjective evaluation would be time-consuming, since it needs huge number of subjectives to take part in the evaluation experiments. An alternative is to resort to the objective evaluation. However, since the real-world noisy images have no corresponding "ground truth" images, the objective evaluation on the quality of denoised images is very hard. Another choice is to resort to some blind image quality assessment (BIQA) methods [66, 81]. However, these BIQA methods are mostly developed based on the commonly used datasets such as TID dataset [75] and LIVE IQA dataset [84], whose images have very different properties from real-world noisy images.

Recently, several works have been done to address the issue of missing corresponding "ground truth" image of the captured real-world noisy image. In [68], a dataset containing 11 scenes is constructed for analyzing the properties of real-world noise produced in the camera imaging pipeline. However, this dataset is limited in several aspects. It contains only printed pictures on the package of several products, having few real objects. Other problems include that the intensity transform does not model heteroscedastic noise, and low-frequency bias is

not removed, etc. In [4] and [74], the corresponding "ground truth" image of the captured real-world noisy image is captured with low ISO values (e.g., ISO=100), with other post-processing steps such as linear intensity changes, spatial misalignment, and low-frequency residual correciton, etc. However, the "ground truth" images with low ISO values may have slightly different illuminations from the corresponding real-world noisy images captured under high ISO values (e.g., ISO=6,400). Besides, the post-processing steps may introduce human bias into the "ground truth" images. The work of [6] proposes a less tedious capture protocol similar to [74], where multiple exposures of a static scene are used to aggregate the measurements at every pixel site temporally. The works of [31, 64] propose to illuminate the sensor with approximately constant irradiation and subsequently aggregates intensity measurements spatially. This is repeated for different irradiation levels to capture the intensity dependence of the noise. In contrast, in [74] the employed Tobit regression allows to estimate the parameters of the noise process by having access to just two images.

In this work, we construct a large dataset of real-world noisy images with reasonably obtained corresponding "ground truth" images. The basic idea is to capture the same and unchanged scene for many (e.g., 500) times and compute their mean image, which can be roughly taken as the "ground truth" image for the real-world noisy images. The rational of this strategy is that for each pixel, the noise is generated randomly larger or smaller than 0. Sampling the same pixel many times and computing the average value will approximate the truth pixel value and alleviate significantly the noise.

6.2 Existing Datasets

Currently, there are some datasets available aiming at benchmarking the denoising methods on real-world noisy images [4, 68, 74].

As far as we know, the RENOIR dataset [4] is the first dataset on real-world noisy images with "ground truth" noise-free images. The cameras used in this dataset are Canon Rebel

Table 6.1 Cameras and camera settings used in the dataset [4].

Camera	Sensor size (mm)	# of Scenes	"Ground Truth"		Noisy Image	
			ISO	Time (s)	ISO	Time (s)
Canon S90	7.4×5.6	40	100	3.2	640, 1k	Auto
Canon T3i	22.3×14.9	40	100	Auto	3.2k, 6.4k	Auto
Xiaomi Mi3	4.69×3.52	40	100	Auto	1.6k, 3.2k	Auto

T3i, Canon S90, and Xiaomi T3i. The authors took photos of a static scene with different ISO values. However, the post-processing is less refined. Image pairs appear to exhibit spatial misalignment, the intensity transform does not model heteroscedastic noise, and low-frequency bias is not removed. In [4], experiments have been conducted to validate that ignoring these factors makes the dataset less usefull. It is often useful to measure the noise characteristics of a sensor at a certain ISO level. It was proposed [4] to illuminate the sensor with approximately constant irradiation and subsequently aggregate intensity measurements spatially. This is repeated for different irradiation levels to capture the intensity dependence of the noise. A less tedious capture protocol was also proposed in [4], where multiple exposures of a static scene are used to aggregate the measurements at every pixel site temporally. The detailed description of this dataset is listed in Table 6.1.

The second work along this direction is reported in [68], which involves 11 static scenes. The real-world noisy images and the corresponding "ground truth" images are collected. For each scene, 500 JPEG images are captured and the mean image of the 500 images is roughly taken as the "ground truth" image. Utilizing the mean of temporal images as "ground truth" image has also been employed in [53, 55], but the authors did not build a benchmark dataset. In the dataset of [68], the images are mostly with resolution of 7630×4912 and captured by Nikon D800 (ISO=1,600, 3,200, and 6,400), Nikon D600 (ISO=3,200), and Canon 5D Mark

Table 6.2 The detailed information of the cropped regions from the dataset [68].

Camera	ISO	# of Images	JPEG	Image size
Canon 5D Mark III	3.2k	3	Fine	512×512
Nikon D600	3.2k	3	Normal	512×512
Nikon D800	1.6k, 3.2k, 6.4k	9	Normal	512×512

III (ISO=3,200). There are totally 15 cropped regions of size 512×512 provided for evaluating different denoising methods. The major problems of this dataset is that the captured images are almost printed scenes, which share similar nosie statistical property. The camera settings such as the ISO values are also somewhat limited. The detailed description of this dataset is listed in Table 6.2.

One recent benchmark is reported in [74]. Different from the previous two datasets in [4] and [68], [74] employs the Tobit regression to estimate the parameters of the noise process by accessing just two images. In order to obviate the unrealistic setting by developing a methodology for benchmarking denoising techniques on real photographs, the authors of [74] captured 50 different pairs of images with different ISO settings and shutter speeds. The image captured with high ISO and faster shutter speed is taken as the real-world noisy image, while the image captured with low ISO and slower shutter speed is roughly taken as the "ground truth" image. To derive better "ground truth", careful post-processing is designed in [74]. The authors corrected spatial misalignment, coped with the inaccurate exposure parameters through a linear intensity transform based on a novel heteroscedastic Tobit regression model, and removed residual low-frequency bias that stems from minor illumination changes, etc. The proposed dataset is called the Darmstadt Noise Dataset (DND) [74], in which the cameras used for capturing the dataset include Sony A7R, Olympus E-M10, Sony RX100 IV, and Huawei Nexus 6P. The authors extracted the linear raw intensities from the captured images using the

Table 6.3 Cameras and camera settings used in the dataset [74].

Camera	# of Scenes	Sensor size (mm)	ISO
Sony A7R	13	36×24	100-25.6k
Olympus E-M10	13	17.3×13	200-25.6k
Sony RX100 IV	12	13.2×8.8	125-8k
Huawei Nexus 6P	12	6.17×4.55	100-6.4k

free software *Dcraw*, and then normalized the image intensities to the range of [0, 1] by scaling the black and white levels. One interesting finding is that various denoising techniques that perform well on synthetic noisy images are clearly outperformed by BM3D [22] on realistic photographs. This benchmark delineates realistic evaluation scenarios that deviate strongly from those commonly used in the scientific literature. The detailed description of this dataset is listed in Table 6.3.

6.3 The Proposed Dataset

6.3.1 Motivation

As discussed previously, existing real-world noisy image datasets [4, 68, 74] have several limitations in evaluating existing and future image denoising methods. These limitations include camera brands, camera settings, and captured scenes, etc.

Camera Brands: In the RENOIR dataset [4], the authors used two different camera brands, Canon (T3i and S90) and Xiaomi (Mi3), for image collection. In the dataset [68], the authors also used two camera brands, i.e., the Canon (5D) and Nikon (D600 and D800), for image collection. In the DND dataset [74], the authors used three different cameras including Sony (A7R and RX100 IV), Olympus (E-M10), and Huawei (Nexus 6P).

Camera Settings: In the RENOIR dataset [4], the "ground truth" images are all captured by setting the ISO as 100. The ISO in noisy images are set as follows: for Xiaomi Mi3, the ISO is set as 1,600 or 3,200; for Canon S90, the ISO is set as 640 or 1,000; for Canon T3i, the ISO is set as 3,200 or 6,400. For all the cases except for the reference image of Canon S90, the shutter speed is set as automatic. For Canon S90, the shutter speed is set as 3.2 seconds. In the dataset [68], three different ISOs (e.g., 1,600, 3,200, and 6,400) are employed when capturing images with Nikon D800, while ISO=3,200 is utilized for Canon 5D and Nikon D600. The DND dataset [74], the ranges of ISO are $100 \sim 25,600$ for Sony A7R, $200 \sim 25,600$ for Olympus E-M10, $125 \sim 8,000$ for Sony RX100 IV, and $100 \sim 6,400$ for Huawei Nexus 6P, respectively.

Captured Scenes: The RENOIR dataset [4] captures 40 scenes for each camera brand, and overall 120 scenes are included in the dataset. However, the noisy images and corresponding "ground truth" images in this dataset have distinct color difference, which is largely caused by inconsistent lighting conditions. The dataset [68] contains only 11 indoor scenes, which are overlapped by similar contents and objects. Though containing 50 different scenes, the "ground truth" images in the DND dataset [74] are not accessible yet. This limits the evaluation of the proposed denoising methods on visual quality.

Discussion. Among the above mentioned factors, the camera settings are very important when we capture the real-world noisy images, while the camera brands and captured scenes are relatively easy to improve. The camera settings include mainly ISO value, the shutter speed, and the aperture, etc. In general, the faster the shutter speed, the darker the captured images when we fix the other settings, and vice versa. Similarly, the smaller the ISO value (or aperture), the darker the captured images when we fix the other settings, and vice versa.

In order to make the image less affected by the change of environment (e.g., object motion, change of illumination, camera shake, etc.), the shutter speed should be set as faster as possible. For example, the shutter speed of the Sony A7II camera is between 1/80,000 second

and 30 seconds. Given suitable aperture and ISO, it is possible to capture images with normal illuminations when we set the shutter speed between 1/100 second and 1 second. The aperture could be set as any value as long as it is in the reasonable range. The aperture of the Sony camera is between F3.5 and F22. Setting the aperture between F3.5 and F15 can allow us to obtain images with normal illumination under the fixed ranges of shutter and ISO. In our capturing process, we fixed the shutter and aperture in a suitable range, and tuned the ISO values according to the given camera. In general, the noise level would be higher when the ISO is higher. We set the ISO values from a low value to a high value with fixed gap to more comprehensively evaluate the denoising methods.

To analyze how ISO, shutter speed, and aperture influence the contents and illumination of the captured images, we perform some heuristic experiments with different camera settings. In Figure 6.1, we show some images captured with different camera settings. Comparing Figures 6.1(a) and 6.1(b) (or 6.1(g) and 6.1(i)), we can find that higher aperture results in darker illumination. Comparing Figures 6.1(b) and 6.1(c) (or 6.1(g) and 6.1(h)), we can find that slower shutter results in brighter illumination. Comparing Figrues 6.1(b), 6.1(d), 6.1(e), 6.1(f), and 6.1(g), we can find that the illumination becomes brighter when the ISO is higher. Besides, given fixed aperture and shutter, the images captured by the camera can avoid the over-exposure or under-exposure when the ISO is set between 400 and 3,200. When ISO=200, the captured images would have the problem of under-exposure, while when ISO=6,400, the captured images would have the problem of over-exposure. However, this can be alleviated by changing the aperture and shutter speed and finally we can obtain images with normal illuminations.

Given fixed shutter speed and aperture, enhancing the camera sensitivity will generate stronger noise than lowering the shutter speed. In the construction of our dataset, we only changed the ISO values while fixing shutter speed and aperture with suitable values to ensure that the images will not suffer over-exposure or under-exposure. It is commonly accepted that

(a) 200,3.5,1/60 (b) 200,6.7,1/60 (c) 200,6.7,1/8

(d) 400,6.7,1/60 (e) 1600,6.7,1/60 (f) 3200,6.7,1/60

(g) 6400,6.7,1/60 (h) 6400,6.7,1/350 (i) 6400,16,1/60

Figure 6.1 Captured images with the Sony A7 II camera under different (ISO, Shutter speed, Aperture) settings.

the noise in images will become stronger when the scene is under darker light conditions.

6.3.2 The Dataset Construction Process

To alleviate the limitations of the previous datasets [4, 68, 74], we propose to construct a new dataset which could: 1) contain more camera brands; 2) contain more carefully designed camera settings; 3) capture more real-world scenes with realistic objects; 4) capture both the raw data and sRGB data for comparison analysis. The captured images are stored in raw data and JPEG format without compression. For each scene, we capture it for 500 times. Figure 6.2 shows how we capture images of a static scens in indoor environment. The camera is fixed by a tripod. The data collection is automatically done with shutter release after the button is pressed by a person. Hence, the misalignment problem can be nearly avoided in the accquisition process of 500 images for one scene. We capture images with different camera settings.

Figure 6.2 The static scene is captured with a camera fixed by tripod. The data collection is automatically done with shutter release after the button is pressed by a person.

The cameras are set based on the following rules. First, the shutter speed should be faster than the blink of the fluorescent lights, otherwise the flickering of the light will make the global luminances of the captured images very different. Second, we set the shutter speed, the aperture, and the ISO value to ensure that the scenes are in a naturally lighting condition. Besides, since the digital single-lens reflex cameras (DSLRs) use mechanical shutter, the shutter speed of each shot is a little different. This small difference results in slightly different brightness of different shots. However, we ignore this small difference in our dataset, as that in [68].

More Camera Brands: In our dataset, we use 5 different cameras of three camera brands, including Canon (Mark 5D, 80D, 600D), Nikon (D800), and Sony (A7 II), to capture real-world noisy images. According to a recent survey [1], the three camera brands occupy 48 of 50 most commonly used camera-lens combinations. Hence, our dataset is more comprehensive than the previous datasets on camera brands.

More Camera Settings: In our new dataset, each scene is captured with 6 different ISO settings, e.g., 800, 1,600, 3,200, 6,400, 12,800, and 25,600. For each ISO setting, we carefully adjust the shutter speed and aperture, and choose other suitable camera settings to make the

Figure 6.3 Some sample images in our newly constructed dataset.

captured scene not under-exposure nor over-exposure. With the increase of ISO, the luminance of the captured images will also increase, and we need tune the shutter speed and apeture accordingly to capture an image with normal luminance. For example, to make the images captured with ISO=25,600 be normally exposed, we set the shutter speed to 1/320 second and aperture to F10.0.

More Captured Scenes: We capture the images with indoor normal lighting condition, dark lighting condition, and outdoor normal lighting condition. The scenes we captured are also versaltile (including the buildings, classrooms, caffe rooms, and outdoor scenes, etc.). The objects in the scenes include books, pens, bottles, boxes, and joys, etc. In summary, we capture totally 40 different scenes by using 5 different cameras in different camera settings, including 12 scenes captured by Canon 5D Mark II, 5 scenes captured by Canon 80D, 3 scenes captured by Canon 600D, 13 scenes captured by Nikon D800, 7 scenes captured by Sony A7 II. Since the images are of large size (3000×3000), we crop some regions from these images and obtain 100 regions of size 512×512.

Removing Outlier Images: The outlier images are those images which have misalignment or different illuminance from the base image (we usually choose the first image of the 500 shots as the base image). In the dataset of [68], the authors did not remove the images with misalignment or different luminances. In the DND dataset [74], the authors corrected the misalignment of each image. However, this operation largely depends on the misalignment detection method and the correction method, which may make the corrected images less natural. Besides, the DND dataset [74] takes the image captured with low ISO as "ground truth", and linearly transfer the noisy image captured with high ISO to the scale of the "ground truth" image. This step, in our opinion, is problematic since the image pixels are not linearly dependent on the ISO values. In our dataset, we browse the captured images and remove the outlier images with clear misalignment or different luminances. For each scene, three volunteers are invited to do the screening successively, and the remaining images are used to compute the

"ground truth" image.

Generating "Ground Truth" Image: The "ground truth" images of the RENOIR dataset [4] are generated when the camera is set with ISO=100, while the other settings are fixed the same as those for the noisy images. The "ground truth" images of the dataset [68] are generated by averaging the static images captured on the same scene under the same camera setting. The "ground truth" images of the DND dataset [74] is generated mainly by using low ISO values (e.g., ISO=100), and other post-processing steps include linear intensity changes, spatial misalignment, and low-frequency residual correciton, etc. In our dataset, we employ the same strategy as that method of [68] due to its simplisity. We capture images of the same static scenes for many (500 $\sim$ 1000) times and average the captured images to obtain the "ground truth" image.

We first remove the images with misalignment by careful subjective evaluation. The images with several pixels displacement will be deleted. After this stage, we will remove the images with inconsistant luminance. The luminance is affected by two factors. One is the lighting conditions of the environment. The other is that the camera will automatically make up the illumination when the scene is in a relatively dark lighting condition. Since we shot the scene for many times, some shots may have different illumination, though captured under the same lighting condition. To remove the images with outlier luminance, we first sample 10,000 pixels uniformly (the pixels are on the 100 equidistantly sampled rows and 100 equidistantly sampled columns) from each image, and then compute the mean luminance of the 10,000 pixels. Each of the captured images will have one value representing its mean luminance. We sort these values in a descending order. The images with the lowest or highest mean luminances will be referred as outlier images. We remove these images until the lowest and highest mean luminances are close enough to the "center" of the mean luminances. Here, "center" means the median of the sorted mean luminances. In this way, the images which are much darker or much brighter than the "center" image with the "center" luminance will be deleted, and the

Table 6.4 Cameras and camera settings used in our new dataset.

Camera	# of Scenes	Sensor size (mm)	# of Cropped regions	ISO
Canon 5D	10	36×24	29	3.2k,6.4k
Canon 80D	6	22.5×15	15	800,1.6k,3.2k,6.4k,12.8k
Canon 600D	5	22.3×14.9	11	1.6k,3.2k
Nikon D800	12	35.9×24	33	1.6k,1.8k,3.2k,5k,6.4k
Sony A7II	7	35.8×23.9	12	1.6k,3.2k,6.4k

remaining images are very close to each other in luminance. The remaining images will be averaged to obtain the mean image, which will be used as the "ground truth" image of each scene.

6.3.3 Summary of the Dataset

In our constructed dataset, we captured images from 40 different scenes with different contents and objects. Figure 6.3 shows some samples of the real-world noisy images in our dataset. The images cover from different types of indoor scenes and versaitile objects, etc.

Since the images we captured are very large in size, we crop 100 regions of size 512×512 from the 40 scenes to evaluate the existing image denoising methods. Some examples of the cropped regions and their corresponding "ground truth" images are listed in Figure 6.4. Besides, one can see that the "ground truth" image contains much less noise than the noisy image and has much better visual quality. Hence, this dataset provides us a good platform for evaluating the image denoising methods. The detailed description on cameras and camera settings is listed in Table 6.4. One can see that in our dataset, the ISO values are more comprehensive than the previous datasets [4, 68, 74].

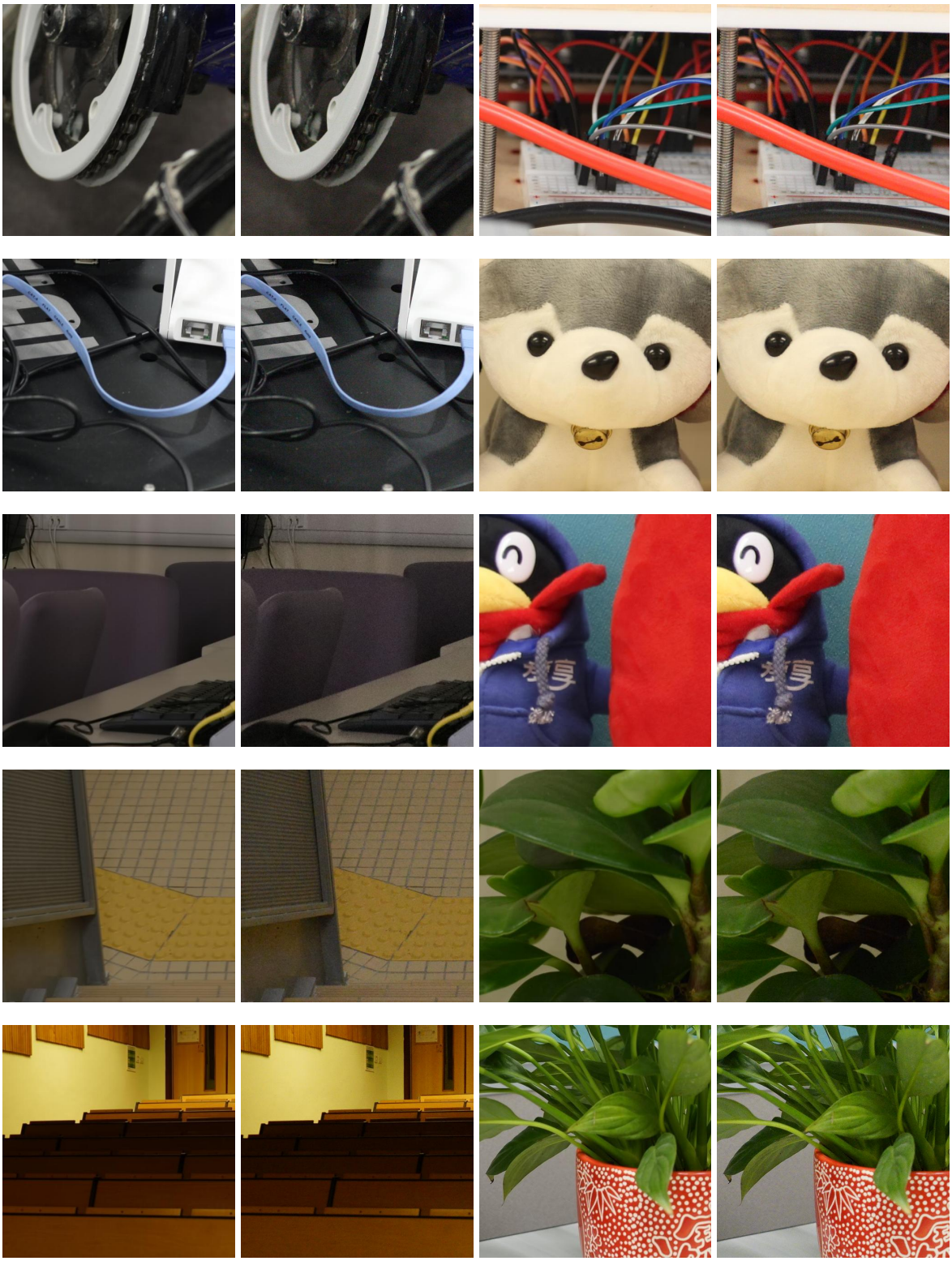

Figure 6.4 Some cropped regions of the "ground truth" images (left) and their corresponding noisy images (right) in our constructed dataset.

6.4 Experiments

6.4.1 Benchmark Datasets

To better evaluate the effectiveness of existing image denoising methods, we apply the competing methods on existing datasets [68, 74] and our constructed new dataset. Since the captured real-world noisy images in [4] have clear color differences with the corresponding "ground truth" images, we do not evaluate image denoising methods on this dataset.

Dataset 1 is provided in [68], which includes noisy images of 11 static scenes captured by Canon 5D Mark 3, Nikon D600, and Nikon D800 cameras. 15 regions of size 512×512 were cropped to evaluate different denoising methods.

Dataset 2 is called the Darmstadt Noise Dataset (DND) [74], which includes 50 different pairs of images of the same scenes captured by Sony A7R, Olympus E-M10, Sony RX100 IV, and Huawei Nexus 6P. The authors cropped 20 bounding boxes of 512×512 pixels from each image in the dataset, yielding 1,000 testing crops in total. However, the "ground truth" images are not open access, and we can only submit the denoising results to the authors' Project Website and get the PSNR and SSIM [92] results.

Dataset 3 is our constructed dataset, which includes noisy images of 40 static scenes captured by Canon 5D Mark II, Canon 80D, Canon 600D, Nikon D800, and Sony A7 II cameras. 100 regions of size 512×512 were cropped to evaluate different denoising methods.

6.4.2 Comparison Methods

With the proposed dataset, we make a comprehensive evaluation on the state-of-the-art image denoising methods, including CBM3D [21], Expected Patch Log Likelihood (EPLL) [111], multi-layer perception (MLP) [13], Nonlocally Centralized Sparse Representations (NCSR) [24], Cascades of Shrinkage Fileds (CSF) [83], Weighted Nuclear Norm Minimiza-

tion (WNNM) [36], Trainable Nonlinear Reactive Diffusion (TNRD) [19], the residual network based method DnCNN [107], the "Noise Clinic" method [50, 51], the commercial software Neat Image [2], and our proposed methods Patch Group Prior based Denoising (PGPD) [103], external prior guided internal prior learning for image denoising (Guided) [100], Multi-channel Weighted Nuclear Norm Minimization (MCWNNM) [102], the Trilateral Weighted Sparse Coding (TWSC) [101]. CBM3D is a state-of-the-art color image denoising method, which assumes that the noise is AWGN. The EPLL, MLP, NCSR, CSF, WNNM, TNRD, DnCNN are state-of-the-art methods for AWGN noise removal on greyscale images, and we apply these methods on each channel of the realsitic color images. The "Noise Clnic" (NC) is a blind image denoising method while Neat Image (NI) is a set of commercial software for image denoising, which has been embedded into Photoshop and Corel Paint Shop. Besides, the method of DnCNN [107] can also deal with real-world noisy images. Our proposed methods includes PGPD, Guided, MCWNNM, and TWSC. The PGPD is proposed for AWGN noise removal, while the Guided, MCWNNM, and TWSC are proposed for real-world noisy image denoising.

Noise level estimation for comparison methods. For the CBM3D method, the standard deviation of noise on color images should be given as a parameter. For methods of NCSR, WNNM, MLP, CSF, and TNRD, the noise level in each color channel should be input. For the DnCNN method, it is trained to deal with noise in a range of levels $0 \sim 55$. We retrain the models of discriminative denoising methods MLP, CSF, and TNRD (using the released codes by the authors) at different noise levels from $\sigma = 5$ to $\sigma = 50$ with a gap of 5. The denoising is performed by processing each channel with the model trained at the same (or nearest) noise level. The noise levels $(\sigma_r, \sigma_g, \sigma_b)$ in R, G, B channels are estimated via some noise estimation methods [18, 54]. In this chapter, we employ the method [54] to estimate the noise level for each channel of the input color image.

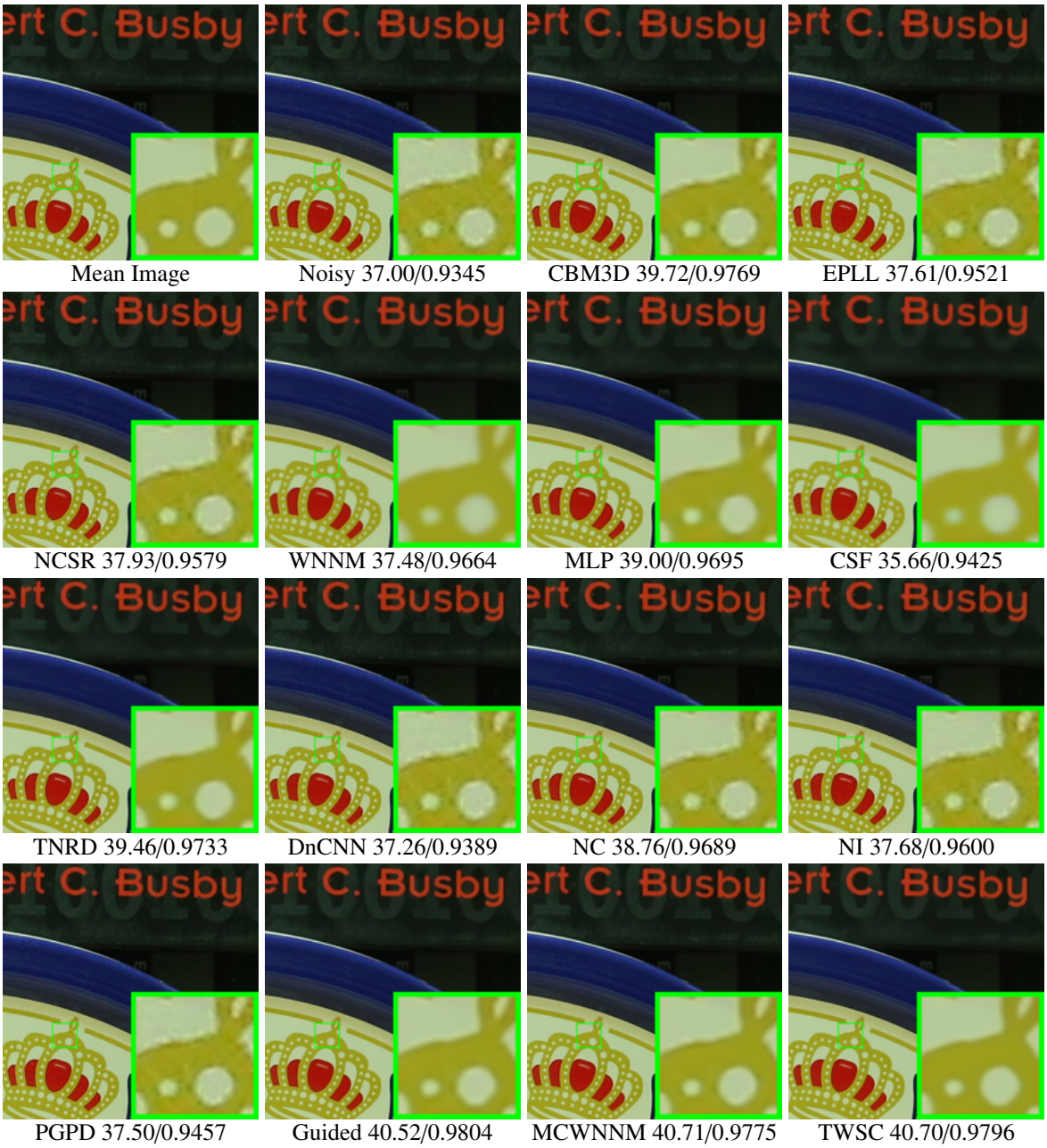

Figure 6.5 Denoised images and PSNR (dB)/SSIM results of the real-world noisy image *Canon 5D Mark 3 ISO 3200 1* [68] by different methods. The images are better to be zoomed in on screen.

Table 6.5 Average results on PSNR(dB) and SSIM of different denoising algorithms on the 15 cropped images in **Dataset 1** [68].

Metric	**CBM3D**	**EPLL**	**NCSR**	**WNNM**	**MLP**	**CSF**	**TNRD**
PSNR	35.19	33.66	33.46	35.77	36.46	35.33	36.61
SSIM	0.8580	0.8591	0.8512	0.9381	0.9436	0.9250	0.9463
Metric	**DnCNN**	**NC**	**NI**	**PGPD**	**Guided**	**MCWNNM**	**TWSC**
PSNR	33.86	36.43	35.49	33.69	37.15	37.71	**37.81**
SSIM	0.8635	0.9364	0.9126	0.8591	0.9504	0.9542	**0.9586**

Table 6.6 Average results on PSNR(dB) and SSIM of different denoising algorithms on the 1,000 cropped images in **Dataset 2** [74].

Metric	**CBM3D**	**EPLL**	**NCSR**	**WNNM**	**MLP**	**CSF**	**TNRD**
PSNR	32.14	32.65	32.81	33.28	34.02	33.87	34.15
SSIM	0.7773	0.7889	0.7912	0.8012	0.8201	0.8128	0.8271
Metric	**DnCNN**	**NC**	**NI**	**PGPD**	**Guided**	**MCWNNM**	**TWSC**
PSNR	32.41	36.07	35.11	33.12	36.41	37.38	**37.94**
SSIM	0.7897	0.9013	0.8778	0.8002	0.9101	0.9294	**0.9403**

6.4.3 Results and Discussion

Results on Dataset 1. The average PSNR and SSIM results on the 15 cropped images by competing methods are listed in Table 6.5. One can see that the proposed TWSC, MCWNNM, and Guided methods perform much better than the other competing methods. Figure 6.5 shows the denoised images of a scene captured by Canon 5D Mark 3 at ISO = 3200. One can see that TWSC, MCWNNM, and Guided methods result in not only higher PSNR and SSIM

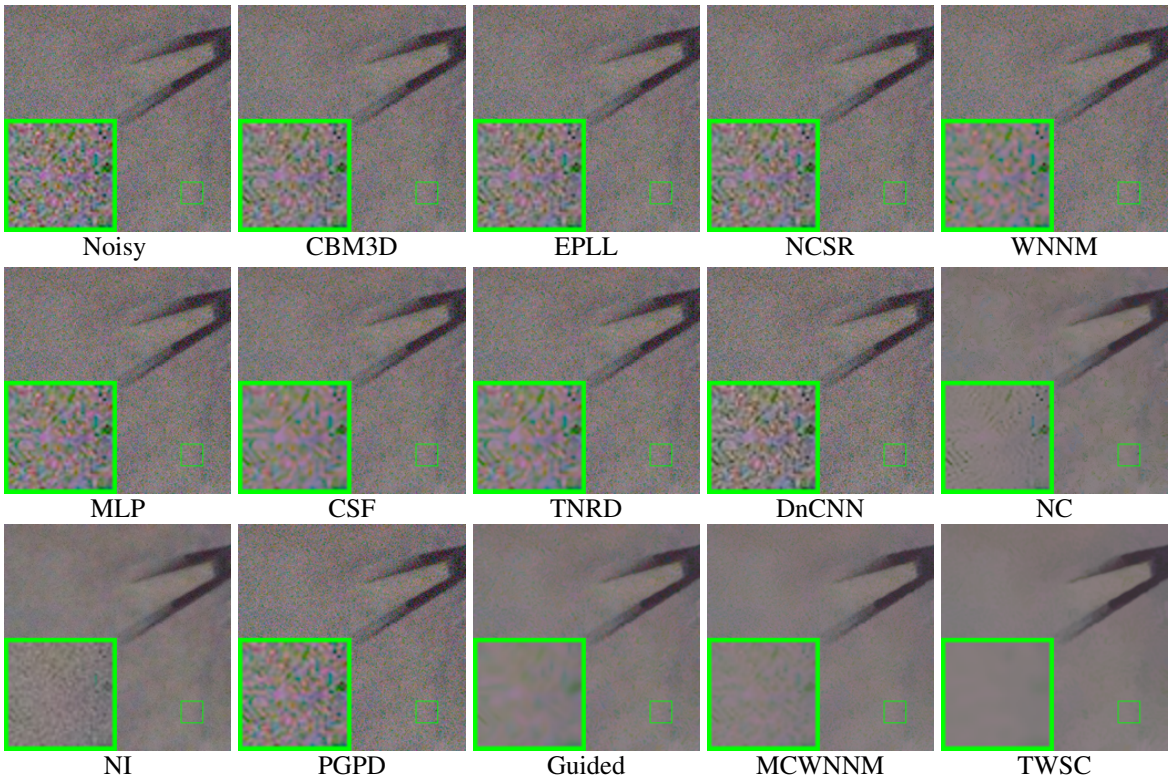

Figure 6.6 Denoised images of the real-world noisy image *0001_1* [74] by different methods. The images are better to be zoomed in on screen.

measurements, but also much better visual quality than other methods.

Results on Dataset 2. In Table 6.6, we list the average PSNR and SSIM results of the competing methods on the 1,000 cropped images in the DND dataset [74]. We can see that on this dataset the TWSC, MCWNNM, and Guided methods achieve much better performance than the other competing methods. Note that the "ground truth" images of this dataset have not been released, but one can submit the denoised images to the project website and get the PSNR and SSIM results. Figure 6.6 shows the denoised images of a scene captured by a Nexus 6P camera. One can see that the TWSC, MCWNNM, and Guided methods result in better visual quality than the other denoising methods.

Results on Dataset 3. The PSNR and SSIM [92] results on 100 images of the cropped regions are listed in Table 6.7. We can see that the traditional methods proposed for AWGN

Table 6.7 Average results on PSNR(dB) and SSIM of different denoising algorithms on the 100 cropped images in our new dataset (**Dataset 3**).

Metric	**CBM3D**	**EPLL**	**NCSR**	**WNNM**	**MLP**	**CSF**	**TNRD**
PSNR	37.40	36.17	36.40	36.59	38.07	37.71	38.17
SSIM	0.9526	0.9216	0.9290	0.9247	0.9615	0.9571	0.9640
Metric	**DnCNN**	**NC**	**NI**	**PGPD**	**Guided**	**MCWNNM**	**TWSC**
PSNR	36.08	36.92	37.77	36.18	38.35	38.51	**38.60**
SSIM	0.9161	0.9449	0.9570	0.9206	0.9669	0.9671	**0.9685**

are no longer effective enough for the real-world noisy images. The discriminative methods achieve slightly better performance than the traditional methods, while still being inferior to the methods designed for real-world nosiy images. The proposed TWSC, MCWNNM, and Guided methods work much better than previous methods. Some visual comparisons are given in Figure 6.7, from which one can see that the TWSC method removes most of the noise while maintaining the details.

Discussion. The experimental results on the three datasets demonstrate that:

- The methods CBM3D, EPLL, NCSR, WNNM, MLP, CSF, TNRD, DnCNN, and PGPD which are designed for AWGN achieve lower PSNR and SSIM compared with the methods developed for real-world noisy image denoising;
- The denoising methods EPLL, NCSR, WNNM, and PGPD which are designed for grey scale images would generate much artifacts since they process each channel of the RGB image individually [59]. They cannot deal with the images which have different noise statistics in different channels as well as different local patches. Hence, these methods may fail to process the real-world noisy images which have complex noise statistics;
- The discriminative learning based methods MLP, CSF, TNRD, and DnCNN are trained

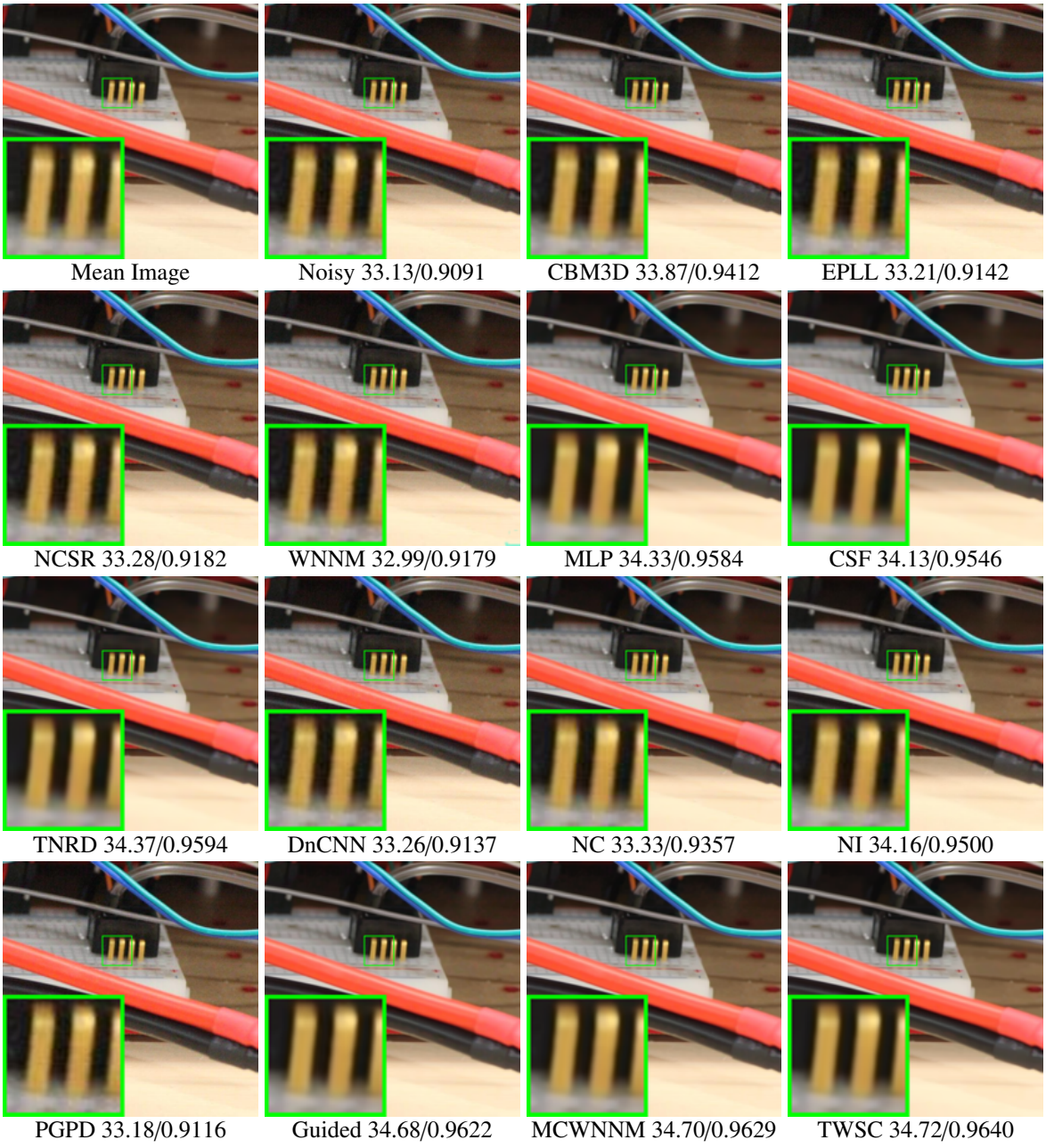

Figure 6.7 Denoised images and PSNR (dB)/SSIM results of the real-world noisy image *Canon5D_2.5_160_6400_circuit_3* in our new dataset by different methods. The images are better to be zoomed in on screen.

on paired clean and noisy images. These methods largely depends on the training dataset, and would achieve inferior performance on images whose noise has different statistics from those in the training images;

- The performance of our proposed denoising methods, i.e., TWSC, MCWNNM, and Guided, on datasets [68, 74] are much better than those of previous denoising methods. As we can see from Tables 6.5 and 6.6, the highest PSNR of our proposed methods (TWSC) and the highest PSNR of previous methods (TNRD on Dataset 1 and NC on Dataset 2) have a difference of over 1.2dB. However, on our new dataset, as we can see from Tables 6.7, the highest PSNR of our proposed methods (TWSC) and the highest PSNR of previous methods (TNRD) only have a difference of around 0.4dB. This indicates that on our new dataset, our proposed methods such as Guided, MCWNNM, and TWSC do not show significant advantages over the previous methods such as TNRD. This is because our dataset is more comprehensive in the scene contents and have more camera settings. This also shows that our dataset is more challenging than previous datasets, and new real-world image denoising methods are needed.

6.5 Conclusion

To evaluate the existing denoising methods on real photographs and promote new methods for removing real-world noise, we constructed a novel dataset which contains comprehensive real-world noisy images of different natural scenes. These images were captured by different cameras under different camera settings. Each scene was shot 500 times in a short time. We first selected the images without misalignment, then deleted the images which do not have consistant lumiance with the baseline image. Since the captured images are very large in size, we cropped smaller regions of size 512×512 to evaluate the existing image denoising methods and the methods we proposed in previous sections. We evaluated the different denoising

methods on the new dataset and previous datasets. The results demonstrated that the proposed methods are more robust than other competing methods, and the newly proposed dataset is more challenging. We will make the constructed dataset of real photographs publicly available for researchers to investigate new real-world image denoising methods.

Chapter 7

Conclusions and Future Work

7.1 Conclusions

In this thesis, we proposed several image denoising methods for both synthetic additive white Gaussian noise (AWGN) and realistic noise in real-world noisy images. These methods can be categorized into external prior based, hybrid prior based, and internal prior based methods.

We firstly proposed an external prior based denoising method for synthetic AWGN. The so-called Patch Group Prior based Denoising (PGPD) method extended existing patch based learning scheme [111] to patch group based learning scheme by modeling the nonlocal self-similarity (NSS) prior of natural images. Extensive experiments demonstrated that PGPD not only achieves highly competitive PSNR results with state-of-the-art denoising methods, but also is highly efficient and preserves better the image edges and textures.

Then we proposed a hybrid prior based method for the real-world image denoising problem. We employed the Gaussian Mixture Model (GMM) to learn the NSS prior and utilized the learned NSS prior to guide the subspace clustering and dictionary learning of the input real-world noisy image. Extensive experiments on three real-world noisy image datasets demonstrated that our proposed Guided method achieves much better performance than state-of-the-art image denoising methods in terms of both quantitative measurement and perceptual

quality.

To fully exploit the internal NSS prior, we proposed a multi-channel model for real-world color image denoising. The multi-channel scheme considers different noise statistics in different channels of the real-world color images. We introduced a weight matrix to the data term in the RGB channel concatenated weighted nuclear norm minimization (WNNM) model, and the resulting MC-WNNM model can process adaptively the different noise in RGB channels. Extensive experiments on synthetic and real-world noisy image datasets demonstrated that the proposed MC-WNNM method outperforms significantly previous image denoising methods, including those methods designed for realistic noise.

We further proposed a novel trilateral weighted sparse coding (TWSC) scheme to exploit the noise properties across different channels and local patches. Specifically, we introduced two weight matrices into the data term of the traditional sparse coding model to adaptively process each patch in each channel, and a weight matrix to better model image priors. The proposed TWSC model was solved via the ADMM algorithm and the solution existence and convergence can be guaranteed. Experiments demonstrated the superior performance of TWSC to the state-of-the-art denoising methods, including those methods designed for realistic noise.

In the final work, we constructed a new real-world noisy image dataset. Specifically, we collected images of 40 different scenes. We evaluated the many denoising methods, including those proposed in this thesis, on two existing benchmark datasets and our proposed dataset. Extensive experiments demonstrated that the proposed TWSC, MCWNNM, and Guided methods achieve much better denoising performance than the previous methods on PSNR, SSIM, and visual quality. Based on our analysis, the real-world image denoising problem is still a challenging task and needs future research for new solutions.

7.2 Future Work

In the future work, we will expand our study in the following directions:

- We will investigate better statistical models for the real-world noise by studying its statistical properties. This remains a not well solved problem which needs more investigations.

- We will develop more robust methods for the learning of image and noise priors. Better priors can always make the denoising algorithms more reliable to remove the realistic noise in real-world applications.

- According to whether the "ground truth" noise-free images is available or not, the potential discriminative methods can be divided into two categories: methods with paired noisy and "ground truth" images and methods without paired noisy and "ground truth" images. With the availability of more real-world noisy image datasets, it is expected to develop new discriminative learning denoising methods for the real-world image denoising problem.

- How to evaluate the visual quality of the denoised images in real-world image denoising problem is another challenging problem which needs more investigations.

- It is essential to develop perceptual quality oriented (real-world) image denoising methods. Besides, task driven (e.g., semantic segmentation) based image denoising methods are also very important for future imaging systems.

We will investigate these research directions in our future work.

Chapter 8

Appendix

8.1 Closed-Form Solution of the Weighted Sparse Coding Problem (2.11)

For notation simplicity, we ignore the indices n, m, t in problem (2.11). The weighted sparse coding problem (2.11) turns into the following problem:

$$\min_{\alpha} \|\boldsymbol{y} - \boldsymbol{D}\boldsymbol{\alpha}\|_2^2 + \sum_{j=1}^{3p^2} \lambda_j |\boldsymbol{\alpha}_j|. \tag{8.1}$$

Since $\boldsymbol{D}$ is an orthogonal matrix, problem (8.1) is equivalent to:

$$\min_{\alpha} \|\boldsymbol{D}^T\boldsymbol{y} - \boldsymbol{\alpha}\|_2^2 + \sum_{j=1}^{3p^2} \lambda_j |\boldsymbol{\alpha}_j|. \tag{8.2}$$

For simplicity, we denote $\boldsymbol{z} = \boldsymbol{D}^T\boldsymbol{y}$. Here we have $\lambda_j > 0$, $j = 1, ..., 3p^2$, then problem (8.2) can be written as:

$$\min_{\alpha} \sum_{j=1}^{3p^2} ((\boldsymbol{z}_j - \boldsymbol{\alpha}_j)^2 + \lambda_j |\boldsymbol{\alpha}_j|). \tag{8.3}$$

The problem (8.1) is separable w.r.t. each $\boldsymbol{\alpha}_j$ and hence can be simplified to $3p^2$ independent scalar minimization problems:

$$\min_{\alpha_j} (\boldsymbol{z}_j - \boldsymbol{\alpha}_j)^2 + \lambda_j |\boldsymbol{\alpha}_j|, \tag{8.4}$$

where $j = 1, ..., 3p^2$. Taking derivative of $\boldsymbol{\alpha}_j$ in problem (2.11) and setting the derivative to be zero. There are two cases for the solution.

(a) If $\boldsymbol{\alpha}_j \geq 0$, we have $2(\boldsymbol{\alpha}_j - \boldsymbol{z}_j) + \lambda_j = 0$, and the solution is $\hat{\boldsymbol{\alpha}}_j = \boldsymbol{z}_j - \frac{\lambda_j}{2} \geq 0$. So $\boldsymbol{z}_j \geq \frac{\lambda_j}{2} > 0$, and the solution $\hat{\boldsymbol{\alpha}}_j$ can be written as $\hat{\boldsymbol{\alpha}}_j = \text{sgn}(\boldsymbol{z}_j) * (|\boldsymbol{z}_j| - \frac{\lambda_j}{2})$, where sgn(•) is the sign function.

(b) If $\boldsymbol{\alpha}_j < 0$, we have $2(\boldsymbol{\alpha}_j - \boldsymbol{z}_j) - \lambda_j = 0$ and the solution is $\hat{\boldsymbol{\alpha}}_j = \boldsymbol{z}_j + \frac{\lambda_j}{2} < 0$. So $\boldsymbol{z}_j < -\frac{\lambda_j}{2} < 0$, and the solution $\hat{\boldsymbol{\alpha}}_j$ can be written as $\hat{\boldsymbol{\alpha}}_j = \text{sgn}(\boldsymbol{z}_j) * (-\boldsymbol{z}_j - \frac{\lambda_j}{2}) = \text{sgn}(\boldsymbol{z}_j) * (|\boldsymbol{z}_j| - \frac{\lambda_j}{2})$.

In summary, we have the final solution of the weighted sparse coding problem (8.1) as:

$$\hat{\boldsymbol{\alpha}} = \text{sgn}(\boldsymbol{D}^T \boldsymbol{y}) \odot \max(|\boldsymbol{D}^T \boldsymbol{y}| - \boldsymbol{\lambda}, 0), \tag{8.5}$$

where $\boldsymbol{\lambda} = \frac{1}{2}[\lambda_1, \lambda_2, ..., \lambda_{3p^2}]^\top$ is the vector of regularization parameter and $\odot$ means element-wise multiplication.

8.2 Proof of the Theorem 3.2.1

Let $\mathcal{A} \in \mathbb{R}^{(3p^2-r)\times M}, \mathcal{Y} \in \mathbb{R}^{3p^2\times M}$ be two given data matrices. Denote by $\mathcal{E} \in \mathbb{R}^{3p^2\times r}$ the external subdictionary and $\mathcal{D} \in \mathbb{R}^{3p^2\times(3p^2-r)}$ the internal subdictionary. For simplicity, we assume $3p^2 \geq M$. The problem in **Theorem 3.2.1** is as follows:

$$\hat{\mathcal{D}} = \arg\min_{\mathcal{D}} \|\mathcal{Y} - \mathcal{D}\mathcal{A}\|_F^2 \text{ s.t. } \mathcal{D}^\top\mathcal{D} = \boldsymbol{I}_{(3p^2-r)\times(3p^2-r)}, \mathcal{E}^\top\mathcal{D} = \boldsymbol{0}_{r\times(3p^2-r)}. \tag{8.6}$$

Proof We firstly prove the necessary condition. Since $\mathcal{D}^\top\mathcal{D} = \boldsymbol{I}_{(3p^2-r)\times(3p^2-r)}$, we have

$$\begin{aligned} \hat{\mathcal{D}} &= \arg\min_{\mathcal{D}} \|\mathcal{Y} - \mathcal{D}\mathcal{A}\|_F^2 = \arg\max_{\mathcal{D}} \text{Tr}(\mathcal{A}\mathcal{Y}^\top\mathcal{D}) \\ \text{s.t.} \quad & \mathcal{D}^\top\mathcal{D} = \boldsymbol{I}_{(3p^2-r)\times(3p^2-r)}, \mathcal{E}^\top\mathcal{D} = \boldsymbol{0}_{r\times(3p^2-r)}. \end{aligned} \tag{8.7}$$

The Lagrange function is $\mathcal{L} = \text{Tr}(\mathcal{A}\mathcal{Y}^\top\mathcal{D}) - \text{Tr}(\Gamma_1(\mathcal{D}^\top\mathcal{D} - \boldsymbol{I}_{(3p^2-r)\times(3p^2-r)})) - \text{Tr}(\Gamma_2(\mathcal{D}^\top\mathcal{E}))$, where Γ_1 and Γ_2 are the Lagrange multipliers. Take the derivative of $\mathcal{L}$ w.r.t. $\mathcal{D}$ and set it to be matrix $\boldsymbol{0}$ of conformal dimensions, we can get

$$\partial\mathcal{L}/\partial\mathcal{D} = \mathcal{Y}\mathcal{A}^\top - \mathcal{D}(\Gamma_1 + \Gamma_1^\top) - \mathcal{E}\Gamma_2^\top = \boldsymbol{0}_{3p^2\times(3p^2-r)}. \tag{8.8}$$

Since $\mathcal{D}^\top\mathcal{D} = \boldsymbol{I}_{(3p^2-r)\times(3p^2-r)}$ and $\mathcal{E}^\top\mathcal{D} = \boldsymbol{0}_{3p^2\times(3p^2-r)}$, by left multiplying both sides of the Eq. (8.8) by $\mathcal{E}^\top$, we have

$$\mathcal{E}^\top\mathcal{Y}\mathcal{A}^\top = \Gamma_2^\top. \tag{8.9}$$

Put the Eq. (8.9) back into Eq. (8.8), we have

$$(\boldsymbol{I}_{3p^2\times 3p^2} - \mathcal{E}\mathcal{E}^\top)\mathcal{Y}\mathcal{A}^\top = \mathcal{D}(\Gamma_1 + \Gamma_1^\top). \tag{8.10}$$

Right multiplying both sides of Eq. (8.10) by $\mathcal{D}^\top$, we have

$$(\boldsymbol{I}_{3p^2\times 3p^2} - \mathcal{E}\mathcal{E}^\top)\mathcal{Y}\mathcal{A}^\top\mathcal{D}^\top = \mathcal{D}(\Gamma_1 + \Gamma_1^\top)\mathcal{D}^\top. \tag{8.11}$$

This shows that $(\boldsymbol{I}_{3p^2\times 3p^2} - \mathcal{E}\mathcal{E}^\top)\mathcal{Y}\mathcal{A}^\top\mathcal{D}^\top$ is a symmetric matrix of order $3p^2 \times 3p^2$. Then we perform economy (or reduced) singular value decomposition (SVD) [28] on $(\boldsymbol{I}_{3p^2\times 3p^2} - \mathcal{E}\mathcal{E}^\top)\mathcal{Y}\mathcal{A}^\top = \mathcal{U}\Sigma\mathcal{V}^\top$, there is

$$(\boldsymbol{I}_{3p^2\times 3p^2} - \mathcal{E}\mathcal{E}^\top)\mathcal{Y}\mathcal{A}^\top\mathcal{D}^\top = \mathcal{U}\Sigma\mathcal{V}^\top\mathcal{D}^\top = \mathcal{D}\mathcal{V}\Sigma\mathcal{U}^\top. \tag{8.12}$$

Hence, we have $\mathcal{U} = \mathcal{D}\mathcal{V}$, or equivalently $\hat{\mathcal{D}} = \mathcal{U}\mathcal{V}^\top$. The necessary condition is proved.

Now we prove the sufficient condition. If $\hat{\mathcal{D}} = \mathcal{U}\mathcal{V}^\top$, then $\hat{\mathcal{D}}^\top\hat{\mathcal{D}} = \boldsymbol{I}_{(3p^2-r)\times(3p^2-r)}$. To prove $\mathcal{E}^\top\hat{\mathcal{D}} = \boldsymbol{0}_{3p^2\times(3p^2-r)}$, we left multiply both sides of Eq. (8.12) by $\mathcal{E}^\top$ and have $\boldsymbol{0}_{3p^2\times(3p^2-r)} = \mathcal{E}^\top(\boldsymbol{I}_{3p^2\times 3p^2} - \mathcal{E}\mathcal{E}^\top)\mathcal{Y}\mathcal{A}^\top\hat{\mathcal{D}}^\top = \mathcal{E}^\top\mathcal{U}\Sigma\mathcal{V}^\top\hat{\mathcal{D}}^\top = \mathcal{E}^\top\mathcal{U}\Sigma\mathcal{U}^\top$. It means that $\mathcal{E}^\top\mathcal{U}\Sigma\mathcal{U}^\top = \boldsymbol{0}_{3p^2\times 3p^2}$. This only happens when $\mathcal{E}^\top\mathcal{U} = \boldsymbol{0}_{3p^2\times(3p^2-r)}$ since $\operatorname{rank}(\Sigma) = 3p^2 - r$ and $\mathcal{U}\Sigma\mathcal{U}^\top$ is positive definite. Then $\mathcal{E}^\top\hat{\mathcal{D}} = \mathcal{E}^\top\mathcal{U}\mathcal{V}^\top = \boldsymbol{0}_{3p^2\times(3p^2-r)}$.

Finally we prove that $\hat{\mathcal{D}} = \mathcal{U}\mathcal{V}^\top$ is the solution of

$$\hat{\mathcal{D}} = \arg\min_{\mathcal{D}} \|\mathcal{Y} - \mathcal{D}\mathcal{A}\|_F^2 = \arg\max_{\mathcal{D}} \operatorname{Tr}(\mathcal{Y}^\top\mathcal{D}\mathcal{A}). \tag{8.13}$$

Note that by cyclic perturbation which retains the trace unchanged and due to $\mathcal{E}^\top\hat{\mathcal{D}} = \boldsymbol{0}_{3p^2\times(3p^2-r)}$, we have $\operatorname{Tr}(\mathcal{Y}^\top\hat{\mathcal{D}}\mathcal{A}) = \operatorname{Tr}(\mathcal{Y}\mathcal{A}^\top\hat{\mathcal{D}}^\top) = \operatorname{Tr}((\boldsymbol{I}_{3p^2\times 3p^2} - \mathcal{E}\mathcal{E}^\top)\mathcal{Y}\mathcal{A}^\top\hat{\mathcal{D}}^\top) = \operatorname{Tr}(\mathcal{U}\Sigma\mathcal{V}^\top\mathcal{V}\mathcal{U}^\top) = \operatorname{Tr}(\Sigma)$. For every $\mathcal{D}$ satisfying that $\mathcal{D}^\top\mathcal{D} = \boldsymbol{I}_{(3p^2-r)\times(3p^2-r)}$, $\mathcal{E}^\top\mathcal{D} = \boldsymbol{0}_{3p^2\times(3p^2-r)}$, we have $\operatorname{Tr}(\mathcal{Y}^\top\mathcal{D}\mathcal{A}) = \operatorname{Tr}((\boldsymbol{I}_{3p^2\times 3p^2} - \mathcal{E}\mathcal{E}^\top)\mathcal{Y}\mathcal{A}^\top\mathcal{D}^\top) = \operatorname{Tr}(\mathcal{U}\Sigma\mathcal{V}^\top\mathcal{D}^\top) = \operatorname{Tr}(\Sigma\mathcal{V}^\top\mathcal{D}^\top\mathcal{U})$. By using a generalization

version [87] of the Kristof's Theorem [48], we have $\mathrm{Tr}(\mathcal{Y}^\top \mathcal{D}\mathcal{A}) = \mathrm{Tr}(\Sigma \mathcal{V}^\top \mathcal{D}^\top \mathcal{U}) \leq \mathrm{Tr}(\Sigma)$. The equality is obtained at $\mathcal{V}^\top \mathcal{D}^\top \mathcal{U} = \boldsymbol{I}_{(3p^2-r)\times(3p^2-r)}$, i.e., $\mathcal{D} = \mathcal{U}\mathcal{V}^\top = \hat{\mathcal{D}}$. This completes the proof.

8.3 Proof of the Theorem 3.2.2

Before we prove the Theorem 3.2.2, we need firstly prove the following Lemma 1.

Lemma 1: Let $\mathcal{E} \in \mathbb{R}^{3p^2\times r}$ be an orthogonal matrix with $\mathcal{E}^\top\mathcal{E} = \boldsymbol{I}_{r\times r}$, then $\mathrm{rank}(\boldsymbol{I}_{3p^2\times 3p^2} - \mathcal{E}\mathcal{E}^\top) \geq 3p^2 - r$.

Proof Since $\mathrm{rank}(\mathcal{E}\mathcal{E}^\top) \leq \min\{\mathrm{rank}(\mathcal{E}), \mathrm{rank}(\mathcal{E}^\top)\} = r$ and $\mathrm{rank}(\mathcal{E}\mathcal{E}^\top) \geq \mathrm{rank}(\mathcal{E}) + \mathrm{rank}(\mathcal{E}^\top) - r = 2r - r = r$ by Sylvester's inequality, we have $\mathrm{rank}(\mathcal{E}\mathcal{E}^\top) = r$. Then, $\mathrm{rank}(\boldsymbol{I}_{3p^2\times 3p^2} - \mathcal{E}\mathcal{E}^\top) \geq \mathrm{rank}(\boldsymbol{I}_{3p^2\times 3p^2}) - \mathrm{rank}(\mathcal{E}\mathcal{E}^\top) \geq 3p^2 - r$.

The $\mathrm{rank}(\Sigma)$ (Σ is defined in Theorem 3.2.1) depends on $\mathrm{rank}(\boldsymbol{I}_{3p^2\times 3p^2} - \mathcal{E}\mathcal{E}^\top)$, $\mathrm{rank}(\mathcal{Y})$ and $\mathrm{rank}(\mathcal{A})$. Note that $\mathrm{rank}(\mathcal{Y}) \geq M$ and $\mathrm{rank}(\mathcal{A}) \geq \min\{3p^2, M\}$ and $\mathrm{rank}(\boldsymbol{I}_{3p^2\times 3p^2} - \mathcal{E}\mathcal{E}^\top) \geq 3p^2 - r$. Hence, $\mathrm{rank}(\Sigma) \leq \min\{3p^2 - r, M\}$.

Now we prove the Theorem 3.2.2:

Proof a) If $(\boldsymbol{I}_{3p^2\times 3p^2} - \mathcal{E}\mathcal{E}^\top)\mathcal{Y}\mathcal{A}^\top \in \mathbb{R}^{3p^2\times(3p^2-r)}$ is nonsingular, i.e., $\mathrm{rank}(\Sigma) = 3p^2 - r$, Σ may have distinct or multiple non-zero singular values. In the SVD [28] of $(\boldsymbol{I}_{3p^2\times 3p^2} - \mathcal{E}\mathcal{E}^\top)\mathcal{Y}\mathcal{A}^\top = \mathcal{U}\Sigma\mathcal{V}^\top$, the singular vectors in $\mathcal{U}$ and $\mathcal{V}$ can be determined up to orientation. Hence, we can reformulate it as

$$(\boldsymbol{I}_{3p^2\times 3p^2} - \mathcal{E}\mathcal{E}^\top)\mathcal{Y}\mathcal{A}^\top = \mathcal{U}^*\mathcal{K}_u\Sigma\mathcal{K}_v(\mathcal{V}^*)^\top, \tag{8.14}$$

where $\mathcal{U}^* \in \mathbb{R}^{3p^2\times(3p^2-r)}$ and $\mathcal{V}^* \in \mathbb{R}^{(3p^2-r)\times(3p^2-r)}$ are arbitrarily orientated singular vectors of $\mathcal{U}$ and $\mathcal{V}$, respectively. The $\mathcal{K}_u$ and $\mathcal{K}_v$ are diagonal matrices with $+1$ or -1 as diagonal elements in arbitrary distribution. $\Sigma \in \mathbb{R}^{(3p^2-r)\times(3p^2-r)}$ is a diagonal matrix with singular values in non-increasing order, i.e., $\Sigma_{11} \geq \Sigma_{22} \geq \ldots \geq \Sigma_{(3p^2-r)(3p^2-r)} \geq 0$. If we fix $\mathcal{K}_u$, then $\mathcal{K}_v$ is

uniquely determined to meet the above requirements of Σ. If the orientations of the singular vectors of $\mathcal{U}^*$ are fixed, then $\mathcal{U} = \mathcal{U}^*\mathcal{K}_u$ is determined, so do the orientations of the singular vectors of $\mathcal{V}^*$ and $\mathcal{V}^\top = \mathcal{K}_v(\mathcal{V}^*)^\top$. In this case, the solution of $\hat{\mathcal{D}} = \mathcal{U}\mathcal{V}^\top = \mathcal{U}^*\mathcal{K}_u\mathcal{K}_v(\mathcal{V}^*)^\top$ is unique. When Σ has multiple singular values, the unique solution of $\hat{\mathcal{D}}$ can be proved in a similar way.

b) If $(\boldsymbol{I}_{3p^2\times 3p^2} - \mathcal{E}\mathcal{E}^\top)\mathcal{Y}\mathcal{A}^\top$ is singular, i.e., $0 \le \text{rank}(\Sigma) < 3p^2 - r$, and Σ has $3p^2 - r - \text{rank}(\Sigma)$ (at least one) zero singular values. The discussion in a) can still be applied to the singular vectors corresponding to the nonzero singular values, and the production of these singular vectors in $\mathcal{U}$ and $\mathcal{V}$ is still unique. However, the singular vectors corresponding to the zero singular values could be in arbitrary orientations as long as they satisfy the conditions of $\mathcal{U}^\top\mathcal{U} = \mathcal{V}^\top\mathcal{V} = \mathcal{V}\mathcal{V}^\top = \boldsymbol{I}_{(3p^2-r)\times(3p^2-r)}$. Since $\mathcal{U} \in \mathbb{R}^{3p^2\times(3p^2-r)}$, $\mathcal{U}\mathcal{U}^\top$ no longer equals to the identity matrix of order $3p^2 \times 3p^2$. From Eq. (8.12), we have

$$\mathcal{U}\Sigma\mathcal{V}^\top\mathcal{D}^\top = \mathcal{D}\mathcal{V}\Sigma\mathcal{U}^\top \tag{8.15}$$

Right multiplying both sides of Eq. (8.15) by $\mathcal{D}\mathcal{V}$ and left multiplying each side by $\mathcal{U}^\top$, we have

$$\Sigma = \mathcal{U}^\top\mathcal{D}\mathcal{V}\Sigma\mathcal{U}^\top\mathcal{D}\mathcal{V} \tag{8.16}$$

Hence, $\Delta = \mathcal{U}^\top\mathcal{D}\mathcal{V} \in \mathbb{R}^{(3p^2-r)\times(3p^2-r)}$ is a diagonal matrix, the diagonal elements of which are

$$\Delta_{ii} = \begin{cases} 1 & \text{if } 1 \le i \le \text{rank}(\Sigma); \\ \pm 1 & \text{if } \text{rank}(\Sigma) < i \le 3p^2 - r. \end{cases}$$

Thus, we have $\mathcal{D} = \mathcal{U}\Delta\mathcal{V}^\top$. That is, if $\text{rank}(\Sigma) < 3p^2 - r$, once we get the solution of $\hat{\mathcal{D}} = \mathcal{U}\mathcal{V}^\top$ in problem (3.11), $\mathcal{D} = \mathcal{U}\Delta\mathcal{V}^\top$ with suitable Δ is also the solution of problem (3.11). In fact, the number of solutions $\hat{\mathcal{D}}$ for problem (3.11) is $2^{3p^2-r-\text{rank}(\Sigma)}$ given fixed $\mathcal{U}, \mathcal{V}$.

8.4 Proof of Theorem 4.2.1

Theorem 8.4.1 *Assume that the weights in* $\boldsymbol{w}$ *are in a non-descending order, the sequence* $\{\boldsymbol{X}_k\}$, $\{\boldsymbol{Z}_k\}$, *and* $\{\boldsymbol{A}_k\}$ *generated in Algorithm 1 satisfy:*

$$(a)\lim_{k\to\infty}\|\boldsymbol{X}_{k+1}-\boldsymbol{Z}_{k+1}\|_F=0;(b)\lim_{k\to\infty}\|\boldsymbol{X}_{k+1}-\boldsymbol{X}_k\|_F=0;(c)\lim_{k\to\infty}\|\boldsymbol{Z}_{k+1}-\boldsymbol{Z}_k\|_F=0. \tag{8.17}$$

Proof 1. Firstly, we prove that the sequence $\{\boldsymbol{A}_k\}$ generated by Algorithm 1 is upper bounded. Let $\boldsymbol{X}_{k+1}+\rho_k^{-1}\boldsymbol{A}_k=\boldsymbol{U}_k\boldsymbol{\Sigma}_k\boldsymbol{V}_k^\top$ be its singular value decomposition (SVD) [28] in the $(k+1)$-th iteration. According to Corollary 1 of [35], we can have the SVD of $\boldsymbol{Z}_{k+1}$ as $\boldsymbol{Z}_{k+1}=\boldsymbol{U}_k\hat{\boldsymbol{\Sigma}}_k\boldsymbol{V}_k^\top=\boldsymbol{U}_k\mathcal{S}_{\frac{\boldsymbol{w}}{\rho_k}}(\boldsymbol{\Sigma}_k)\boldsymbol{V}_k^\top$. Then we have

$$\begin{aligned}\|\boldsymbol{A}_{k+1}\|_F&=\|\boldsymbol{A}_k+\rho_k(\boldsymbol{X}_{k+1}-\boldsymbol{Z}_{k+1})\|_F=\rho_k\|\rho_k^{-1}\boldsymbol{A}_k+\boldsymbol{X}_{k+1}-\boldsymbol{Z}_{k+1}\|_F &(8.18)\\&=\rho_k\|\boldsymbol{U}_k\boldsymbol{\Sigma}_k\boldsymbol{V}_k^\top-\boldsymbol{U}_k\mathcal{S}_{\frac{\boldsymbol{w}}{\rho_k}}(\boldsymbol{\Sigma}_k)\boldsymbol{V}_k^\top\|_F=\rho_k\|\boldsymbol{\Sigma}_k-\mathcal{S}_{\frac{\boldsymbol{w}}{\rho_k}}(\boldsymbol{\Sigma}_k)\|_F &(8.19)\\&=\rho_k\sqrt{\sum_i(\boldsymbol{\Sigma}_k^{ii}-\mathcal{S}_{\frac{w_i}{\rho_k}}(\boldsymbol{\Sigma}_k^{ii}))^2}\le\rho_k\sqrt{\sum_i(\frac{w_i}{\rho_k})^2}=\sqrt{\sum_i w_i^2}. &(8.20)\end{aligned}$$

The inequality in the second last step can be proved as follows: given the diagonal matrix $\boldsymbol{\Sigma}_k$, we define $\boldsymbol{\Sigma}_k^{ii}$ as the i-th element of $\boldsymbol{\Sigma}_k$. If $\boldsymbol{\Sigma}_k^{ii}\ge\frac{w_i}{\rho_k}$, we have $\mathcal{S}_{\frac{w_i}{\rho_k}}(\boldsymbol{\Sigma}_k^{ii})=\boldsymbol{\Sigma}_k^{ii}-\frac{w_i}{\rho_k}$. If $\boldsymbol{\Sigma}_k^{ii}<\frac{w_i}{\rho_k}$, we have $\mathcal{S}_{\frac{w_i}{\rho_k}}(\boldsymbol{\Sigma}_k^{ii})=0$. Overall, we have $|\boldsymbol{\Sigma}_k^{ii}-\mathcal{S}_{\frac{w_i}{\rho_k}}(\boldsymbol{\Sigma}_k^{ii})|\le\frac{w_i}{\rho_k}$ and hence the inequality holds. Hence, the sequence $\{\boldsymbol{A}_k\}$ is upper bounded.

2. Secondly, we prove that the sequence of Lagrangian function $\{\mathcal{L}(\boldsymbol{X}_{k+1},\boldsymbol{Z}_{k+1},\boldsymbol{A}_k,\rho_k)\}$ is also upper bounded. Since we have the globally optimal solution of $\boldsymbol{X}$ and $\boldsymbol{Z}$ in their corresponding subproblems, we always have

$$\mathcal{L}(\boldsymbol{X}_{k+1},\boldsymbol{Z}_{k+1},\boldsymbol{A}_k,\rho_k)\le\mathcal{L}(\boldsymbol{X}_k,\boldsymbol{Z}_k,\boldsymbol{A}_k,\rho_k). \tag{8.21}$$

Based on the updating rule that $\boldsymbol{A}_{k+1} = \boldsymbol{A}_k + \rho_k(\boldsymbol{X}_{k+1} - \boldsymbol{Z}_{k+1})$, we have

$$\mathcal{L}(\boldsymbol{X}_{k+1}, \boldsymbol{Z}_{k+1}, \boldsymbol{A}_{k+1}, \rho_{k+1}) \tag{8.22}$$

$$= \mathcal{L}(\boldsymbol{X}_{k+1}, \boldsymbol{Z}_{k+1}, \boldsymbol{A}_k, \rho_k) + \langle \boldsymbol{A}_{k+1} - \boldsymbol{A}_k, \boldsymbol{X}_{k+1} - \boldsymbol{Z}_{k+1} \rangle + \frac{\rho_{k+1} - \rho_k}{2} \|\boldsymbol{X}_{k+1} - \boldsymbol{Z}_{k+1}\|_F^2 \tag{8.23}$$

$$= \mathcal{L}(\boldsymbol{X}_{k+1}, \boldsymbol{Z}_{k+1}, \boldsymbol{A}_k, \rho_k) + \frac{\rho_{k+1} + \rho_k}{2\rho_k^2} \|\boldsymbol{A}_{k+1} - \boldsymbol{A}_k\|_F^2. \tag{8.24}$$

Since the sequence $\{\boldsymbol{A}_k\}$ is upper bounded, the sequence $\{\boldsymbol{A}_{k+1} - \boldsymbol{A}_k\}$ is also upper bounded. Denote by a the upper bound of $\{\boldsymbol{A}_{k+1} - \boldsymbol{A}_k\}$, i.e., $\|\boldsymbol{A}_{k+1} - \boldsymbol{A}_k\|_F \leq a$ holds for $\forall k \geq 0$, we have

$$\mathcal{L}(\boldsymbol{X}_{k+1}, \boldsymbol{Z}_{k+1}, \boldsymbol{A}_{k+1}, \rho_{k+1}) \leq \mathcal{L}(\boldsymbol{X}_1, \boldsymbol{Z}_1, \boldsymbol{A}_0, \rho_0) + a^2 \sum_{k=0}^{\infty} \frac{\rho_{k+1} + \rho_k}{2\rho_k^2} \tag{8.25}$$

$$= \mathcal{L}(\boldsymbol{X}_1, \boldsymbol{Z}_1, \boldsymbol{A}_0, \rho_0) + a^2 \sum_{k=0}^{\infty} \frac{\mu + 1}{2\mu^k \rho_0} \tag{8.26}$$

$$\leq \mathcal{L}(\boldsymbol{X}_1, \boldsymbol{Z}_1, \boldsymbol{A}_0, \rho_0) + \frac{a^2}{\rho_0} \sum_{k=0}^{\infty} \frac{1}{\mu^{k-1}}. \tag{8.27}$$

The last inequality holds since $\mu > 1$ and $\mu + 1 < 2\mu$. Therefore, we have $\sum_{k=0}^{\infty} \frac{1}{\mu^{k-1}} < \infty$ and the sequence of Lagrangian function $\{\mathcal{L}(\boldsymbol{X}_{k+1}, \boldsymbol{Z}_{k+1}, \boldsymbol{A}_{k+1}, \rho_{k+1})\}$ is upper bounded.

3. Thirdly, we prove that the sequences of $\{\boldsymbol{X}_k\}$ and $\{\boldsymbol{Z}_k\}$ are upper bounded. Since

$$\|\boldsymbol{W}(\boldsymbol{Y} - \boldsymbol{X}_k)\|_F^2 + \|\boldsymbol{Z}_k\|_{\boldsymbol{w},*} \tag{8.28}$$

$$= \mathcal{L}(\boldsymbol{X}_k, \boldsymbol{Z}_k, \boldsymbol{A}_{k-1}, \rho_{k-1}) - \langle \boldsymbol{A}_{k-1}, \boldsymbol{X}_k - \boldsymbol{Z}_k \rangle - \frac{\rho_{k-1}}{2} \|\boldsymbol{X}_k - \boldsymbol{Z}_k\|_F^2 \tag{8.29}$$

$$= \mathcal{L}(\boldsymbol{X}_k, \boldsymbol{Z}_k, \boldsymbol{A}_{k-1}, \rho_{k-1}) + \frac{1}{2\rho_{k-1}} (\|\boldsymbol{A}_{k-1}\|_F^2 - \|\boldsymbol{A}_k\|_F^2), \tag{8.30}$$

both $\{\boldsymbol{W}(\boldsymbol{Y} - \boldsymbol{X}_k)\}$ and $\{\boldsymbol{Z}_k\}$ are upper bounded, and hence the sequence $\{\boldsymbol{X}_k\}$ is bounded by the Cauchy-Schwarz inequality and triangle inequality. We can obtain that

$$\lim_{k \to \infty} \|\boldsymbol{X}_{k+1} - \boldsymbol{Z}_{k+1}\|_F = \lim_{k \to \infty} \rho_k^{-1} \|\boldsymbol{A}_{k+1} - \boldsymbol{A}_k\|_F = 0, \tag{8.31}$$

and the equation (a) is proved.

4. Then we can prove that

$$\lim_{k\to\infty} \|\boldsymbol{X}_{k+1} - \boldsymbol{X}_k\|_F \tag{8.32}$$

$$= \lim_{k\to\infty} \|(\boldsymbol{W}^\top\boldsymbol{W} + \frac{\rho_k}{2}\boldsymbol{I})^{-1}(\boldsymbol{W}^\top\boldsymbol{W}\boldsymbol{Y} - \boldsymbol{W}^\top\boldsymbol{W}\boldsymbol{Z}_k - \frac{1}{2}\boldsymbol{A}_k) - \rho_{k-1}^{-1}(\boldsymbol{A}_k - \boldsymbol{A}_{k-1})\|_F \tag{8.33}$$

$$\leq \lim_{k\to\infty}(\|(\boldsymbol{W}^\top\boldsymbol{W} + \frac{\rho_k}{2}\boldsymbol{I})^{-1}(\boldsymbol{W}^\top\boldsymbol{W}\boldsymbol{Y} - \boldsymbol{W}^\top\boldsymbol{W}\boldsymbol{Z}_k - \frac{1}{2}\boldsymbol{A}_k)\|_F + \rho_{k-1}^{-1}\|\boldsymbol{A}_k - \boldsymbol{A}_{k-1}\|_F) \tag{8.34}$$

$$=0, \tag{8.35}$$

and hence the equation (b) is proved.

5. Finally, the equation (c) can be proved by checking that

$$\lim_{k\to\infty} \|\boldsymbol{Z}_{k+1} - \boldsymbol{Z}_k\|_F \tag{8.36}$$

$$= \lim_{k\to\infty} \|\boldsymbol{X}_k + \rho_{k-1}^{-1}\boldsymbol{A}_{k-1} - \boldsymbol{Z}_k + \boldsymbol{X}_{k+1} - \boldsymbol{X}_k - \rho_{k-1}^{-1}\boldsymbol{A}_{k-1} + \rho_k^{-1}\boldsymbol{A}_k - \rho_k^{-1}\boldsymbol{A}_{k+1}\|_F \tag{8.37}$$

$$\leq \lim_{k\to\infty}(\|\boldsymbol{\Sigma}_{k-1} - \mathcal{S}_{\boldsymbol{w}/\rho_{k-1}}(\boldsymbol{\Sigma}_{k-1})\|_F + \|\boldsymbol{X}_{k+1} - \boldsymbol{X}_k\|_F + \|\rho_{k-1}^{-1}\boldsymbol{A}_{k-1} + \rho_k^{-1}\boldsymbol{A}_{k+1} - \rho_k^{-1}\boldsymbol{A}_k\|_F) \tag{8.38}$$

$$\leq \lim_{k\to\infty}(\rho_{k-1}^{-1}\|\boldsymbol{w}\|_F + \|\boldsymbol{X}_{k+1} - \boldsymbol{X}_k\|_F + \|\rho_{k-1}^{-1}\boldsymbol{A}_{k-1} + \rho_k^{-1}\boldsymbol{A}_{k+1} - \rho_k^{-1}\boldsymbol{A}_k\|_F) \tag{8.39}$$

$$=0, \tag{8.40}$$

where $\boldsymbol{U}_{k-1}\boldsymbol{\Sigma}_{k-1}\boldsymbol{V}_{k-1}^\top$ is the SVD of the matrix $\boldsymbol{X}_k + \rho_{k-1}^{-1}\boldsymbol{A}_{k-1}$.

8.5 Proofs of Theorem 5.2.1 and Theorem 5.3.1

Theorem 8.5.1 *Given $\rho_{k+1} = \mu\rho_k$ ($\rho_0 > 0$) for $k \geq 0$ and $\mu > 1$, the sequences $\{\boldsymbol{C}_k\}$ and $\{\boldsymbol{Z}_k\}$ generated in Algorithm 1 satisfy:*

$$(a)\ \|\boldsymbol{C}_{k+1} - \boldsymbol{Z}_{k+1}\|_F = O(\rho_k^{-1})\ \text{as}\ k \to +\infty,\ \textit{i.e.},\ \lim_{k\to+\infty} \|\boldsymbol{C}_{k+1} - \boldsymbol{Z}_{k+1}\|_F = 0; \tag{8.41}$$

$$(b)\ \textit{If}\ \|\boldsymbol{Z}_{k+1} - \boldsymbol{Z}_k\|_F = O(\rho_k^{-1})\ \text{as}\ k \to +\infty,\ \textit{then}\ \lim_{k\to+\infty} \|\boldsymbol{C}_{k+1} - \boldsymbol{C}_k\|_F = 0; \tag{8.42}$$

$$(c)\ \textit{If}\ \lim_{k\to+\infty} \|\boldsymbol{C}_{k+1} - \boldsymbol{C}_k\|_F = 0,\ \textit{then}\ \lim_{k\to+\infty} \|\boldsymbol{Z}_{k+1} - \boldsymbol{Z}_k\|_F = 0. \tag{8.43}$$

Proof

1. Firstly, we prove that the sequence $\{\boldsymbol{\Delta}_k\}$ generated by Algorithm 1 is upper bounded. Denote

by $\boldsymbol{T}_k = \boldsymbol{C}_{k+1} + \rho_k^{-1}\boldsymbol{\Delta}_k$ in the $(k+1)$-th iteration. According to Eq. (5.16) in the Section 5, we have $\boldsymbol{Z}_{k+1} = \mathcal{S}_{\frac{1}{2\rho_k}}(\boldsymbol{T}_k)$. Then we have

$$\|\boldsymbol{\Delta}_{k+1}\|_F = \|\boldsymbol{\Delta}_k + \rho_k(\boldsymbol{C}_{k+1} - \boldsymbol{Z}_{k+1})\|_F = \rho_k\|\rho_k^{-1}\boldsymbol{\Delta}_k + \boldsymbol{C}_{k+1} - \boldsymbol{Z}_{k+1}\|_F \tag{8.44}$$

$$= \rho_k\|\boldsymbol{T}_k - \mathcal{S}_{\rho_k^{-1}}(\boldsymbol{T}_k)\|_F = \rho_k\sqrt{\sum_{i,j}(\boldsymbol{T}_k^{ij} - \mathcal{S}_{\rho_k^{-1}}(\boldsymbol{T}_k^{ij}))^2} \tag{8.45}$$

$$\leq \rho_k\sqrt{\sum_{i,j}\rho_k^{-2}} = 3p^2M. \tag{8.46}$$

The inequality in Eq. (8-46) can be proved as follows: given the matrix $\boldsymbol{T}_k$, we define $\boldsymbol{T}_k^{ij}$ as the element of the i-th row and j-th column of $\boldsymbol{T}_k$. If $\boldsymbol{T}_k^{ij} \geq \rho_k^{-1}$, we have $\mathcal{S}_{\rho_k^{-1}}(\boldsymbol{T}_k^{ij}) = \boldsymbol{T}_k^{ij} - \rho_k^{-1}$. If $\boldsymbol{T}_k^{ij} < \rho_k^{-1}$, we have $\mathcal{S}_{\rho_k^{-1}}(\boldsymbol{T}_k^{ij}) = 0$. Overall, we have $|\boldsymbol{T}_k^{ij} - \mathcal{S}_{\rho_k^{-1}}(\boldsymbol{T}_k^{ij})| \leq \rho_k^{-1}$ and the inequality holds. Hence, the sequence $\{\boldsymbol{\Delta}_k\}$ is upper bounded.

2. Secondly, we prove that the sequence of Lagrangian function $\{\mathcal{L}(\boldsymbol{C}_{k+1}, \boldsymbol{Z}_{k+1}, \boldsymbol{\Delta}_k, \rho_k)\}$ is also upper bounded. Since we have the globally optimal solution of $\boldsymbol{C}$ and $\boldsymbol{Z}$ in their corresponding subproblems, we always have

$$\mathcal{L}(\boldsymbol{C}_{k+1}, \boldsymbol{Z}_{k+1}, \boldsymbol{\Delta}_k, \rho_k) \leq \mathcal{L}(\boldsymbol{C}_k, \boldsymbol{Z}_k, \boldsymbol{\Delta}_k, \rho_k). \tag{8.47}$$

Based on the updating rule that $\boldsymbol{\Delta}_{k+1} = \boldsymbol{\Delta}_k + \rho_k(\boldsymbol{C}_{k+1} - \boldsymbol{Z}_{k+1})$, we have

$$\mathcal{L}(\boldsymbol{C}_{k+1}, \boldsymbol{Z}_{k+1}, \boldsymbol{\Delta}_{k+1}, \rho_{k+1}) \tag{8.48}$$

$$= \mathcal{L}(\boldsymbol{C}_{k+1}, \boldsymbol{Z}_{k+1}, \boldsymbol{\Delta}_k, \rho_k) + \langle\boldsymbol{\Delta}_{k+1} - \boldsymbol{\Delta}_k, \boldsymbol{C}_{k+1} - \boldsymbol{Z}_{k+1}\rangle + \frac{\rho_{k+1} - \rho_k}{2}\|\boldsymbol{C}_{k+1} - \boldsymbol{Z}_{k+1}\|_F^2 \tag{8.49}$$

$$= \mathcal{L}(\boldsymbol{C}_{k+1}, \boldsymbol{Z}_{k+1}, \boldsymbol{\Delta}_k, \rho_k) + \frac{\rho_{k+1} + \rho_k}{2\rho_k^2}\|\boldsymbol{\Delta}_{k+1} - \boldsymbol{\Delta}_k\|_F^2. \tag{8.50}$$

Since the sequence $\{\boldsymbol{\Delta}_k\}$ is upper bounded, the sequence $\{\boldsymbol{\Delta}_{k+1} - \boldsymbol{\Delta}_k\}$ is also upper bounded.

Denote by a the upper bound of $\{\boldsymbol{\Delta}_{k+1} - \boldsymbol{\Delta}_k\}$, i.e., $\|\boldsymbol{\Delta}_{k+1} - \boldsymbol{\Delta}_k\|_F \leq a$ holds for $\forall k \geq 0$, we have

$$\mathcal{L}(\boldsymbol{C}_{k+1}, \boldsymbol{Z}_{k+1}, \boldsymbol{\Delta}_{k+1}, \rho_{k+1}) \tag{8.51}$$

$$\leq \mathcal{L}(\boldsymbol{C}_1, \boldsymbol{Z}_1, \boldsymbol{A}_0, \rho_0) + a^2 \sum_{k=0}^{+\infty} \frac{\rho_{k+1} + \rho_k}{2\rho_k^2} \tag{8.52}$$

$$= \mathcal{L}(\boldsymbol{C}_1, \boldsymbol{Z}_1, \boldsymbol{A}_0, \rho_0) + a^2 \sum_{k=0}^{+\infty} \frac{\mu + 1}{2\mu^k \rho_0} \tag{8.53}$$

$$\leq \mathcal{L}(\boldsymbol{C}_1, \boldsymbol{Z}_1, \boldsymbol{A}_0, \rho_0) + \frac{a^2}{\rho_0} \sum_{k=0}^{+\infty} \frac{1}{\mu^{k-1}}. \tag{8.54}$$

The last inequality holds since $\mu > 1$ and $\mu + 1 < 2\mu$. Therefore, we have $\sum_{k=0}^{+\infty} \frac{1}{\mu^{k-1}} < +\infty$ and the sequence of Lagrangian function $\{\mathcal{L}(\boldsymbol{C}_{k+1}, \boldsymbol{Z}_{k+1}, \boldsymbol{\Delta}_{k+1}, \rho_{k+1})\}$ is upper bounded.

3. Thirdly, we prove that the sequences of $\{\boldsymbol{C}_k\}$ and $\{\boldsymbol{Z}_k\}$ are upper bounded. Since

$$\|\boldsymbol{W}_1(\boldsymbol{Y} - \boldsymbol{D}\boldsymbol{W}_3\boldsymbol{C}_k)\boldsymbol{W}_2\|_F^2 + \|\boldsymbol{Z}_k\|_1 \tag{8.55}$$

$$= \mathcal{L}(\boldsymbol{C}_k, \boldsymbol{Z}_k, \boldsymbol{\Delta}_{k-1}, \rho_{k-1}) - \langle \boldsymbol{\Delta}_{k-1}, \boldsymbol{C}_k - \boldsymbol{Z}_k \rangle - \frac{\rho_{k-1}}{2} \|\boldsymbol{C}_k - \boldsymbol{Z}_k\|_F^2 \tag{8.56}$$

$$= \mathcal{L}(\boldsymbol{C}_k, \boldsymbol{Z}_k, \boldsymbol{\Delta}_{k-1}, \rho_{k-1}) + \frac{1}{2\rho_{k-1}} (\|\boldsymbol{\Delta}_{k-1}\|_F^2 - \|\boldsymbol{\Delta}_k\|_F^2), \tag{8.57}$$

both $\{\boldsymbol{W}_1(\boldsymbol{Y} - \boldsymbol{D}\boldsymbol{W}_3\boldsymbol{C}_k)\boldsymbol{W}_2\}$ and $\{\boldsymbol{Z}_k\}$ are upper bounded, and hence the sequence $\{\boldsymbol{C}_k\}$ is bounded by the Cauchy-Schwarz inequality and triangle inequality. We can obtain that

$$\lim_{k \to +\infty} \|\boldsymbol{C}_{k+1} - \boldsymbol{Z}_{k+1}\|_F = \lim_{k \to +\infty} \rho_k^{-1} \|\boldsymbol{\Delta}_{k+1} - \boldsymbol{\Delta}_k\|_F = 0. \tag{8.58}$$

Since the sequence of $\{\boldsymbol{\Delta}_k\}$ is upper bounded, we can also easily obtain that $\|\boldsymbol{C}_{k+1} - \boldsymbol{Z}_{k+1}\|_F = O(\rho_k^{-1})$ as $k \to +\infty$ and the equation (a) is proved.

4. Now we prove the equation (b). Denote by $\boldsymbol{A} = \boldsymbol{W}_3^\top \boldsymbol{D}^\top \boldsymbol{W}_1^\top \boldsymbol{W}_1 \boldsymbol{D} \boldsymbol{W}_3$, $\boldsymbol{B} = \frac{1}{2}(\boldsymbol{W}_2 \boldsymbol{W}_2^\top)^{-1}$, and $\boldsymbol{E} = \boldsymbol{W}_3^\top \boldsymbol{D}^\top \boldsymbol{W}_1^\top \boldsymbol{W}_1 \boldsymbol{Y}$, and $\boldsymbol{F}_k = \rho_k(\boldsymbol{Z}_k - \frac{1}{\rho_k}\boldsymbol{\Delta}_k)\boldsymbol{B}$. According to the Eq. (5.13) in the main paper, we have

$$\boldsymbol{A}\boldsymbol{C}_{k+1} + \rho_k \boldsymbol{C}_{k+1}\boldsymbol{B} = \boldsymbol{E} + \boldsymbol{F}_k, \tag{8.59}$$

$$\boldsymbol{A}\boldsymbol{C}_k + \rho_{k-1} \boldsymbol{C}_k \boldsymbol{B} = \boldsymbol{E} + \boldsymbol{F}_{k-1}. \tag{8.60}$$

By calculating the difference between the Eq. (8.60) and Eq. (8.59), we have

$$\begin{aligned}
&\boldsymbol{A}(\boldsymbol{C}_{k+1}-\boldsymbol{C}_k)+\rho_k(\boldsymbol{C}_{k+1}-\boldsymbol{C}_k)\boldsymbol{B}\\
=&\boldsymbol{F}_k-\boldsymbol{F}_{k-1}+\rho_{k-1}\boldsymbol{C}_k\boldsymbol{B}-\rho_k\boldsymbol{C}_k\boldsymbol{B}\\
=&\rho_k(\boldsymbol{Z}_k-\boldsymbol{C}_k)\boldsymbol{B}+(\boldsymbol{\Delta}_{k-1}-\boldsymbol{\Delta}_k)\boldsymbol{B}-\rho_{k-1}(\boldsymbol{Z}_{k-1}-\boldsymbol{C}_k)\boldsymbol{B}\\
=&\rho_k(\boldsymbol{Z}_k-\boldsymbol{C}_k)\boldsymbol{B}+(\boldsymbol{\Delta}_{k-1}-\boldsymbol{\Delta}_k)\boldsymbol{B}+\rho_{k-1}(\boldsymbol{C}_k-\boldsymbol{Z}_k)\boldsymbol{B}+\rho_{k-1}(\boldsymbol{Z}_k-\boldsymbol{Z}_{k-1})\boldsymbol{B}\\
=&\mu(\boldsymbol{\Delta}_{k-1}-\boldsymbol{\Delta}_k)\boldsymbol{B}+\rho_{k-1}(\boldsymbol{Z}_k-\boldsymbol{Z}_{k-1})\boldsymbol{B}.
\end{aligned}\tag{8.61}$$

This equation can be transformed into the following Sylvester equation

$$(\boldsymbol{I}_n\otimes\mathbf{A}+\rho_k\boldsymbol{B}^\top\otimes\mathbf{I}_m)\mathrm{vec}(\boldsymbol{C}_{k+1}-\boldsymbol{C}_k)=\mathrm{vec}(\mu(\boldsymbol{\Delta}_{k-1}-\boldsymbol{\Delta}_k)\boldsymbol{B}+\rho_{k-1}(\boldsymbol{Z}_k-\boldsymbol{Z}_{k-1})\boldsymbol{B}),\tag{8.62}$$

Since $\|\boldsymbol{Z}_{k+1}-\boldsymbol{Z}_k\|_F=O(\rho_k^{-1})$ as $k\to+\infty$, there exist constants $N\in\mathbb{Z}$ and $c\in\mathbb{R}_+$ such that,

$$\rho_k\|\boldsymbol{Z}_{k+1}-\boldsymbol{Z}_k\|_F\le c\quad\text{for all}\quad k>N.\tag{8.63}$$

Note that $\lim_{k\to+\infty}\rho_k=0$ and the solution of the above Sylvester equation is

$$\mathrm{vec}(\boldsymbol{C}_{k+1}-\boldsymbol{C}_k)=(\boldsymbol{I}_n\otimes\mathbf{A}+\rho_k\boldsymbol{B}^\top\otimes\mathbf{I}_m)^{-1}\mathrm{vec}(\mu(\boldsymbol{\Delta}_{k-1}-\boldsymbol{\Delta}_k)\boldsymbol{B}+\rho_{k-1}(\boldsymbol{Z}_k-\boldsymbol{Z}_{k-1})\boldsymbol{B}).\tag{8.64}$$

By Cauchy-Schwarz inequality, we can obtain that

$$\begin{aligned}
&\|\boldsymbol{C}_{k+1}-\boldsymbol{C}_k\|_F=\|\mathrm{vec}(\boldsymbol{C}_{k+1}-\boldsymbol{C}_k)\|_2 &(8.65)\\
=&\|(\boldsymbol{I}_n\otimes\mathbf{A}+\rho_k\boldsymbol{B}^\top\otimes\mathbf{I}_m)^{-1}\mathrm{vec}(\mu(\boldsymbol{\Delta}_{k-1}-\boldsymbol{\Delta}_k)\boldsymbol{B}+\rho_{k-1}(\boldsymbol{Z}_k-\boldsymbol{Z}_{k-1})\boldsymbol{B})\|_2 &(8.66)\\
\le&(\mu a+c)\|(\boldsymbol{I}_n\otimes\mathbf{A}+\rho_k\boldsymbol{B}^\top\otimes\mathbf{I}_m)^{-1}\|_F\|\boldsymbol{B}\|_F. &(8.67)
\end{aligned}$$

Since $\lim_{k\to+\infty}\rho_k=+\infty$, we have that $\lim_{k\to+\infty}\|(\boldsymbol{I}_n\otimes\mathbf{A}+\rho_k\boldsymbol{B}^\top\otimes\mathbf{I}_m)^{-1}\|_F=0$ and

$$\lim_{k\to+\infty}\|\boldsymbol{C}_{k+1}-\boldsymbol{C}_k\|_F=0.\tag{8.68}$$

The equation (b) is proved.

5. Now we prove the argument (c). Denote by $\boldsymbol{T}_{k-1} = \boldsymbol{C}_k + \rho_{k-1}^{-1}\boldsymbol{\Delta}_{k-1}$. Since $\lim_{k\to+\infty}\rho_k = +\infty$ and $\lim_{k\to+\infty}\|\boldsymbol{C}_{k+1} - \boldsymbol{C}_k\|_F = 0$, the argument (c) can be proved by checking that

$$\lim_{k\to+\infty}\|\boldsymbol{Z}_{k+1} - \boldsymbol{Z}_k\|_F \tag{8.69}$$

$$= \lim_{k\to+\infty}\|\boldsymbol{C}_k + \rho_{k-1}^{-1}\boldsymbol{\Delta}_{k-1} - \boldsymbol{Z}_k + \boldsymbol{C}_{k+1} - \boldsymbol{C}_k - \rho_{k-1}^{-1}\boldsymbol{\Delta}_{k-1} + \rho_k^{-1}\boldsymbol{\Delta}_k - \rho_k^{-1}\boldsymbol{\Delta}_{k+1}\|_F \tag{8.70}$$

$$\leq \lim_{k\to+\infty}(\|\boldsymbol{T}_{k-1} - \mathcal{S}_{\rho_{k-1}^{-1}}(\boldsymbol{T}_{k-1})\|_F + \|\boldsymbol{C}_{k+1} - \boldsymbol{C}_k\|_F + \|\rho_{k-1}^{-1}\boldsymbol{\Delta}_{k-1} + \rho_k^{-1}\boldsymbol{\Delta}_{k+1} - \rho_k^{-1}\boldsymbol{\Delta}_k\|_F) \tag{8.71}$$

$$\leq \lim_{k\to+\infty}(3p^2M\rho_{k-1}^{-1} + \|\boldsymbol{C}_{k+1} - \boldsymbol{C}_k\|_F + \|\rho_{k-1}^{-1}\boldsymbol{\Delta}_{k-1} + \rho_k^{-1}\boldsymbol{\Delta}_{k+1} - \rho_k^{-1}\boldsymbol{\Delta}_k\|_F) = 0. \tag{8.72}$$

That is the end of the proof.

Theorem 8.5.2 *Assume that $\boldsymbol{A} \in \mathbb{R}^{3p^2\times 3p^2}$, $\boldsymbol{B} \in \mathbb{R}^{M\times M}$ are both symmetric and positive semi-definite matrices. If at least one of $\boldsymbol{A}, \boldsymbol{B}$ is positive definite, the Sylvester equation $\boldsymbol{AC} + \boldsymbol{CB} = \boldsymbol{E}$ has a unique solution for $\boldsymbol{C} \in \mathbb{R}^{3p^2\times M}$.*

Proof Since $\boldsymbol{A}, \boldsymbol{B}$ are symmetric matrices, they can be diagonalized as $\boldsymbol{A} = \boldsymbol{U_A}\boldsymbol{\Sigma_A}\boldsymbol{U_A}^\top$, $\boldsymbol{B} = \boldsymbol{U_B}\boldsymbol{\Sigma_B}\boldsymbol{U_B}^\top$, where $\boldsymbol{\Sigma_A} = \mathrm{diag}(\lambda_A^1, ..., \lambda_A^{3p^2})$ and $\boldsymbol{\Sigma_B} = \mathrm{diag}(\lambda_B^1, ..., \lambda_B^M)$ are diagonal matrices. Since $\boldsymbol{A}, \boldsymbol{B}$ are positive semi-definite matrices, their corresponding eigenvalues are non-negative, i.e., $\lambda_A^i \geq 0$ for $\forall i = 1, ..., 3p^2$ and $\lambda_B^j \geq 0$ for $\forall j = 1, ..., M$. If at least one of the matrices $\boldsymbol{A}, \boldsymbol{B}$ is positive definite, then $\lambda_A^i + \lambda_B^j > 0$ holds true for $\forall i, j$ and $\sigma(\boldsymbol{A}) \cap \sigma(-\boldsymbol{B}) = \emptyset$. Therefore, the Sylvester equation $\boldsymbol{AC} + \boldsymbol{CB} = \boldsymbol{E}$ has a unique solution.

Bibliography

[1] The most commonly used camera-lens combinations. https://explorecams.com/stats/top/models. Accessed: 2017-09-11. 132

[2] Neatlab ABSoft. Neat Image. https://ni.neatvideo.com/home. 10, 11, 13, 42, 43, 46, 47, 60, 64, 68, 74, 75, 85, 86, 100, 101, 116, 139

[3] M. Aharon, M. Elad, and A. Bruckstein. The K-SVD: An algorithm for designing overcomplete dictionaries for sparse representation. *IEEE Transactions on Signal Processing*, 54(11):4311–4322, 2006. 7, 8, 17

[4] Josue Anaya and Adrian Barbu. Renoir - a dataset for real low-light noise image reduction. *arXiv preprint arXiv:1409.8230*, 2014. xxii, 123, 125, 126, 127, 128, 129, 131, 135, 136, 138

[5] P. Arbelaez, M. Maire, C. Fowlkes, and J. Malik. Contour detection and hierarchical image segmentation. *IEEE Trans. Pattern Anal. Mach. Intell.*, 33(5):898–916, 2011. 28, 34

[6] European Machine Vision Association. Emva standard 1288: Standard for characterization of image sensors and cameras. 2012. 125

[7] Adrian Barbu. Training an active random field for real-time image denoising. *IEEE Transactions on Image Processing*, 18(11):2451–2462, 2009. 42, 43, 44, 45

[8] E. Bareiss. Sylvesters identity and multistep integer-preserving gaussian elimination. *Mathematics of computation*, 22(103):565–578, 1968. 111

[9] R. H. Bartels and G. W. Stewart. Solution of the matrix equation AX + XB = C. *Commun. ACM*, 15(9):820–826, 1972. 111

[10] C. M. Bishop. *Pattern recognition and machine learning*. New York: Springer, 2006. 4, 8, 16, 21

[11] S. Boyd, N. Parikh, E. Chu, B. Peleato, and J. Eckstein. Distributed optimization and statistical learning via the alternating direction method of multipliers. *Found. Trends Mach. Learn.*, 3(1):1–122, January 2011. 76, 80, 102, 106, 107

[12] A. Buades, B. Coll, and J. M. Morel. A non-local algorithm for image denoising. *IEEE Conference on Computer Vision and Pattern Recognition (CVPR)*, pages 60–65, 2005. 7, 8, 15, 17, 18, 42, 43, 45, 73

[13] H. C. Burger, C. J. Schuler, and S. Harmeling. Image denoising: Can plain neural networks compete with BM3D? *IEEE Conference on Computer Vision and Pattern Recognition (CVPR)*, pages 2392–2399, 2012. 7, 9, 42, 43, 44, 45, 60, 64, 68, 73, 77, 85, 86, 93, 100, 101, 138

[14] J. Cai, E. J. Candès, and Z. Shen. A singular value thresholding algorithm for matrix completion. *SIAM Journal on Optimization*, 20(4):1956–1982, 2010. 76

[15] Emmanuel J Candès and Michael B Wakin. An introduction to compressive sampling. *IEEE signal processing magazine*, 25(2):21–30, 2008. 8

[16] S. G. Chang, B. Yu, and M. Vetterli. Adaptive wavelet thresholding for image denoising and compression. *Image Processing, IEEE Transactions on*, 9(9):1532–1546, 2000. 7, 15, 16, 42, 43, 45

[17] Fei Chen, Lei Zhang, and Huimin Yu. External patch prior guided internal clustering for image denoising. *Proceedings of the IEEE international conference on computer vision*, pages 603–611, 2015. 42, 43, 44, 45

[18] G. Chen, F. Zhu, and A. H. Pheng. An efficient statistical method for image noise level estimation. *IEEE International Conference on Computer Vision (ICCV)*, December

2015. 62, 85, 104, 116, 139

[19] Y. Chen, W. Yu, and T. Pock. On learning optimized reaction diffusion processes for effective image restoration. *IEEE Conference on Computer Vision and Pattern Recognition (CVPR)*, pages 5261–5269, 2015. 7, 9, 42, 43, 44, 45, 60, 64, 68, 73, 77, 85, 86, 93, 100, 101, 112, 113, 116, 139

[20] R. Courant. Variational methods for the solution of problems of equilibrium and vibrations. *Bull. Amer. Math. Soc.*, 49(1):1–23, 1943. 80

[21] K. Dabov, A. Foi, V. Katkovnik, and K. Egiazarian. Color image denoising via sparse 3D collaborative filtering with grouping constraint in luminance-chrominance space. *IEEE International Conference on Image Processing (ICIP)*, pages 313–316, 2007. 10, 42, 43, 45, 60, 74, 75, 85, 86, 100, 101, 116, 138

[22] K. Dabov, A. Foi, V. Katkovnik, and K. Egiazarian. Image denoising by sparse 3-D transform-domain collaborative filtering. *IEEE Transactions on Image Processing*, 16(8):2080–2095, 2007. 3, 7, 8, 10, 11, 15, 17, 18, 23, 31, 42, 43, 45, 64, 67, 68, 73, 74, 75, 77, 100, 101, 112, 113, 128

[23] A. P. Dempster, N. M. Laird, and D. B. Rubin. Maximum likelihood from incomplete data via the EM algorithm. *Journal of the Royal Statistical Society. Series B (methodological)*, pages 1–38, 1977. 21

[24] W. Dong, L. Zhang, G. Shi, and X. Li. Nonlocally centralized sparse representation for image restoration. *IEEE Transactions on Image Processing*, 22(4):1620–1630, 2013. 7, 9, 11, 15, 17, 18, 31, 42, 43, 44, 45, 59, 73, 77, 100, 101, 103, 112, 113, 138

[25] D. L. Donoho. De-noising by soft-thresholding. *IEEE Trans. Inf. Theory*, 41(3):613–627, 1995. 7, 15

[26] D. L. Donoho. Compressed sensing. *IEEE Transactions on Information Theory*, 52(4):1289–1306, 2006. 8

[27] D. L. Donoho and X. Huo. Uncertainty principles and ideal atomic decomposition.

IEEE Transactions on Information Theory, 47(7):2845–2862, 2001. 50

[28] C. Eckart and G. Young. The approximation of one matrix by another of lower rank. *Psychometrika*, 1(3):211–218, 1936. 49, 52, 53, 76, 152, 153, 155

[29] J. Eckstein and D. P. Bertsekas. On the Douglas–Rachford splitting method and the proximal point algorithm for maximal monotone operators. *Mathematical Programming*, 55(1):293–318, 1992. 80, 106

[30] M. Elad and M. Aharon. Image denoising via sparse and redundant representations over learned dictionaries. *IEEE Transactions on Image Processing*, 15(12):3736–3745, 2006. 3, 7, 8, 11, 15, 17, 20, 42, 43, 44, 45, 73, 77, 100, 101, 103

[31] A. Foi, S. Alenius, V. Katkovnik, and K. Egiazarian. Noise measurement for raw-data of digital imaging sensors by automatic segmentation of nonuniform targets. *IEEE Sensors Journal*, 7(10):1456–1461, 2007. 125

[32] A. Foi, M. Trimeche, V. Katkovnik, and K. Egiazarian. Practical poissonian-gaussian noise modeling and fitting for single-image raw-data. *IEEE Transactions on Image Processing*, 17(10):1737–1754, 2008. 2, 3, 42

[33] G. Golub and C. Van Loan. *Matrix Computations (3rd Ed.)*. Johns Hopkins University Press, 1996. 111

[34] Z. Gong, Z. Shen, and K.-C. Toh. Image restoration with mixed or unknown noises. *Multiscale Modeling & Simulation*, 12(2):458–487, 2014. 42, 43, 46, 47

[35] S. Gu, Q. Xie, D. Meng, W. Zuo, X. Feng, and L. Zhang. Weighted nuclear norm minimization and its applications to low level vision. *International Journal of Computer Vision*, pages 1–26, 2016. 75, 76, 78, 80, 81, 82, 85, 155

[36] S. Gu, L. Zhang, W. Zuo, and X. Feng. Weighted nuclear norm minimization with application to image denoising. *IEEE Conference on Computer Vision and Pattern Recognition (CVPR)*, pages 2862–2869, 2014. 7, 9, 11, 13, 15, 17, 18, 31, 42, 43, 45, 60, 64, 67, 68, 73, 74, 75, 76, 77, 85, 100, 101, 112, 113, 116, 139

[37] Kaiming He, Xiangyu Zhang, Shaoqing Ren, and Jian Sun. Deep residual learning for image recognition. In *Proceedings of the IEEE conference on computer vision and pattern recognition*, pages 770–778, 2016. 9

[38] G. E Healey and R. Kondepudy. Radiometric CCD camera calibration and noise estimation. *IEEE Transactions on Pattern Analysis and Machine Intelligence*, 16(3):267–276, 1994. 2, 45, 46, 123

[39] N. J. Higham. Computing the nearest correlation matrix: a problem from finance. *IMA Journal of Numerical Analysis*, 22(3):329, 2002. 99

[40] Haijuan Hu, Bing Li, and Quansheng Liu. Removing mixture of gaussian and impulse noise by patch-based weighted means. *Journal of Scientific Computing*, 67(1):103–129, 2016. 42

[41] P. J. Huber. *Robust statistics*. Springer, 2011. 10

[42] H. Ji, C. Liu, Z. Shen, and Y. Xu. Robust video denoising using low rank matrix completion. *CVPR*, pages 1791–1798, 2010. 7, 9, 15, 17

[43] Jielin Jiang, Lei Zhang, and Jian Yang. Mixed noise removal by weighted encoding with sparse nonlocal regularization. *IEEE transactions on image processing*, 23(6):2651–2662, 2014. 42

[44] Z. Jiang, Z. Lin, and L. S. Davis. Label consistent k-svd: Learning a discriminative dictionary for recognition. *IEEE Transactions on Pattern Analysis and Machine Intelligence*, 35(11):2651–2664, 2013. 8, 17

[45] H. C. Karaimer and M. S. Brown. A software platform for manipulating the camera imaging pipeline. *European Conference on Computer Vision (ECCV)*, October 2016. 3, 10, 11, 46, 75

[46] C. Kervrann, J. Boulanger, and P. Coupé. Bayesian non-local means filter, image redundancy and adaptive dictionaries for noise removal. *International Conference on Scale Space and Variational Methods in Computer Vision*, pages 520–532, 2007. 11, 46, 74,

75

[47] S. J. Kim, H. T. Lin, Z. Lu, S. Ssstrunk, S. Lin, and M. S. Brown. A new in-camera imaging model for color computer vision and its application. *IEEE Transactions on Pattern Analysis and Machine Intelligence*, 34(12):2289–2302, 2012. 46

[48] Walter Kristof. A theorem on the trace of certain matrix products and some applications. *Journal of Mathematical Psychology*, 7(3):515 – 530, 1970. 153

[49] M. Lebrun, A. Buades, and J. M. Morel. A nonlocal Bayesian image denoising algorithm. *SIAM Journal on Imaging Sciences*, 6(3):1665–1688, 2013. 11, 42, 43, 45, 46

[50] M. Lebrun, M. Colom, and J. M. Morel. The noise clinic: a blind image denoising algorithm. http://www.ipol.im/pub/art/2015/125/. Accessed 01 28, 2015. xiv, xv, xvii, xix, 11, 43, 46, 47, 56, 57, 60, 61, 62, 63, 64, 68, 74, 75, 85, 89, 91, 93, 94, 95, 115, 118, 119, 139

[51] M. Lebrun, M. Colom, and J.-M. Morel. Multiscale image blind denoising. *IEEE Transactions on Image Processing*, 24(10):3149–3161, 2015. 10, 11, 42, 43, 46, 47, 60, 64, 68, 74, 75, 85, 86, 100, 101, 116, 139

[52] B. Leung, G. Jeon, and E. Dubois. Least-squares luma-chroma demultiplexing algorithm for bayer demosaicking. *IEEE Transactions on Image Processing*, 20(7):1885–1894, 2011. 11, 75, 78, 79, 104

[53] C. Liu, R. Szeliski, S. Bing Kang, C. L. Zitnick, and W. T. Freeman. Automatic estimation and removal of noise from a single image. *IEEE Transactions on Pattern Analysis and Machine Intelligence*, 30(2):299–314, 2008. 10, 11, 42, 43, 46, 47, 74, 75, 78, 100, 101, 126

[54] X. Liu, M. Tanaka, and M. Okutomi. Single-image noise level estimation for blind denoising. *IEEE Transactions on Image Processing*, 22(12):5226–5237, 2013. 62, 85, 139

[55] X. Liu, M. Tanaka, and M. Okutomi. Practical signal-dependent noise parameter estimation from a single noisy image. *IEEE Transactions on Image Processing*, 23(10):4361–4371, 2014. 126

[56] F. Luisier, T. Blu, and M. Unser. Image denoising in mixed Poisson-Gaussian noise. *IEEE Transactions on Image Processing*, 20(3):696–708, 2011. 42

[57] Enming Luo, Stanley H Chan, and Truong Q Nguyen. Adaptive image denoising by targeted databases. *IEEE Transactions on Image Processing*, 24(7):2167–2181, 2015. 43, 44, 45

[58] J. Mairal, F. Bach, J. Ponce, G. Sapiro, and A. Zisserman. Non-local sparse models for image restoration. *IEEE International Conference on Computer Vision (ICCV)*, pages 2272–2279, 2009. 7, 9, 11, 15, 17, 18, 19, 20, 31, 42, 43, 44, 45, 73, 77, 100, 101, 103, 112, 113

[59] J. Mairal, M. Elad, and G. Sapiro. Sparse representation for color image restoration. *IEEE Transactions on Image Processing,*, 17(1):53–69, 2008. 7, 8, 17, 19, 143

[60] J. Mairal, M. Elad, and G. Sapiro. Sparse representation for color image restoration. *IEEE Transactions on Image Processing*, 17(1):53–69, 2008. 74, 75

[61] Julien Mairal, Francis Bach, Jean Ponce, and Guillermo Sapiro. Online dictionary learning for sparse coding. In *Proceedings of the 26th Annual International Conference on Machine Learning*, ICML, pages 689–696, New York, NY, USA, 2009. ACM. 7, 8

[62] M. Makitalo and A. Foi. Optimal inversion of the generalized anscombe transformation for poisson-gaussian noise. *IEEE Transactions on Image Processing*, 22(1):91–103, 2013. 7, 42, 60, 64, 67, 68

[63] P. McCullagh. Generalized linear models. *European Journal of Operational Research*, 16(3):285–292, 1984. 104

[64] Teodor Mihai Moldovan, Stefan Roth, and Michael J Black. Denoising archival films using a learned bayesian model. In *Image Processing, 2006 IEEE International Con-*

ference on, pages 2641–2644. IEEE, 2006. 125

[65] Y. Le Montagner, E. D. Angelini, and J. C. Olivo-Marin. An unbiased risk estimator for image denoising in the presence of mixed poisson-gaussian noise. *IEEE Transactions on Image Processing*, 23(3):1255–1268, 2014. 42

[66] Anush Krishna Moorthy and Alan Conrad Bovik. A two-step framework for constructing blind image quality indices. *IEEE Signal processing letters*, 17(5):513–516, 2010. 5, 6, 124

[67] I. Mosseri, M. Zontak, and M. Irani. Combining the power of internal and external denoising. *IEEE International Conference on Computational Photography (ICCP)*, pages 1–9, 2013. 42, 43, 44, 45

[68] S. Nam, Y. Hwang, Y. Matsushita, and S. J. Kim. A holistic approach to cross-channel image noise modeling and its application to image denoising. *IEEE Conference on Computer Vision and Pattern Recognition (CVPR)*, pages 1683–1691, 2016. xiv, xv, xvi, xviii, xix, xx, xxi, xxii, 3, 10, 11, 42, 43, 44, 45, 46, 47, 56, 58, 59, 60, 61, 62, 63, 64, 65, 66, 67, 68, 69, 70, 74, 75, 78, 85, 89, 90, 92, 93, 94, 96, 97, 98, 99, 100, 101, 115, 116, 117, 120, 121, 122, 123, 124, 125, 126, 127, 128, 129, 131, 132, 134, 135, 136, 138, 140, 141, 145

[69] B. A. Olshausen and D. J. Field. Emergence of simple-cell receptive field properties by learning a sparse code for natural images. *Nature*, 381(6583):607–609, 1996. 8, 17

[70] B. A. Olshausen and D. J. Field. Sparse coding with an overcomplete basis set: A strategy employed by V1? *Vision research*, 37(23):3311–3325, 1997. 8, 17

[71] S. Osher, M. Burger, D. Goldfarb, J. Xu, and W. Yin. An iterative regularization method for total variation-based image restoration. *Multiscale Modeling & Simulation*, 4(2):460–489, 2005. 7, 9, 10, 15, 16, 26

[72] P. Perona and J. Malik. Scale-space and edge detection using anisotropic diffusion. *Pattern Analysis and Machine Intelligence, IEEE Transactions on*, 12(7):629–639, 1990.

7, 9, 15

[73] G. Peyré, S. Bougleux, and L. D. Cohen. Non-local regularization of inverse problems. *Inverse Problems and Imaging*, 5(2):511–530, 2011. 17

[74] Tobias Plötz and Stefan Roth. Benchmarking denoising algorithms with real photographs. *CVPR*, 2017. xx, xxii, 10, 11, 123, 125, 127, 128, 129, 131, 134, 135, 136, 138, 141, 142, 145

[75] Nikolay Ponomarenko, Vladimir Lukin, Alexander Zelensky, and Karen Egiazarian. Tid2008-a database for evaluation of full-reference visual quality assessment metrics. 10(4):30–45, 2009. 124

[76] J. Portilla. Full blind denoising through noise covariance estimation using Gaussian scale mixtures in the wavelet domain. *IEEE International Conference on Image Processing (ICIP)*, 2:1217–1220, 2004. 10, 11, 42, 43, 46, 47

[77] J. Portilla, V. Strela, M.J. Wainwright, and E.P. Simoncelli. Image denoising using scale mixtures of Gaussians in the wavelet domain. *Image Processing, IEEE Transactions on*, 12(11):1338–1351, 2003. 7, 8, 10, 16, 42, 43, 44, 45

[78] T. Rabie. Robust estimation approach for blind denoising. *IEEE Transactions on Image Processing*, 14(11):1755–1765, 2005. 10, 11, 43, 46, 47

[79] S. Roth and M. J. Black. Fields of experts. *International Journal of Computer Vision*, 82(2):205–229, 2009. 7, 8, 16, 42, 43, 44, 45, 74, 77

[80] L. I. Rudin, S. Osher, and E. Fatemi. Nonlinear total variation based noise removal algorithms. *Physica D: Nonlinear Phenomena*, 60(1):259–268, 1992. 7, 9, 10, 15, 16

[81] Michele A Saad, Alan C Bovik, and Christophe Charrier. Blind image quality assessment: A natural scene statistics approach in the dct domain. *IEEE transactions on Image Processing*, 21(8):3339–3352, 2012. 5, 6, 124

[82] Joseph Salmon, Zachary Harmany, Charles-Alban Deledalle, and Rebecca Willett. Poisson noise reduction with non-local pca. *Journal of mathematical imaging and*

vision, 48(2):279–294, 2014. 42

[83] U. Schmidt and S. Roth. Shrinkage fields for effective image restoration. *IEEE Conference on Computer Vision and Pattern Recognition (CVPR)*, pages 2774–2781, June 2014. 7, 9, 16, 42, 43, 44, 45, 60, 64, 68, 73, 77, 100, 101, 138

[84] H. R. Sheikh, M. F. Sabir, and A. C. Bovik. A statistical evaluation of recent full reference image quality assessment algorithms. *IEEE Transactions on Image Processing*, 15(11):3440–3451, Nov 2006. 124

[85] V. Simoncini. Computational methods for linear matrix equations. *SIAM Review*, 58(3):377–441, 2016. 107

[86] J. L. Starck, E. J. Candès, and D. L. Donoho. The curvelet transform for image denoising. *IEEE Transactions on Image Processing*, 11(6):670–684, 2002. 7, 15, 42, 43, 45

[87] Jos M. F. Ten Berge. A generalization of kristof's theorem on the trace of certain matrix products. *Psychometrika*, 48(4):519–523, 1983. 153

[88] Robert Tibshirani. Regression shrinkage and selection via the lasso. *Journal of the Royal Statistical Society. Series B (Methodological)*, pages 267–288, 1996. 4, 101, 103

[89] C. Tomasi and R. Manduchi. Bilateral filtering for gray and color images. *IEEE International Conference on Computer Vision (ICCV)*, pages 839–846, 1998. 7, 15, 42, 43, 45

[90] Y. Tsin, Visvanathan Ramesh, and Takeo Kanade. Statistical calibration of ccd imaging process. *IEEE International Conference on Computer Vision (ICCV)*, 1:480–487, 2001. 46, 123

[91] S. Wang, L. Zhang, and Y. Liang. Non-local spectral prior model for low-level vision. *ACCV*, pages 231–244, 2013. 17

[92] Z. Wang, A. C. Bovik, H. R. Sheikh, and E. P. Simoncelli. Image quality assessment: from error visibility to structural similarity. *IEEE Transactions on Image Processing*,

13(4):600–612, 2004. xxi, xxii, 5, 64, 65, 68, 69, 112, 116, 138, 142

[93] Zhou Wang, Eero P Simoncelli, and Alan C Bovik. Multiscale structural similarity for image quality assessment. In *Signals, Systems and Computers, 2004. Conference Record of the Thirty-Seventh Asilomar Conference on*, volume 2, pages 1398–1402. IEEE, 2003. 5, 6

[94] Y. Weiss and W. T. Freeman. What makes a good model of natural images? *CVPR*, pages 1–8, 2007. 10, 16

[95] J. Wright, Y. Ma, J. Mairal, G. Sapiro, T. S. Huang, and S. Yan. Sparse representation for computer vision and pattern recognition. *Proceedings of the IEEE*, 98(6):1031–1044, 2010. 8, 17

[96] J. Wright, A. Y. Yang, A. Ganesh, S. S. Sastry, and Y. Ma. Robust face recognition via sparse representation. *IEEE Transactions on Pattern Analysis and Machine Intelligence*, 31(2):210–227, 2009. 101

[97] C. F. Wu. On the convergence properties of the EM algorithm. *The Annals of Statistics*, pages 95–103, 1983. 21

[98] Junyuan Xie, Linli Xu, and Enhong Chen. Image denoising and inpainting with deep neural networks. *Advances in Neural Information Processing Systems*, pages 341–349, 2012. 42, 43, 44, 45

[99] Jun Xu, Dongwei Ren, Lei Zhang, and David Zhang. Patch group based bayesian learning for blind image denoising. *Asian Conference on Computer Vision (ACCV) New Trends in Image Restoration and Enhancement Workshop*, pages 79–95, 2016. 42

[100] Jun Xu, Lei Zhang, and David Zhang. External prior guided internal prior learning for real noisy image denoising. *https://arxiv.org/abs/1705.04505*, 2017. 139

[101] Jun Xu, Lei Zhang, and David Zhang. A trilateral weigted sparse coding scheme for robust image denoising. *Unpublished Draft*, 2017. 139

[102] Jun Xu, Lei Zhang, David Zhang, and Xiangchu Feng. Multi-channel weighted nuclear

norm minimization for real color image denoising. In *ICCV*, 2017. 139

[103] Jun Xu, Lei Zhang, Wangmeng Zuo, David Zhang, and Xiangchu Feng. Patch group based nonlocal self-similarity prior learning for image denoising. In *ICCV*, 2015. 42, 43, 44, 45, 48, 49, 73, 77, 100, 101, 139

[104] Jianchao Yang, John Wright, Thomas S Huang, and Yi Ma. Image super-resolution via sparse representation. *IEEE transactions on image processing*, 19(11):2861–2873, 2010. 101

[105] G. Yu, G. Sapiro, and S. Mallat. Solving inverse problems with piecewise linear estimators: From Gaussian mixture models to structured sparsity. *IEEE Transactions on Image Processing*, 21(5):2481–2499, 2012. 7, 8, 11, 17, 20, 22

[106] B. Zhang, J. M. Fadili, and J. L. Starck. Wavelets, ridgelets, and curvelets for poisson noise removal. *IEEE Transactions on Image Processing*, 17(7):1093–1108, 2008. 42

[107] K. Zhang, W. Zuo, Y. Chen, D. Meng, and L. Zhang. Beyond a gaussian denoiser: Residual learning of deep cnn for image denoising. *IEEE Transactions on Image Processing*, 2017. 7, 9, 42, 43, 44, 45, 60, 64, 68, 73, 77, 85, 86, 100, 101, 112, 113, 116, 139

[108] Q. Zhao, D. Meng, Z. Xu, W. Zuo, and L. Zhang. Robust principal component analysis with complex noise. *ICML*, pages 55–63, 2014. 101, 102

[109] Mingyuan Zhou, Haojun Chen, John Paisley, Lu Ren, Lingbo Li, Zhengming Xing, David Dunson, Guillermo Sapiro, and Lawrence Carin. Nonparametric bayesian dictionary learning for analysis of noisy and incomplete images. *IEEE Transactions on Image Processing*, 21(1):130–144, 2012. 42, 43, 44, 45

[110] F. Zhu, G. Chen, and P.-A. Heng. From noise modeling to blind image denoising. *IEEE Conference on Computer Vision and Pattern Recognition (CVPR)*, June 2016. 10, 11, 43, 46, 47, 74, 75, 100, 101, 102

[111] D. Zoran and Y. Weiss. From learning models of natural image patches to whole image

restoration. *IEEE International Conference on Computer Vision (ICCV)*, pages 479–486, 2011. 7, 8, 12, 17, 20, 22, 23, 31, 42, 43, 44, 45, 49, 73, 77, 100, 101, 138, 147

[112] D. Zoran and Y. Weiss. Natural images, Gaussian mixtures and dead leaves. *NIPS*, pages 1736–1744, 2012. 7, 8, 17